

# **CRYSTAL STRUCTURES AND PHASE TRANSITIONS IN THE RARE EARTH OXIDES**

**STUART C. ATKINSON**

School of Computing, Science and Engineering

University of Salford, Salford, UK

Submitted in partial fulfilment of the requirements of the degree of

Doctor of Philosophy

July 2013

# TABLE OF CONTENTS

|  |             |
|--|-------------|
| <b>LIST OF FIGURES</b>   | <b>VII</b>  |
| <b>LIST OF TABLES</b>  | <b>XIII</b> |
| <b>ACKNOWLEDGEMENTS</b>  | <b>XV</b>   |
| <b>DECLARATION</b>   | <b>XVI</b>  |
| <b>ABSTRACT</b>  | <b>XVII</b> |
| <br>   |             |
| <b>1 INTRODUCTION</b>  | <b>1</b>    |
| <b>1.1 THE RARE EARTHS</b>   | <b>1</b>    |
| <b>1.2 THE STABILITY OF THE TRIPOSITIVE OXIDATION STATE</b>                            | <b>3</b>    |
| <b>1.3 THE LANTHANIDE CONTRACTION</b>  | <b>6</b>    |
| 1.3.1 The lanthanide contraction illustrated in unit cell parameters                   | 9           |
| <b>1.4 LANTHANOID COMPOUNDS</b>  | <b>12</b>   |
| 1.4.1 Overview   | 12          |
| 1.4.2 The lanthanoid sesquioxides  | 13          |
| 1.4.3 The praseodymium-oxygen system   | 17          |
| <b>1.5 AIMS OF THIS WORK</b>   | <b>19</b>   |
| 1.5.1 Determination of structures resulting from temperature-induced phase transitions | 19          |
| 1.5.2 Kinetic studies  | 21          |
| 1.5.3 Investigating and redrawing phase diagrams                                       | 22          |
| <br>   |             |
| <b>2 X-RAY DIFFRACTION</b>   | <b>23</b>   |
| <b>2.1 THEORY</b>  | <b>23</b>   |
| 2.1.1 The Bragg Construction   | 23          |
| 2.1.2 Describing crystal planes and reflections  | 24          |
| 2.1.3 Crystal planes   | 27          |

|  |           |
|--|-----------|
| 2.1.4 The Bragg equation reflected in crystal symmetry | 28        |
| 2.1.5 Point groups and space groups                    | 30        |
| <b>2.2 EXPERIMENTAL DETAILS</b>                        | <b>31</b> |
| 2.2.1 The X-ray powder diffraction (XRPD) pattern      | 31        |
| 2.2.2 The factors that contribute to a powder pattern  | 33        |
| 2.2.2.1 Peak position and intensity                    | 33        |
| 2.2.2.2 Peak width                                     | 37        |
| 2.2.2.3 Short range order                              | 38        |
| 2.2.3 Sources of X-rays                                | 38        |
| 2.2.3.1 The X-ray tube                                 | 38        |
| 2.2.3.2 Synchrotron source                             | 41        |
| 2.2.3.2.1 Introduction                                 | 41        |
| 2.2.3.2.2 Parts of the synchrotron machine             | 43        |
| 2.2.3.2.3 Beamline Schematic                           | 45        |
| 2.2.4 The X-ray powder diffractometer                  | 46        |
| 2.2.4.1 Introduction                                   | 46        |
| 2.2.4.2 The parts of the diffractometer                | 47        |
| 2.2.4.3 Sample preparation                             | 49        |
| 2.2.4.4 Calibration standard                           | 50        |
| 2.2.4.5 Data collection                                | 51        |
| 2.2.4.6 Output data                                    | 51        |
| <b>2.3 STRUCTURE DETERMINATION</b>                     | <b>51</b> |
| 2.3.1 Treatment of data from the diffractometer        | 52        |
| 2.3.1.1 Raw data                                       | 52        |
| 2.3.1.2 Background removal                             | 53        |
| 2.3.1.3 $K\alpha_2$ stripping                          | 53        |
| 2.3.1.4 Peak identification                            | 53        |
| 2.3.1.5 Corrections factors                            | 53        |
| 2.3.2 Indexing   | 54        |
| 2.3.2.1 Graphical methods                              | 54        |
| 2.3.2.2 Arithmetical methods                           | 56        |
| 2.3.2.2.1 Cubic system                                 | 56        |
| 2.3.2.2.2 Tetragonal system                            | 59        |

|   |            |
|---|------------|
| 2.3.2.2.3 Hexagonal system  | 61         |
| 2.3.2.2.5 Monoclinic system   | 64         |
| 2.3.2.2.6 Triclinic system  | 64         |
| 2.3.2.3 The indexing suite  | 65         |
| 2.3.3 Assigning the space group   | 66         |
| 2.3.4 Establishing the atom positions   | 66         |
| 2.3.5 Full profile refinement   | 68         |
| 2.3.5.1 Introduction  | 68         |
| 2.3.5.2 Factors contributing to the wave envelope   | 69         |
| 2.3.5.3 Least squares parameters  | 72         |
| 2.3.5.4 Measuring the quality of the refinement   | 73         |
| <b>3 DIFFERENTIAL SCANNING CALORIMETRY</b>  | <b>75</b>  |
| <b>3.1 INTRODUCTION</b>   | <b>75</b>  |
| <b>3.2 INSTRUMENTATION</b>  | <b>75</b>  |
| <b>3.3 INSTRUMENTAL OUTPUT</b>  | <b>80</b>  |
| <b>4 REACTION KINETICS</b>  | <b>85</b>  |
| <b>4.1 INTRODUCTION</b>   | <b>85</b>  |
| <b>4.2 PHASE BOUNDARIES</b>   | <b>85</b>  |
| <b>4.3 DATA USED IN KINETIC MODELLING</b>   | <b>86</b>  |
| 4.3.1 Data from XRPD  | 86         |
| 4.3.2 Data from DSC   | 87         |
| <b>4.4 SHRINKING SPHERE MODEL</b>   | <b>87</b>  |
| <b>4.5 THE JMAK MODEL</b>   | <b>92</b>  |
| <b>4.6 KISSINGER ANALYSIS</b>   | <b>98</b>  |
| <b>5 SOFTWARE USED IN THIS WORK</b>   | <b>102</b> |
| <b>5.1 SOFTWARE FOR XRPD</b>  | <b>102</b> |
| 5.1.1 Determining the peak positions, calculating peak area, stacking of patterns –<br>PowderX and WINPLOTR | 102        |

|  |            |
|--|------------|
| 5.1.2 Indexing – the Crysfire Indexing Suite and GRAPHPRO        | 104        |
| 5.1.3 Space group determination – CHEKCELL                       | 106        |
| 5.1.4 Full profile refinement – GSAS                             | 108        |
| <b>5.2 SOFTWARE FOR DSC-TG</b>                                   | <b>109</b> |
| <br>   |            |
| <b>6 SAMPLE PREPARATION AND EXPERIMENTAL CONDITIONS</b>          | <b>111</b> |
| <b>6.1 AMBIENT TEMPERATURE XRPD</b>                              | <b>111</b> |
| 6.1.1 Preliminary XRPD patterns on untreated samples             | 111        |
| 6.1.2 Sample annealing   | 112        |
| 6.1.3 Post-annealing XRPD  | 112        |
| <b>6.2 IN SITU HIGH-TEMPERATURE XRPD</b>                         | <b>113</b> |
| 6.2.1 Praseodymia ramp in air                                    | 113        |
| 6.2.2 Praseodymia isothermal hold in air - phase change at 275°C | 113        |
| 6.2.3 Praseodymia quench in air                                  | 113        |
| <b>6.3 DSC-TG</b>  | <b>114</b> |
| 6.3.1 Praseodymia  | 114        |
| 6.3.1.1 Wide run in nitrogen                                     | 114        |
| 6.3.1.2 Wide run in air  | 114        |
| 6.3.1.3 Ramps in nitrogen  | 114        |
| 6.3.1.4 Ramps in air   | 115        |
| 6.3.1.5 Gas absorption   | 115        |
| 6.3.2 Terbia   | 115        |
| 6.3.2.1 Wide run in nitrogen                                     | 115        |
| <br>   |            |
| <b>7 RESULTS FROM X-RAY POWDER DIFFRACTION</b>                   | <b>116</b> |
| <b>7.1 AMBIENT TEMPERATURE XRPD</b>                              | <b>116</b> |
| 7.1.1 Diffraction patterns                                       | 116        |
| 7.1.2 Ambient temperature cell types                             | 123        |
| 7.1.3 Ambient temperature crystal structures                     | 125        |
| 7.1.3.1 The C-type phase   | 125        |

|  |            |
|--|------------|
| 7.1.3.2 The B-type phase   | 127        |
| 7.1.3.3 The A-type phase   | 128        |
| 7.1.4 Discussion on ambient temperature results  | 128        |
| <b>7.2 XRPD AFTER ANNEALING</b>  | <b>130</b> |
| 7.2.1 Diffraction patterns   | 130        |
| 7.2.2 Cell types following annealing   | 136        |
| 7.2.3 High-temperature crystal structures  | 137        |
| 7.2.3.1 The B-type phase   | 138        |
| 7.2.3.2 Praseodymia $\beta$ phase ( $\text{Pr}_6\text{O}_{11}$ )   | 139        |
| 7.2.3.3 Praseodymia $\iota$ phase ( $\text{Pr}_7\text{O}_{12}$ )   | 139        |
| 7.2.4 Discussion on annealed sample results  | 139        |
| 7.2.4.1 Europia  | 139        |
| 7.2.4.2 Gadolinia  | 139        |
| 7.2.4.3 Ytterbia   | 144        |
| <b>7.3 IN-SITU HIGH TEMPERATURE XRPD</b>   | <b>146</b> |
| 7.3.1 Praseodymia ramp in air  | 146        |
| 7.3.2 Praseodymia isothermal holds in air - conversion from $\text{Pr}_2\text{O}_3$ to $\text{Pr}_6\text{O}_{11}$ at 275°C | 152        |
| 7.3.2.1 Peak heights and intensities   | 152        |
| 7.3.2.2 Shrinking Sphere model   | 154        |
| 7.3.2.3 JMAK model   | 156        |
| 7.3.3 Praseodymia quench in air  | 159        |
| 7.3.4 Change in cell parameter with temperature  | 159        |
| <b>7.4 COMPARISON WITH OTHER WORK</b>  | <b>160</b> |
| <br>   |            |
| <b>8 RESULTS FROM DIFFERENTIAL SCANNING CALORIMETRY</b>  | <b>162</b> |
| <b>8.1 FULL RANGE DSC-TG IN NITROGEN</b>   | <b>162</b> |
| <b>8.2 FULL RANGE DSC-TG IN AIR</b>  | <b>167</b> |
| <b>8.3 RAMPS IN NITROGEN</b>   | <b>169</b> |
| <b>8.4 RAMPS IN AIR</b>  | <b>174</b> |
| 8.4.1 Ramp performed between 20°C and 600°C  | 174        |

|  |            |
|--|------------|
| 8.4.2 Ramp performed between 20°C and 1500°C               | 177        |
| 8.4.3 Summary of activation energies                       | 181        |
| <b>8.5 TWO-DIRECTIONAL DSC-TG: 20°C TO 1400°C AND BACK</b> | <b>181</b> |
| <b>8.6 GAS ABSORPTION</b>                                  | <b>184</b> |
| <b>8.7 RELATING THE DSC-TG TO THE PHASE DIAGRAM</b>        | <b>186</b> |
| <b>8.8 COMPARISON WITH OTHER WORK</b>                      | <b>195</b> |

## **9 CONCLUSIONS AND SUGGESTIONS FOR FUTURE**

|   |            |
|---|------------|
| <b>WORK</b>   | <b>200</b> |
| <b>9.1 SUMMARY</b>                                      | <b>200</b> |
| <b>9.2 LANTHANIDE OXIDE CRYSTAL STRUCTURES</b>          | <b>200</b> |
| <b>9.3 INDEXING</b>                                     | <b>202</b> |
| <b>9.4 COMPARISON OF KINETIC DATA FROM XRPD AND DSC</b> | <b>203</b> |
| <b>9.5 COMPARISON OF DSC-TG DATA WITH HISTORIC DATA</b> | <b>205</b> |
| <b>9.6 REDRAWING THE PHASE DIAGRAMS</b>                 | <b>206</b> |
| <b>9.7 SUGGESTED FUTURE WORK</b>                        | <b>209</b> |

## LIST OF FIGURES

|  |    |
|--|----|
| 1.1 $\Sigma IP_{1-3}$ and $IP_4$ for the lanthanoids.  | 5  |
| 1.2 Ionic radii for the tripositive ions $Z=57$ to $71$ .  | 8  |
| 1.3 Atomic number versus cell parameter for the cubic series $Rb_2NaLnF_6$ .                             | 10 |
| 1.4 Atomic number versus unit cell parameters for the tetragonal series $LiLnF_4$ .                      | 11 |
| 1.5 Phase diagram for the lanthanoid sesquioxides.   | 14 |
| 1.6 A-type (hexagonal) $Ln_2O_3$ (where Ln represents any lanthanoid).                                   | 15 |
| 1.7 B-type (monoclinic) $Ln_2O_3$ .  | 16 |
| 1.8 C-type (cubic) $Ln_2O_3$ .   | 16 |
| 1.9 Phase diagram for the praseodymium-oxygen system.  | 18 |
| 2.1 The Bragg Construction.  | 24 |
| 2.2 A unit cell.   | 25 |
| 2.3 The 14 Bravais Lattices.   | 26 |
| 2.4 A set of parallel planes in a crystal.   | 27 |
| 2.5 A section of a 2-dimensional lattice.  | 28 |
| 2.6 X-ray diffraction from a single crystal versus powder.   | 31 |
| 2.7 Peak positions and peak intensities.   | 33 |
| 2.8 How cell parameter affects peak positions.   | 34 |
| 2.9 How cell contents affect peak intensities.   | 35 |
| 2.10 Scattering of X-rays by a single atom.  | 37 |
| 2.11 A peak from a powder diffraction pattern.   | 37 |
| 2.12 The basic elements of an X-ray tube.  | 39 |
| 2.13 An X-ray emission spectrum.   | 40 |
| 2.14 Electron transitions giving rise to X-rays.   | 40 |
| 2.15 Schematic of the Diamond Light Source site.   | 42 |
| 2.16 Insertion device consisting of alternately-arranged magnets causing the electron beam to oscillate. | 45 |
| 2.17 Schematic of beamline I11 at Diamond.   | 45 |
| 2.18 Diffractometer with Bragg-Brentano geometry.  | 46 |
| 2.19 Schematic of a powder diffractometer.   | 48 |
| 2.20 Philips PANalytical powder diffractometer.  | 48 |
| 2.21 Penetration of incident beam into sample.   | 50 |

|   |     |
|---|-----|
| 2.22 A graphical method for indexing the cubic system.  | 55  |
| 2.23 Lorentz Polarisation factor profile.   | 71  |
| 2.24 Full profile refinement of an XRPD pattern using the program GSAS.   | 74  |
| 3.1 DSC schematic.  | 77  |
| 3.2 Netzsch ST449 F3 Jupiter DSC.   | 78  |
| 3.3 Sample carrier with reference and sample pans atop.   | 79  |
| 3.4 Cut-away schematic of the DSC.  | 80  |
| 3.5 DSC curve showing heat flow against temperature (exothermic is 'up').   | 81  |
| 3.6 20K/min ramp for praseodymium oxide.  | 84  |
| 4.1 Changes in peak intensity over time.  | 87  |
| 4.2 Sigmoidal function (top) and its linearised form.   | 93  |
| 4.3 Germ nucleation, grain growth and grain impingement.  | 94  |
| 4.4 Illustration of extended volume.  | 95  |
| 5.1 Raw data (intensity versus $2\theta$ ) displayed in PowderX.  | 102 |
| 5.2 Histogram after removal of $K\alpha_2$ contribution and background, and identification of peak positions.                   | 103 |
| 5.3 Crysfire peak position input screen.  | 104 |
| 5.4 Summary file of indexing results.   | 105 |
| 5.5 CHEKCELL main screen showing trial cells (top half) and comparison of measured and calculated peak positions (bottom half). | 106 |
| 5.6 Best solution from CHEKCELL.  | 107 |
| 5.7 Unit cell refinement in CHEKCELL (mean square deviation for the refined parameters is lower than initial parameters).       | 107 |
| 5.8 Histogram after refinement in GSAS.   | 109 |
| 5.9 Combined DSG-TG plot.   | 110 |
| 7.1 XRPD pattern for sample (1) $\text{Eu}_2\text{O}_3$ .   | 117 |
| 7.2 XRPD pattern for sample (1) $\text{Eu}_2\text{O}_3$ showing the region between $46^\circ$ and $64^\circ$ in more detail.    | 117 |
| 7.3 XRPD pattern for sample (2) $\text{Gd}_2\text{O}_3$ .   | 118 |
| 7.4 XRPD pattern for sample (2) $\text{Gd}_2\text{O}_3$ showing the region between $46^\circ$ and $64^\circ$ in more detail.    | 118 |
| 7.5 XRPD pattern for sample (3) $\text{Yb}_2\text{O}_3$ .   | 119 |

|  |     |
|--|-----|
| 7.6 XRPD pattern for sample (3) Yb <sub>2</sub> O <sub>3</sub> showing the region between 46° and 64° in more detail.  | 119 |
| 7.7 XRPD pattern for sample (4) Pr <sub>2</sub> O <sub>3</sub> .   | 120 |
| 7.8 XRPD pattern for sample (4) Pr <sub>2</sub> O <sub>3</sub> showing the region between 46° and 64° in more detail.  | 120 |
| 7.9 XRPD pattern for sample (5) Tb <sub>2</sub> O <sub>3</sub> .   | 121 |
| 7.10 XRPD pattern for sample (5) Tb <sub>2</sub> O <sub>3</sub> showing the region between 46° and 64° in more detail.   | 121 |
| 7.11 XRPD pattern for sample (9) Nd <sub>2</sub> O <sub>3</sub> .  | 122 |
| 7.12 XRPD pattern for sample (10) Sm <sub>2</sub> O <sub>3</sub> .   | 122 |
| 7.13 XRPD pattern for sample (11) Eu <sub>2</sub> O <sub>3</sub> .   | 123 |
| 7.14 Plot of cell parameter against atomic number for the C-type cell.   | 124 |
| 7.15 Crystal structure of the C-type cubic phase in space group <i>Ia-3</i> .  | 125 |
| 7.16 Crystal structure of the B-type monoclinic phase in space group <i>C2/m</i> .   | 127 |
| 7.17 Crystal structure of the A-type hexagonal phase in space group <i>P-3m1</i> .   | 128 |
| 7.18 XRPD pattern for sample (1) Eu <sub>2</sub> O <sub>3</sub> following 1 hour anneal at 1334°C and slow cooling.  | 131 |
| 7.19 XRPD pattern for sample (2) Gd <sub>2</sub> O <sub>3</sub> following 1 hour anneal at 1334°C and slow cooling.  | 131 |
| 7.20 XRPD pattern for sample (2) Gd <sub>2</sub> O <sub>3</sub> following 1 hour anneal at 1500°C and quenching.   | 132 |
| 7.21 XRPD pattern for sample (2) Gd <sub>2</sub> O <sub>3</sub> following 7 hour anneal at 1500°C and quenching.   | 132 |
| 7.22 XRPD pattern for sample (2) Gd <sub>2</sub> O <sub>3</sub> following 7 hour anneal at 1500°C and quenching showing the region between 28° and 35° in more detail. | 133 |
| 7.23 XRPD pattern for sample (3) Yb <sub>2</sub> O <sub>3</sub> following 1 hour anneal at 1500°C and quenching.   | 133 |
| 7.24 XRPD pattern for sample (3) Yb <sub>2</sub> O <sub>3</sub> following 5 hour anneal at 1500°C and quenching.   | 134 |
| 7.25 XRPD pattern for sample (7) Yb <sub>2</sub> O <sub>3</sub> following 5 hour anneal at 1800°C and quenching.   | 134 |
| 7.26 XRPD pattern for sample (8) Gd <sub>2</sub> O <sub>3</sub> following 7 hour anneal at 1500°C and quenching.   | 135 |

|  |     |
|--|-----|
| 7.27 XRPD pattern for sample (8) Gd <sub>2</sub> O <sub>3</sub> following 7 hour anneal at 1500°C and quenching showing the region between 14° and 18° in more detail.                 | 135 |
| 7.28 Plot of cell parameter against atomic number for the B-type cell.   | 137 |
| 7.29 Diffraction pattern of Gd <sub>2</sub> O <sub>3</sub> following 1 hour anneal at 1334°C showing low-intensity reflections due to the monoclinic phase.                            | 140 |
| 7.30 Diffraction pattern of Gd <sub>2</sub> O <sub>3</sub> following 1 hour anneal at 1500°C showing low-intensity reflections due to the monoclinic phase.                            | 141 |
| 7.31 Cubic (upper image) and monoclinic (following 7 hour anneal at 1500°C) patterns for Gd <sub>2</sub> O <sub>3</sub> .  | 142 |
| 7.32 Estimation of unit cell parameter 'a' for monoclinic Gd <sub>2</sub> O <sub>3</sub> by a method of interpolation.   | 143 |
| 7.33 XRPD pattern of Yb <sub>2</sub> O <sub>3</sub> post-heating to 1500°C showing low-intensity reflections due to the monoclinic phase.  | 145 |
| 7.34 Praseodymia ramp 25°C to 275°C showing the appearance of the ceria-type β phase (Pr <sub>6</sub> O <sub>11</sub> ) at 275°C.  | 147 |
| 7.35 Praseodymia ramp 300°C to 550°C showing the ceria cell throughout.  | 148 |
| 7.36 Praseodymia ramp 575°C to 800°C showing the appearance of the ι phase (Pr <sub>7</sub> O <sub>12</sub> ) at 625°C.  | 149 |
| 7.37 Final stage of refinement of the β phase (Pr <sub>6</sub> O <sub>11</sub> ) of praseodymia.   | 150 |
| 7.38 Final stage of refinement of the ι phase (Pr <sub>7</sub> O <sub>12</sub> ) of praseodymia.   | 150 |
| 7.39 Praseodymia ramp 800°C to 450°C showing the loss of the ι phase of Pr <sub>7</sub> O <sub>12</sub> at 575°C.  | 151 |
| 7.40 Praseodymia ramp 425°C to 125°C showing the ceria cell throughout.  | 152 |
| 7.41 The five Bragg peaks of the β phase emerging from the ambient mixed phase during the 250°C isothermal hold.   | 153 |
| 7.42 Conversion against time for Pr <sub>2</sub> O <sub>3</sub> to Pr <sub>6</sub> O <sub>11</sub> phase change using the increase in intensity of the 47.2° (β phase 220 plane) peak. | 154 |
| 7.43 Shrinking Sphere kinetic isotherms for the 47.2° (β phase 220 plane) peak.  | 155 |
| 7.44 Plot of ln k against 1/T for the 47.2° (β phase 220 plane) peak.  | 156 |
| 7.45 JMAK kinetic isotherms for the 47.2° (β phase 220 plane) peak.  | 157 |
| 7.46 Plot of ln k against 1/T for the 47.2° (β phase 220 plane) peak.  | 158 |
| 7.47 Variation in unit cell parameter with temperature for Pr <sub>6</sub> O <sub>11</sub> .   | 160 |

|   |     |
|---|-----|
| 8.1 DSC-TG recorded on sample (4) Pr <sub>2</sub> O <sub>3</sub> from 20°C to 1550°C at 10K/min under nitrogen.   | 162 |
| 8.2 DSC-TG recorded on sample (4) Pr <sub>2</sub> O <sub>3</sub> from 20°C to 1550°C at 10K/min under nitrogen. 2 <sup>nd</sup> attempt.                  | 163 |
| 8.3 DSC-TG recorded on sample (4) Pr <sub>2</sub> O <sub>3</sub> from 20°C to 1550°C at 10K/min under nitrogen following heating at 170°C for 10 minutes. | 165 |
| 8.4 DSC 4 recorded on sample (4) Pr <sub>2</sub> O <sub>3</sub> from 20°C to 1550°C at 10K/min under nitrogen following heating at 380°C for 10 minutes.  | 165 |
| 8.5 Mettler DSC-TG recorded on sample (4) Pr <sub>2</sub> O <sub>3</sub> from 20°C to 1100°C  | 167 |
| 8.6 DSC-TG recorded on sample (6) from 20°C to 1500°C at 10K/min under air.   | 168 |
| 8.7 DSC recorded on sample (4) Pr <sub>2</sub> O <sub>3</sub> from 200°C to 500°C under nitrogen.   | 169 |
| 8.8 Temperature of maximum deflection, $T_m$ , versus heating rate, $\phi$ , for sample   | 170 |
| 8.9 Plot of $\ln(\phi/T_m^2)$ against $1/T_m$ for sample (4) Pr <sub>2</sub> O <sub>3</sub> 1 <sup>st</sup> endotherm.                                    | 171 |
| 8.10 Temperature of maximum deflection, $T_m$ , versus heating rate, $\phi$ , for sample (4) Pr <sub>2</sub> O <sub>3</sub> 2 <sup>nd</sup> endotherm.    | 172 |
| 8.11 Plot of $\ln(\phi/T_m^2)$ against $1/T_m$ for sample (4) Pr <sub>2</sub> O <sub>3</sub> 2 <sup>nd</sup> endotherm.                                   | 172 |
| 8.12 Temperature of maximum deflection, $T_m$ , versus heating rate, $\phi$ , for sample (4) Pr <sub>2</sub> O <sub>3</sub> 3 <sup>rd</sup> endotherm.    | 173 |
| 8.13 Plot of $\ln(\phi/T_m^2)$ against $1/T_m$ for sample (4) Pr <sub>2</sub> O <sub>3</sub> 3 <sup>rd</sup> endotherm.                                   | 174 |
| 8.14 DSC ramps on sample (6) Pr <sub>2</sub> O <sub>3</sub> from 200°C to 600°C in air.   | 175 |
| 8.15 Temperature of maximum deflection, $T_m$ , versus heating rate, $\phi$ , for sample (6) Pr <sub>2</sub> O <sub>3</sub> 1 <sup>st</sup> exotherm.     | 176 |
| 8.16 Plot of $\ln(\phi/T_m^2)$ against $1/T_m$ , for sample (6) Pr <sub>2</sub> O <sub>3</sub> 1 <sup>st</sup> exotherm.                                  | 176 |
| 8.17 DSC ramps on sample (6) Pr <sub>2</sub> O <sub>3</sub> from 20°C to 1500°C in air.   | 177 |
| 8.18 Temperature of maximum deflection, $T_m$ , versus heating rate, $\phi$ , for sample (6) Pr <sub>2</sub> O <sub>3</sub> 1 <sup>st</sup> exotherm.     | 178 |
| 8.19 Plot of $\ln(\phi/T_m^2)$ against $1/T_m$ for sample (6) Pr <sub>2</sub> O <sub>3</sub> 1 <sup>st</sup> exotherm.                                    | 179 |
| 8.20 Temperature of maximum deflection, $T_m$ , versus heating rate, $\phi$ , for sample (6) 1250°C endotherm.  | 180 |
| 8.21 Plot of $\ln(\phi/T_m^2)$ against $1/T_m$ , for sample (6) 1250°C endotherm.   | 180 |

|  |     |
|--|-----|
| 8.22 DSC recorded on sample (6) Pr <sub>2</sub> O <sub>3</sub> from 20°C to 1400°C and back at 10K/min in air. The data collected from 20°C to 1500°C (from figure 8.6) is shown on the left for comparison. | 182 |
| 8.23 DSC-TG recorded on sample (6) Pr <sub>2</sub> O <sub>3</sub> from 20°C to 1400°C and back at 10K/min in air.  | 183 |
| 8.24 DSC-TG recorded on sample (6) Pr <sub>2</sub> O <sub>3</sub> from 20°C to 1400°C and back at 10K/min in air. Image wrapped to compare associated transitions.   | 184 |
| 8.25 DSC-TG recorded on sample (6) Pr <sub>2</sub> O <sub>3</sub> from 20°C to 1400°C and back at 10K/min in air. Mass changes are shown.  | 184 |
| 8.26. Gas loss from sample (6) Pr <sub>2</sub> O <sub>3</sub> after 85 days' exposure to air.  | 186 |
| 8.27 DSC-TG recorded on sample (6) Pr <sub>2</sub> O <sub>3</sub> from 20°C to 1500°C at 10K/min in air. Mass changes are indicated.   | 188 |
| 8.28 Temperature versus oxygen in the Pr-O system for DSC recorded on sample (6) Pr <sub>2</sub> O <sub>3</sub> at 10K/min in air.   | 189 |
| 8.29 Temperature versus oxygen content for all DSC recorded on sample (6) Pr <sub>2</sub> O <sub>3</sub> from 20°C to 1500°C in air.   | 190 |
| 8.30 DSC recorded on sample (6) Pr <sub>2</sub> O <sub>3</sub> at 2K/min in air with phases marked.  | 192 |
| 8.31 Phases attained during ramps on sample (6) Pr <sub>2</sub> O <sub>3</sub> .   | 193 |
| 8.32 Hysteresis loop for the $\alpha$ phase to $\iota$ phase (Pr <sub>7</sub> O <sub>12</sub> ) transition.  | 195 |
| 8.33 Temperature-composition plot for the $\iota$ - $\sigma$ - $\theta$ region.  | 196 |
| 8.34 Isobaric runs on Pr <sub>2</sub> O <sub>3</sub> .   | 198 |
| 9.1 Amended phase diagram for the lanthanoid sesquioxides.   | 207 |
| 9.2. Amended phase diagram for the praseodymium-oxygen system showing the $\sigma$ phase.  | 209 |

## LIST OF TABLES

|  |     |
|--|-----|
| 1.1 Electron configurations of the lanthanoid atoms and their tripositive ions.        | 4   |
| 1.2 Electron configurations of the lanthanoids.  | 6   |
| 1.3 Unit cell parameters for the cubic series $\text{Rb}_2\text{NaLnF}_6$ (ICDD 1995). | 9   |
| 1.4 Unit cell parameters for the tetragonal series $\text{LiLnF}_4$ (ICDD 1995).       | 10  |
| 1.5 Discrete phases in the praseodymium-oxygen system.                                 | 17  |
| 2.1 The seven crystal systems.   | 25  |
| 2.2 Values of $h$ , $k$ and $l$ for cubic lattices.                                    | 30  |
| 2.3 X-ray wavelengths for typical anode metals. All values in Angströms.               | 41  |
| 2.4 Arithmetic derivation of unit cell parameter for a cubic cell.                     | 57  |
| 2.5 Arithmetic method for indexing the cubic system.                                   | 58  |
| 2.6 Arithmetic method for indexing the tetragonal system.                              | 60  |
| 2.7 Values of $Q_{hkl}$ expressed using reciprocal cell parameters.                    | 66  |
| 4.1 Values of the Avrami exponent and corresponding geometries.                        | 97  |
| 6.1 Samples obtained for XRPD and DSC-TG.  | 111 |
| 6.2 XRPD schedule for samples.   | 112 |
| 6.3 Heating scheme for samples.  | 112 |
| 6.4 XRPD schedule for annealed samples.  | 113 |
| 6.5 Pre-DSC-TG heating schedule for sample (4).  | 114 |
| 7.1 Refined unit cell parameters for samples (1) to (5) and (9) to (11).               | 123 |
| 7.2 Crystal structure of cubic $\text{Pr}_2\text{O}_3$ .                               | 125 |
| 7.3 Crystal structure of cubic $\text{Eu}_2\text{O}_3$ .                               | 125 |
| 7.4 Crystal structure of cubic $\text{Eu}_2\text{O}_3$ .                               | 126 |
| 7.5 Crystal structure of cubic $\text{Gd}_2\text{O}_3$ .                               | 126 |
| 7.6 Crystal structure of cubic $\text{Tb}_2\text{O}_3$ .                               | 126 |
| 7.7 Crystal structure of cubic $\text{Yb}_2\text{O}_3$ .                               | 126 |
| 7.8 Crystal structure of monoclinic $\text{Sm}_2\text{O}_3$ .                          | 127 |
| 7.9 Crystal structure of hexagonal $\text{Pr}_2\text{O}_3$ .                           | 128 |
| 7.10 Crystal structure of hexagonal $\text{Nd}_2\text{O}_3$ .                          | 128 |
| 7.11 Unit cell parameters for samples (1), (2), (3), (7) and (8) post-heating.         | 136 |

|   |     |
|---|-----|
| 7.12 Crystal structure of monoclinic $\text{Eu}_2\text{O}_3$ .  | 138 |
| 7.13 Crystal structure of monoclinic $\text{Gd}_2\text{O}_3$ .  | 138 |
| 7.14 Crystal structure of monoclinic $\text{Gd}_2\text{O}_3$ from synchrotron data.   | 138 |
| 7.15 Crystal structure of $\text{Pr}_6\text{O}_{11}$ .  | 139 |
| 7.16 Crystal structure of $\text{Pr}_7\text{O}_{12}$ .  | 139 |
| 7.17 Values of the rate constant, $k$ , for the $47.2^\circ$ ( $\beta$ phase 220 plane) peak.   | 155 |
| 7.18 Values of the rate constant and Avrami exponent for the $47.2^\circ$ ( $\beta$ phase 220 plane) peak.  | 157 |
| 7.19 Values for activation energy.  | 159 |
| 7.20 Activation energies for the lanthanide oxides.   | 161 |
| 8.1 Kissinger analysis for 1 <sup>st</sup> endotherm - sample (4) $\text{Pr}_2\text{O}_3$ .   | 170 |
| 8.2 Kissinger analysis for 2 <sup>nd</sup> endotherm - sample (4) $\text{Pr}_2\text{O}_3$ .   | 171 |
| 8.3 Kissinger analysis for 3 <sup>rd</sup> endotherm - sample (4) $\text{Pr}_2\text{O}_3$ .   | 173 |
| 8.4 Kissinger analysis for 1 <sup>st</sup> exotherm - sample (6) $\text{Pr}_2\text{O}_3$ . Data recorded from $200^\circ\text{C}$ to $600^\circ\text{C}$ .          | 175 |
| 8.5 Kissinger analysis for 1 <sup>st</sup> exotherm - sample (6) $\text{Pr}_2\text{O}_3$ , Data recorded from $20^\circ\text{C}$ to $1500^\circ\text{C}$ .          | 178 |
| 8.6 Kissinger analysis for endotherm at $1250^\circ\text{C}$ - sample (6) $\text{Pr}_2\text{O}_3$ . Data recorded from $20^\circ\text{C}$ to $1500^\circ\text{C}$ . | 179 |
| 8.7 Activation energies for phase changes in samples (4) and (6).   | 181 |
| 8.8 Transition temperatures for sample (6) $\text{Pr}_2\text{O}_3$ taken from 10K/min DSC-TG data.  | 185 |
| 8.9 Weight loss on sample (6) $\text{Pr}_2\text{O}_3$ on exposing to air.   | 186 |
| 8.10 Values of $x$ in $\text{PrO}_x$ for DSC-TG recorded on sample (6).   | 190 |
| 8.11 Order of appearance of phases in the Pr-O system with temperature for the 2K/min ramp.   | 191 |
| 8.12 Kinetic data for the Pr-O system.  | 199 |
| 9.1 Comparison of activation energy data from XRPD and DSC.   | 205 |
| 9.2 Activation energies for the lanthanide oxides.  | 205 |
| 9.3 Kinetic data for the Pr-O system.   | 206 |
| 9.4 Temperatures of phase transformations in $\text{Ln}_2\text{O}_3$ .  | 207 |

## ACKNOWLEDGEMENTS

Thanks are due to my academic supervisors Professor Susan H. Kilcoyne and Professor Neil M. Boag, who provided advice and support through the course of my work.

Additional thanks are due to:

Geoff Parr of Salford Analytical Services for running samples on the Siemens D500 and Bruker D8 X-ray powder diffractometers and for his technical advice;

Peter Skingle of Manchester Metropolitan University for access to the Heraeus furnace;

Dr Tim Comyn of Leeds University for access to the Philips PANalytical X'Pert powder diffractometer;

Dr Wei Loh and Zhenggang Lian of Southampton University for access to the 1800°C glass furnace;

Professor Chiu Tang, Principal Beamline Scientist on Beamline I11 at Diamond Light Source, for obtaining XRPD data;

Phil Williams of Mettler Toledo for obtaining additional DSC data;

and my family for their patience and support.

## **DECLARATION**

The research in this thesis is my own work with the following exceptions.

All XRPD data collected on the Siemens and Bruker machines were performed by Geoff Parr of Salford Analytical Services.

Sample (7) of  $\text{Yb}_2\text{O}_3$  was annealed by Zhenggang Lian of Southampton University.

The XRPD pattern obtained at Diamond Light Source was collected on beamline I11 by Professor Chiu Tang.

The DSC data represented in figure 8.5 was collected by Phil Williams of Mettler Toledo.

## ABSTRACT

The lanthanoid sesquioxides exhibit a number of distinct structural phases. Below 2000°C these oxides exist in three crystal systems, namely the A-type hexagonal phase, the B-type monoclinic phase and the C-type cubic phase. With increasing temperature the stability of these structures is generalised by the order  $C \rightarrow B \rightarrow A$ , although not every oxide will exhibit all phases; this general transition is typical of the middle members of the group. Under ambient conditions, the A phase is preferred for  $\text{La}_2\text{O}_3$  to  $\text{Pm}_2\text{O}_3$ . Both the C and B phases exist for  $\text{Sm}_2\text{O}_3$ ,  $\text{Eu}_2\text{O}_3$  and  $\text{Gd}_2\text{O}_3$ . The C phase is stable at room temperature from  $\text{Sm}_2\text{O}_3$  onwards, and at the high atomic number end of the series this phase is preferred.

Traditionally, the structures of the heavier sesquioxides ( $\text{Er}_2\text{O}_3$  to  $\text{Lu}_2\text{O}_3$ ) have been believed to be cubic from ambient temperature all the way up to their melting points. However, contrary to the current phase diagram, my work has shown that not only are B-type  $\text{Sm}_2\text{O}_3$ ,  $\text{Eu}_2\text{O}_3$  and  $\text{Gd}_2\text{O}_3$  very stable at ambient temperature, but it is also possible to create 1% monoclinic  $\text{Yb}_2\text{O}_3$  by heating and then quenching back to ambient temperature.

Of the lanthanoids, praseodymium and terbium are known for their existence in both the +3 and +4 oxidation states. The praseodymium-oxygen system is notable for its multiple stoichiometries. This work presents kinetic data for the  $\phi \rightarrow \beta$  phase and the  $\sigma \rightarrow \theta$  phase transitions in this system, the results obtained via high-temperature X-ray powder diffraction and differential scanning calorimetry.

The crystal structures of B-type  $\text{Gd}_2\text{O}_3$  and  $\text{Yb}_2\text{O}_3$  are reported, the former obtained using both laboratory and synchrotron X-ray data and the latter using laboratory data alone. It is proposed that this is the first time these two structures have been determined following the application of temperature alone, without the additional application of pressure.

## **DEDICATION**

For Phyllis Margaret Skinner

*Told you I'd get there one day*

# 1 INTRODUCTION

## 1.1 THE RARE EARTHS

The rare earths constitute a series of highly electropositive elements occupying period 6 of the periodic table between the 6s and 5d blocks and their occurrence marks the first occupying of the 4f atomic orbitals in the ground state. Unlike the d block elements their chemistry is fairly uniform across the series, with the +3 oxidation state dominating.

The series corresponds to the filling of the 4f atomic orbitals from lanthanum, which has an electronic configuration  $[\text{Xe}]5d^16s^2$ , to lutetium,  $[\text{Xe}]4f^{14}5d^16s^2$ . As the members of the series have similar properties they are referred to in the IUPAC scheme as the *lanthanoids*, after the first element in the series, lanthanum, which itself takes its name from the Greek *λανθανειν* (lanthanein), meaning *to lie hidden*. Despite this, the term *lanthanides* is still widely in use. All the lanthanoids have similar chemical properties, since the 4f atomic orbitals are of a smaller radial extension than the 6s and 5d atomic orbitals in which the valence electrons lie and hence do not greatly affect the chemistry of the elements. The f orbitals are said to be buried inside the atom and shielded from its external environment by the valence electrons. This means that the chemistry of the lanthanoids is largely determined by their atomic radii.

All the lanthanoids show the +3 oxidation state. An unusual deviation from this is seen with cerium, which can exhibit the +4 state, achieving the electronic stability of the noble gas xenon. Europium exhibits the +2 state, achieving the stability of a half-filled f shell. The +4 oxidation state is also seen with praseodymium and terbium. The element promethium does not occur in nature.

Although not actually lanthanoids, yttrium and scandium are often considered to be rare earths as they occur in the same sources. Yttrium,  $[\text{Kr}]4d^15s^2$ , is the immediate vertical neighbour of lanthanum, has a similar electronic configuration and shows a great chemical resemblance to the lanthanoids. The radius of its tripositive ion lies between those of  $\text{Ho}^{3+}$  and  $\text{Er}^{3+}$  and, as might be expected, its chemistry resembles these

elements more strongly than it does any of the other lanthanoids. Scandium,  $[\text{Ar}]3d^14s^2$ , the lightest member of the transition elements and again vertical to lanthanum, also resembles the lanthanoids closely in its chemical properties.

The term *rare earths* is actually a misnomer. Cerium is the twenty-fifth most abundant element in the earth and is as common as copper. Even the least-common rare earth, thulium, occurs in greater proportion than mercury. However, because the rare earths have a similar chemistry and tend to occur naturally together, historically their separation from each other has been difficult. It is this fact that has given the impression of their rarity. The phrase *to lie hidden* indicates that the metals are difficult to separate i.e. they lie hidden behind each other. Originally, separation was performed by a laborious series of fractional crystallisations. As the lanthanoid ions have subtly different radii, the lattice energies of their salts and their hydration energies are also different. This means that they have slight differences in solubility and hence different metal salts will precipitate from solution at slightly different concentrations. In recent times, separation of ions has been achieved by solvent extraction and ion exchange. Both methods rely on the small differences in ionic radii across the group.

Typical sources of rare earths are monazite sand, the mineral xenotime (which both contain a mixture of the phosphates of lanthanoids and thorium) and bastnaesite (which contains lanthanoid fluorocarbonates). In terms of their occurrence in the earth's crust, lanthanum, cerium and neodymium are by far the most common. The rare earths have many applications. Their most common use is in catalytic converters for internal combustion engines. They also have use as refining catalysts in the petrochemical industry. Other uses include alloying material in permanent magnets, colours for glass and ceramics, phosphors, and doping agents for lasers. Cerium is contained in the alloy known as misch metal, used as the flint of cigarette lighters. It is also used as an anti-knock agent in petrol. Europium is used within nuclear fuel control rods and also within the red phosphor in CRT television screens. Ytterbium has been shown to have an application in thermophotovoltaic devices (Krishna *et al* 1999) and a lanthanum-doped sodium tantalate catalyst has recently been shown to be effective in the photolysis of water as a means of generating hydrogen fuel (Kato *et al* 2003).

## 1.2 THE STABILITY OF THE TRIPOSITIVE OXIDATION STATE

The ground state electronic configurations of the uncharged lanthanoid atoms and their tripositive ions are given in table 1.1. For the atoms, the 4f orbitals are generally more stable than the 5d, illustrated by the fact that the 5d orbitals are only occupied in a few cases. After lanthanum the 5d orbitals are empty and only when gadolinium is reached is the extra stability of the half-filled 4f orbitals sufficient to induce reoccupation of the 5d orbitals. For the tripositive ions, chemically the most important oxidation state, the 4f orbitals are much more stable and the 5d and 6s orbitals are not occupied at all. The electron configurations of the tripositive ions reveal a sequential filling of the 4f atomic orbitals from lanthanum at  $f^0$  to lutetium at  $f^{14}$ .

The 4f electrons occupy space inside the  $n = 5$  shell. They are more stable and have greater ionisation potentials than the 5d and 6s electrons. Consequently the loss of the 6s and 5d electrons is always seen before that of the 4f electrons. This is illustrated by electronic absorption spectra of compounds of tripositive lanthanoid ions. As a general trend, ionisation energy increases with atomic number and shows marked half-shell effects. Table 1.1 lists both the sum of the first three ionisation potentials and the fourth ionisation potential for the lanthanoids. These values are plotted in figure 1.1.

| Z  | Element | Electron config.                                     | Electron config. for Ln <sup>3+</sup> | Ionic radius (pm) 6CN <sup>†</sup> | ΣIP <sub>1-3</sub> * kJ.mol <sup>-1</sup> | IP <sub>4</sub> ** kJ.mol <sup>-1</sup> |
|----|---------|--|---------------------------------------|------------------------------------|---|---|
| 57 | La      | [Xe]5d <sup>1</sup> 6s <sup>2</sup>                  | f <sup>0</sup>                        | 117.2                              | 3455                                      | 4819                                    |
| 58 | Ce      | [Xe]4f <sup>1</sup> 5d <sup>1</sup> 6s <sup>2</sup>  | f <sup>1</sup>                        | 115                                | 3523                                      | 3547                                    |
| 59 | Pr      | [Xe]4f <sup>3</sup> 6s <sup>2</sup>                  | f <sup>2</sup>                        | 113                                | 3627                                      | 3761                                    |
| 60 | Nd      | [Xe]4f <sup>4</sup> 6s <sup>2</sup>                  | f <sup>3</sup>                        | 112.3                              | 3697                                      | 3899                                    |
| 61 | Pm      | [Xe]4f <sup>5</sup> 6s <sup>2</sup>                  | f <sup>4</sup>                        | 111                                | 3740                                      | 3966                                    |
| 62 | Sm      | [Xe]4f <sup>6</sup> 6s <sup>2</sup>                  | f <sup>5</sup>                        | 109.8                              | 3869                                      | 3994                                    |
| 63 | Eu      | [Xe]4f <sup>7</sup> 6s <sup>2</sup>                  | f <sup>6</sup>                        | 108.7                              | 4036                                      | 4110                                    |
| 64 | Gd      | [Xe]4f <sup>7</sup> 5d <sup>1</sup> 6s <sup>2</sup>  | f <sup>7</sup>                        | 107.8                              | 3749                                      | 4245                                    |
| 65 | Tb      | [Xe]4f <sup>9</sup> 6s <sup>2</sup>                  | f <sup>8</sup>                        | 106.3                              | 3791                                      | 3839                                    |
| 66 | Dy      | [Xe]4f <sup>10</sup> 6s <sup>2</sup>                 | f <sup>9</sup>                        | 105.2                              | 3911                                      | 4001                                    |
| 67 | Ho      | [Xe]4f <sup>11</sup> 6s <sup>2</sup>                 | f <sup>10</sup>                       | 104.1                              | 3924                                      | 4101                                    |
| 68 | Er      | [Xe]4f <sup>12</sup> 6s <sup>2</sup>                 | f <sup>11</sup>                       | 103                                | 3934                                      | 4115                                    |
| 69 | Tm      | [Xe]4f <sup>13</sup> 6s <sup>2</sup>                 | f <sup>12</sup>                       | 102                                | 4045                                      | 4119                                    |
| 70 | Yb      | [Xe]4f <sup>14</sup> 6s <sup>2</sup>                 | f <sup>13</sup>                       | 100.8                              | 4194                                      | 4220                                    |
| 71 | Lu      | [Xe]4f <sup>14</sup> 5d <sup>1</sup> 6s <sup>2</sup> | f <sup>14</sup>                       | 100.1                              | 3887                                      | 4360                                    |

Table 1.1 Electron configurations of the lanthanoid atoms and their tripositive ions.

<sup>†</sup> metal cation showing six-fold coordination (Shannon 1976)

As a generalisation,  $IP_4 \sim 2(IP_3) \sim 4(IP_2) \sim 8(IP_1)$  and  $IP_4 > (IP_1 + IP_2 + IP_3)$

\* sum of first three ionisation potentials (Bernal et al 2004)

\*\* fourth ionisation potential (Bernal et al 2004)

[Xe] represents a xenon atomic core i.e.  $[1s^2 2s^2 2p^6 3s^2 3p^6 4s^2 3d^{10} 4p^6 5s^2 4d^{10} 5p^6]$

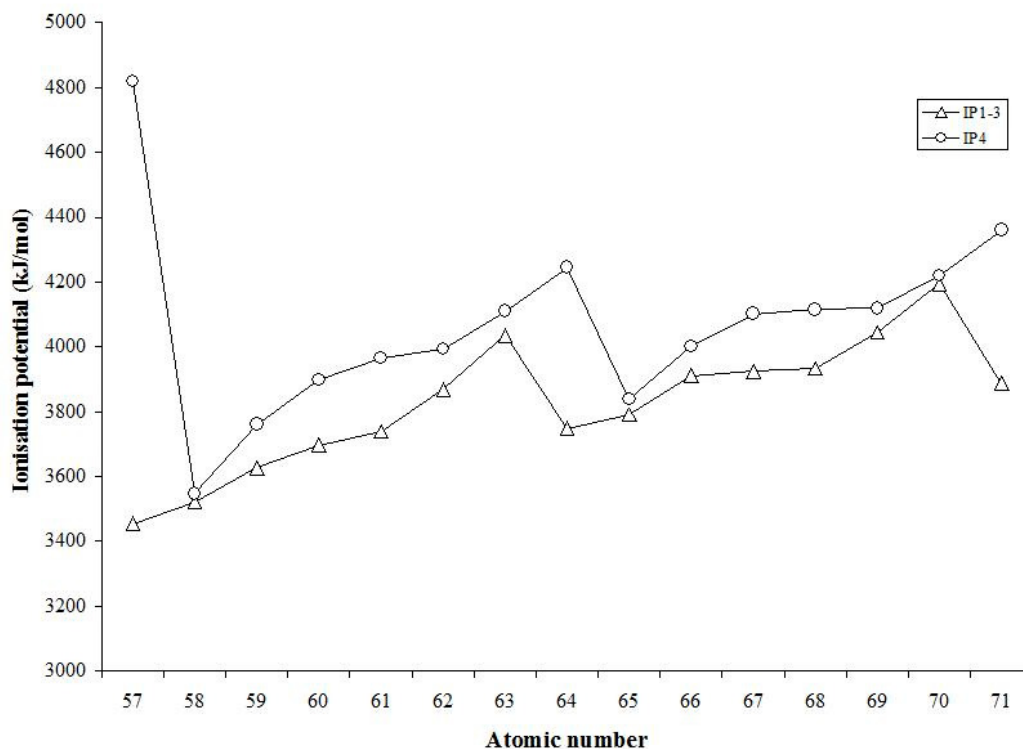


Figure 1.1  $\Sigma IP_{1-3}$  and  $IP_4$  for the lanthanoids (Bernal et al 2004).

Table 1.1 shows that the sum of the first three ionisation potentials for the lanthanoids is fairly consistent across the series, indicating the +3 state to be a common one. Indeed, this state is the preferred one under ambient conditions for most elements in the series, other than those with a relatively low second or fourth ionisation potential. Cerium, praseodymium and terbium all exhibit the +4 state, as well as displaying oxides with mixed +3/+4 valencies such as  $\text{Pr}_6\text{O}_{11}$  and  $\text{Tb}_4\text{O}_7$ . Cerium is the only lanthanoid to be stable in the +4 oxidation state in aqueous solution. The only binary cerium IV compounds known are  $\text{CeF}_4$  and  $\text{CeO}_2$ . There are several stable complexes containing  $\text{Ce}^{4+}$ , for example  $(\text{NH}_4)_2[\text{Ce}(\text{NO}_3)_6]$ , in which the nitrate ion acts as a bidentate ligand, the co-ordination of the  $\text{Ce}^{4+}$  being icosahedral. Only europium shows a marked tendency for lower oxidation states, for example  $\text{Eu}^{2+}$  exists in  $\text{EuO}$  and  $\text{EuC}_2\text{O}_4$ , although neodymium, samarium and ytterbium also show some tendency for this oxidation state. Table 1.2 below lists the oxidation states attainable by the lanthanoids and their corresponding electron configurations.

| Element | Oxidation state | Electron configuration          |
|---------|-----------------|---------------------------------|
| La      | +3              | [Xe] noble gas                  |
| Ce      | +3              | [Xe]4f <sup>1</sup>             |
|         | +4              | [Xe] noble gas                  |
| Pr      | +3              | [Xe]4f <sup>2</sup>             |
|         | +4              | [Xe]4f <sup>1</sup>             |
| Nd      | +2              | [Xe]4f <sup>4</sup>             |
|         | +3              | [Xe]4f <sup>3</sup>             |
| Pm      | +3              | [Xe]4f <sup>4</sup>             |
| Sm      | +2              | [Xe]4f <sup>6</sup>             |
|         | +3              | [Xe]4f <sup>5</sup>             |
| Eu      | +2              | [Xe]4f <sup>7</sup> half shell  |
|         | +3              | [Xe]4f <sup>6</sup>             |
| Gd      | +3              | [Xe]4f <sup>7</sup> half shell  |
| Tb      | +3              | [Xe]4f <sup>8</sup>             |
|         | +4              | [Xe]4f <sup>7</sup> half shell  |
| Dy      | +3              | [Xe]4f <sup>9</sup>             |
| Ho      | +3              | [Xe]4f <sup>10</sup>            |
| Er      | +3              | [Xe]4f <sup>11</sup>            |
| Tm      | +3              | [Xe]4f <sup>12</sup>            |
| Yb      | +2              | [Xe]4f <sup>14</sup> full shell |
|         | +3              | [Xe]4f <sup>13</sup>            |
| Lu      | +3              | [Xe]4f <sup>14</sup> full shell |

Table 1.2 Electron configurations of the lanthanoids.

### 1.3 THE LANTHANIDE CONTRACTION

The elements in the first row of the f block exhibit a decrease in atomic radius from lanthanum,  $Z=57$  to lutetium,  $Z=71$ . Because of this phenomenon, termed the *lanthanide contraction*, vertically-adjacent elements in the 2nd and 3rd rows of the d block, which appear before and after the lanthanoids, have very similar atomic radii even though they contain very different numbers of electrons. For example, the atomic radii of zirconium and hafnium are 1.60Å and 1.59Å respectively; for silver and gold the figures are both 1.44Å. With a significant increase in atomic weight and little or no change in atomic radius there is an associated increase in density. For example, gold has approximately twice the density of silver. Moving from left to right across the 1st

row of the f block there is a steady decrease in atomic radius with increasing atomic number. This contraction is also shown in the radii of the tripositive ions, illustrated in figure 1.2. This decrease in ion size is accompanied by the filling of the 4f orbitals.

Before the electronic structures of the lanthanoids were elucidated by spectroscopy, they could only be assumed. It was correctly believed that the electronic structure of the lanthanum atom was  $[\text{Xe}]5d^16s^2$ . It was therefore easy to explain the existence of the +3 oxidation state by the loss of the three outer electrons. Assuming that the  $5d^16s^2$  electrons were retained across the series of atoms from  $[\text{Xe}]5d^16s^2$  to  $[\text{Xe}]4f^{14}5d^16s^2$  and that moving across the lanthanoids corresponded to the filling of the 4f shell, the predominance of the +3 oxidation state could be explained as each atom could lose the  $5d^16s^2$  electrons to form the tripositive ion. However, spectroscopy has revealed that the atoms and ions do not all have the  $[\text{Xe}]4f^n5d^16s^2$  and  $[\text{Xe}]4f^n$  structures respectively. The removal of electrons from a lanthanoid atom proceeds in the manner of first the outer 6s electrons, secondly the outer 5d electrons and thirdly the 4f electrons. Because of their greater affinity for the nucleus and hence the shorter radial extension of their atomic orbitals, the 4f electrons are termed *inner* or *core* electrons.

In a multi-electron atom, the distance an electron exists from the nucleus is determined by both the shell in which it lies and the nuclear charge. Increasing nuclear charge causes a shrinking of the atomic radius. However, this shrinkage is offset to some degree by the presence of the inner electrons. This is due to a shielding effect; inner electrons shield the outer electrons from the nucleus. Therefore, rather than experience the full nuclear charge,  $Z$ , the outer electrons experience an effective nuclear charge,  $Z_{eff}$ . The shielding effect of occupied atomic orbitals decreases in the order  $s > p > d > f$ . Because of their limited radial extension and their highly angular shapes, the 4f atomic orbitals have a poor shielding effect and the shielding gained on adding electrons to the 4f orbitals on crossing the lanthanoid series fails to compensate for the increasing nuclear charge. For the lanthanoids,  $Z_{eff}$  is seen to increase steadily with increasing atomic number, causing the electrons to be drawn in towards the nucleus. Consequently there is a steady and almost linear decrease in atomic radius with increasing atomic number. This contraction is also shown in the radii of the tripositive ions, shown in figure 1.2.

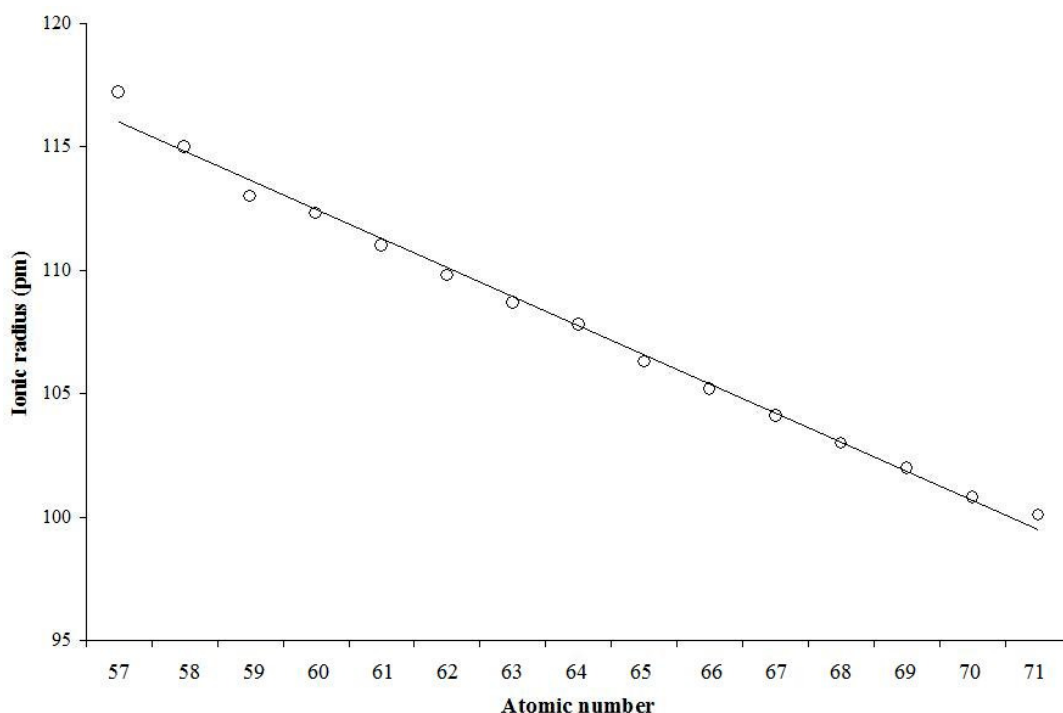


Figure 1.2 Ionic radii for the tripositive ions  $Z=57$  to  $71$  (Shannon 1999).

This poor shielding ability of the 4f electrons is believed to be the major contributor to the lanthanide contraction, although studies reveal about 10% of the contraction is due to relativistic effects (Pyykkö and Descleaux 1979). In heavy atoms such as the lanthanoids, the effects of special relativity become significant for high-speed electrons and result in both a contraction of the radial extension of atomic orbitals and an increase in the rest mass of electrons. Consequently there is a decrease in the atomic radius. Other notable examples of chemical relativistic effects are the physical state of mercury at ambient temperature and the colour of gold. Mercury is known to exist as the monoatomic species Hg in the gaseous state. The contraction of the valence electron shell means it does not play a significant role in bonding and so the atoms in the liquid are held together by weak Van der Waals forces alone. With gold, the contraction of the 6s orbital means the  $5d \rightarrow 6s$  energy transition is shifted from the ultra-violet into the visible part of the electromagnetic spectrum. The wavelength of light concerned is in the blue region of the spectrum, resulting in the metal having its distinctive yellow colour (Norrby 1991).

### 1.3.1 The lanthanide contraction illustrated in unit cell parameters

Because of the existence of the lanthanide contraction the possibility arises that the unit cell parameters for particular series of compounds might also follow a contraction. For example, if a particular lanthanoid compound exhibits cubic symmetry, then the rest of the lanthanoids when present in the same type of compound might also exhibit the same symmetry. Furthermore, a plot of the unit cell parameter against atomic number might show a trend similar to that of the lanthanide contraction. There are many references citing cases of series of lanthanoid compounds exhibiting a common structure (Siddiqui and Hoppe 1975), (Feldner and Hoppe 1980), (Urland *et al* 1980), (Aléone and Pouzet 1968). Aléone and Pouzet consider the series of compounds  $\text{Rb}_2\text{NaLnF}_6$  and  $\text{Cs}_2\text{NaLnF}_6$ , where Ln is a lanthanoid, and state that all are cubic with the perovskite structure and of space group  $Fm\bar{3}m$ . Unit cell data for the series of cubic structures  $\text{Rb}_2\text{NaLnF}_6$  is given in table 1.3 and illustrated in figure 1.3. It is clear that the trend in the cell size across the series is similar to that of the tripositive ionic radii. Data for the series of tetragonal structures  $\text{LiLnF}_4$  is given in table 1.4 and illustrated in figure 1.4. ICDD is the International Centre for Diffraction Data.

| Z  | Element | ICDD ref | Cell $a$ (Å) | Crystal system | Space group  |
|----|---------|----------|--------------|----------------|--------------|
| 62 | Sm      | 21-1041  | 8.988        | Cubic          | $Fm\bar{3}m$ |
| 65 | Tb      | 21-1042  | 8.921        | Cubic          | $Fm\bar{3}m$ |
| 67 | Ho      | 21-1040  | 8.881        | Cubic          | $Fm\bar{3}m$ |
| 68 | Er      | 20-1384  | 8.867        | Cubic          | $Fm\bar{3}m$ |
| 70 | Yb      | 21-1043  | 8.816        | Cubic          | $Fm\bar{3}m$ |

Table 1.3 Unit cell parameters for the cubic series  $\text{Rb}_2\text{NaLnF}_6$  (ICDD 1995).

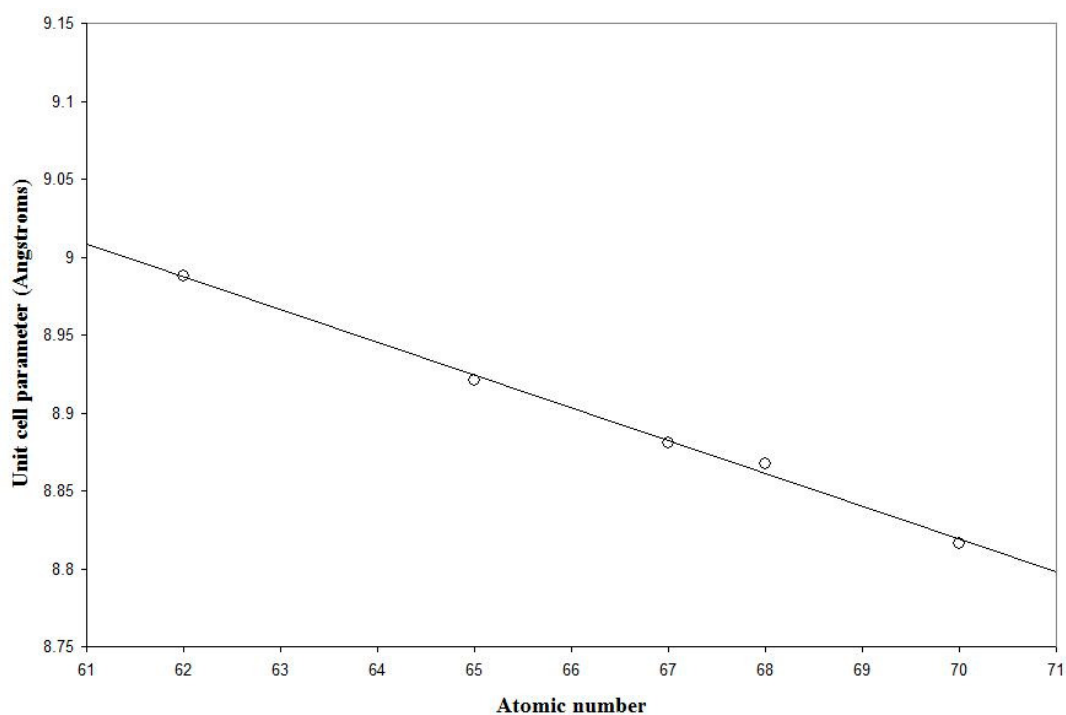


Figure 1.3 Atomic number versus unit cell parameter for the cubic series  $Rb_2NaLnF_6$  (ICDD 1995).

| Z  | Element | ICDD ref | Cell $a$ (Å) | Cell $c$ (Å) | Crystal System | Space group |
|----|---------|----------|--------------|--------------|----------------|-------------|
| 63 | Eu      | 27-0292  | 5.21         | 11.02        | Tetragonal     | $I4_1/a$    |
| 64 | Gd      | 27-1236  | 5.21         | 11.00        | Tetragonal     | $I4_1/a$    |
| 65 | Tb      | 27-1262  | 5.19         | 10.89        | Tetragonal     | $I4_1/a$    |
| 66 | Dy      | 27-1233  | 5.19         | 10.81        | Tetragonal     | $I4_1/a$    |
| 67 | Ho      | 27-1243  | 5.16         | 10.75        | Tetragonal     | $I4_1/a$    |
| 68 | Er      | 27-1235  | 5.16         | 10.70        | Tetragonal     | $I4_1/a$    |
| 69 | Tm      | 27-1265  | 5.15         | 10.64        | Tetragonal     | $I4_1/a$    |
| 70 | Yb      | 23-0371  | 5.13         | 10.58        | Tetragonal     | $I4_1/a$    |
| 71 | Lu      | 27-1251  | 5.13         | 10.53        | Tetragonal     | $I4_1/a$    |

Table 1.4 Unit cell parameters for the tetragonal series  $LiLnF_4$  (ICDD 1995).

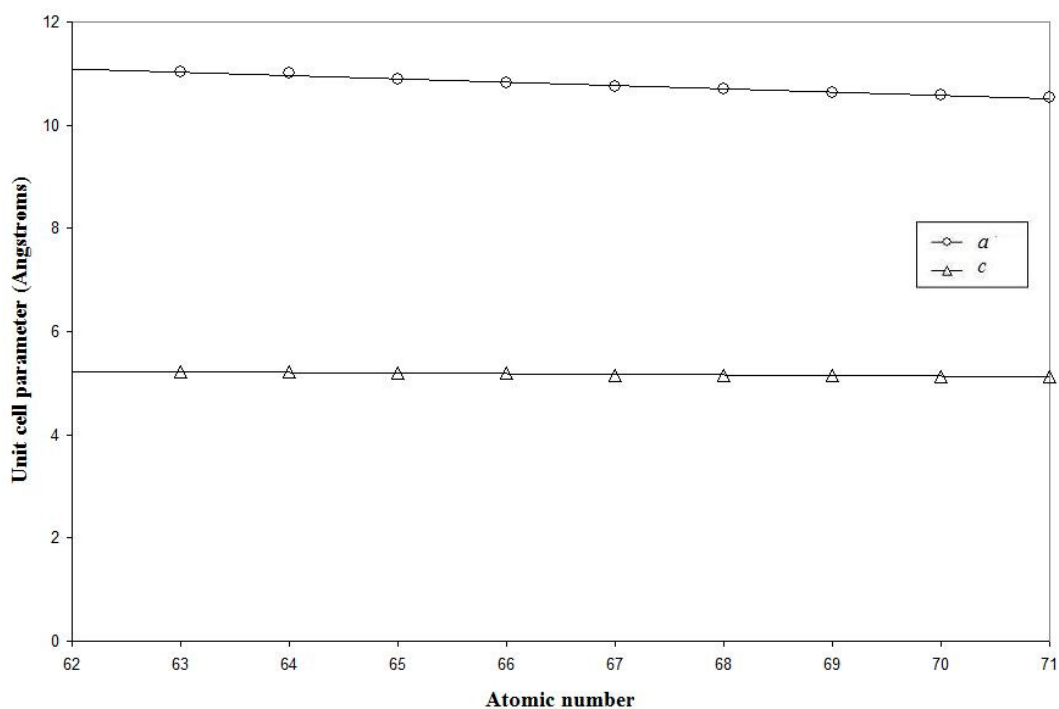


Figure 1.4 Atomic number versus unit cell parameters for the tetragonal series  $\text{LiLnF}_4$  (ICDD 1995).

Because of this trend across series of lanthanoid compounds, it is often a good starting point when considering an unknown structure to look at the structures of the same compounds of the adjacent metals. In many cases the cell type and space group will be the same. Furthermore, the unit cell parameters may be the same, subject to an adjustment according to the lanthanide contraction. In such a case, the atom positions are also likely to be the same. However, a single cell type is not generally representative of any one series of lanthanoids. There are series of compounds where the shrinking co-ordination sphere of the metal induces a change in cell type. For example, with the lanthanoid sesquioxides there is a shift from the 7-fold co-ordination of a hexagonal structure, to the 6-fold co-ordination of a cubic structure. In such a series a break would be seen in the plot of unit cell parameters; a pair of lines corresponding to the values for  $a$  and  $c$  in the hexagonal cell would switch to a single line corresponding to the single cubic cell parameter. For both cell types the plots would still follow the downward trend of the lanthanide contraction.

## 1.4 LANTHANOID COMPOUNDS

### 1.4.1 Overview

The crystal structure of the simple compounds such as the sesquioxides and halides exhibit high co-ordination numbers due to the large sizes of the tripositive lanthanoid ions. The sesquioxides are the most stable oxides, except for those of cerium, praseodymium and terbium, whose oxides contain the metal wholly (cerium) or partly (praseodymium and terbium) in the +4 oxidation state. At ambient temperature the sesquioxides of the lighter lanthanoids exhibit hexagonal symmetry. Heavier sesquioxides exhibit cubic symmetry. The monoxide of europium is known but there is doubt as to the phases of other low-oxygen species. Higher oxides exist, notably that of cerium. Ceric oxide,  $\text{CeO}_2$ , has the fluorite structure (as do  $\text{PrO}_2$  and  $\text{TbO}_2$ ) but a range of phases is known to exist, with some intermediate between  $\text{Ce}_2\text{O}_3$  and  $\text{CeO}_2$ , for example  $\text{Ce}_{32}\text{O}_{58}$ ,  $\text{Ce}_{32}\text{O}_{57}$  and  $\text{Ce}_{18}\text{O}_{31}$ . The compound  $\text{Pr}_6\text{O}_{11}$  exists as a mixed phase of the +3 and +4 oxides in the ratio 1:4 and may be converted to  $\text{Pr}_2\text{O}_3$  with hydrogen at high temperature. As with cerium there exists a range of phases between the sesquioxide and the dioxide. The intermediate oxide  $\text{Ln}_7\text{O}_{12}$  is also known for lanthanum, cerium, praseodymium and terbium. The general property of many rare earth oxides is that they have defect lattices in which some  $\text{O}^{2-}$  vacancies in the  $\text{LnO}_2$  fluorite structure are compensated for by the presence of  $\text{Ln}^{3+}$  ions.

The sulphides, selenides and tellurides exhibit the compounds  $\text{LnS}$ ,  $\text{Ln}_3\text{S}_4$ ,  $\text{Ln}_2\text{S}_3$  and  $\text{LnS}_2$  but there are many non-stoichiometric compounds in addition to these. The interest in these compounds lies in their semi-conducting properties.

The hydroxide ion has a similar radius to the fluoride ion and consequently, for the light lanthanoid trifluorides and hydroxides, the same crystal structure is exhibited, that of tysonite,  $\text{LnF}_3$ , with each lanthanoid co-ordinated to 9 fluorides anions. For the trichlorides of the elements lanthanum to gadolinium the  $\text{UCl}_3$  structure is adopted with nine-fold co-ordination around a trigonal prism with 3 chlorides against the three vertical faces. Terbium trichloride adopts the eight-fold co-ordination  $\text{PuBr}_3$  structure and for the metals dysprosium to lutetium the six-fold co-ordination of  $\text{FeCl}_3$  is evident.

The tribromides adopt the same structures as the trichlorides. The triiodides adopt the  $\text{PuBr}_3$  structure for lanthanum to neodymium and the  $\text{FeCl}_3$  structure for samarium to lutetium. Lower halides are known; the difluorides of samarium, europium and ytterbium exhibit the fluorite structure. The difluorides of thulium and ytterbium exhibit the structure of  $\text{CaI}_2$ . The dichlorides of neodymium, samarium, europium, dysprosium and ytterbium are prepared by the reduction of the trichloride with the lanthanoid. The dibromides of samarium, europium, thulium and ytterbium and the diiodides of lanthanum, cerium, praseodymium, neodymium and gadolinium are prepared in a similar way. Diiodides are also obtained by thermal decomposition of the triiodides. Tetrafluorides of cerium, praseodymium and terbium are known, having the  $\text{UF}_4$  structure of a square anti-prism. Attempts to make other tetrafluorides have been unsuccessful but the complexes  $\text{Cs}_3[\text{NdF}_7]$  and  $\text{Cs}_3[\text{DyF}_7]$  have been made by fluorination of a mixture of caesium chloride and the lanthanoid trichloride. As a general rule, for all classes of compounds there is a trend of decreasing co-ordination number with decreasing ionic radius.

#### 1.4.2 The lanthanoid sesquioxides

Historically the lanthanoid sesquioxides have been extensively studied, the first notable publication being in 1925 (Goldschmidt *et al* 1925). This study first highlighted the three structural types, A, B and C. Their crystallographic forms and polymorphism have been reviewed on a number of occasions (Brauer 1968), (Haire and Eyring 1994), (Adachi and Imanaka 1998), (Zinkevich 2007). Below  $2000^\circ\text{C}$  the sesquioxides exist in three crystal systems i.e. the cubic C-type, the monoclinic B-type and the hexagonal A-type. With increasing temperature the stability of the structures is generalised by the order  $\text{C} \rightarrow \text{B} \rightarrow \text{A}$ , although not every oxide will exhibit all phases; this general transition is typical of the middle members of the group. Under ambient conditions the A-type oxide is preferred for lanthanum to promethium, although it may exist in combination with the C-type. C-type cerium sesquioxide is actually a non-stoichiometric oxide showing a range of oxygen content, but designated  $\text{Ce}_2\text{O}_3$ . Both C and B-type oxides exist for samarium, europium and gadolinium. The C-type is stable under ambient conditions from samarium onwards and for the heavier metals of the series this phase is preferred, although it may exist in combination with the B-type

oxide, the fraction of B-type falling with increasing weight of the metal. For lutetium the C-type oxide is the only phase known, as there is a direct transition to the molten state at approximately 2400°C.

Above 2000°C an additional two types, denoted by H and X, are present (Föex and Traverse 1966). These are believed to be modifications of the hexagonal and cubic phases, respectively (Aldebert and Traverse 1979). Only a very few lanthanoid sesquioxides exhibit all five phases (promethium, samarium and europium). A phase diagram showing all five modifications is given in figure 1.5.

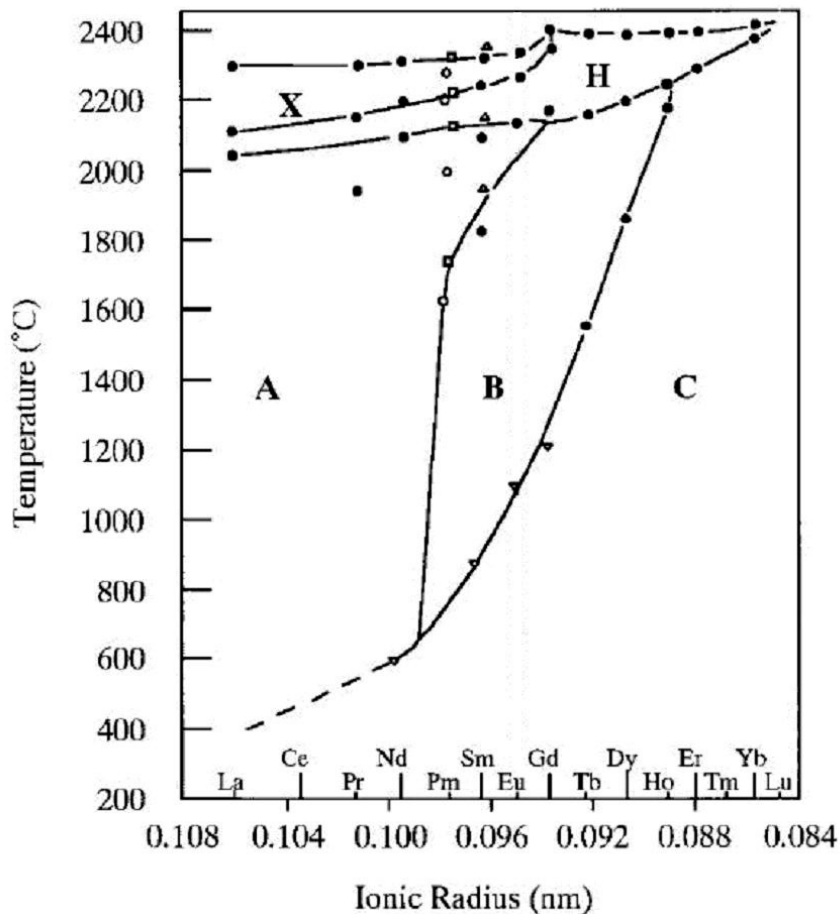
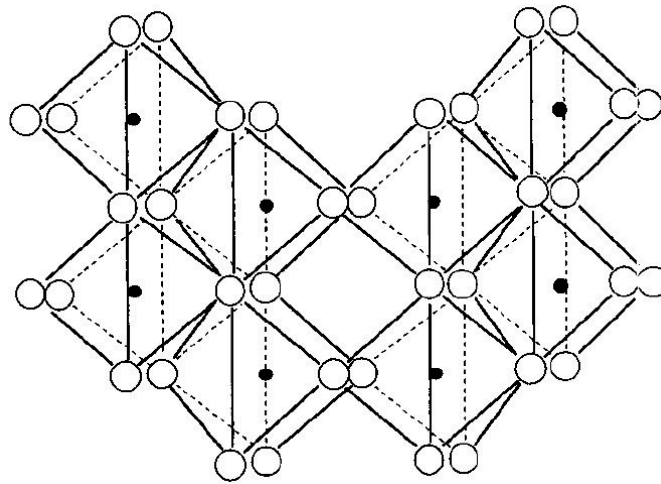


Figure 1.5 Phase diagram for the lanthanoid sesquioxides (Föex and Traverse 1966).

The accepted phase diagram for these 5 polymorphs was constructed from two data sources (Warshaw and Roy 1961), (Föex and Traverse 1966). The diagram shows the three structure types that exist at ambient temperature. For the lighter oxides, the ambient phase is hexagonal and this phase exists until the exotic high temperature H-

and X-types are reached at over 2000°C. For the intermediate oxides, the ambient phase is cubic. On heating, there is a transition to the monoclinic phase before the H and X-types are reached. After holmium sesquioxide, the only phase is cubic until the H phase is reached.

The structures of the three main phases are well known. The A-type exists in space group  $P-3m1$  with one formula unit per unit cell. The metal atoms occupy the 4f sites of the space group. 4 of the oxygen atoms occupy the same sites; the remaining 2 oxygen atoms occupy the 2a sites. The metal atoms are in seven-fold co-ordination to oxygen with four oxygen atoms closer than the other three.



*Figure 1.6 A-type (hexagonal)  $Ln_2O_3$  (where Ln represents any lanthanoid). Solid dots represent metal centres (Eyring 1979).*

The B phase, a distortion of the A-type, exists in space group  $C2/m$  with six formula units per unit cell. All 12 metal atoms occupy the 4i sites of this space group. 16 oxygen atoms also occupy the 4i sites, with a further 2 oxygens occupying the 2b sites. The metal atoms in this phase are six-fold and seven-fold co-ordinated to oxygen.

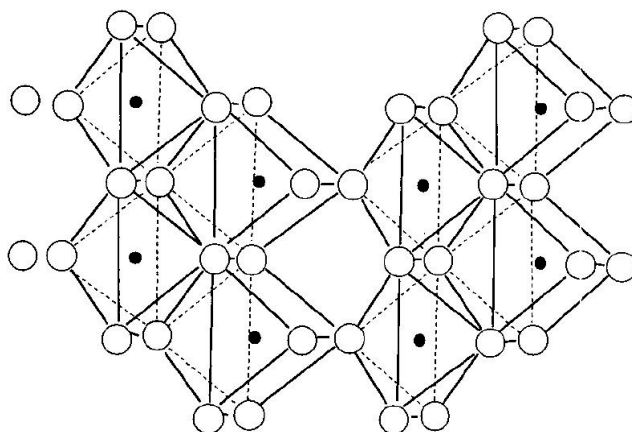


Figure 1.7 B-type (monoclinic)  $Ln_2O$  (Eyring 1979).

The C-type has the bixbyite structure in space group  $Ia-3$ , bixbyite having its most common form as  $Mn_2O_3$ . The unit cell contains 32 metal atoms (on the 8b and 24d sites) and 48 oxygen atoms (occupying all 48e sites). The structure is effectively a fluorite lattice with a quarter of the oxygen sites vacant. In this structure the metal atoms are six-fold co-ordinated to oxygen.

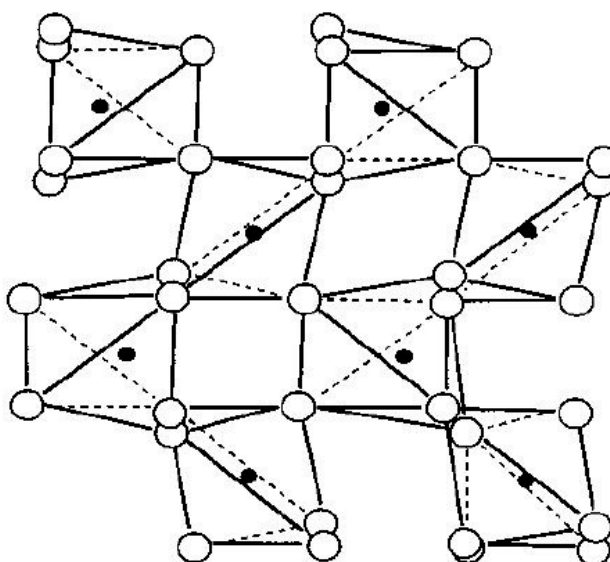


Figure 1.8 C-type (cubic)  $Ln_2O_3$  (Eyring 1979).

### 1.4.3 The praseodymium-oxygen system

When the ratio of oxygen to metal is variable, the praseodymium-oxygen system shows a number of discrete phases. In fact, of all the rare earth oxides, the praseodymium-oxygen system is the most complex. In addition to the green-coloured sesquioxide there are six well-established and well-studied oxides. The majority of work on the praseodymium-oxygen system comes from Eyring and co-workers in a series of papers, the most significant of which (Hyde *et al* 1965) established the phase diagram in figure 1.9. Here is confirmed the existence of the  $\iota$  ( $x = 1.71$ ),  $\xi$  ( $x = 1.78$ ),  $\epsilon$  ( $x = 1.80$ ) and  $\beta$  ( $x = 1.83$ ) phases, together with two wide-ranging non-stoichiometric phases. These are the face-centred  $\alpha$  phase, with  $2.00 \geq x \geq 1.72$  and the body-centred  $\sigma$  phase, with  $1.7 \geq x \geq 1.6$ . Observed for the first time is the  $\delta$  ( $x = 1.816$ ) phase. It was also established that the discrete monophasic species were members of an incomplete homologous series corresponding to the formula  $\text{Pr}_n\text{O}_{2n-2}$  for values of  $n = 4, 7, 9, 10, 11, 12$  and  $\infty$ . These phases are listed in table 1.5.

| $n$      | Formula                       | phase      | $x$ in $\text{PrO}_x$ | Cell             | Existence                       |
|----------|-------------------------------|------------|-----------------------|------------------|---------------------------------|
| 4        | $\text{Pr}_2\text{O}_3$       | $\phi$     | 1.5                   | B-type BCC       | $<275^\circ\text{C}$            |
|          |                               | $\theta$   | 1.5                   | A-type Hexagonal | $>900^\circ\text{C}$            |
| 7        | $\text{Pr}_7\text{O}_{12}$    | $\iota$    | 1.714                 | Rhombohedral     | $500\text{-}1000^\circ\text{C}$ |
| 9        | $\text{Pr}_9\text{O}_{16}$    | $\xi$      | 1.778                 | Rhombohedral     | $450\text{-}600^\circ\text{C}$  |
| 10       | $\text{Pr}_5\text{O}_9$       | $\epsilon$ | 1.8                   | FCC              | $300\text{-}500^\circ\text{C}$  |
| 11       | $\text{Pr}_{11}\text{O}_{20}$ | $\delta$   | 1.818                 | FCC              | $375\text{-}475^\circ\text{C}$  |
| 12       | $\text{Pr}_6\text{O}_{11}$    | $\beta$    | 1.833                 | FCC              | $275$ to $475^\circ\text{C}$    |
| $\infty$ | $\text{PrO}_2$                | $\alpha$   | 2                     | FCC              | $>500^\circ\text{C}$            |

Table 1.5 Discrete phases in the praseodymium-oxygen system.

Aside from the sesquioxide  $\text{Pr}_2\text{O}_3$ , the red-black material  $\text{Pr}_6\text{O}_{11}$ , sometimes referred to as the *air-ignited* oxide, is the only other oxide stable at ambient temperature. On heating the pale green sesquioxide it is the first oxide to be created. Other than  $\text{PrO}_2$ , this material contains the greatest ratio of oxygen to metal. Further heating gradually reduces this ratio through the phases  $\text{Pr}_{11}\text{O}_{20}$ ,  $\text{Pr}_5\text{O}_9$ ,  $\text{Pr}_9\text{O}_{16}$ ,  $\text{Pr}_7\text{O}_{12}$  and eventually back to  $\text{Pr}_2\text{O}_3$ . The various known phases are shown in figure 1.9.

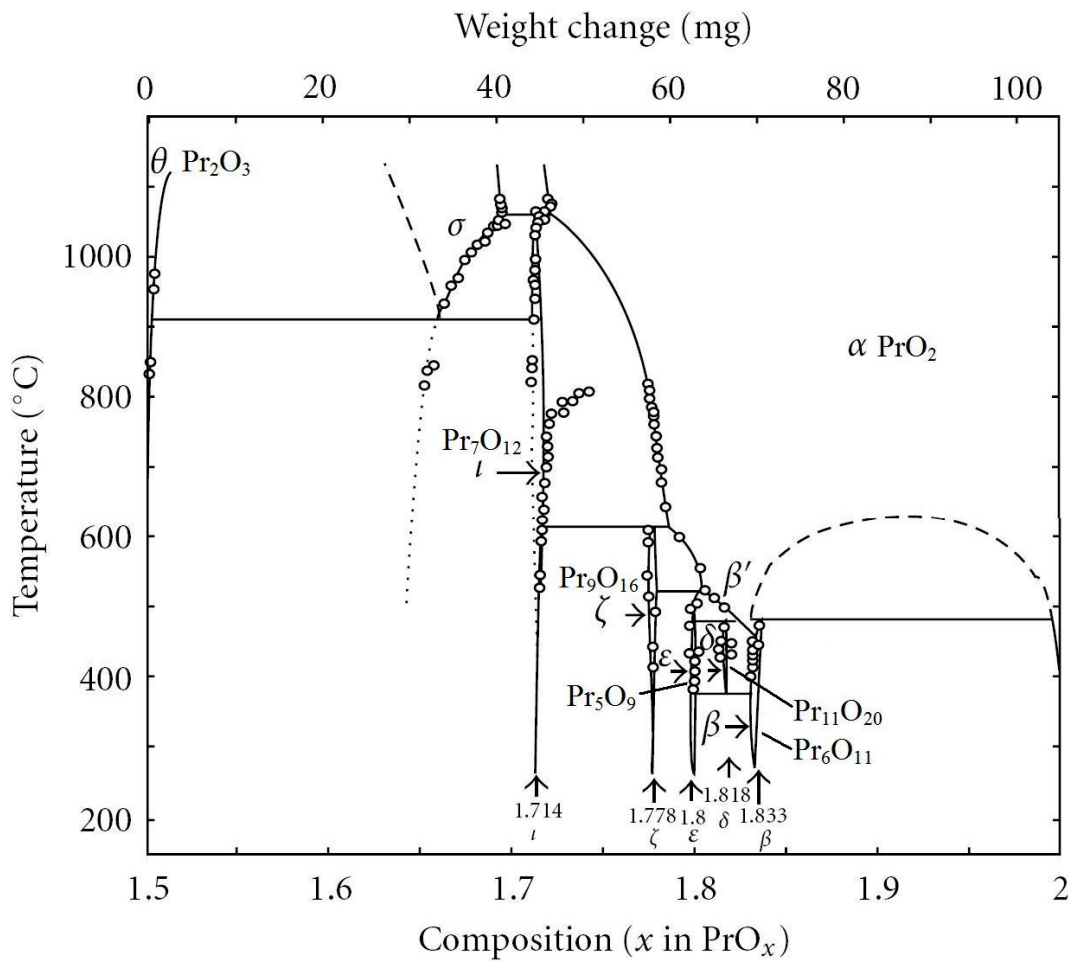


Figure 1.9 Phase diagram for the praseodymium-oxygen system (Hyde et al 1965).

It has been claimed that praseodymium may exhibit the +5 oxidation state (Prandtl 1925) and that the air-ignited oxide has the formula  $2\text{Pr}_2\text{O}_3 \cdot \text{Pr}_2\text{O}_5$ . However, later work (Marsh 1946) shows that the highest oxidation state attainable by praseodymium is +4. This is supported by other work (Zintl and Morawietz 1940) and shows  $\text{Pr}_6\text{O}_{11}$  as the double oxide  $4\text{PrO}_2 \cdot \text{Pr}_2\text{O}_3$ .

## 1.5 AIMS OF THIS WORK

### 1.5.1 Determination of structures resulting from temperature-induced phase transitions

Investigation and characterisation of the structural changes in ceramic materials at high temperature are particularly important. For example, europium sesquioxide is used within nuclear reactor control rods because of its neutron absorbing ability, while ytterbium sesquioxide has been proposed as a component within thermophotovoltaic energy conversion devices (Krishna 1999), (Durisch and Bitnar 2010). Both applications cause structure changes in the oxides and hence an understanding of these changes is important to their operation.

Although the series has been extensively studied, there are a number of omissions in the published work. Not all structures indicated by the phase diagram have been synthesised and their structures recorded. Some of these omissions are addressed in this thesis. Two databases were used as the main source of reference material in this work. The first is the Daresbury ICSD database (ICSD website), existing until January 2013 but now commissioned by the RSC (Royal Society of Chemistry). The second is the ICDD Powder Diffraction File PDF-2 (ICDD 1995).

Of particular interest to this study was the unpublished structure of the B-type phase of  $\text{Gd}_2\text{O}_3$ . Within the Daresbury database there are three distinct structural types of  $\text{Gd}_2\text{O}_3$ , all of which are cubic. They are  $a = 10.80\text{\AA}$ , space group  $Ia\bar{3}$  (Saiki *et al* 1984),  $a = 10.81\text{\AA}$ , space group  $I213$  (Zachariasen 1928) and  $a = 5.21\text{\AA}$ , space group  $Fm\bar{3}m$  (Kashaev *et al* 1975). The PDF-2 database lists 5 entries for  $\text{Gd}_2\text{O}_3$ , two of which are cubic, space group  $Ia\bar{3}$ , 1 is hexagonal (Föex 1966) and 2 are monoclinic, space group  $C2/m$  (Guentert and Mozzi 1958), (Grier and McCarthy 1991).

The phase diagram for the sesquioxides implies that there are no monoclinic phases existing at ambient temperature. Goldschmidt *et al* were unable to identify the cell for the B-type oxide, stating it to be pseudotrigonal, orthorhombic or monoclinic. The first publication of the monoclinic cell was over thirty years later (Douglass and Staritsky 1956) with the atom positions established the following year (Cromer 1957).

Historically there have been a number of studies on B-type  $\text{Gd}_2\text{O}_3$  (Guentert and Mozzi 1958), (Grier and McCarthy 1991). Although none of these studies published a description of the unit cell, both concur that the system is analogous to that of B-type  $\text{Sm}_2\text{O}_3$ . Furthermore, and contrary to the phase diagram, Guentert and Mozzi remark that their B form was stable at ambient temperatures. The known structures of both  $\text{Eu}_2\text{O}_3$  and  $\text{Sm}_2\text{O}_3$ , both having similar unit cell parameters and the same space group, would therefore be a useful starting point for the determination of the structure of monoclinic  $\text{Gd}_2\text{O}_3$  and for determining if this high temperature modification could be retained on cooling.

It is interesting to note that there is a general lack of entries in the Daresbury database for the B-types. The phase diagram indicates that for increasing atomic number of the lanthanoid, an increasingly high temperature is required to convert the C-type to the B-type. However, the diagram also indicates that after  $\text{Ho}_2\text{O}_3$  the C-type converts either to the H-type before melting, or just melts, and that no B-type exists. It is only quite recently that heavy ( $\text{Ho}_2\text{O}_3$  and above) monoclinic sesquioxides have been reported. Just prior to the construction of the sesquioxide phase diagram it had been stated that no monoclinic phases existed beyond  $\text{Dy}_2\text{O}_3$  (Warshaw and Roy 1961). The ICSD database reports monoclinic structures for  $\text{Sm}_2\text{O}_3$ ,  $\text{Eu}_2\text{O}_3$  and  $\text{Tb}_2\text{O}_3$ , together with a recent entry for  $\text{Er}_2\text{O}_3$  (Wontcheu and Schleid 2008). There is also a recent study reporting the structures of a number of A and B-types across the series, although these have been obtained theoretically (Wu *et al* 2007). Considering the report of the existence of B-type  $\text{Er}_2\text{O}_3$  (contrary to the phase diagram), it was decided to investigate the possibility of there being a B-type cell for the only monoclinic species without any entry whatsoever in the ICSD database, namely ytterbium sesquioxide. There are reports of these heavy atom B-type oxides being obtained via temperature *and* pressure, including those of ytterbia and lutetia (Hoekstra and Gingerich 1964), (Hoekstra 1966). The use of inductively coupled radio frequency plasma spraying to create a residual monoclinic phase of lutetia within an otherwise cubic sample has also been reported (Sun *et al* 2007). However, my work was concerned only with structural conversions obtained via increased temperature. A recent high-pressure study (Meyer *et al* 1995) has shown the structure of monoclinic  $\text{Yb}_2\text{O}_3$ . A study at ambient pressure (Guo, Harvey *et al* 2007) has shown the creation of nanoparticles of B-type Dy, Ho, Er, Tm

and Yb sesquioxides by a method of flame synthesis. Another study (Guo *et al* 2007) has shown the creation of B-type  $\text{Er}_2\text{O}_3$  under pressure, which could be quenched to ambient conditions. These references imply that there are modifications to be made to the phase diagram i.e. the lines drawn thereupon are not absolute. The inference is that it might be possible to create monoclinic ytterbia in the bulk material at high temperature and retain it to ambient temperature.

### 1.5.2 Kinetic studies

There has been considerable work done on the kinetics of the  $\text{C} \rightarrow \text{B}$  transition of the intermediate oxides ( $\text{Sm}_2\text{O}_3$ ,  $\text{Eu}_2\text{O}_3$  and  $\text{Gd}_2\text{O}_3$ ). There are two notable references (Stecura 1966), (Ainscough *et al* 1975), but to date no kinetic work has been carried out on the heavier oxides. In addition, there are gaps in work on the kinetics of the  $\text{C} \leftrightarrow \text{A}$  transitions for the lighter oxides. Although Stecura did look at the kinetics for  $\text{La}_2\text{O}_3$  and  $\text{Nd}_2\text{O}_3$ , there has been no work done on  $\text{Ce}_2\text{O}_3$  (presumably because of the lack of a pure sesquioxide) and  $\text{Pr}_2\text{O}_3$ . All kinetic studies have involved the raising of a sample to a number of temperatures and at each temperature noting the degree of conversion with time. Using XRPD data, Stecura measured this variation by noting the change in the integrated intensity of the 222 Bragg reflection from the low temperature modification. Ainscough measured it by comparing the patterns to a series of standards containing both cubic and monoclinic phases in varying proportions.

Although their respective structures are well documented, there is no kinetic data for the  $\text{C} \rightarrow \text{A}$  phase transition in  $\text{Pr}_2\text{O}_3$ . It was therefore decided to perform a kinetic study of this phase change by taking powder diffraction patterns in situ.

Further, there is no data for the  $\theta \rightarrow \beta$  or the higher temperature phase transitions in the Pr-O system, or the  $\text{C} \rightarrow \text{B}$  phase transition in  $\text{Tb}_2\text{O}_3$ . It was decided to investigate the former by a combination of DSC and XRPD and the latter by DSC alone.

### *1.5.3 Investigating and redrawing phase diagrams*

Finally, the above results would be compared to the current phase diagrams for the oxides and an attempt would be made at redrawing them.

## 2 X-RAY DIFFRACTION

### 2.1 THEORY

#### *2.1.1 The Bragg Construction*

In 1912 Walter Friedrich and Paul Knipping, working under Max von Laue, demonstrated the diffraction of X-rays, using a single crystal of copper sulphate for a grating. Laue was subsequently awarded the Nobel Prize for demonstrating the both wave-like nature of X-rays and the periodic internal structure of a crystal. The explanation of these results in terms of crystal structure and the behaviour of X-rays inside the crystal was carried out by W.H and W.L. Bragg in 1913 for which they jointly won the Nobel Prize. Since then X-ray crystallography has become a powerful and well-established tool for structure determination in the solid state.

Laue's postulate that a crystal consisted of regularly spaced particles was confirmed by this famous experiment. A photographic plate placed beyond the sample showed a series of dark spots where X-rays had fallen after reflection from the crystal. He proposed that different spots on the photograph were caused by different wavelengths of X-rays. The Braggs interpreted these spots quite differently, explaining them as showing diffraction occurring only in certain definite directions from the three-dimensional periodic structure of the crystal. Rather than the slits of a diffraction grating, the spacing now corresponded to the perpendicular distance between adjacent parallel planes of atoms in the crystal. In certain directions, the wavelets propagating from successive planes would constructively interfere and produce a dark spot, or Bragg peak.

The Braggs considered the crystal as a series of parallel planes separated by a distance,  $d$ , which, for the purpose of the construction, act like mirrors. This is illustrated in figure 2.1. X-rays arriving from the left are incident on the parallel crystal planes at an angle  $\theta$  and leave the crystal at the same angle. The path difference between the top and bottom waves is a multiple of the wavelength,  $\lambda$ .

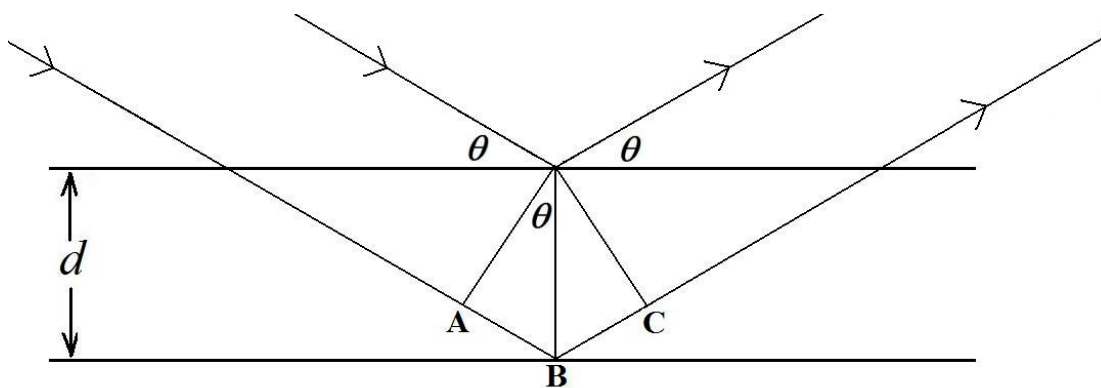


Figure 2.1 The Bragg Construction.

From figure 2.1

$$AB + BC = n\lambda \quad (2.1)$$

Therefore:

$$\sin \theta = \frac{n\lambda}{2d} \quad (2.2)$$

Rearranging gives the Bragg equation:

$$n\lambda = 2d \sin \theta \quad (2.3)$$

where  $n$  is an integer corresponding to the order of the diffracted beam.

The Bragg equation describes the condition for constructive interference from any set of parallel planes of the crystal, separated by a distance  $d$ .

### 2.1.2 Describing crystal planes and reflections

A crystal is a repeat structure in three dimensions and the basic building block from which it is constructed is called the unit cell. To illustrate this, figure 2.2 shows a unit cell. The 3 side lengths in 3-dimensional space are termed  $a$ ,  $b$  and  $c$ . The 3 interaxial angles are termed  $\alpha$ ,  $\beta$  and  $\gamma$ .

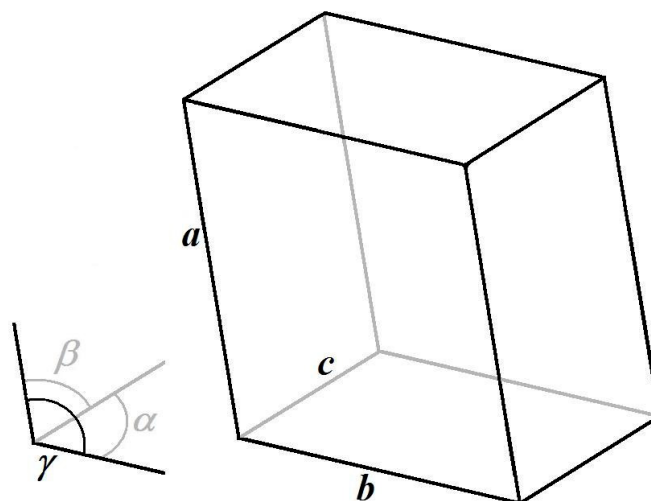


Figure 2.2 A unit cell. Cell edges are represented by  $a$ ,  $b$  and  $c$ , interaxial angles by  $\alpha$ ,  $\beta$  and  $\gamma$ .

In the simplest terms there are seven types of cell, each displaying different symmetries. The highest symmetry is expressed by the cubic cell, which has one parameter, namely the length of its edge. The lowest symmetry is shown by the triclinic cell, with three different cell edges and three different interaxial angles. The seven crystal systems are detailed in table 2.1, along with their associated degrees of freedom and the restrictions placed on the unit cell parameters.

| Crystal system | Degrees of freedom | Restrictions  |
|----------------|--------------------|---|
| Cubic          | 1                  | $a = b = c ; \alpha = \beta = \gamma = 90^\circ$                |
| Tetragonal     | 2                  | $a = b \neq c ; \alpha = \beta = \gamma = 90^\circ$             |
| Hexagonal      | 2                  | $a = b \neq c ; \alpha = \beta = 90^\circ ; \gamma = 120^\circ$ |
| Trigonal       | 2                  | $a = b = c ; \alpha = \beta = \gamma \neq 90^\circ$             |
| Orthorhombic   | 3                  | $a \neq b \neq c ; \alpha = \beta = \gamma = 90^\circ$          |
| Monoclinic     | 4                  | $a \neq b \neq c ; \alpha = \gamma = 90^\circ \neq \beta$       |
| Triclinic      | 6                  | $a \neq b \neq c ; \alpha \neq \beta \neq \gamma \neq 90^\circ$ |

Table 2.1 The seven crystal systems.

The seven crystal systems represent the building blocks of a crystal at its most basic level. If we consider any of these cells to contain a single repeat unit i.e. only one point of symmetry (at each of its 8 vertices) then we obtain the 7 primitive cells. However, when translational symmetry is also taken into consideration it is found that there are

actually 14 cell types, called the Bravais Lattices (or Space Lattices). These take into account all possible combinations of cell-centered and face-centered symmetry points. The 14 Bravais Lattices are illustrated in figure 2.3.

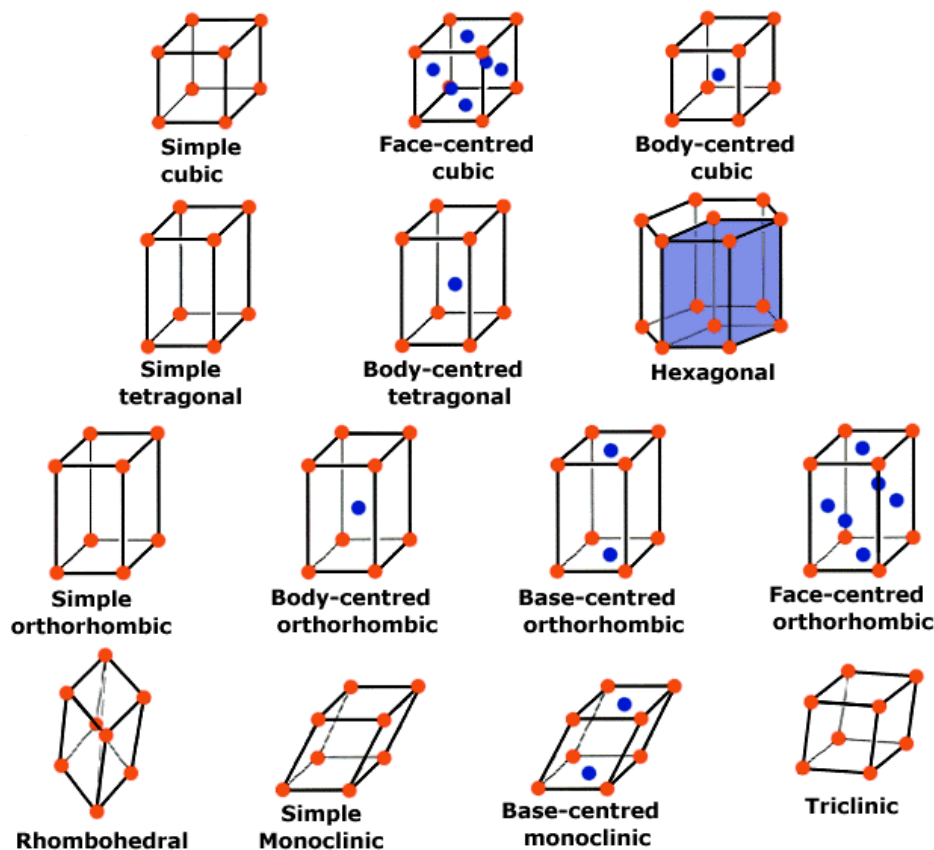


Figure 2.3 The 14 Bravais Lattices. Image from <http://www.seas.upenn.edu/~chem101/sschem/solidstatechem.html>

A crystal lattice is a repeat structure in 3-dimensional space with each point in the lattice representing a physical unit. For example, the primitive cubic cell has one repeat unit at each vertex. This unit may be as simple as a single atom. It might be a group of atoms or an organic molecule. Since each of these 8 points is shared amongst 8 adjoining unit cells, there is actually only one repeat unit per cell. The body-centred unit cell has the one repeat unit by virtue of its 8 vertices and another repeat unit at the body centre, making a total of 2 in the unit cell. The face-centred unit cell again has the one repeat unit of the primitive cell plus another 3 by virtue of its face-centred units, making a total of 4 in the unit cell.

### 2.1.3 Crystal planes

Any set of parallel planes within a crystal lattice can be described by 3 numbers, called the Miller indices of the planes. The numbers represent the number of intercepts on each of the 3 spatial axes within a single unit cell. Figure 2.4 illustrates this concept.

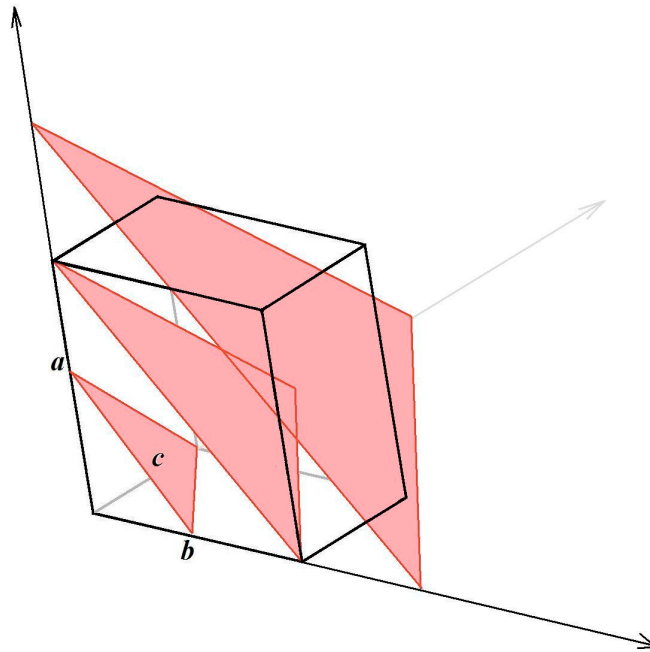


Figure 2.4 A set of parallel planes in a crystal.

In figure 2.4 the set of parallel planes illustrated intersect the  $a$  axis twice per unit cell, the  $b$  axis twice and the  $c$  axis once. Hence this set of planes is termed (221). The value of  $n$  in the Bragg equation then becomes incorporated into the description of the set of planes i.e.  $n$  is always taken to be 1.

### 2.1.4 The Bragg equation reflected in crystal symmetry

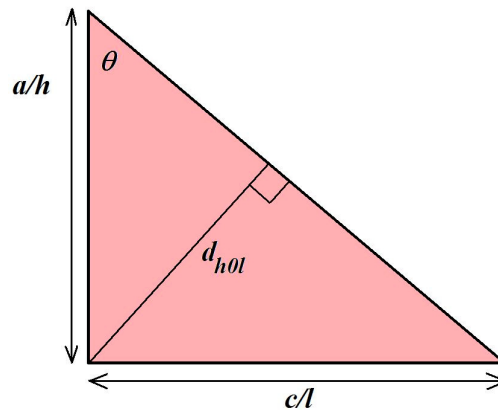


Figure 2.5 A section of a 2-dimensional lattice.

Figure 2.5 shows a section of a 2-dimensional lattice, where  $d$  is the interplanar spacing,  $a$  and  $c$  are the unit cell parameters and  $h$  and  $l$  are the Miller indices of the set of planes under consideration. It follows from trigonometry that:

$$\sin \theta = \frac{d_{(h0l)}}{a/h} \quad (2.4)$$

$$\text{and } \cos \theta = \frac{d_{(h0l)}}{c/l} \quad (2.5)$$

Using the relationship  $\sin^2 \theta + \cos^2 \theta = 1$

$$\frac{d_{(h0l)}^2 h^2}{a^2} + \frac{d_{(h0l)}^2 l^2}{c^2} = 1 \quad (2.6)$$

Factorising

$$d_{(h0l)}^2 \left( \frac{h^2}{a^2} + \frac{l^2}{c^2} \right) = 1 \quad (2.7)$$

Rearranging

$$\frac{1}{d_{(h0l)}^2} = \frac{h^2}{a^2} + \frac{l^2}{c^2} \quad (2.8)$$

By analogy, in three dimensions the equation becomes:

$$\frac{1}{d_{(hkl)}^2} = \frac{h^2}{a^2} + \frac{k^2}{b^2} + \frac{l^2}{c^2} \quad (2.9)$$

This equation represents the orthorhombic system. Combining the above with the Bragg equation  $n\lambda = 2d \sin\theta$  gives:

$$\sin^2 \theta_{(hkl)} = Ah^2 + Bk^2 + Cl^2 \quad (2.10)$$

$$\text{where } A = \frac{\lambda^2}{4a^2}, B = \frac{\lambda^2}{4b^2}, C = \frac{\lambda^2}{4c^2}$$

This provides a simple expression relating the angles at which Bragg diffraction can occur and the respective planes giving rise to it. It can be simplified for higher symmetry systems. For the tetragonal system, where  $a = b$ , the equations become

$$\frac{1}{d_{(hkl)}^2} = \frac{h^2 + k^2}{a^2} + \frac{l^2}{c^2} \quad (2.11)$$

$$\sin^2 \theta_{(hkl)} = A(h^2 + k^2) + Cl^2 \quad (2.12)$$

and for the cubic system, where  $a = b = c$ , the equations reduce to:

$$\frac{1}{d_{(hkl)}^2} = \frac{h^2 + k^2 + l^2}{a^2} \quad (2.13)$$

$$\sin^2 \theta_{(hkl)} = A(h^2 + k^2 + l^2) \quad (2.14)$$

These equations for the orthogonal cells illustrate that Bragg diffraction may occur only at specific angles (or specific interplanar spacings). It is possible to derive selection rules for the Miller indices for different lattices. Table 2.2 shows the possible values of  $h$ ,  $k$  and  $l$  for cubic lattices.

| <b>Bravais lattice</b> | <b>Allowed reflections</b> | <b>Forbidden reflections</b> | <b>Examples</b> |
|------------------------|----------------------------|------------------------------|-----------------|
| Primitive (P)          | Any $hkl$                  | None                         | CsCl            |
| Body-centred (I)       | $h+k+l$ even               | $h+k+l$ odd                  | Fe              |
| Face-centred (F)       | $hkl$ all even or odd      | $hkl$ mixed even or odd      | NaCl, Ag        |

*Table 2.2 Values of  $h$ ,  $k$  and  $l$  for cubic lattices.*

### 2.1.5 Point groups and space groups

Once the cell type has been identified, the crystal can be assigned to one of the 230 space groups. A space group represents the most specific description possible for a crystal lattice and categorically defines the structure. The symmetry operations present in the lattice are described by the point group (or crystal class), of which there are 32 in total. Any such symmetry operation leaves the structure visually unchanged and at least one point unmoved. They consist of rotation (where the structure is rotated a specific fraction of a circle), reflection (where the structure is reflected through a plane) and inversion (where the signs of co-ordinates are reversed with respect to a centre of symmetry). When the point group operations are combined with certain translational operations, we arrive at the 230 point groups. The relevant translations are a pure translation (moving in a line a certain fraction of a unit cell), a screw axis (rotation followed by translation parallel to the axis of rotation) and a glide plane (translation along a plane then reflection through the plane).

## 2.2 EXPERIMENTAL DETAILS

### 2.2.1 The X-ray powder diffraction (XRPD) pattern

The Bragg equation defines the planes,  $d$ -spacings and directions at which constructive interference occurs with a crystal. For a single crystal of sufficient size, the various reflections can be identified as the detector is moved around the sample. This means that together with a list of angles, interplanar spacings and intensities of the Bragg peaks, the Miller indices of the planes are also known. However, if a single crystal of sufficient size cannot be grown, X-ray powder diffraction (XRPD) is employed. Now rather than a single crystal lattice having one orientation relative to the incident X-ray beam, the bulk sample consists of a large number of randomly oriented microcrystallites. An incident beam may strike a particular set of planes within a microcrystal and Bragg reflection will occur at the corresponding angle. However, the specific direction that the diffracted beam leaves the sample will depend on the orientation of the microcrystal relative to the bulk powder. This is illustrated in figure 2.6.

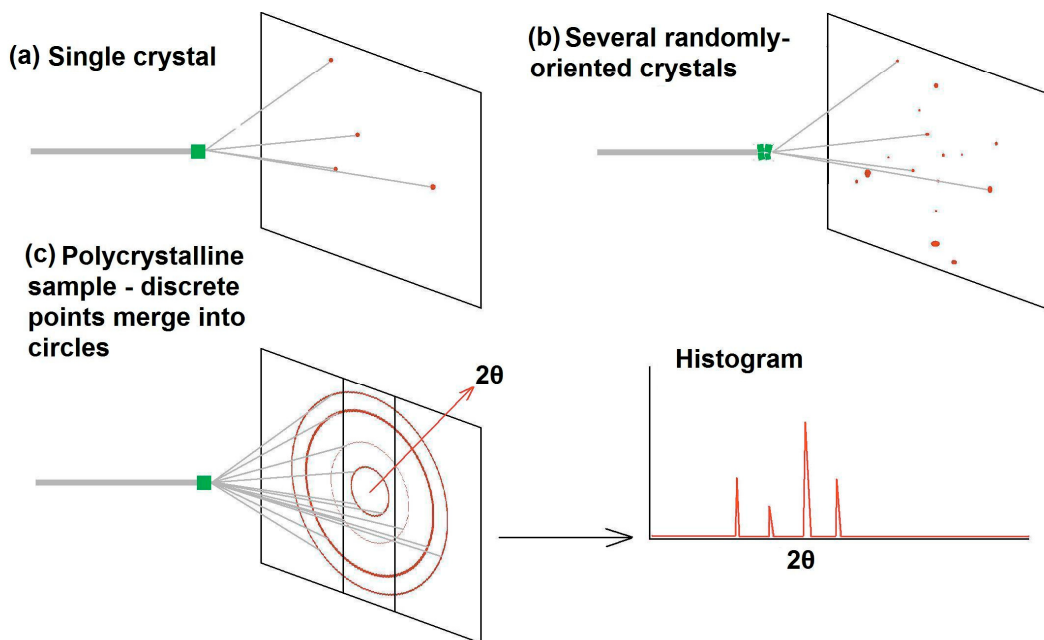


Figure 2.6 X-ray diffraction from a single crystal versus powder.

Figure 2.6(a) shows an X-ray beam incident on a single crystal. Bragg diffraction occurs from a number of planes and spots are seen on the photographic plate. As in figure 2.1, the Bragg construction, the angle between incident and scattered rays is  $2\theta$ . Figure 2.6(b) shows four randomly oriented single crystals. Again Bragg diffraction occurs and four sets of spots now appear on the plate. Figure 2.6(c) shows the effect of placing a polycrystalline material in the beam. The crystallites now lie in every possible orientation, and so each set of parallel planes in the sample gives rise to a cone of scattered radiation with a semi-vertex angle of  $2\theta$ . The spots merge into circles where they intersect with the plate, producing so-called Debye-Scherrer rings, named after the camera invented by Debye, Scherrer and Hull. A modern X-ray powder diffractometer measures intensity against  $2\theta$ , extending radially from the centre of the circle in figure 2.6(c). With a single crystal there is directional anisotropy as well as angular information to the image. With the powder the directional information is lost and only the angles are measurable. Thus an XRPD pattern consists of a set of  $2\theta$  values (readily convertible to  $d$ -spacings via the Bragg equation) and the associated intensities of the reflections.

## 2.2.2 The factors that contribute to a powder pattern

### 2.2.2.1 Peak position and intensity

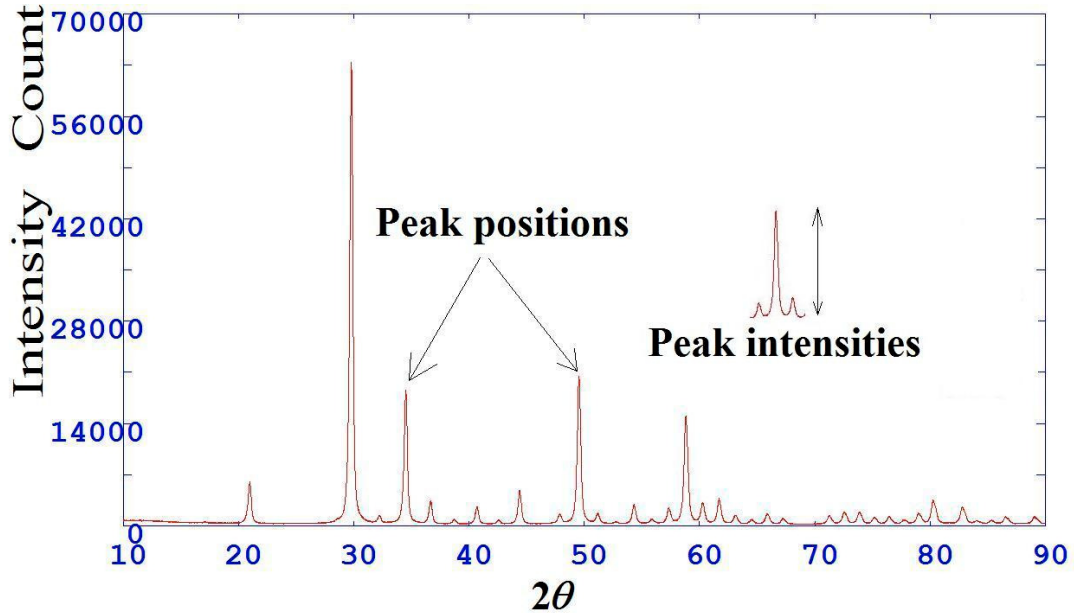
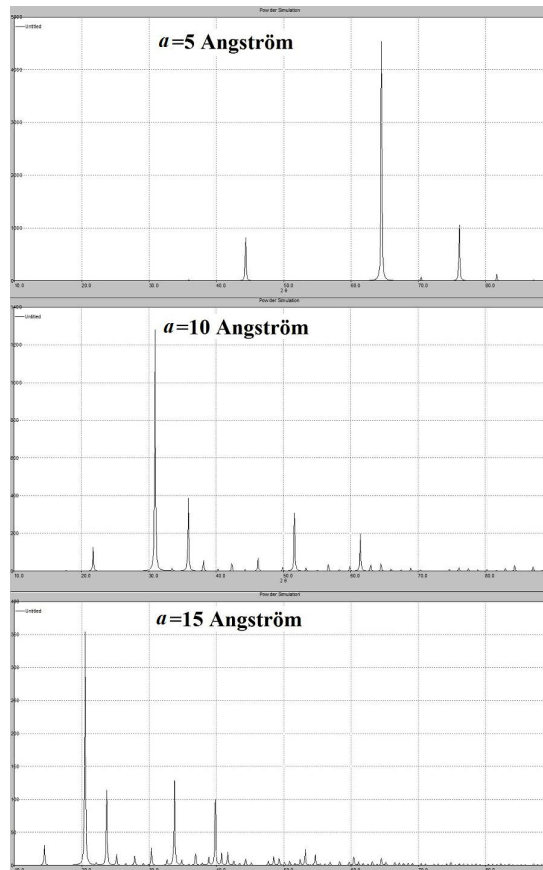


Figure 2.7 Peak positions and peak intensities.

The two most important features of an XRPD pattern are both expressions of the unit cell. These features are illustrated in figure 2.7. Firstly the positions of the peaks in the pattern i.e. the specific angles at which Bragg diffraction can occur are determined solely by the cell type. The unit cell parameters of the lattice generate a series of possible  $d$ -spacings. Essentially, all XRPD patterns of the same cell type will have the same series of peaks, albeit there will be differences of scale between patterns due to different cell sizes. For example, potassium chloride and elemental silver both have face-centred cubic lattices and so both will have the same series of Miller indices from which Bragg reflections occur. To illustrate how peak positions vary with unit cell parameter, figure 2.8 shows a number of patterns for a cubic cell.



*Figure 2.8 How unit cell parameter affects peak positions.*

For each cell in figure 2.8 only the unit cell parameter,  $a$ , has been changed. As the cell shrinks, the magnitudes of the possible interplanar spacings decrease according to the Bragg equation. Hence the angles at which Bragg diffraction occur increase in inverse proportion.

Secondly, the intensities of the peaks are determined by atomic weights and the positions of the atoms in the unit cell. To illustrate how peak intensities are affected by changing the cell contents whilst leaving the peak positions unaffected, figure 2.9 shows 2 XRPD patterns based on the structure of the mineral europia ( $\text{Eu}_2\text{O}_3$ ). The top image gives the actual pattern based on the known structure. The second gives a calculated pattern where the europium atoms are replaced by scandium, a much lighter metal with fewer electrons to scatter the incident X-ray beam.

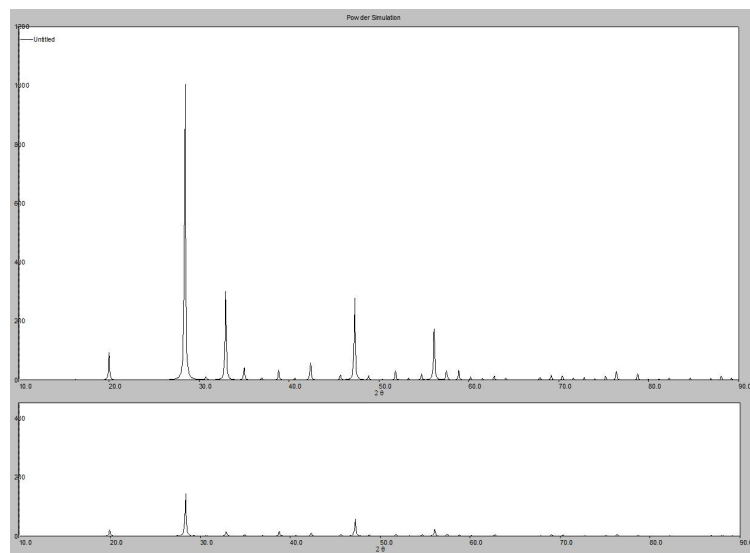


*Figure 2.9 How cell contents affect peak intensities. Upper pattern  $\text{Eu}_2\text{O}_3$ , lower pattern  $\text{Sc}_2\text{O}_3$ .*

Although an ideal powder pattern would contain sharp Bragg reflections, there is always a profile to each peak. The height of the peak is determined by other factors in addition to the atomic positions, the major factors being multiplicity and preferred orientation. Multiplicity is the number of reflections contributing to a peak. If we consider the equation for the cubic cell,  $\sin^2\theta_{(hkl)} = A(h^2 + k^2 + l^2)$ , it is clear that for some values of  $2\theta$  there can be more than one set of planes with the same  $d$ -spacing. To illustrate this, the (221) planes and the (300) planes both have  $h^2 + k^2 + l^2 = 9$ . Therefore, some peaks in the pattern are actually the summation of several peaks, but because the diffraction pattern is condensed into the one dimension of  $2\theta$  space (compared to the 3 dimensions of a single crystal pattern), these peaks are superimposed and a single peak is recorded. Preferred orientation becomes important when the crystal morphology is elongated in one or more direction. In either case, the material tends to line up in certain directions rather than the random orientation desirable for XRPD. The result is that the intensities of particular peaks will tend to be enhanced. This can be obviated somewhat by grinding the powder sufficiently prior to analysis.

For an ideal powder sample the intensity is given by:

$$I(hkl) = c L(2\theta) P(2\theta) A(2\theta) j_{hkl} |\mathbf{F}(hkl)|^2 \quad (2.15)$$

where  $c$  is a scale factor

$L$  is the geometric (Lorentz) factor

$P$  is the polarisation of the X-ray source

$A$  is the absorption factor

$j_{hkl}$  is the multiplicity of the reflection

$\mathbf{F}(hkl)$  is the structure factor, a measure of the scattering power of the electrons of the unit cell

$L, P$  are correction factors for the diffractometer;  $A$  is a correction factor for the sample.

Each atom in the unit cell is surrounded by an electron cloud and it is this that is responsible for the scattering of incident X-rays. The scattering due to all atoms throughout the unit cell is a vector quantity called the structure factor. This vector quantity is a summation over all the atoms in the unit cell and is given by

$$F(hkl) = \sum s_n o_n e^{-W_n} e^{(2\pi i(hx_n + ky_n + lz_n))} \quad (2.16)$$

where  $s_n$  is the atomic scattering length, the ratio of the atom X-ray scattering factor (proportional to atomic number) to the electron radius  $2.818 \times 10^{-15} \text{m}$

$o_n$  is the atomic occupation on a particular site

$\exp(2\pi i(hx_n + ky_n + lz_n))$  is the wave interference term

$W_n$  is a thermal factor called the Debye-Waller factor, dependent upon both temperature and atomic displacement.

Whereas the structure factor is a vector quantity and contains phase information, the intensity contains the modulus of the square of the structure factor. Therefore the intensity, which is the quantity measured in a powder pattern, can provide no information on the phases of interfering wavelets. Hence nothing of the cell contents can be inferred directly from the pattern. How the intensity relationship is employed in structure solution will be explained further in 2.3.5.

### 2.2.2.2 Peak width

Since the electron cloud of an atom has size, scattered X-rays arising from different points on its surface will experience different degrees of interference.

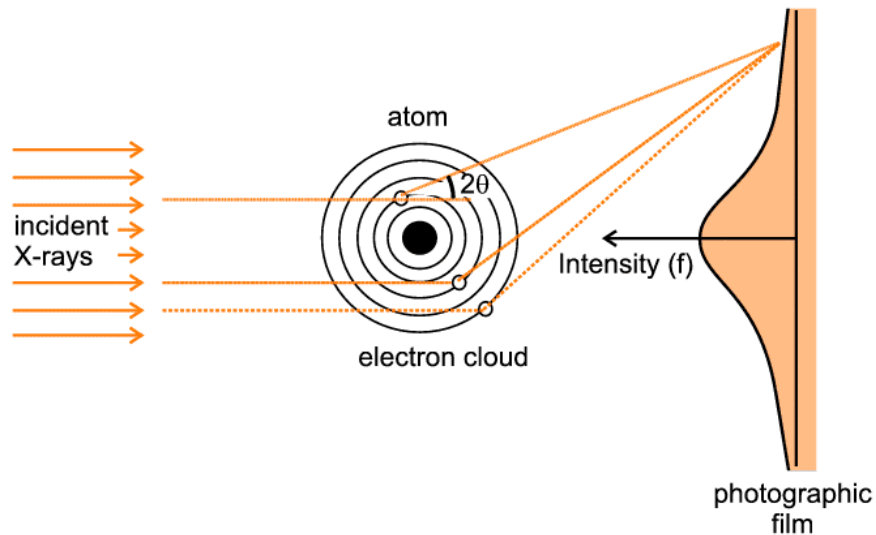


Figure 2.10 Scattering of X-rays by a single atom. Image from <http://pd.chem.ucl.ac.uk/pdnn/peaks/peakcon.htm>

Figure 2.10 shows that X-rays leaving the atom from different points may have a different path length to the detector. This is one factor leading to peak widening. Peak width is also determined by the size and strain of the crystallites. Figure 2.11 shows a typical peak.

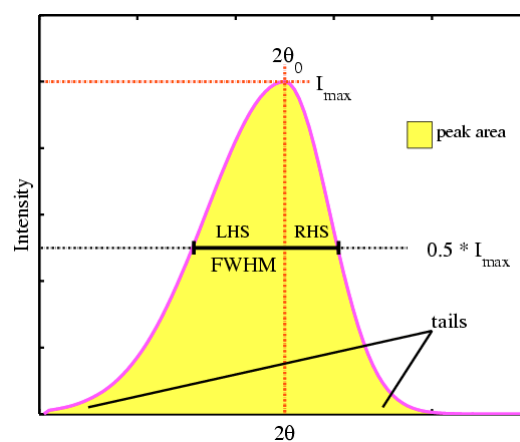


Figure 2.11 A peak from a powder diffraction pattern. Image from <http://pd.chem.ucl.ac.uk/pdnn/peaks/peakcon.htm>

Looking at the peak, there are two important features to note. First, the peak has a distribution of intensities rather than a single value. Second, the assigned  $2\theta$  value may not occur at the middle of the peak i.e. there may be some asymmetry. The quantity used to measure the peak width is FWHM (full width at half maximum). It is clear from this image that care must be taken to record the pattern as accurately as possible in order that the most appropriate value for  $2\theta$  can be determined, as it is the  $2\theta$  values that will be used in indexing in order to determine the cell type.

### *2.2.2.3 Short-range order*

The regions between the peaks may contain information about short-range order in the material. This may be important if the material shows only part crystallinity, or is mixed with such a material. This might occur with a polymer, where there is a degree of alignment in a certain direction, but this is not extended through the whole material.

### *2.2.3 Sources of X-rays*

#### *2.2.3.1 The X-ray tube*

The modern X-ray tube is in principle no different to the cathode ray tubes employed by Crookes in the late 19<sup>th</sup> century. Indeed, it was Röntgen's experiments with a Crookes tube in 1895 that led to his discovery of X-rays. An evacuated glass tube has at one end a hot tungsten filament, which, by virtue of its temperature, emits electrons. A large potential difference, of the order of 100kV, is applied across the tube and the electrons are accelerated to the anode, with which they interact. X-rays are then produced, leaving the tube through a window perpendicular to the electron beam. About 1% of the incident energy is converted to X-rays, the rest being converted to heat. Because of the intense heat created in the anode it is mounted on a heat sink, which is cooled with water. A schematic for an X-ray tube is shown in figure 2.12.

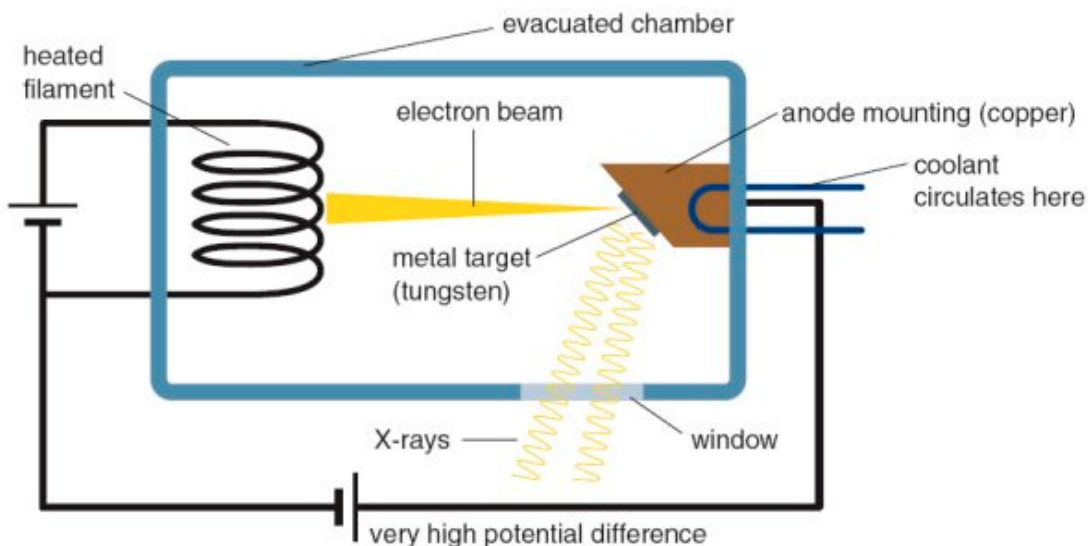


Figure 2.12 The basic elements of an X-ray tube. In this example the anode metal is shown as tungsten.

Image from [http://www.genesis.net.au/~ajs/projects/medical\\_physics/x-rays/](http://www.genesis.net.au/~ajs/projects/medical_physics/x-rays/)

In a vacuum tube, X-rays are generated in two ways. Firstly, the characteristic curve of the emission spectrum, known as white radiation, represents the incident electrons losing kinetic energy in the form of X-rays. This deceleration, caused by the electron interacting with the metal nucleus, can occur over multiple events and so there is a corresponding range of emitted X-ray energies, peaking with the incident electron decelerating in one sudden burst of radiation. The term for this phenomenon is Bremsstrahlung, or 'braking radiation'. Bremsstrahlung refers to any emission of radiation due to change of velocity of a charged particle, for example the generation of synchrotron radiation. However, the term is often used more specifically to identify the white radiation output of an X-ray tube. Figure 2.13 shows a typical X-ray emission spectrum. Secondly, the characteristic spikes in the spectrum are due to specific electron transitions in the atomic orbitals of the anode metal. An incoming electron may knock out a low energy electron, close to the nucleus. A high-energy electron then 'falls back' to replace it, releasing radiation in the form of an X-ray photon. If the drop is to the K shell, the emission is termed  $K\alpha$  or  $K\beta$ , depending upon the exact state from which it fell.

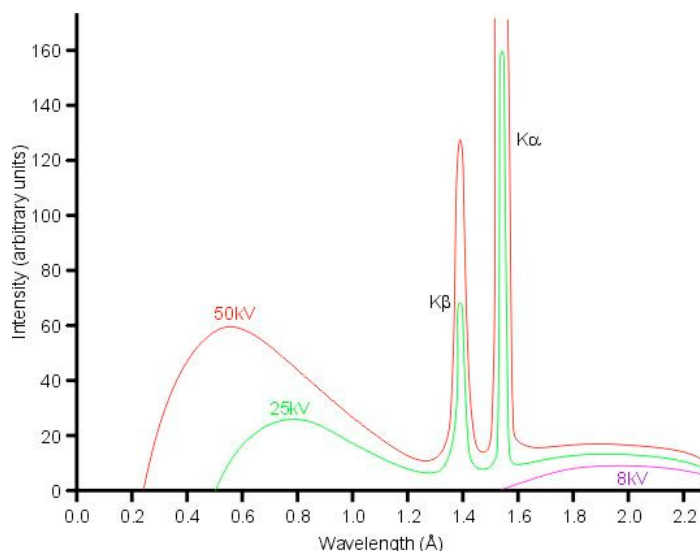


Figure 2.13 An X-ray emission spectrum. Image from <http://pd.chem.ucl.ac.uk/pdnn/inst1/xrays.htm>

Characteristic emissions are designated by the name of the shell to which the electron falls back (K, L, M etc). If the transition is between adjacent shells it is termed an  $\alpha$  line. If the transition is across 2 shells it is called a  $\beta$  line. It is these specific X-ray energies in the spectrum which are employed in X-ray crystallography and typically the  $K\alpha$  emission is used. A number of transitions are shown in figure 2.14.

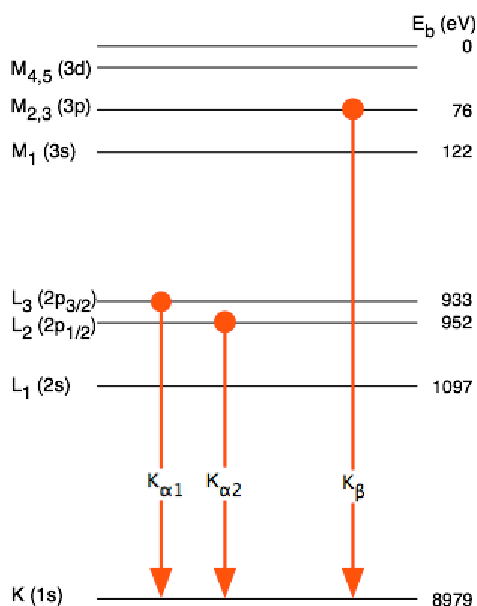


Figure 2.14 Electron transitions giving rise to characteristic X-rays. Image from <http://en.wikipedia.org/wiki/K-alpha>

The  $K\alpha$  line results when an electron drops to the K shell (principal quantum number 1) from a 2p orbital of the L shell (principal quantum number 2). The line is actually a doublet, consisting of lines termed  $K\alpha_1$  and  $K\alpha_2$ . The two lines have slightly different energies, which arise from spin-orbit interaction energy between the electron spin and the orbital momentum of the 2p orbital. The  $K\alpha$  emission is generally the most intense one in the spectrum. For copper, a typical target material, it is about 1.54Å. A list of wavelengths is given in table 2.3.

| <b>Element</b> | <b><math>K\alpha</math><br/>(weight average)</b> | <b><math>K\alpha_2</math><br/>(strong)</b> | <b><math>K\alpha_1</math><br/>(very strong)</b> | <b><math>K\beta</math><br/>(weak)</b> |
|----------------|--|--|---|---------------------------------------|
| Cr             | 2.29100  | 2.29361                                    | 2.28970   | 2.08487                               |
| Fe             | 1.93736  | 1.93998                                    | 1.93604   | 1.75661                               |
| Co             | 1.79026  | 1.79285                                    | 1.78897   | 1.62079                               |
| Cu             | 1.54184  | 1.54439                                    | 1.54056   | 1.39222                               |
| Mo             | 0.71073  | 0.71359                                    | 0.70930   | 0.63229                               |

*Table 2.3 X-ray wavelengths for typical anode metals. All values in Ångströms.*

### 2.2.3.2 Synchrotron source

#### 2.2.3.2.1 Introduction

Synchrotron radiation is emitted when charged particles moving at relativistic speed experience a change in velocity. In practice this is obtained by forcing them to travel in a circuit consisting of straight sections joined by dipole bending magnets. It is the change in direction at each corner of this multi-sided polygon that forces the emission of synchrotron radiation. Modern synchrotron sources are housed in large toroidal buildings and typically have a circumference measured in hundreds of metres.

Synchrotron radiation is emitted in a broad continuum, typically from X-ray to far infra-red. Compared to the X-rays generated in a lab-based powder diffractometer, synchrotron radiation is of high intensity and hence the signal-to-noise ratio is low, giving a high resolution pattern. The synchrotron radiation passes through a double crystal monochromator, from which a specific wavelength can be selected. Thus the output incident beam is highly monochromatic with no  $K\alpha$  couplet and is highly collimated. Peak positions are insensitive to sample shape or incorrect alignment and

peak widths are unaffected by the parafocussing condition as the detector is rotated around the sample. Because of this, peak widths are generally narrow. XRPD patterns obtained via synchrotron radiation are therefore superior in many ways to their lab equivalents.

Photon energies emitted by a synchrotron source are measured in keV rather than Ångströms. This is shown by the equation

$$\lambda (\text{Ångström}) \times \text{energy (keV)} = 12.3984 \quad (2.17)$$

Therefore Cu  $K\alpha_1$  radiation at  $1.54056\text{Å}$  can also be expressed as 8.05 keV.

The synchrotron radiation used in this work was generated at Diamond Light Source, Oxfordshire and collected on beamline I11.

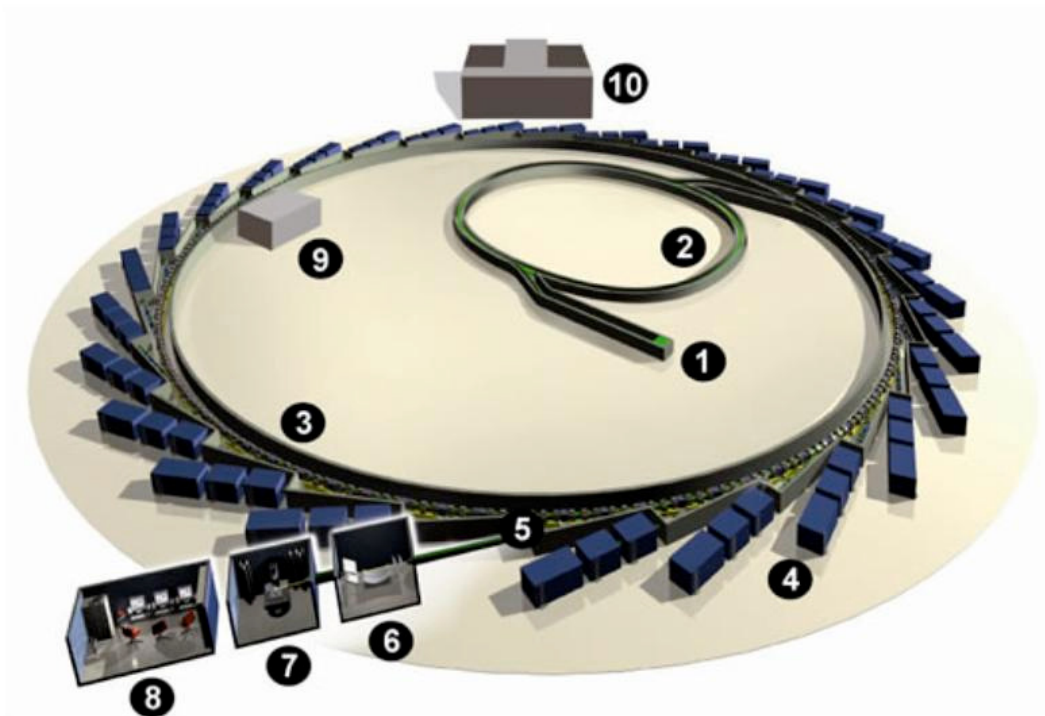


*Figure 2.15 Schematic of the Diamond Light Source site. Image from <http://www.diamond.ac.uk/Home/Technology/Components/storagering.html>*

#### 2.2.3.2.2 *Parts of the synchrotron machine*

There are four main components to the synchrotron source. These are an electron gun to generate low-energy electrons; a linear accelerator (linac) to increase the velocity of the electrons; a small booster synchrotron to accelerate the electrons further before injection into the storage ring; and a storage ring to confine the electrons in orbit and maintain their energy as they generate synchrotron radiation.

The electron gun and linac are essentially the same as the X-ray tube in a powder diffractometer. These are labelled '1' in figure 2.15. Electrons are released by thermionic emission from a hot tungsten cathode under vacuum. From here they are attracted to the anode, but are grouped into bunches by a grid which is turned on and off alternately. As the grid opens, a bunch of electrons passes through before the grid closes again. This bunch is accelerated by the anode to 90keV before entering the 30m linac. Within the linac, the electron bunch is accelerated further by tuning an electric field to its speed. This ensures that the electrons experience a permanently positive field. On exiting the linac, electrons are travelling at near light speed, with an energy of 100MeV before entering the booster synchrotron.

The 158m booster synchrotron, labelled '2', is able to accelerate electrons to an energy of 3GeV before entering the main storage ring. Rather than a regular polygon, it consists of two straight sections and two curved sections, rather like an athletics track. A series of 36 dipole magnets operating at up to 0.8 Tesla are needed to maintain the electron beam around these curves as the energy of the beam increases to its maximum. The electrons are accelerated along the straight sections by a radio-frequency voltage source.

The 561.6m storage ring, labelled '3', actually consists of 24 straight sections connected by a total of 48 bending magnets. Each of these magnets is capable of diverting the electron beam by  $7.5^\circ$ , meaning that a closed orbit is maintained around the building. At an energy of 3GeV, an electron will orbit the ring over 500,000 times per second. The storage ring is under high vacuum to minimise energy loss from the beam striking air molecules and at this pressure the beam lifetime is defined as the time

for the energy to drop to 37% ( $e^{-1}$ ) of its starting value. This equates to about 20 hours. The beam will eventually dissipate, colliding with the occasional air molecule and eventually with the outer wall of the storage ring. Therefore the beam energy is maintained by use of the linac and booster synchrotron to periodically top up the storage ring. In addition, on each circuit of the ring the electron beam passes through a radio frequency cavity (labelled '9'). This ensures that energy lost as synchrotron radiation via the bending magnets or insertion devices is replaced and the beam orbit is maintained.

Much of the power consumed by the synchrotron machine is due to the bending magnets. Operating at 1.4 Tesla, each coil carries 1,300A of current. The magnetic field and electron energy also determines the continuum of synchrotron radiation. At Diamond, the average energy photons are 8keV.

The electron beam is highly contained; the gap through the bending magnets is only 50mm, whilst the beam itself averages 0.25mm wide and 0.017mm high.

Beamlines at Diamond designated with a 'B' use only the polychromatic synchrotron radiation emitted by the bending magnets at the ends of the straight sections. There are currently 4 'B' beamlines at Diamond. Beamlines designated with an 'I' use insertion devices to stimulate the emission of high-intensity X-rays. These are placed in the straight section before the beamline. They consist of magnets alternately arranged so that the beam experiences a rapid oscillation as it passes the device, analogous to driving a vehicle over a cattle grid at speed. There are two types of insertion device, namely wigglers and undulators, both consisting of magnetic arrays. A wiggler produces a wide spectrum of very high energy X-rays; undulators are more commonly employed and create a narrow energy range of X-rays, which can be changed by adjusting the separation of the magnets.

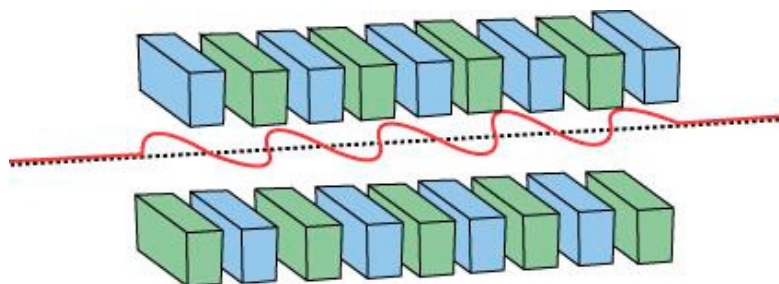


Figure 2.16 Insertion device consisting of alternately-arranged magnets causing the electron beam to oscillate. Image from

<http://www.diamond.ac.uk/Home/About/FAQs/Science.html#storagering>

The various beamlines, labelled '4', are arranged tangentially to the storage ring. These are the points at which synchrotron radiation is emitted, as the electron beam is forced to change direction by the bending magnets. Each beamline consists of 3 sections: an optics hutch ('6') where the particular X-rays required are filtered, an experimental hutch ('7') where the X-rays are incident upon the sample, and a control cabin ('8') where the experimental data is collected.

### 2.2.3.2.3 Beamline Schematic

The beamline used at Diamond Light Source was I11. A schematic of the beamline is shown below.

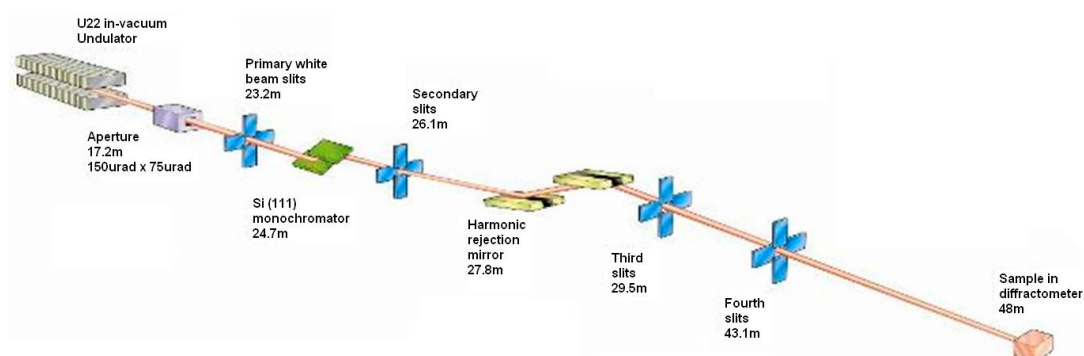


Figure 2.17 Schematic of beamline I11 at Diamond. Image from <http://confluence.diamond.ac.uk/display/I11Doc/Technical+Documentation>

## 2.2.4 The X-ray powder diffractometer

### 2.2.4.1 Introduction

In its simplest terms an X-ray powder diffractometer is a machine whereby a monochromatic X-ray source is targeted at a microcrystalline sample and the intensity of reflected radiation measured against angle. In principle the source emitting from the tube anode is, of course, polychromatic. It is also divergent and so measures are taken to produce a straight, flat monochromatic beam of a similar width to the sample size. The usual geometry used in a diffractometer is reflection, although some machines employ transmission geometry. The diffractometer geometry used in this work is known as Bragg-Brentano and is shown in figure 2.18. The incident beam and detector move on the circumference of a circle centred on the sample in what is known as a parafocussing mode. The powder sample is held in a shallow, circular well. The powder is pressed into the well and its surface made level with the top of the well. The sample holder is then aligned on the goniometer axis of the diffractometer at an angle  $\theta$  to the incident beam. The detector, a scintillation counter, rotates around the sample at twice this angle, meaning that a set of readings for  $2\theta$  against intensity is obtained. In theory this information is all that is needed to arrive at a full crystal structure for the material, although it will be shown later that this is by no means a straightforward task.

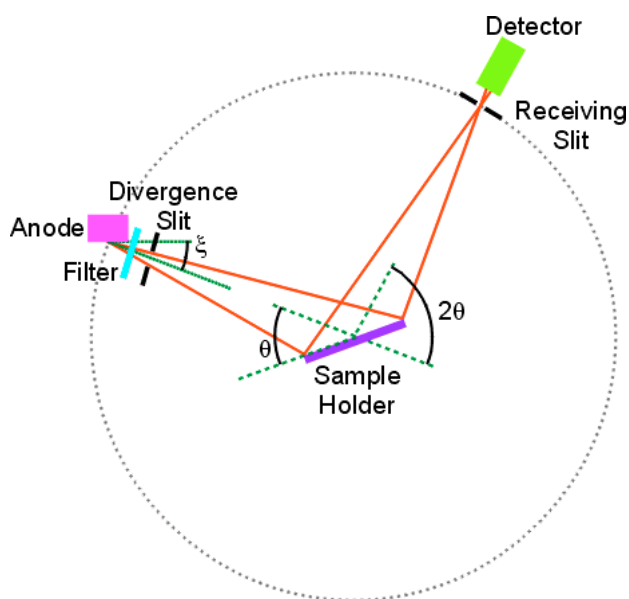
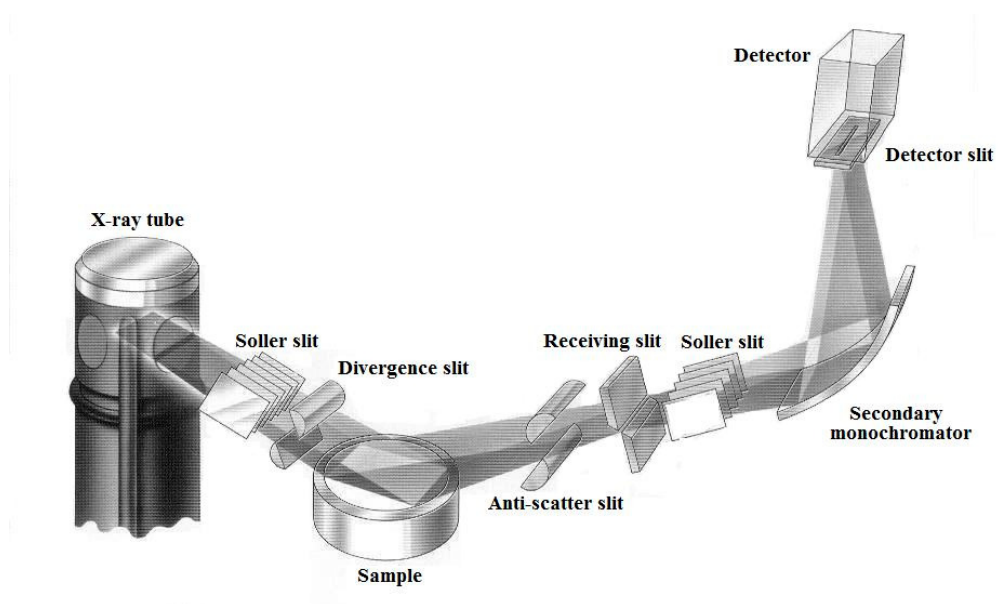


Figure 2.18 Diffractometer with Bragg-Brentano geometry. Image from <http://pd.chem.ucl.ac.uk/pd/welcome.htm>

#### *2.2.4.2 The parts of the diffractometer*

After leaving the X-ray tube the polychromatic beam strikes the primary monochromator, which consists of a single crystal. The crystal used is oriented such that the Bragg condition is satisfied for radiation at the  $K\alpha$  wavelength.  $K\alpha$  radiation exiting the crystal then passes through a Soller slit. This is a set of metal plates used to slice a single source of X-rays into a series of thinner, parallel beams. The purpose of this is to limit the out-of-plane (axial) divergence of the X-ray beam whilst maintaining a significant width. This means that the beam can be targeted accurately and will strike the full width of the sample. The beam then passes through a divergence slit. As the spread of the beam across the sample increases at low angle, in some diffractometers these slits are variable so that this variation can be compensated for prior to striking the sample. The monochromatic beam then strikes the sample and the diffracted beam passes through an anti-scatter slit and a receiving slit. After passing through another Soller slit the beam strikes the secondary monochromator, if present. The beam then passes through the detector slit to meet the detector, where a scintillant is used to convert X-ray excitation of electrons into visible light. Light photons give rise to an electrical signal, which can be amplified. A schematic of a diffractometer is given in figure 2.19.



*Figure 2.19 Schematic of a powder diffractometer. Image from PANalytical X'Pert manual.*

Figure 2.20 shows the PANalytical X'Pert diffractometer used in this work.

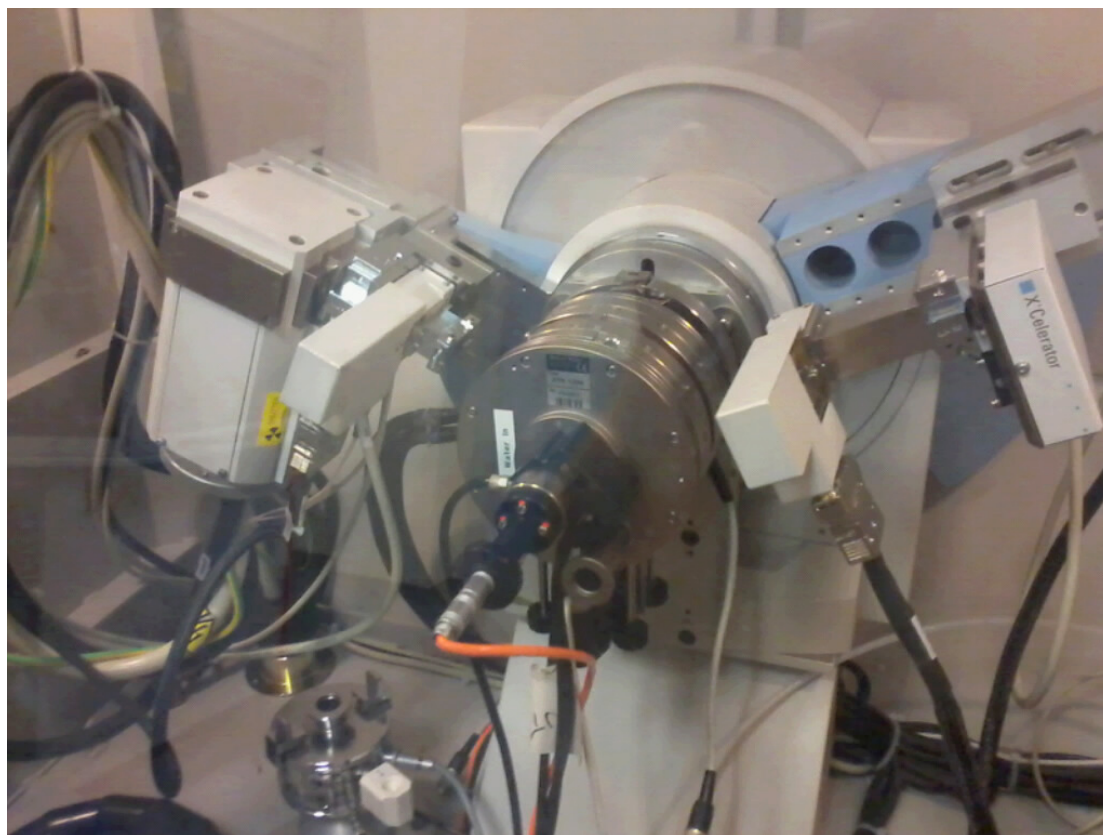


*Figure 2.20 PANalytical powder diffractometer.*

In the above image the X-ray tube is positioned on the left, identified by the radiation label. The sample holder is inserted from below the central section (steel cylinder) and held in place by four bolts. The incident X-ray beam passes from the X-ray tube into the sample, at an incident angle  $\theta$ , and exits the sample at an angle  $2\theta$  to its original direction. The diffracted beam is then recorded by the detector on the right of the image, marked 'X-Celerator'.

#### *2.2.4.3 Sample preparation*

There are a number of issues to consider when preparing a sample for the collection of XRPD data. All are designed to ensure that the reflected beam positions and intensities are representative of the polycrystalline material. Grinding of the powder ensures that particle sizes are similar and small, preferably  $<10\mu\text{m}$ . This is essential if peak intensities are to be measured accurately; large differences between crystallite sizes lead to inaccuracies in measured intensities. Grinding can also obviate preferred orientation to a lesser degree.

The sample needs to be flat and level with the sample holder; if not the peaks will be displaced. If the sample is flat but not level with the sample holder then a zero shift can be added to the line peak positions. However, if the sample surface is rough then adding this shift is impracticable. An uneven surface also tends to reduce intensities at low angles.

The sample needs to be of sufficient depth. In this example the well needs to be filled; if not, intensities will again be affected at different angles. In a thick sample the incident beam penetrates the same volume of sample irrespective of angle. At low angle it will only penetrate the sample to a shallow depth but for a longer horizontal distance than if it were at high angle, where it penetrates deeply but not for as long horizontally. This is illustrated in figure 2.21.

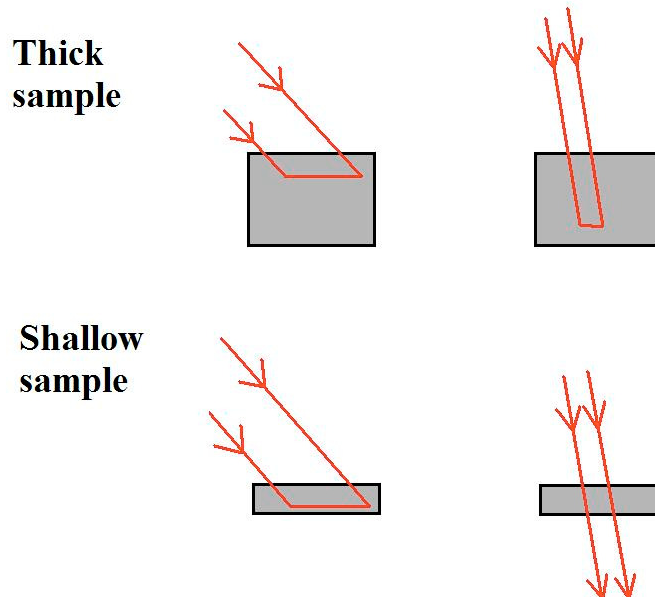


*Figure 2.21 Penetration of incident beam into sample.*

In figure 2.21, each sample is shown with 2 different incident beams. For the thick sample the volume of material probed by the beam is the same for both angles. For the shallow sample, the high angle beam passes through the sample before the relevant volume is probed. This leads to peak intensity reduction at high angle. Additionally, the incident beam needs to strike within the sample for all angles. If not, the beam overspill at low angle will not give rise to Bragg diffraction and leads to a reduction in peak intensity.

#### *2.2.4.4 Calibration standard*

It is common practice to calibrate the diffractometer with a material that has a small number of well-established peaks. In this work the mineral quartz was used. When XRPD data is collected from the standard, any deviation from the expected peak positions will provide the adjustment needed to the peak positions recorded in subsequent diffraction patterns.

#### *2.2.4.5 Data collection*

The diffractometer can be set up to scan the sample at a desired rate. In practice there are two factors to consider. Firstly, the  $2\theta$  step determines the angle the detector moves between readings. Typically this might be  $0.01^\circ$ . Secondly, for each reading a time to collect the diffracted radiation is stated. This speed would depend on the information required. If the sample was being analysed for the presence of a known structure, a rapid scan could be performed; in this case the signal to noise ratio would not prevent the identification of a set of known peaks in the pattern from the sample. If the sample was of unknown structure then a slow scan would be required, in order to get the sharpest peaks possible which in turn would allow precise determination of their positions and intensities.

#### *2.2.4.6 Output data*

The output from the diffractometer consists of values of  $2\theta$  and intensity. When plotted these create a histogram, examples of which are given in figures 2.7 to 2.9. It is clear from the images that Bragg diffraction is occurring in certain directions because of the appearance of discrete, sharp peaks in the histogram. From these values for  $2\theta$  and intensity, together with the molecular formula, it should now be possible to determine the full crystal structure. This will be explored in the following chapter.

### **2.3 STRUCTURE DETERMINATION**

Crystal structure determination from XRPD data is extremely challenging for a number of reasons. First, as discussed in 2.2.2.1, a powder pattern is essentially a single crystal pattern but compressed into the one dimension of  $2\theta$  space. This means that all the directional information obtained from a single crystal diffractometer (i.e. the relevant planes giving rise to Bragg diffraction) is not immediately available, although it is possible to determine this information if the peak positions and intensities can be sufficiently resolved. Whereas a single crystal would generate a single point on the detector for each plane, a polycrystalline sample generates a cone of radiation; where the cone intersects the detector a peak is measured. Second, all planes which have the

same spacing will give rise to superimposed Bragg reflection at the same  $2\theta$  position and therefore only one peak is seen. For example, in the cubic system, planes (200), (020) and (002) will give rise to Bragg reflection at the same angle. A knowledge of all possible planes giving rise to the peak is therefore required in order to work back and assign intensities to individual reflections. Third, peaks which are close together may be subject to significant overlap, especially if there are instrumental or sample preparation errors. Peaks may even overlap so much as to be indistinguishable. Fourth, if more than one phase is present then there may be overlap of peaks from unrelated structures. Fifth, once the peak positions are ascertained, the task of assigning Miller indices to the reflections is necessary in order to establish the unit cell. Sixth, in order to index a pattern, an adequate number of peaks needs to be recorded. For many of the automated programs available this number needs to be at least 20. This process of assigning Miller indices to reflections and determining unit cell parameters is called *indexing* and is widely regarded as the most challenging part of the whole process (LeBail and Cranswick 2002). For increasing degrees of freedom this becomes increasingly difficult to perform. For the cubic cell it is usually an easy task, but at the other extreme, the triclinic cell, indexing often fails to find the correct structure; there are so many possible combinations of the 6 unit cell parameters that a multitude of potential cells might be found. This is why it is so important to obtain the best data possible from the diffractometer, particularly establishing with great precision where the peaks lie.

### *2.3.1 Treatment of data from the diffractometer*

#### *2.3.1.1 Raw data*

Raw data from the diffractometer consists primarily of a two-column text file containing values for  $2\theta$  and intensity. The value of  $2\theta$  increase in equal steps, specified at the beginning of the file.

### 2.3.1.2 Background removal

Based on the known emission profile from the diffractometer, a subtraction from the recorded pattern is made. This has the effect of dropping the peak profiles slightly so that their tails lie on the  $2\theta$  axis.

### 2.3.1.3 $K\alpha_2$ stripping

At low angle, the  $K\alpha_1$  and  $K\alpha_2$  peaks are closely overlapped. It is possible to mathematically remove the  $K\alpha_2$  peak, since both their respective wavelengths and the ratio between their intensities are known (see table 2.3). The measured intensity is therefore reduced to take account of this.

### 2.3.1.4 Peak identification

Bragg peaks are measured as envelopes rather than sharp lines. This necessitates the allocation of an absolute position for the particular line. Generally this is done automatically by peak finding software, although it is possible to assign peak positions manually.

### 2.3.1.5 Corrections factors

A correction factor  $\Delta 2\theta$  can be applied to measured peak positions  $2\theta_{\text{obs}}$  to determine the theoretical position  $2\theta_{\text{calc}}$

$$2\theta_{\text{obs}} = 2\theta_{\text{calc}} + \Delta 2\theta \quad (2.18)$$

The factors affecting peak position are given by:

$$\Delta 2\theta = \frac{p1}{\tan 2\theta} + \frac{p2}{\sin 2\theta} + \frac{p3}{\tan 2\theta} + p4 \sin \theta + p5 \cos \theta + p6 \quad (2.19)$$

where  $p_1$  and  $p_2$  are measures of the incident beam axial divergence and peak asymmetry. Axial divergence is corrected by use of Soller slits. Peak asymmetry is caused by the finite detector receiving slit length.

$p_3$  is the incident beam in-plane divergence. This arises because the sample is not curved i.e. it does not all fall on the diffractometer focussing circle. However, the effect is small.

$p_4$  is the absorption error, which is important for thick samples with low absorption coefficients.

$p_5$  is the sample displacement, due to displacement of the sample off the goniometer axis

$p_6$  is the zero error, caused by misalignment of the source and detector.

### 2.3.2 Indexing

Historically there have been two main methods employed for indexing XRPD patterns, namely graphical and arithmetical. Graphical methods work well for high-symmetry systems (cubic, tetragonal, hexagonal). Arithmetical methods may be employed for all symmetry systems, although the chance of success decreases with decreasing symmetry. There has also been some development of software employing global optimisation methods.

#### 2.3.2.1 Graphical methods

The equation relating  $\sin^2\theta$  and the Miller indices for the cubic system is:

$$\sin^2\theta_{(hkl)} = A(h^2 + k^2 + l^2) \quad (2.20)$$

$$\text{where } A = \frac{\lambda^2}{4a^2}$$

The expression shows that for all cubic cells the peak positions will arise in the same distribution, subject to a scaling factor  $A$  (which is dependent upon the unit cell parameter,  $a$ ). That is, the ratios between peak positions for any pattern will be identical. There may be missing peaks due to the particular internal symmetry of the

cell but the essential list of peaks will be the same. Thus, if this peak distribution is found in the diffraction pattern, the presence of a cubic cell can be established. Historically this has been achieved by a graphical method, as shown in figure 2.22.

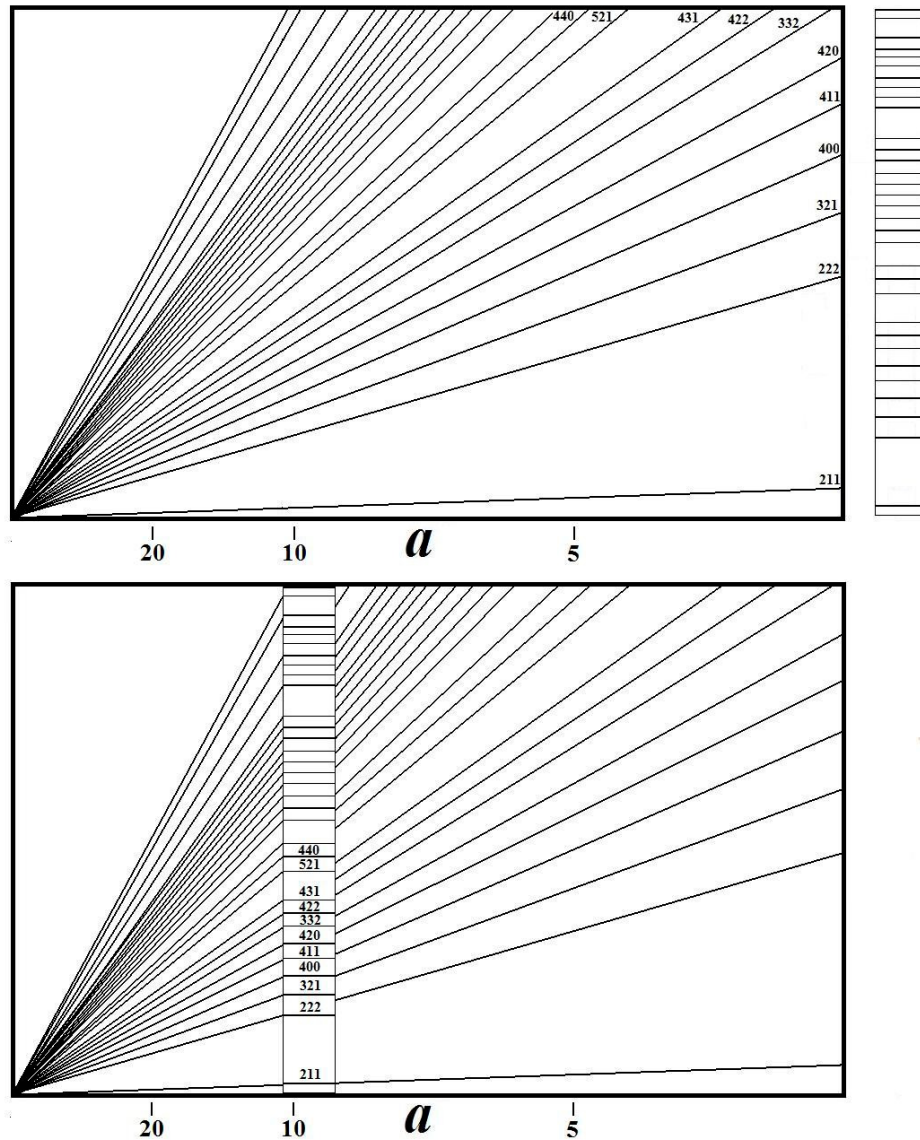


Figure 2.22 A graphical method for indexing the cubic system.

A chart as in figure 2.22 is issued upon which is printed a set of lines corresponding to the possible Miller planes for the cubic system. The spacing of these lines increases as they fan out across the card from left to right, the horizontal axis marked in Ångströms. Each line is marked with its corresponding Miller plane. The relative positions of the recorded Bragg peaks are marked on a thin strip of card which is moved across the chart until the lines on each match up. At this position the corresponding point on the

horizontal axis gives the unit cell parameter. The Miller planes can then be assigned directly from the fan diagram. Similar charts exist for the tetragonal and hexagonal systems. Methods have been developed for determining the tetragonal system (Hull and Davey 1921), (Bjurström 1931), (Bunn 1961). Charts do exist for the orthorhombic system although with increasing degrees of freedom they become increasingly complicated.

### 2.3.2.2 *Arithmetical methods*

#### 2.3.2.2.1 *Cubic system*

Rearranging equation 2.20 gives

$$a = d\sqrt{h^2 + k^2 + l^2} \quad (2.21)$$

The expression indicates that for the cubic system, there is a relationship between the inter-planar spacing,  $d$ , of any set of planes ( $hkl$ ) values and the unit cell parameter,  $a$ . The possible values of  $\sqrt{h^2 + k^2 + l^2}$  are known. Therefore if we multiply the highest recorded  $d$ -spacing by each of these values, a list of possible unit cell parameters is generated. If this is repeated for the next peak, another list of candidate values is obtained. Some of the values in both lists will match. If the process is repeated for subsequent peaks, the list of matching values will eventually collapse to one value,  $a$ . This is illustrated in table 2.4. The material concerned is iron chromium oxide, JDPDS reference 24-512. The table looks at the first 5 peaks in the XRPD pattern.

| <i>hkl</i> | <i>d1</i> | <i>d2</i> | Matches | <i>d3</i> | Matches | <i>d4</i> | matches | <i>d5</i> | Matches |
|------------|-----------|-----------|---------|-----------|---------|-----------|---------|-----------|---------|
|            | 2.956Å    | 2.517Å    |         | 2.415Å    |         | 2.091Å    |         | 1.708Å    |         |
| 100        | 2.9560    | 2.5170    | 8.3608  | 2.4150    | 8.3608  | 2.0910    | 8.3608  | 1.7080    | 8.3608  |
| 110        | 4.1804    | 3.5596    | 9.3477  | 3.4153    | 11.0603 | 2.9571    | 11.8240 | 2.4155    |         |
| 111        | 5.1199    | 4.3596    | 10.6580 | 4.1829    | 11.8240 | 3.6217    | 12.5413 | 2.9583    |         |
| 200        | 5.9120    | 5.0340    | 11.0603 | 4.8300    | 12.5413 | 4.1820    |         | 3.4160    |         |
| 210        | 6.6098    | 5.6282    | 11.8240 | 5.4001    | 14.4814 | 4.6756    |         | 3.8192    |         |
| 211        | 7.2407    | 6.1654    | 12.5413 | 5.9155    | 14.7800 | 5.1219    |         | 4.1837    |         |
| 220        | 8.3608    | 7.1192    | 13.5461 | 6.8307    |         | 5.9142    |         | 4.8310    |         |
| 300        | 8.8680    | 7.5510    | 14.4814 | 7.2450    |         | 6.2730    |         | 5.1240    |         |
| 310        | 9.3477    | 7.9595    | 15.0727 | 7.6369    |         | 6.6123    |         | 5.4012    |         |
| 311        | 9.8039    | 8.3479    |         | 8.0096    |         | 6.9351    |         | 5.6648    |         |
| 222        | 10.2399   | 8.7191    |         | 8.3658    |         | 7.2434    |         | 5.9167    |         |
| 320        | 10.6580   | 9.0752    |         | 8.7074    |         | 7.5392    |         | 6.1583    |         |
| 321        | 11.0603   | 9.4178    |         | 9.0361    |         | 7.8238    |         | 6.3908    |         |
| 400        | 11.8240   | 10.0680   |         | 9.6600    |         | 8.3640    |         | 6.8320    |         |
| 322        | 12.1879   | 10.3779   |         | 9.9573    |         | 8.6214    |         | 7.0423    |         |
| 330        | 12.5413   | 10.6787   |         | 10.2460   |         | 8.8714    |         | 7.2464    |         |
| 331        | 12.8849   | 10.9714   |         | 10.5267   |         | 9.1145    |         | 7.4450    |         |
| 420        | 13.2196   | 11.2564   |         | 10.8002   |         | 9.3512    |         | 7.6384    |         |
| 421        | 13.5461   | 11.5343   |         | 11.0669   |         | 9.5822    |         | 7.8270    |         |
| 332        | 13.8649   | 11.8058   |         | 11.3274   |         | 9.8077    |         | 8.0112    |         |
| 422        | 14.4814   | 12.3307   |         | 11.8310   |         | 10.2438   |         | 8.3675    |         |
| 430        | 14.7800   | 12.5850   |         | 12.0750   |         | 10.4550   |         | 8.5400    |         |
| 431        | 15.0727   | 12.8342   |         | 12.3141   |         | 10.6621   |         | 8.7091    |         |
| 333        | 15.3598   | 13.0787   |         | 12.5487   |         | 10.8652   |         | 8.8750    |         |
| 432        | 15.9185   | 13.5545   |         | 13.0052   |         | 11.2604   |         | 9.1979    |         |
| 440        | 16.7217   | 14.2383   |         | 13.6613   |         | 11.8285   |         | 9.6619    |         |
| 441        | 16.9809   | 14.4591   |         | 13.8731   |         | 12.0119   |         | 9.8117    |         |
| 433        | 17.2363   | 14.6765   |         | 14.0817   |         | 12.1925   |         | 9.9593    |         |
| 442        | 17.7360   | 15.1020   |         | 14.4900   |         | 12.5460   |         | 10.2480   |         |
| 443        | 18.9276   | 16.1167   |         | 15.4635   |         | 13.3889   |         | 10.9365   |         |

Table 2.4 Arithmetical derivation of unit cell parameter for a cubic cell. All values are in Ångströms.

Although it is possible to work in terms of  $d$ -spacings and Miller indices for cells of high symmetry, using the relationship between  $\sin^2 \theta$  and the Miller indices is a useful method for dealing with all crystal systems. Recalling equation 2.20, the relation between  $\sin^2 \theta$  and the Miller indices:

$$\sin^2 \theta_{(hkl)} = A(h^2 + k^2 + l^2)$$

$$\text{where } A = \frac{\lambda^2}{4a^2}$$

This equation shows a relationship between the sum of the squares of the possible Miller indices in the cubic system and the angle at which diffraction occurs. For each peak the value of  $\sin^2\theta$  can be determined. If the cell is cubic there should be found whole number ratios between the values of  $\sin^2\theta$ . For example, if the (400) and (200) reflections are present, then the ratios of their corresponding  $\sin^2\theta$  values should be 4:1. This method of indexing is suggested by D'Eye and Wait (D'Eye and Wait 1960) and an example of this process is shown in table 2.5.

| Line        | $2\theta$ | $\sin^2\theta$ | ratio to<br>0.006444 | INTEGER<br>ratio | $hkl$ | $\sin^2\theta$ calc | ABS<br>difference |
|-------------|-----------|----------------|----------------------|------------------|-------|---------------------|-------------------|
| 1           | 15.9800   | 0.0193         | 3.0000               | 3                | 111   | 0.0193              | 0.0000            |
| 2           | 18.4700   | 0.0258         | 3.9963               | 4                | 200   | 0.0258              | 0.0000            |
| 3           | 26.2600   | 0.0516         | 8.0120               | 8                | 220   | 0.0516              | 0.0001            |
| 4           | 30.8000   | 0.0706         | 10.9483              | 11               | 311   | 0.0709              | 0.0003            |
| 5           | 32.2500   | 0.0772         | 11.9741              | 12               | 222   | 0.0773              | 0.0002            |
| 6           | 37.3700   | 0.1027         | 15.9321              | 16               | 400   | 0.1031              | 0.0004            |
| 7           | 42.0000   | 0.1285         | 19.9374              | 20               | 420   | 0.1289              | 0.0004            |
| 8           | 46.2500   | 0.1543         | 23.9434              | 24               | 422   | 0.1547              | 0.0004            |
| 9           | 49.2600   | 0.1737         | 26.9611              | 27               | 333   | 0.1740              | 0.0003            |
| 10          | 54.1300   | 0.2071         | 32.1353              | 32               | 440   | 0.2062              | 0.0009            |
| <b>SUM</b>  |           | <b>1.0107</b>  |                      | <b>157</b>       |       |                     |                   |
| Estimated A |           | 0.0064         |                      |                  |       |                     |                   |
| Refined A   |           | 0.0064         |                      |                  |       |                     |                   |
| <b>a</b>    |           | <b>9.6005</b>  |                      |                  |       |                     |                   |

*Table 2.5 Arithmetical method for indexing the cubic system.*

Looking at the list of  $\sin^2\theta$  values, if the ratio of each peak to peak 1 is taken, the first and second ratios are 1 and 1.33 respectively, meaning that the divisor is smaller than the value of  $\sin^2\theta$  for line 1. By scaling up from 1 and 1.33 we can take the ratios to be 3 and 4, making the divisor one third of the first  $\sin^2\theta$  i.e. the divisor (the constant A) is taken to be 0.06444. Dividing throughout gives ratios close to whole numbers. The value of A can be refined by calculating:

$$A = \frac{\sum \sin^2 \theta}{\sum ratio} \quad (2.22)$$

The unit cell parameter is then calculated from the relationship  $A = \frac{\lambda^2}{4a^2}$ . The lower is the difference between experimental and calculated values for  $\sin^2 \theta$  then the more likely it is that the pattern has been indexed correctly. D'Eye and Wait recommend that differences up to 0.0005 can be accepted but state that poor correlation is often due to the weaker intensities in the pattern which have a lower accuracy of measurement than the stronger lines. It is therefore essential that an XRPD pattern is measured accurately. In this case, all differences except for that of line 10 are less than 0.0005, which implies that the system is indeed cubic.

#### 2.3.2.2.2 Tetragonal system

For the tetragonal system the relationship becomes:

$$\sin^2 \theta_{(hkl)} = A(h^2 + k^2) + Cl^2 \quad (2.23)$$

the volume of the unit cell being  $a^2c$

A method used for the indexing of tetragonal and orthorhombic systems (D'Eye and Wait 1960) is based on two sources (Hesse 1948), (Lipson 1949). Hesse states that the indexing of tetragonal photographs has been successful in several cases where he did not know the crystal system. His method is to look for ratios in the lines where one of the Miller indices is zero, for example the  $hk0$  planes. The relationship would then be simplified to  $\sin^2 \theta_{(hk0)} = A(h^2 + k^2)$ . The first possible nine values of  $\sin^2 \theta_{(hk0)}$  for these planes are shown in table 2.6.

| $hk0$           | 100 | 110 | 200 | 210 | 220 | 300 | 310 | 320 | 330 |
|-----------------|-----|-----|-----|-----|-----|-----|-----|-----|-----|
| $\sin^2 \theta$ | A   | 2A  | 4A  | 5A  | 8A  | 9A  | 10A | 13A | 18A |

Table 2.6 Arithmetic method for indexing the tetragonal system.

It can be seen that ratios of two occur between the first and second values, the second and third values, and the third and fifth values, and so on. In fact, there are a total of five ratios of two for these nine lines. This ratio of two cannot occur in any other system other than the cubic and the tetragonal. Assuming the cubic system has been discounted, it is likely that the system is tetragonal and an attempt can be made at finding the other constant,  $C$ . In the above case, because the plane (100) was present, the constant  $A$  was identifiable as the smallest factor to give a ratio of two. However, if this line had been absent and the first line had been due to the (110) plane, the lowest factor would have been  $2A$ . If the first line was due to the (200) plane then the lowest factor would have been  $4A$ . It is important to be aware that a value that appears to be  $A$  may in fact be a multiple of  $A$ , otherwise known as a *harmonic*; if the pattern cannot be indexed satisfactorily, the value may be divided by two and then re-tested. If necessary it may be divided by four, and so on.

The method for finding  $C$  is to subtract all possible values for  $A(h^2 + k^2)$  from the observed lines. For example, subtracting  $2A$  from the  $\sin^2 \theta_{(hkl)}$  for a (201) line would give  $C$ , or subtracting  $5A$  from the  $\sin^2 \theta_{(hkl)}$  for a (212) line would give  $4C$ . Values of  $A$ ,  $2A$ ,  $4A$ ,  $5A$ ,  $8A$  etc are subtracted from the values of  $\sin^2 \theta_{(hkl)}$  to leave a value of  $C$  (or  $4C$ ,  $9C$ ,  $16C$  etc depending on the Miller indices for the plane giving rise to line 1) somewhere in each column of the difference table. In addition, there will be multiples of  $A$  present due to subtractions from  $hk0$  lines.

For each possible value of  $A$  there may be several possible values of  $C$ . Using each pair of  $A$  and  $C$ , theoretical  $\sin^2 \theta_{(hkl)}$  values are calculated by using all possible Miller indices for the tetragonal system and are then compared against the experimental values. The combination of  $A$  and  $C$  that gives the highest number of matches is likely to be the correct combination. The values of the constants and hence the unit cell parameters can then be refined.

### 2.3.2.2.3 Hexagonal system

For the hexagonal system the equation is:

$$\sin^2 \theta_{(hkl)} = A(h^2 + hk + k^2) + Cl^2 \quad (2.24)$$

where  $A = \frac{\lambda^2}{3a^2}$  and  $C = \frac{\lambda^2}{4c^2}$ , the volume of the unit cell being  $a^2c \sin \theta$

### 2.3.2.2.4 Orthorhombic system

For the orthorhombic system the relationship is:

$$\sin^2 \theta_{(hkl)} = Ah^2 + Bk^2 + Cl^2 \quad (2.25)$$

The volume of the unit cell is given by  $abc$ .

The orthorhombic system is an example of an intermediate symmetry order and tends to be the cut-off point between the likelihood of success or failure with manual indexing methods. It has been shown that the cubic and tetragonal systems can be recognised by a constantly recurring factor, or by ratios of 2 appearing in the  $\sin^2 \theta_{(hkl)}$  values. For the orthorhombic system there are no such relationships but, as Hess states, this may be overcome if enough lines are present. The general equation for the orthorhombic system has 3 constants. If all three constants are unknown it is necessary to break the equation down using the lines of the pattern. The  $A$  component is only dependent on  $h$ , the  $B$  component on  $k$  and the  $C$  component on  $l$ . This generates the following relationships:

$$\sin^2 \theta_{(h00)} = Ah^2 \quad (2.26)$$

$$\sin^2 \theta_{(0k0)} = Bk^2 \quad (2.27)$$

$$\sin^2 \theta_{(00l)} = Cl^2 \quad (2.28)$$

Therefore:

$$\sin^2 \theta_{(hkl)} = Ah^2 + Bk^2 \quad (2.29)$$

Because each Miller index has its own constant, the values of  $Ah^2$ ,  $Bk^2$  and  $Cl^2$  can be treated independently. Additions of  $\sin^2 \theta_{(hkl)}$  values of lines, each with two indices of zero, can be done to generate the  $\sin^2 \theta_{(hkl)}$  value of some other line. For example  $\sin^2 \theta_{(100)} = A$ ,  $\sin^2 \theta_{(010)} = B$  and  $\sin^2 \theta_{(001)} = C$

This leads to equations of the following types:

$$\sin^2 \theta_{(110)} = \sin^2 \theta_{(100)} + \sin^2 \theta_{(010)} = A + B \quad (2.31)$$

$$\sin^2 \theta_{(011)} = \sin^2 \theta_{(010)} + \sin^2 \theta_{(001)} = B + C \quad (2.32)$$

$$\sin^2 \theta_{(101)} = \sin^2 \theta_{(100)} + \sin^2 \theta_{(001)} = A + C \quad (2.33)$$

$$\sin^2 \theta_{(111)} = \sin^2 \theta_{(100)} + \sin^2 \theta_{(010)} + \sin^2 \theta_{(001)} = A + B + C \quad (2.34)$$

and generally:

$$\sin^2 \theta_{(hkl)} = \sin^2 \theta_{(h00)} + \sin^2 \theta_{(0k0)} + \sin^2 \theta_{(00l)} = Ah^2 + Bk^2 + Cl^2 \quad (2.35)$$

Therefore, if two or three lines at the low angle end of the pattern can be added together to produce a third line it is likely that the first two lines corresponded to planes having two Miller indices equal to zero. However, the chance of there being all (100), (010) and (001) planes in the pattern is low. It would be useful to make use of the subtraction of lines, thereby generating a much better chance of finding at least one of the constants. Rewriting the above equations:

$$\sin^2 \theta_{(100)} = \sin^2 \theta_{(110)} - \sin^2 \theta_{(010)} = A \quad (2.36)$$

$$\sin^2 \theta_{(100)} = \sin^2 \theta_{(101)} - \sin^2 \theta_{(001)} = A \quad (2.37)$$

and generally:

$$\sin^2 \theta_{(100)} = \sin^2 \theta_{(1kl)} - \sin^2 \theta_{(0kl)} = A \quad (2.38)$$

Equations of a similar type can be written for  $B$  and  $C$ . If a difference table is set up

such that each  $\sin^2 \theta_{(hkl)}$  value is subtracted from every other value there should arise recurring differences. The differences that occur most frequently are likely to be one or more of the constants.

However, if insufficient lines are present, the recurring numbers may all be harmonics. These multiples will not necessarily be of magnitude 4, 9, 16, 25 etc as the multiplier is generated by subtraction of two lines. The possible multipliers produced by the subtraction of two square numbers are 3, 4, 5, 7, 8, 9, 11, 12, 15, 16, 20, 21, 24, 25, 32, 35, 36 etc. If a number recurs but does not generate another constant when used as below, then it may be one of these multiples. Dividing by each multiple in turn and testing for generation of another constant should locate the first constant.

Once the first constant has been found, a second can be found, again by a process of subtractions. For  $(hk0)$  lines the quadratic form can be written as  $\sin^2 \theta_{(hkl)} - Bk^2 = Ah^2$ . Subtracting values of  $Bk^2$  from  $\sin^2 \theta$  should generate  $A$  or a multiple of  $A$

It should now be relatively easy to find  $C$ . To do this, values of  $Ah^2 + Bk^2$  are subtracted from  $\sin^2 \theta$ . Any recurring values in the table should be equal to  $C, 4C, 9C$  etc. Once a choice of constants has been decided upon, an attempt can be made at indexing the diffraction pattern.

Compared with the relatively straightforward use of graphical charts, the manual arithmetical indexing of XRPD patterns is not always a straightforward problem and often relies on some degree of intuition on the part of the investigator. To write a computer program to automatically index a pattern, even one of orthorhombic symmetry, is a substantial task. The methods employed so far approach the problem from the high symmetry end. If the pattern cannot be indexed on a cubic cwill then the system of next lowest symmetry is looked for. For each system the task becomes increasingly difficult, until the problem is either solved or abandoned. The following sections discuss methods that approach the problem from the low symmetry side.

### 2.3.2.2.5 Monoclinic system

For the monoclinic system the equation is:

$$\sin^2 \theta_{(hkl)} = Ah^2 + Bk^2 + Cl^2 - Dhl \quad (2.39)$$

where  $A = \frac{\lambda^2}{4a^2 \sin^2 \theta}$ ,  $B = \frac{\lambda^2}{4b^2}$ ,  $C = \frac{\lambda^2}{4c^2 \sin^2 \theta}$  and  $D = \frac{\lambda^2 \cos \theta}{2ac \sin^2 \theta}$ , the volume of the unit cell being  $abc(1 - \cos^2 \theta)$

### 2.3.2.2.6 Triclinic system

For the triclinic system the equation for  $\sin^2 \theta$  is written in terms of the reciprocal lattice:

$$\sin^2 \theta_{(hkl)} = \lambda^2 / 4 (h^2 a^{*2} + k^2 b^{*2} + l^2 c^{*2} + 2klb^*c^* \cos \theta^* + 2hlc^*a^* \cos \theta^* + 2hka^*b^* \cos \theta^*) \quad (2.40)$$

$$\text{where } a^* = \frac{bc \sin \alpha}{V}, \cos \alpha^* = \frac{\cos \beta \cos \gamma - \cos \alpha}{\sin \beta \sin \gamma}$$

$$b^* = \frac{ac \sin \beta}{V}, \cos \beta^* = \frac{\cos \alpha \cos \gamma - \cos \beta}{\sin \alpha \sin \gamma}$$

$$c^* = \frac{ab \sin \lambda}{V}, \cos \gamma^* = \frac{\cos \alpha \cos \beta - \cos \gamma}{\sin \alpha \sin \beta}$$

the volume of the unit cell given by:

$$V = abc (1 + 2 \cos \alpha \cos \beta \cos \gamma - \cos^2 \alpha - \cos^2 \beta - \cos^2 \gamma)$$

The expression for the triclinic system is the equation from which most of the auto-indexing methods in current use are derived. Its use makes no assumptions about the

symmetry of a material under investigation. The complexity of the equation illustrates that recognition of the cell type for the triclinic system from XRPD data alone is a problem of formidable complexity. A number of methods attempt this task (Ito 1949), (DeWolff 1957), (Visser 1969). Arithmetical methods work well for crystal systems up to orthorhombic and can be extended to the monoclinic system, although successful indexing is not always certain. For systems of the lowest symmetry these approaches often fail to provide a general solution to the problem.

The method for the cubic system in 2.3.2.2.1 was that used by the program GRAPHPRO in chapter 7. Another program has been written by the author and has proved successful for orthogonal systems.

### 2.3.2.3 *The indexing suite*

In 1999 an attempt was made to bring together a number of indexing programs into one user-friendly format. This has developed into the CRYSFIRE indexing suite (Shirley 2002). CRYSFIRE works by allowing the user to input observed Bragg reflections via a graphical user interface. Reflections may be entered as either  $2\theta$  values or as  $d$ -spacings. Nine indexing programs, including the widely-used ITO (Visser 1969), TREOR (Werner *et al* 1985) and DICVOL (Louër and Boultif 2004) can be individually selected and applied to the data. Each possible solution consists of a set of unit cell parameters and is awarded a figure of merit. CRYSFIRE puts all candidate solutions into a single file so that results from each indexing program can be compared and then loaded into other software such as CHECKCELL to look for the best fit to the experimental data. CRYSFIRE, its indexing programs and CHECKCELL will be discussed further in chapter 5.

Indexing programs make use of the relationship:

$$\frac{1}{d_{hkl}^2} = (r_{hkl}^*)^2 \quad (2.41)$$

where  $r^*$  is the reciprocal lattice vector.

The quantity  $\frac{1}{d_{hkl}^2}$  is referred to in crystallography as  $Q_{hkl}$ . The expressions for  $Q_{hkl}$  according to crystal system are given in table 2.7.

| Cell type    | $Q_{hkl}$  |
|--------------|--|
| Cubic        | $(h^2 + k^2 + l^2).a_{11}$   |
| Tetragonal   | $(h^2 + k^2).a_{11} + l^2.a_{33}$  |
| Hexagonal    | $(h^2 + hk + k^2).a_{11} + l^2.a_{33}$                                     |
| Orthorhombic | $h^2.a_{11} + k^2.a_{22} + l^2.a_{33}$                                     |
| Monoclinic   | $h^2.a_{11} + k^2.a_{22} + l^2.a_{33} + hl.a_{13}$                         |
| Triclinic    | $h^2.a_{11} + k^2.a_{22} + l^2.a_{33} + kh.a_{12} + kl.a_{23} + hl.a_{13}$ |

Table 2.7 Values of  $Q_{hkl}$  expressed using reciprocal unit cell parameters

where  $a_{11} = a^{*2}$ ,  $a_{22} = b^{*2}$ ,  $a_{33} = c^{*2}$ ,  $a_{12} = a^*b^* \cos \gamma^*$ ,  $a_{13} = 2a^*c^* \cos \beta^*$  and  $a_{23} = 2b^*c^* \cos \alpha^*$

The expressions in table 2.7 are visually similar to those for  $\sin^2 \theta$  and are the ones used in most indexing programs.

### 2.3.3 Assigning the space group

Once the unit cell has been established, the next task is to assign it to one of the 230 space groups. The cell type and the systematic absences in the Miller indices should provide sufficient information for a list of trial space groups to be arrived at. For the purpose of this work, the program Checkcell was used to find the most likely space group.

### 2.3.4 Establishing the atom positions

The cell and space group is sufficient information to generate a list of peak positions. However, it is the set of atomic positions which determines the intensities of the peaks. There are a number of ways by which this information can be obtained, but the main method used in this work was to look at a similar structure. If a material under

investigation is part of a series, or similar structures are known, these structures can be used as starting points for the unknown structure. For example, many of the rare earth oxides exhibit a monoclinic phase at high temperature. If the structure for gadolinia is not known we could turn to its immediate neighbours europia and terbia and use their known structures as starting points. If the unit cell parameters follow the lanthanide contraction, we could reasonably expect the atoms in gadolinia to lie at the same points.

With the advent of computers with fast processing speeds, it has become possible to work out structures *ab initio*, that is, without any prior knowledge of possible atom positions. Global optimisation is a way of reaching a good approximation to a solution when exploring a large search space. All global optimisation methods begin with a series of trial structures. These are generated by randomly populating the unit cell with atoms, so long as the known empirical formula and density are complied with. For each structure a theoretical diffraction pattern is created and compared with the measured pattern. A measure of fitness is then applied to each trial structure. It is these measures of fitness which determine whether a trial structure is rejected, or accepted and used as the basis for the next generation of trial structures. After many iterations the objective is to converge upon a single solution. In principle this can be difficult for a number of reasons, most notably the problem of becoming trapped in local minima. For this reason, there is provision in the software for random new structures to be introduced even when convergent solutions are evident.

Monte Carlo methods are essentially trial and error algorithms using random numbers. The most widely used Monte Carlo algorithm is the Metropolis-Harrison algorithm. Originally proposed in 1953 (Metropolis 1953) it was first employed in crystal structure determination in the 1990s (Harris *et al* 1994). A Monte Carlo method is used in the programs ESPOIR (Le Bail 2001) and Fullprof (Rodriguez-Carvajal 1993). It is also the basis for the indexing program McMaille (Le Bail 2006).

Simulated annealing is a specific Monte Carlo method. It models a process employed in the heat treatment of metals, where a material is heated and then cooled slowly. This has the effect of allowing unfavourable jumps at high energy, but as the temperature falls, these jumps become less likely. Although a jump in the 'wrong' direction is

unfavourable if it results in a lower fit for the new structure, it is encouraged more at higher temperature. The longer the time the algorithm is run for and the slower the rate of cooling, the better the result should be. Simulated annealing has been applied to structure solution (Kirkpatrick *et al* 1983), (Černý 1985) and is employed by structure solution programs such as DASH (David *et al* 2006) and Fox (Favre-Nicolin and Černý 2002).

The genetic algorithm is a subset of the methods termed *evolutionary algorithms*. Rather than modelling their operation on thermodynamic processes as with the Monte Carlo method, they employ phenomena seen in nature such as inheritance and mutation. The system being studied is encoded in strings called chromosomes, usually as binary 1s and 0s. As with the Monte Carlo method, a means of generating starting structures is employed and these are all given some measure of fitness to the solution. A percentage of these structures, again including some with poor fit, are then selected for reproduction. Two or more parent strings are combined to generate an offspring string. This could be by randomly varying a part of the string (mutation) or crossover (cutting the chromosomes at a specific point and splicing them together). This new generation is then tested for fitness to the solution and the algorithm continues, again always including some poor fits to avoid local minima. Genetic algorithms were first used in crystal structure determination in the 1990s (Harris *et al* 1998).

### 2.3.5 Full profile refinement

#### 2.3.5.1 Introduction

Once the atomic positions have been established with some accuracy the final stage in the process of structure solution is full profile refinement. Rietveld's method (Rietveld 1969) was the method used in this work. The approximate crystal structure (unit cell and atom positions) combined with information on the instrument (such as zero shift, axial divergence and a background factor) together with adjustments for structural parameters (such as thermal motion and preferred orientation) are used to generate a theoretical diffraction pattern. A method of fit is used to compare this to the experimental pattern and the various parameters then varied using least squares

refinement in order to bring this calculated pattern as close to the experimental one as possible.

Prior to Rietveld, structure determination from XRPD data was difficult because of the overlap in peaks that tends to occur in the 1-dimensional data space. Rietveld's method is important in that it finds a way of modelling the XRPD pattern by looking at individual contributions to the diffraction envelope at any point along the  $2\theta$  axis. By doing this it is possible to work with individual overlapping peaks.

Rietveld refinement uses a least squares minimisation on the following function:

$$WSS = \sum w_i (I_i^{\text{exp}} - I_i^{\text{calc}})^2, w_i = \frac{1}{I_i^{\text{exp}}} \quad (2.42)$$

where  $I^{\text{calc}}$  is given by the classical intensity equation:

$$I_i^{\text{calc}} = S_F \sum_{j=1}^{N_{\text{phases}}} \frac{f_j}{V_j^2} \sum_{k=1}^{N_{\text{peaks}}} L_k |F_{k,j}|^2 S_j (2\theta_i - 2\theta_{k,j}) P_{k,j} A_j + bkg_i \quad (2.43)$$

The wave envelope is determined by a range of factors. The material under analysis has contributions due to cell size, space group, atom positions, texture, stress and strain. The sample in the diffractometer will affect the wave envelope due to its position, shape and orientation. The diffractometer itself has a contribution, due to beam intensity, Lorentz Polarisation, background and radiation. The important point to note is that each of these contributing factors can be expressed mathematically and can be refined.

### 2.3.5.2 Factors contributing to the wave envelope

The refineable factors are identified below in the intensity equation.



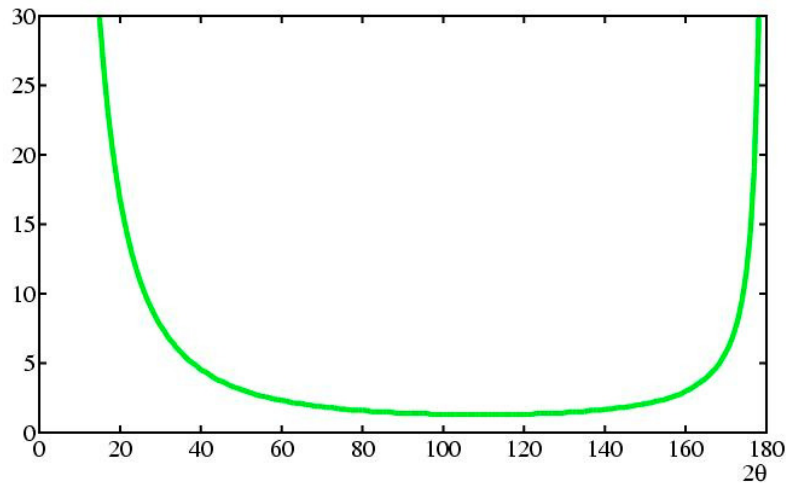


Figure 2.23 Lorentz Polarisation factor profile. Image from <http://pd.chem.ucl.ac.uk/pdnn/diff2/loren.htm>

The structure factor is given by:

$$|F_{k,j}|^2 = m_k \left| \sum_{n=1}^N f_n e^{-B_n \frac{\sin^2 \theta}{\lambda^2}} (e^{2\pi i(hx_n + ky_n + lz_n)}) \right|^2 \quad (2.46)$$

where  $m_k$  represents the multiplicity of the  $k$  reflection,

$N$  the number of atoms,

$B_n$  the temperature (Debye-Waller) factor,

$x_n, y_n, z_n$  the coordinates of the  $n^{\text{th}}$  atom,

and  $f_n$  the atomic scattering factor.

The X-ray atomic scattering factor,  $f_n$ , is proportional to the number of electrons and decreases with  $2\theta$ .

Rietveld assumes a Gaussian shape for each peak in the diffraction envelope. For a Gaussian distribution, peak width is given by:

$$H_k^2 = U \tan^2 \theta_k + V \tan \theta_k + W \quad (2.47)$$

where  $U, V$  and  $W$  are the half width parameters,

and  $\theta_k$  is the centre of the peak.

To incorporate preferred orientation,  $P_{k,j}$ , Rietveld employs the March-Dollase formula:

$$P_{k,j} = \frac{1}{m_k} \sum_{n=1}^{m_k} \left( P_{MD}^2 \cos^2 \alpha_n + \frac{\sin^2 \alpha_n}{P_{MD}} \right)^{\frac{3}{2}} \quad (2.48)$$

where  $P_{MD}$  is the March-Dollase parameter,

$\alpha_n$  is the angle between the scattering vector and the crystallographic plane  $hkl$ .

Again, summation is made over all equivalent  $hkl$  reflections,  $m_k$ .

For Bragg-Brentano geometry involving a thick sample, the absorption factor,  $A_j$ , is given by:

$$A_j = \frac{1}{2\mu} \quad (2.49)$$

where  $\mu$  is the linear absorption coefficient of the sample. For a thin sample the absorption depends upon  $2\theta$ , as detailed in 2.2.4.3.

The background term,  $bk_{g,i}$ , is a polynomial function in  $2\theta$ , given by:

$$bk_{g,i}(2\theta_i) = \sum_{n=0}^{N_b} a_n (2\theta_i)^n \quad (2.50)$$

where  $N_b$  is the polynomial degree,

$a_n$  the polynomial coefficient.

### 2.3.5.3 Least squares parameters

Rietveld defines two lists of parameters for use in the least squares process. The first list contains the profile parameters. These give the the positions, the halfwidths and the asymmetry of the Bragg peaks, plus the preferred orientation. These parameters are:

|                    |                       |
|--------------------|-----------------------|
| $U, V, W$          | half width parameters |
| $Z$                | zero point            |
| $A, B, C, D, E, F$ | unit cell parameters  |

|     |                                 |
|-----|---------------------------------|
| $P$ | asymmetry parameter             |
| $G$ | preferred orientation parameter |

His second list contains what he calls structural parameters. These relate to the cell contents:

|                 |  |
|-----------------|--|
| $c$             | scale factor, such that $y_{calc} = c \cdot y_{obs}$ |
| $Q$             | overall isotropic temperature parameter              |
| $x_i, y_i, z_i$ | fractional coordinates of $i^{\text{th}}$ atom       |
| $B_i$           | atomic isotropic temperature parameter               |
| $n_i$           | occupation number                                    |

#### 2.3.5.4 Measuring the quality of the refinement

Least squares refinement can be measured in a number of ways. Rietveld refinement minimises the weighted sum of the squares (equation 2.42):

$$WSS = \sum w_i (I_i^{\text{exp}} - I_i^{\text{calc}})^2, w_i = \frac{1}{I_i^{\text{exp}}}$$

A common measure for the quality of refinement is the weighted R profile:

$$R_{wp} = \sqrt{\frac{\sum_{i=1}^N [w_i (I_i^{\text{exp}} - I_i^{\text{calc}})]^2}{\sum_{i=1}^N [w_i I_i^{\text{exp}}]^2}}, w_i = \frac{1}{\sqrt{I_i^{\text{exp}}}} \quad (2.51)$$

Rietveld states that a computer program based on his method allows the refinement or otherwise of any parameter in the least square process. This is essentially the same process used today in programs such as GSAS (Larson and Von Dreele 1994), which will be discussed further in chapter 5. An image showing this program in operation is given in figure 2.24.

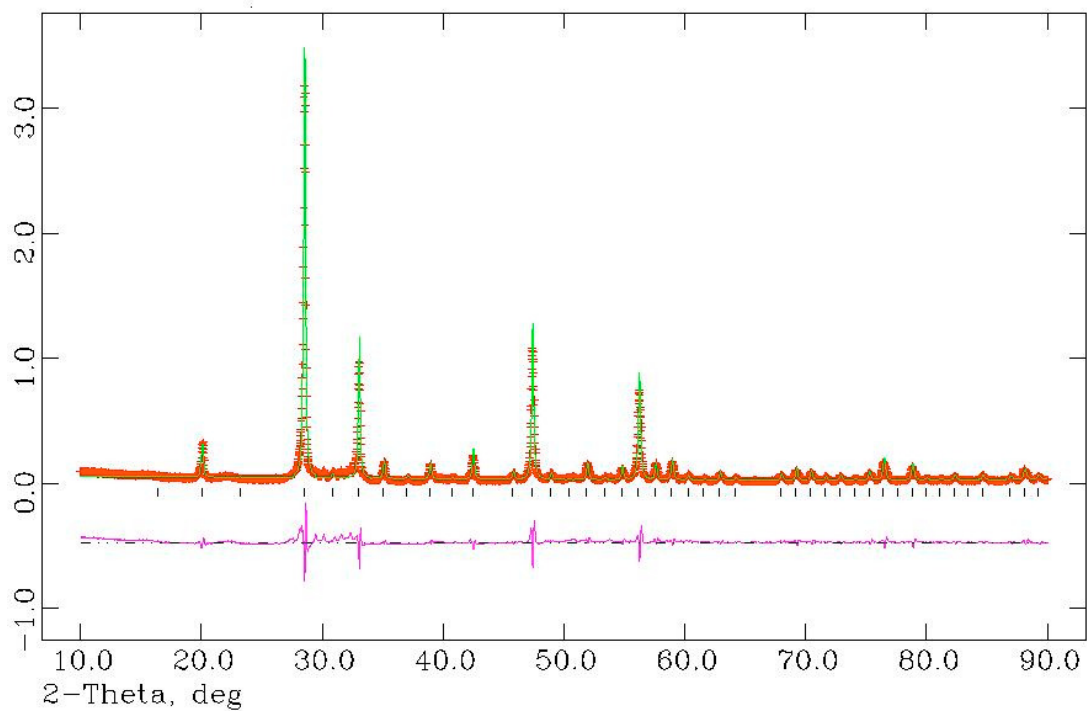


*Figure 2.24 Full profile refinement of an XRPD pattern using the program GSAS.*

Figure 2.24 shows the experimental data as a series of horizontal ticks marking the wave envelope. The calculated pattern follows the same profile but as a solid line. The difference between the two histograms is shown by the lower line. The peak positions are shown by vertical ticks.

## **3 DIFFERENTIAL SCANNING CALORIMETRY**

### **3.1 INTRODUCTION**

Differential Scanning Calorimetry (DSC) is a thermal analysis technique used primarily to investigate enthalpy changes, such as those associated with change of phase, crystallisation or chemical reactions. It is defined by the ASTM as '*a technique in which the difference in energy input into a substance and a reference material is measured as a function of temperature, while the substance and reference material are subjected to a controlled temperature program*' (ASTM).

There are typically two types of DSC program: isothermal hold and temperature ramp. During an isothermal hold the sample is heated to a defined temperature and held there for a certain period of time. A temperature ramp involves heating the sample across a temperature range at a defined rate. In both situations, the purpose of the experiment is to follow a physical change in the sample by observing its absorption or release of heat.

All the DSC experiments in this thesis involved temperature ramps. When a material is heated there is generally a correlation between heat input and temperature. That is, with continued heating the material increases in temperature. However, at certain points where events such as phase changes exist, there occur anomalies in the DSC output. These thermal events involve additional heat either being taken in or given out by the material, as the structure rearranges in some manner. At some temperature, the material starts to undergo a chemical or physical transformation that involves the release or absorption of heat and no further change in temperature is seen until the reaction has completed. The ordinate value in the DSC output at any given time or temperature is related to the difference in heat flow between a reference sample and the material under analysis.

### **3.2 INSTRUMENTATION**

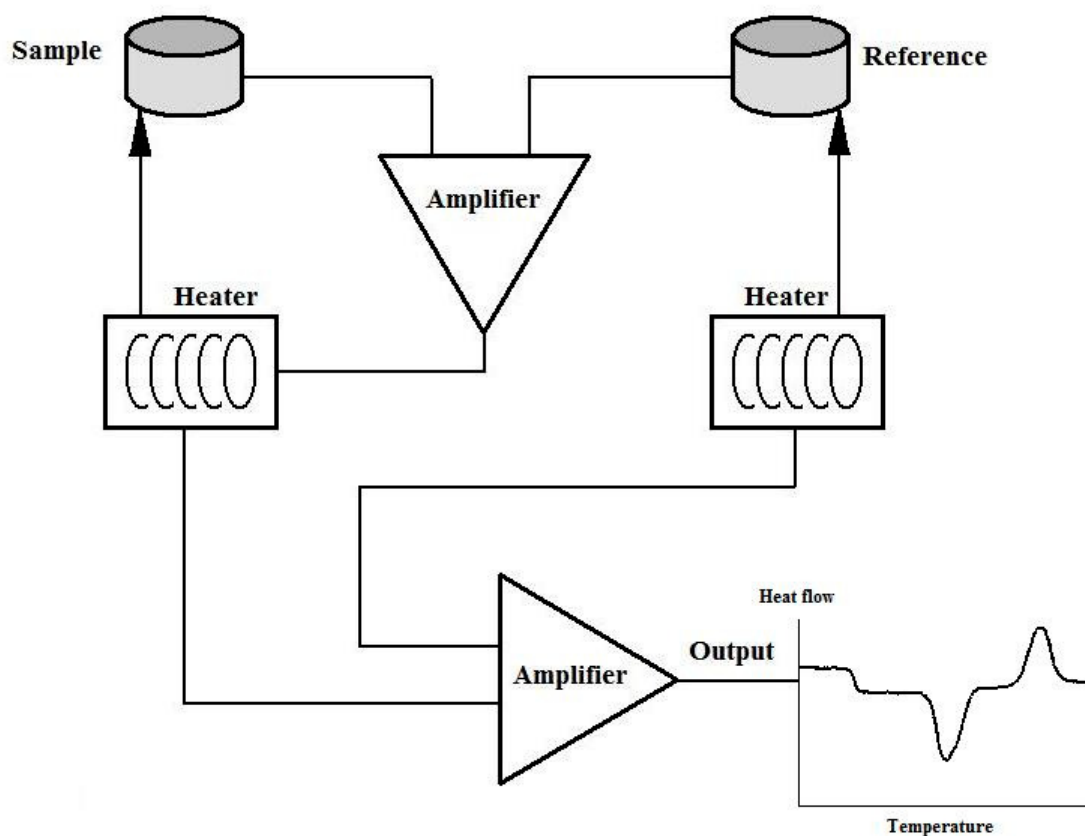
Both sample and reference are held in small pans, often made from alumina. In some cases the reference may just be an empty pan, which was the experimental set up

employed during this work. It is important that the specific heat capacities of the pans are as close as possible; generally this means that pans of identical size and material are used. If a reference sample is used in the reference pan then it is also important that it is of a similar mass to the sample material. Both pans are equipped with a thermocouple for determination of temperature, and a heating element. The pans may be blanketed with a chosen gas during the experimental run. Typically the sample and reference are heated slowly through a pre-determined temperature range. When the sample undergoes a physical change, which may be endothermic or exothermic, the device measures the heat input or output difference which then arises between the sample and the reference. The electrical input to the sample pan is then adjusted to bring the temperatures in line. This input, which is measured in mW, is convertible into the amount of heat needed to keep the sample and reference at the same temperature. Therefore the DSC effectively measures the heat involved in the transition.

The heater connected to the reference pan supplies power at the pre-determined rate, heating the reference in a linear manner according to the experiment in progress. The sample heater adjusts in proportion to the temperature difference between the two pans. The difference in the power consumption of the 2 heaters is amplified and plotted as a function of temperature.

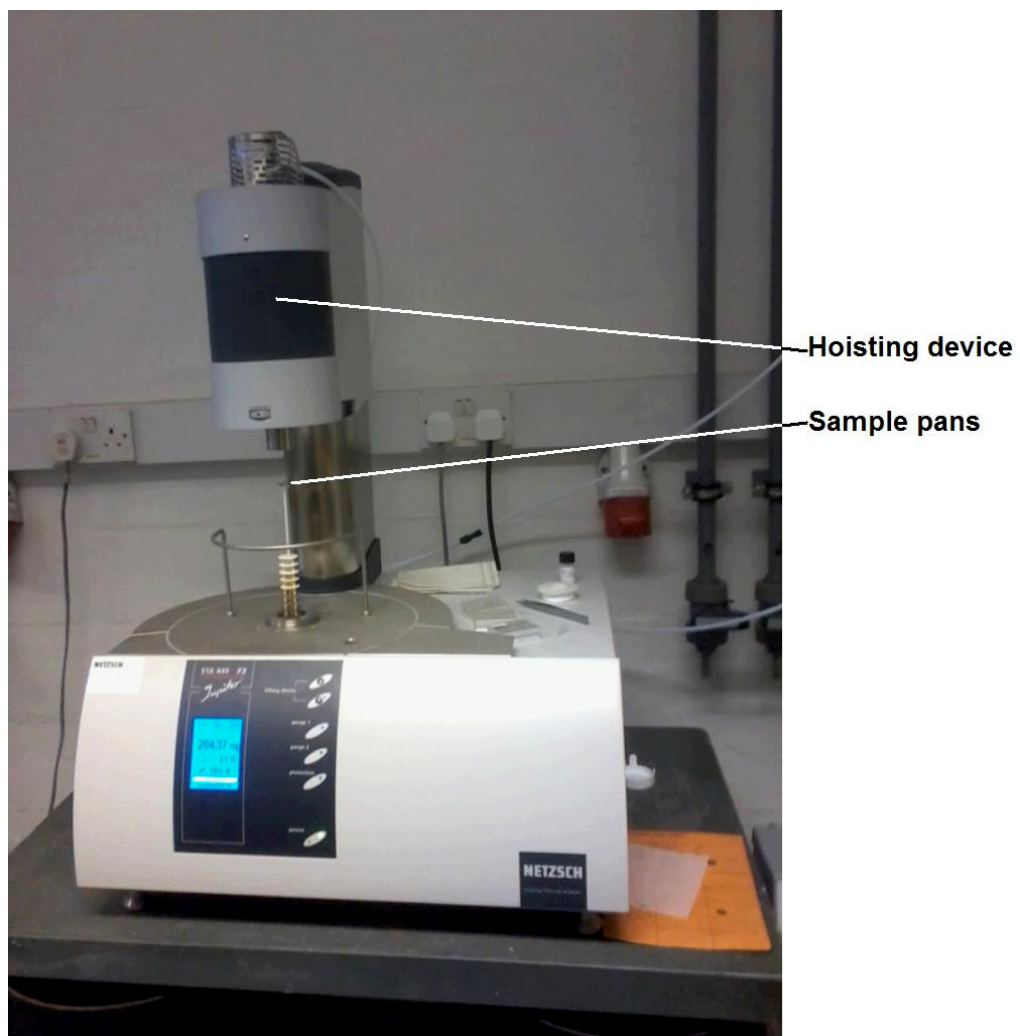
It is important to note that the alumina pans themselves will have their own contribution to the signal and therefore their effect is measured via a preliminary run with both pans empty, using the same conditions (heating rate, gas atmosphere and flow). The resulting signal can then be subtracted from the experimental signal to determine the contribution from the sample alone.

A schematic of a DSC is shown in figure 3.1.



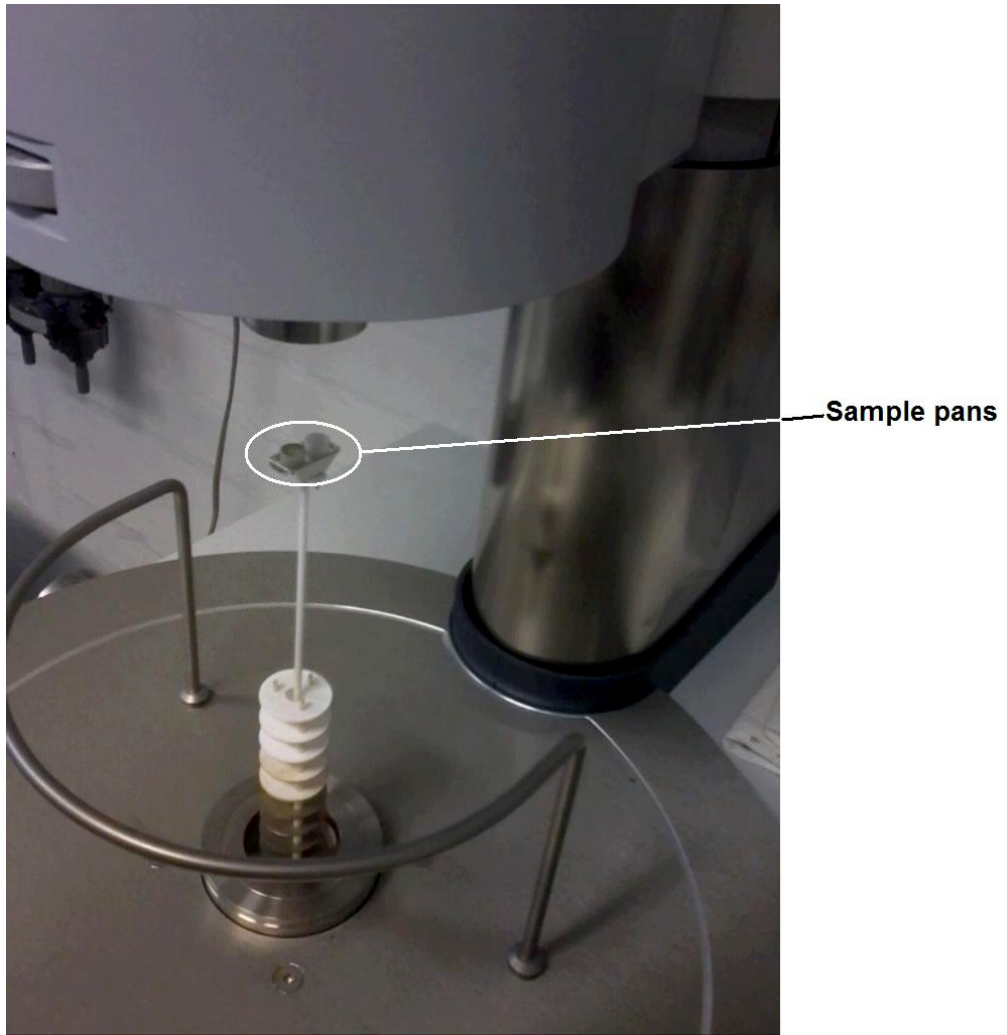
*Figure 3.1 DSC schematic.*

Figure 3.2 shows the instrument used in this work, a Netzsch ST449 F3 Jupiter. This instrument is capable of heating a sample up to 1500°C. It is also capable of weighing the sample throughout the run, allowing a TG (thermogravimetric) analysis of the reaction. The base unit (below) and the hoisting device/furnace (above) can be clearly seen. The sample carrier is the thin white alumina rod between the two, upon which sit the sample and reference pans.



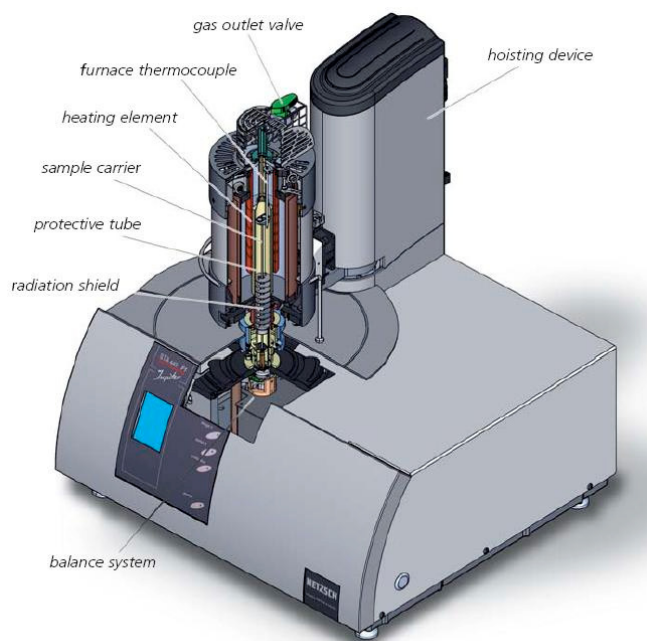
*Figure 3.2 Netzsch ST449 F3 Jupiter DSC.*

Figure 3.3 shows the two alumina pans. The pan nearer the camera is the one containing the sample, which in this case is the pale green powder of  $\text{Pr}_2\text{O}_3$ .



*Figure 3.3 Sample carrier with reference and sample pans atop.*

Figure 3.4 shows a cut-away schematic of the instrument.



*Figure 3.4 Cut-away schematic of the DSC. Image taken from NETZSCH manual (NETZSCH).*

The base unit of the instrument contains the connections for the thermocouples and the gas flow. Gas is introduced from a cylinder beside the instrument, although it is possible to run the machine without any carrier/protective gas. The sample carrier is plugged into a socket and can therefore be easily exchanged. The experimental setup, data acquisition and analysis are performed by an associated computer running NETZSCH software.

### **3.3 INSTRUMENTAL OUTPUT**

The data from the instrument can give a number of pieces of information. The shape of the curve at the transition temperature indicates the nature of the reaction e.g. a sharp peak may imply it occurs suddenly; a broad peak may indicate that an increasing energy input is needed to convert the material across the ramp. Integration of the area under the heat flow curve yields the enthalpy change associated with the thermal event. The shift in position of the transition over ramps of different rates can be used to determine the activation energy.

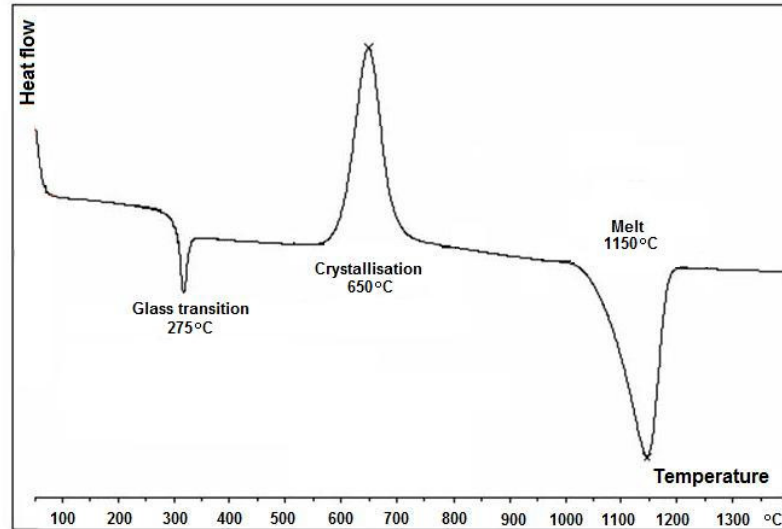


Figure 3.5 DSC curve showing heat flow against temperature (exothermic is 'up').

Figure 3.5 shows typical features associated with a typical DSC curve. The glass transition at low temperature represents a shift in structure from amorphous to some degree of short range order. Once a glass transition has taken place the level of the trace is taken as the new baseline. Crystallisation is an exothermic process, whereby a system attains a greater stability by the release of heat. It is represented by a negative peak in the trace i.e.  $\Delta \frac{dH}{dt}$  is negative. Melting is an endothermic process, whereby heat is taken in to the sample, represented by a positive peak i.e.  $\Delta \frac{dH}{dt}$  is positive. The area between a particular peak and the baseline represents the enthalpy change giving rise to it, assuming the heat capacity of the reference is unchanging across the peak.

$$\int \left( \frac{dH}{dt} \right)_{sample} dt = \Delta H_{sample} \quad (3.1)$$

As the DSC is held at constant pressure, the measured heat flow is proportionate to the enthalpy change:

$$\left(\frac{dq}{dt}\right)_p = \frac{dH}{dt} \quad (3.2)$$

The heat flow difference between the pans is given by:

$$\Delta \frac{dH}{dt} = \left(\frac{dH}{dt}\right)_{sample} - \left(\frac{dH}{dt}\right)_{reference} \quad (3.3)$$

Heat capacity for a transition,  $C_p$ , can be determined from the baseline shift and is given by:

$$C_p = \left(\frac{dq}{dT}\right)_p = \left(\frac{dH}{dT}\right)_p \quad (3.4)$$

Using the chain rule:

$$C_p = \left(\frac{dH}{dt}\right) \cdot \left(\frac{dt}{dT}\right) \quad (3.5)$$

$\frac{dH}{dt}$  represents the baseline shift,  $\frac{dt}{dT}$  is the inverse of the scan rate of the machine.

By finding the area under the curve it is possible to make use of the following relationship:

$$\Delta H = kA \quad (3.6)$$

where  $\Delta H$  is the enthalpy change

$k$  is the calorimetric constant, which is particular to the machine used

$A$  is the area under the curve

The equilibrium constant  $k$  and the standard enthalpy change for the process,  $\Delta H^\ominus$ , can be found from the van't Hoff equation:

$$\Delta H^{\ominus} = RT^2 \left( \frac{d \ln k}{dT} \right) \quad (3.7)$$

the standard free energy change from:

$$\Delta G^{\ominus} = -RT \ln k \quad (3.8)$$

the standard entropy change from:

$$\Delta S^{\ominus} = \Delta H^{\ominus} - T \Delta S^{\ominus} \quad (3.9)$$

The instrument has particular limitations, which need to be borne in mind. A high sample mass increases the signal strength, but can reduce resolution if there are overlapping peaks. The greater the heating rate, the greater is the signal strength, but as with sample mass, there is a trade-off with peak resolution. If a gas is used, one with high thermal conductivity, such as helium, causes lower signal strength but better peak separation. Additionally, there is a limit to the heating rate that can be employed to prolong longevity of the furnace. Typically a rate no greater than 20K/min is used with this instrument, as in the figure below.

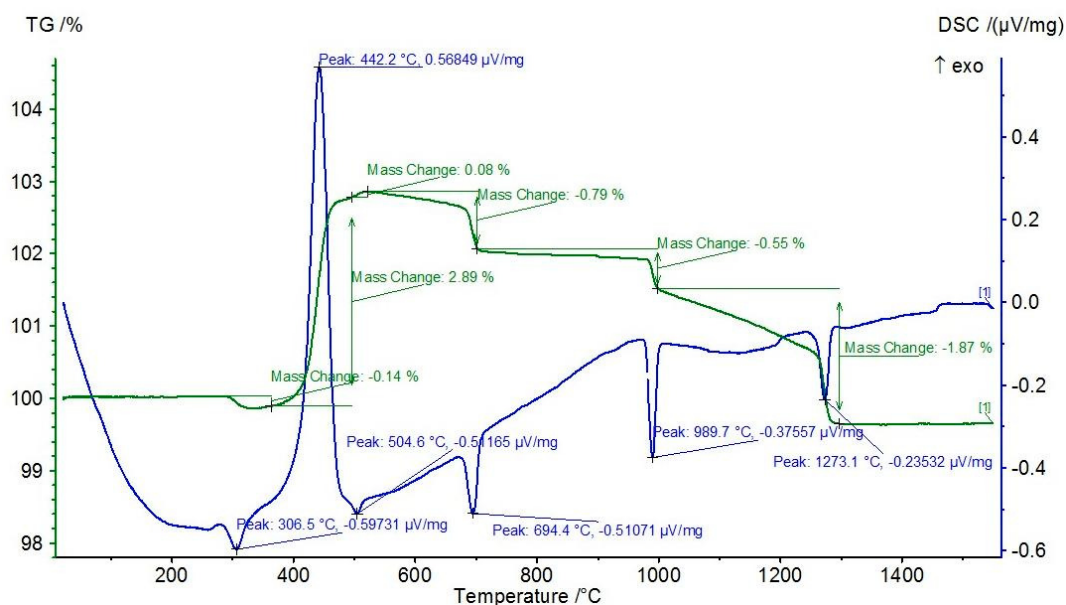


Figure 3.6 20K/min ramp for praseodymium sesquioxide.

As an example of the information that can be obtained, figure 3.6 shows a combined DSC-TG plot for the praseodymium-oxygen system over the temperature range 20°C to 1550°C. As indicated in Chapter 1, the system is rich in that it shows a large number of stoichiometries, each existing in its own temperature range. The lower line, showing sharp peaks, represents the DSC and shows that, for example, a significant thermal event occurs at 442°C, with an accompanying mass increase of 2.83% shown by the TG plot (upper line). A small endotherm at about 500°C is associated with a further but small mass increase. Following this, there are three more endotherms, each associated with a mass loss. More detailed analyses of the DSC-TG plots obtained will be presented in Chapter 8.

## 4 REACTION KINETICS

### 4.1 INTRODUCTION

The purpose of any kinetic study is to record how a reaction progresses with time under certain environmental conditions. To do this, it is necessary to establish how much conversion from reactant to product has taken place at any moment. By creating a mathematical model for the reaction, the rate constant at any temperature can be derived and subsequently used to derive the activation energy for the process.

The fundamental aims of a kinetic model are to:

- (1) visualise how the transformation arises and propagates;
- (2) express the degree of conversion as a function of time;
- (3) determine the rate constants and activation energy.

In this study the work has been concerned with conversion against temperature only. Data used in the analyses were obtained from both XRPD and DSC. Three models have been used to determine the rate constants activation energies, namely the Shrinking Sphere Model, the JMAK model and Kissinger Analysis.

### 4.2 PHASE BOUNDARIES

As a general rule, the heavier is the lanthanoid under investigation, the more effort is required to induce a particular phase change. Figure 1.5 shows the C  $\rightarrow$  B phase boundary to be an upwardly sloping line. That is, the transition temperature increases with the atomic number of the lanthanoid. Consequently, the heating temperature and/or heating time required to convert a particular low temperature phase to a high temperature one for a specific lanthanoid sesquioxide will increase with the atomic weight of the lanthanoid. For example, the C  $\rightarrow$  B transition in europia is easily achieved by heating to 1300°C for one hour. However, heating the C form of gadolinia to even 1500°C for an hour produces little change. It is only when the oxide is kept at this temperature for an extended period that the transition occurs. Gadolinium is the adjacent element to europium and yet the change in kinetics is considerable. We would

therefore expect that for the heaviest oxides the heating times would be considerably extended and the product materials would show less metastability on quenching.

### 4.3 DATA USED IN KINETIC MODELLING

#### 4.3.1 Data from XRPD

As one phase converts to another there is an associated change in peak intensities within the XRPD pattern. The peaks for the reactant phase will fall in height as the peaks for the product emerge from the baseline. A method of measuring the degree of conversion at any point is to select a prominent Bragg reflection arising from the reactant phase. For the lanthanoid sesquioxides, the most comprehensive historic study (Stecura 1966) looked at the change in intensity of the 222 Bragg reflection in the reactant phase. In my work this was identified at  $2\theta$  of  $28.45^\circ$  for  $\text{Eu}_2\text{O}_3$  and  $29.65^\circ$  for  $\text{Yb}_2\text{O}_3$ . An alternative method would be to look for the peaks arising from the product phase. Two prominent peaks in the monoclinic phase are the 401 and 11-2 reflections. These occur at  $2\theta$  of  $29.3^\circ$  and  $32.3^\circ$  for  $\text{Eu}_2\text{O}_3$  and  $30.15^\circ$  and  $33.7^\circ$  for  $\text{Yb}_2\text{O}_3$ . However, it would be more practical to use the 222 reflection in the reactant phase. Firstly, the maximum intensity is known from the start and so any decrease in the peak (and associated increase in the peak of the high-temperature modification) can be immediately ascribed a fractional conversion. With the product phase, the final heights of the new peaks are not known at the start of the experiment. Secondly, the 222 peak is readily discernible in the reactant pattern whereas the emerging peaks in the product pattern will not be so in the initial stages.

Figure 4.1 shows a series of XRPD patterns taken over time, clearly showing a reactant peak at  $40.2^\circ$  of  $2\theta$  falling in intensity. What is not as clear is the magnitude of the corresponding rise in the product peak at  $38.1^\circ$ .

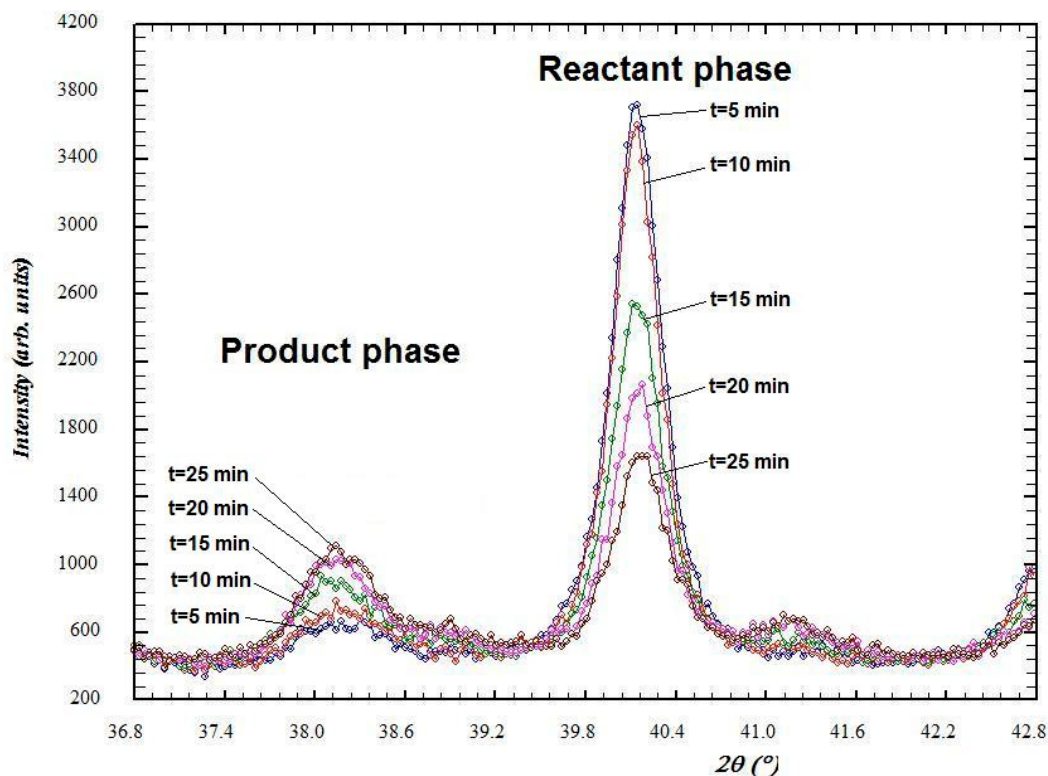


Figure 4.1 Changes in peak intensity over time.

#### 4.3.2 Data from DSC

The data used from the DSC work are the heating rate and the temperature of onset of conversion. For each material the approximate temperature at which the product starts to convert to reactant is determined by a wide range temperature ramp. Once this conversion point has been established, a number of temperature ramps up to the conversion temperature are carried out, each at a different heating rate. The onset temperature is known to vary with the heating rate (generally a slower heating rate has a lower conversion temperature). A process called Kissinger Analysis (Kissinger 1955) can then be applied to this information to determine the rate constant and activation energy.

#### 4.4 SHRINKING SPHERE MODEL

A model historically adopted for kinetic work in the solid state is based on a shrinking sphere model (Tammann 1925), (Jander 1927). This model states that the nucleating

sites of the new phase are created quickly in comparison to their propagation throughout the bulk material. This means the growth of the phase boundary is the rate-determining factor. Tamman postulated that the rate of increase of the high-temperature phase at the phase boundary was inversely proportional to time.

$$\frac{dy}{dt} = \frac{k_T}{t} \quad (4.1)$$

where  $y$  is the thickness of high-temperature phase layer,  $t$  is time and  $k_T$  is a constant.

On integration this becomes:

$$y = k_T \ln t + A_1 \quad (4.2)$$

where  $A_1$  is a constant of integration.

Jander noted that some phase reactions did not agree with Tamman's postulate. He found that for some reactions it was the square of the thickness of the product layer that was proportional to time.

$$y^2 = 2k_j t \quad (4.3)$$

This is an integrated form of  $\frac{dy}{dt} = \frac{k_j}{y}$

This equation states that the rate of growth is inversely proportional to the thickness at time  $t$ . In this situation the existence of product slows the reaction as it progresses. This equation is known as Jander's law. It is one of three possible reactions in the solid state.

The second type of reaction occurs if the phase boundary moves at a constant rate:

$$\frac{dy}{dt} = k \quad (4.4)$$

Then the product does not influence the rate of reaction. On integration this equation becomes:

$$y = kt + A_2 \quad (4.5)$$

where  $A_2$  is a constant of integration. However,  $A_2$  is equal to zero because at  $t=0$  the thickness of product is also zero.

The third type of reaction is where the rate of reaction is proportional to the thickness of product i.e. it is catalysed by the thickness of product. It is given by:

$$\frac{dy}{dt} = k_A y \quad (4.6)$$

On integration this becomes:

$$\ln y = k_A t = A_3 \quad (4.7)$$

where  $A_3$  is a constant of integration, again equal to zero.

Both Stecura and Ainscough employed Jander's second equation in relation to the rare earth sesquioxides. However, before the equation can be used it is necessary to ascertain the degree of conversion to the high-temperature modification.

Assuming the reactant particles are spherical, an increase in the product thickness results in a decrease in the radius,  $r$ , of the reactant particle, to  $r-y$ . The density of the reactant particle prior to reaction is:

$$\rho_A = \frac{M_1}{V_1} \quad (4.8)$$

where  $\rho_A$  is the density,  $M_1$  is the mass of the reactant particle and  $V_1$  is the volume of the reactant particle. After reaction, the density of the reactant particle is:

$$\rho_A = \frac{M_2}{V_2} \quad (4.9)$$

where  $M_2$  is the mass of reactant particle at time  $t$  and  $V_2$  is the volume of the reactant particle at time  $t$ . As the density of the reactant material does not change, equations 4.8 and 4.9 can be equated.

$$\rho_A = \frac{M_1}{V_1} = \frac{M_2}{V_2} \quad (4.10)$$

Rearranging:

$$\frac{1}{V_1} = \frac{M_2}{M_1 \cdot V_2} \quad (4.11)$$

If  $\alpha$  is the fraction of the particle which has reacted then  $(1-\alpha)$  represents  $M_2/M_1$ . Substituting  $(1-\alpha)$  into equation 4.11 gives:

$$\frac{1}{V_1} = \frac{1-\alpha}{V_2} \quad (4.12)$$

The volume of the reactant particle before reaction is  $\frac{4}{3}\pi r^3$  and its volume after time  $t$  is  $\frac{4}{3}\pi(r-y)^3$ . Substituting into equation 4.12 gives:

$$(1-\alpha) \cdot \frac{4}{3}\pi r^3 = \frac{4}{3}\pi(r-y)^3 \quad (4.13)$$

Rearranging:

$$r - y = r(1 - \alpha)^{1/3} \quad (4.14)$$

Expressing as  $y$ , the thickness of the product layer, gives

$$y = r(1 - (1 - \alpha)^{1/3}) \quad (4.15)$$

Equating this with equation 4.5:

$$kt = r(1 - (1 - \alpha)^{1/3}) \quad (4.16)$$

where  $k$  is the linear rate of propagation.

Rearranging:

$$(1 - \alpha) = \left(1 - \frac{kt}{r}\right)^3 \quad (4.17)$$

Expanding the polynomial and keeping only the first term:

$$1 - \alpha = e^{\frac{-3kt}{r}} \quad (4.18)$$

Rearranging:

$$\ln\left(\frac{1}{1 - \alpha}\right) = kt \quad (4.19)$$

where  $k$  is the rate constant. This is the equation presented by Stecura. Ainscough uses the equivalent:

$$-\ln(1 - x) = kt \quad (4.20)$$

where  $x = \alpha$ . This is a first order rate equation. A plot of  $-\ln(1 - \alpha)$  against  $t$  should yield a straight line with gradient  $k$ . Therefore for any set of isotherms the rate constant

at that temperature can be determined. The activation energy can then be determined by use of the Arrhenius equation:

$$k = Ae^{\frac{-E_A}{RT}} \quad (4.21)$$

where  $k$  is the rate constant,  $A$  is a constant,  $E_A$  is the activation energy,  $R$  is the gas constant and  $T$  is the temperature. The Arrhenius equation can be rewritten as:

$$\ln k = \ln A - \frac{E_A}{RT} \quad (4.22)$$

A plot of  $\ln k$  against  $\frac{1}{T}$  should yield a straight line with gradient  $-\frac{E_A}{R}$ . Therefore the activation energy for a particular phase transformation may be determined.

#### 4.5 THE JMAK MODEL

The Johnson-Mehl-Avrami-Kolmogorov (JMAK) model comes from work carried out during the late 1930s and early 1940s. The equations involved are often referred to as Avrami equations; Avrami published extensively during this period, in a series of papers in the Journal of Chemical Physics, all of which are still referenced today whenever the model is discussed (Avrami 1939, 1940, 1941).

The model assumes that the new phase is created from randomly-distributed germ nuclei already existing in the reactant phase. If there is no further nucleation during the reaction i.e. all nuclei are present at the start, the material is termed *site saturated*. With increasing temperature some of these germ nuclei become growth nuclei, creating grains in the product phase. These grains grow at a linear rate. As the reaction progresses the degree of transformation follows a sigmoidal or S-type curve. That is, conversion is initially slow but increases exponentially. There comes a point of inflexion in the curve, which represents a running out of space in the product phase, where grains are impinging on one another. The curve then decreases in gradient until it

flattens out. A typical sigmoidal curve is shown in red in figure 4.2. The sigmoidal curve is typical of many processes in nature involving growth.

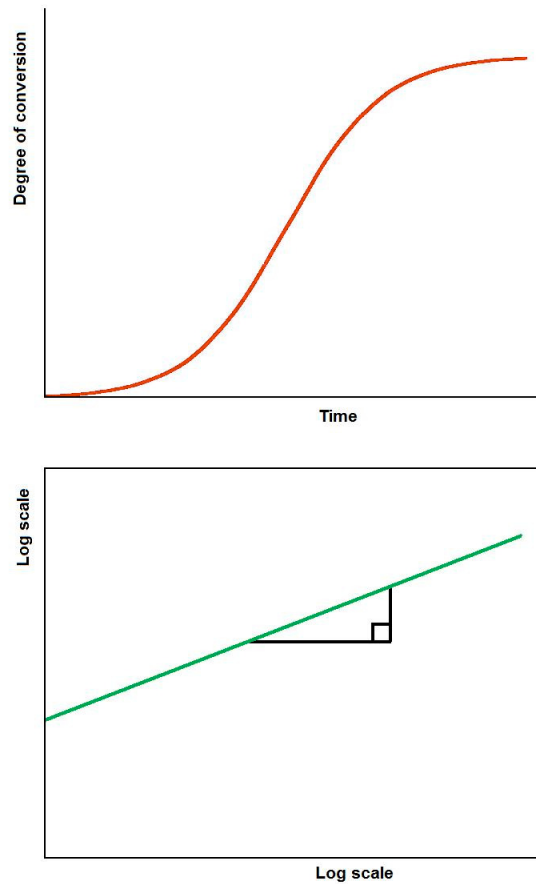


Figure 4.2 Sigmoidal function (top) and its linearised form.

The basic sigmoid curve, called the logistic curve, is given by:

$$P(t) = \frac{1}{1 + e^{-t}} \quad (4.23)$$

where  $P$  is the population and  $t$  is time. This basic relationship, or variations upon it, is used in many fields, including biology, economics and artificial neural networks. Its basic feature is that for small values of  $t$  growth appears exponential and there is an equilibrium point at which it begins to slow.

The fundamental principle in the derivation of the JMAK equation is to express the change in fractional volume of product relative to the existing fractional volume. The fractional volume changed to product is given by:

$$f = \frac{V}{V_{total}} \quad (4.24)$$

where  $f$  is the fraction changed,  $V$  is the volume of product and  $V_{total}$  is the total volume of the reaction space (reactant plus product). As the reaction progresses, germ nuclei grow into grains of the new phase. Eventually some of these grains impinge on one another, as shown in figure 4.3.

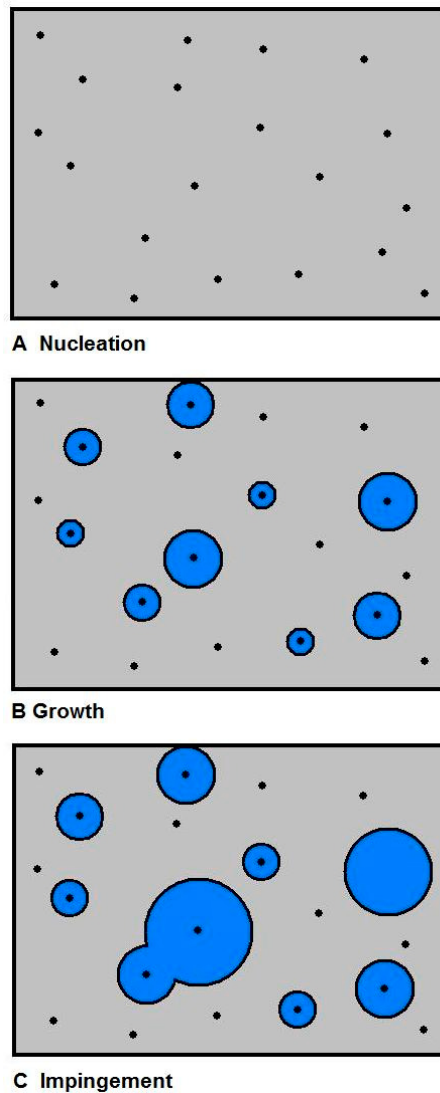


*Figure 4.3 Germ nucleation, grain growth and grain impingement.*

Avrami appreciated that as grains grow they eventually come into contact with one another (figure 4.3C) and growth would cease. He therefore defined an extended volume fraction, as if the grains always had free reactant space in which to grow and no impingement occurs.

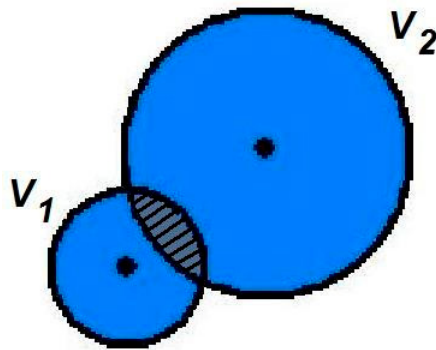


Figure 4.4 Illustration of extended volume.

Figure 4.4 shows an enlarged region of figure 4.3C where 2 grains have grown against one another. The volume of the smaller grain is given by  $V_1$  and that of the larger grain by  $V_2$ . The fraction changed by virtue of the extended volume is given by:

$$f_{ext} = \frac{V_1 + V_2}{V_{total}} \quad (4.25)$$

The actual fraction changed is given by:

$$f = \frac{V_1 \cup V_2}{V_{total}} \quad (4.26)$$

where  $\cup$  represents the union of the two circles i.e. the area of both but including their overlap just once. The relationship between increments in  $f$  and  $f_{ext}$  can be expressed by the following differential equation:

$$df = df_{ext}(1 - f) \quad (4.27)$$

As is typical of any growth, the amount of material already transformed,  $f$ , acts as a feedback in the above equation, limiting the change possible at any moment by the volume already transformed. At reaction completion, the volume of a grain transformed is given by:

$$V = \frac{4}{3} \pi r^3 \quad (4.28)$$

where  $r$  is the radius of the grain, assuming a spherical reaction volume. The radius  $r$  can be expressed as a distance  $st$  where  $s$  is the radial speed of propagation of the grain surface and  $t$  is time. Therefore:

$$V = \frac{4}{3} \pi (st)^3 \quad (4.29)$$

Multiplying the volume of the grain by  $N$ , the density of nuclei, gives the extended volume:

$$f_{ext} = \frac{4}{3} \pi N (st)^3 \quad (4.30)$$

The extended fraction increment,  $df_{ext}$ , is given by:

$$df_{ext} = 4\pi N s^3 t^2 .dt \quad (4.31)$$

Substituting into equation 4.27:

$$df = 4\pi N s^3 t^2 .dt (1-f) \quad (4.32)$$

Rearranging:

$$\frac{df}{1-f} = 4\pi N s^3 t^2 .dt \quad (4.33)$$

A constant  $k$  is defined, which contains the nucleation and growth terms:

$$k = \frac{4}{3}\pi Ns^3 \quad (4.34)$$

Recognising that  $\frac{d}{dx}\left(\frac{1}{x}\right) = -\frac{1}{x^2}$ :

$$-\ln(1 - f) = kt^3 \quad (4.35)$$

Rearranging:

$$f = 1 - e^{-kt^3} \quad (4.36)$$

This is the specific Avrami equation for site saturated growth in three dimensions. The general form is given by:

$$f = 1 - e^{-kt^n} \quad (4.37)$$

Whereas the value of  $k$  is determined by energy-dependent terms, the value of  $n$ , called the Avrami exponent, is interpreted as defining the geometry of the transformation. Generally the number of dimensions involved in the growth is equal to  $n$ , although it is quite possible to have fractional values for  $n$ . Therefore it is not always straightforward to deduce the geometry from the value. For any reaction, the value of  $n$  should be a constant irrespective of temperature. Typical values for  $n$  are given in table 4.1.

| Value of $n$ | Geometry | Type of growth  |
|--------------|----------|---|
| $1 < n < 2$  | 1D       | Needle  |
| $2 < n < 3$  | 2D       | Platelet  |
| $3 < n < 4$  | 3D       | Spherical – all nucleation sites present from start       |
| 4            | 3D       | Spherical – nucleation occurs throughout, slowing to zero |

*Table 4.1 Values of the Avrami exponent,  $n$ , and corresponding geometries.*

The more familiar form of the JMAK equation is the linear form, resulting from taking the double logarithm of the general equation. It is given by:

$$\ln(-\ln(1 - f)) = \ln k + n \ln t \quad (4.38)$$

or

$$\ln \left( \ln \left( \frac{1}{1 - f} \right) \right) = \ln k + n \ln t \quad (4.39)$$

Thus a plot of  $\ln(-\ln(1 - f))$  against  $\ln t$  should yield a straight line with intercept  $\ln k$  and gradient  $n$ . In practice it is possible to use a variety of quantities to calculate the value of  $f$ . If the fractional conversion is inferred by the change in peak intensity in an XRPD pattern, the following relationship can be used:

$$\ln \left( \ln \left( \frac{1}{1 - I_t} \right) \right) = \ln k + n \ln t \quad (4.40)$$

where  $I_t$  is the intensity arising from a selected peak of the new phase. Alternatively, this could be determined from the decrease in the intensity of a selected peak in the reactant phase. For example, if the intensity had fallen to 90% of its original value, the intensity  $I_t$  attributable to the product phase would be taken to be 0.1.

As with a Shrinking Sphere Model, the activation energy can then be determined by use of the Arrhenius equation (equation 4.22). Again, a plot of  $\ln k$  against  $\frac{1}{T}$  should yield a straight line with gradient  $\frac{-E_A}{R}$ .

#### 4.6 KISSINGER ANALYSIS

Kissinger noted that the temperature of maximum deflection during a DSC analysis varied with temperature. This variation is determined by the activation energy. By

linearising a function relating heating rate and temperature it is possible to derive the activation energy. Kissinger started with a generic equation describing a solid  $\rightarrow$  solid + gas reaction process:

$$\frac{dx}{dt} = A(1-x)^n \cdot e^{\frac{-E_A}{RT}} \quad (4.41)$$

where  $x$  is the fraction converted,  $\frac{dx}{dt}$  is the reaction rate,  $n$  is the reaction order,  $R$  is the gas constant,  $E_A$  is the activation energy and  $T$  is the temperature. When the reaction rate is at a maximum,  $\frac{d^2x}{dt^2}$  is equal to zero. Solving the above equation for  $\frac{d^2x}{dt^2}$

$$\frac{d^2x}{dt^2} = \frac{dx}{dt} \left[ \frac{E_A}{RT^2} \cdot \frac{dT}{dt} - An(1-x)^{n-1} \cdot e^{\frac{-E_A}{RT}} \right] \quad (4.42)$$

Substituting  $\varphi$  for the heating rate,  $\frac{dT}{dt}$

$$\frac{d^2x}{dt^2} = \frac{dx}{dt} \left[ \frac{E_A}{RT^2} \cdot \varphi - An(1-x)^{n-1} \cdot e^{\frac{-E_A}{RT}} \right] \quad (4.43)$$

The expression  $n(1-x)^{n-1}$  approximates to 1, therefore:

$$\frac{d^2x}{dt^2} = \frac{dx}{dt} \left[ \frac{E_A}{RT^2} \cdot \varphi - Ae^{\frac{-E_A}{RT}} \right] \quad (4.44)$$

Equating this with zero gives:

$$\frac{E_A}{RT^2} \cdot \varphi = Ae^{\frac{-E_A}{RT}} \quad (4.45)$$

Differentiating:

$$\frac{d(\ln \frac{\phi}{T_m^2})}{d(\frac{1}{T_m})} = \frac{-E_A}{R} \quad (4.46)$$

Therefore a plot of  $\ln \frac{\phi}{T_m^2}$  against  $\frac{1}{T_m}$  should yield a straight line with gradient

$\frac{-E_A}{R}$ . Once  $E_A$  is known,  $A$  can be calculated from equation 4.45, above.

An alternative method of calculating the activation energy is by use of the Arrhenius relationship:

$$\frac{1}{\tau} = \frac{1}{\tau_0} \exp\left(-\frac{E_A}{k_B T}\right) \quad (4.47)$$

where  $1/\tau$  is the inverse rate constant,  $k^{-1}$ , or *time constant*,  $E_A$  is the activation energy,  $k_B$  is the Boltzman constant and  $T$  is the isothermal annealing temperature. The use of this expression assumes that the transformation takes place at a single temperature and in a single step. The expression can also be written as:

$$k(T) = k_0 \cdot e^{\frac{-E_A}{k_B T}} \quad (4.48)$$

Both equations can be linearised as:

$$\ln \frac{1}{\tau} = \ln \frac{1}{\tau_0} - \frac{E_A}{k_B T} \quad (4.49)$$

and

$$\ln k(T) = \ln k_0 - \frac{E_A}{k_B T} \quad (4.51)$$

A series of isothermal anneals carried out close to the transition temperature will give a series of values for  $\tau$  (or  $k$ ) against  $T$ . A plot of  $\ln \frac{1}{\tau}$  (or  $\ln k$ ) against  $\frac{1}{k_B T}$  should yield a straight line with gradient  $-E_A$ .

## 5 SOFTWARE USED IN THIS WORK

### 5.1 SOFTWARE FOR XRPD

All the software mentioned in section 5.1 is hosted on the CCP14 (Collaborative Computational Projects 14) website [www.ccp14.ac.uk](http://www.ccp14.ac.uk). This is a site dedicated to the promotion of freely available single crystal and powder diffraction software for academic use.

#### *5.1.1 Determining the peak positions, calculating peak area, stacking of patterns – PowderX and WINPLOTR*

PowderX (Dong 1998) is a graphical program for XRPD data analysis. Data from the diffractometer in the form of intensities against  $2\theta$  is used as the input information. The output from the Siemens D500 diffractometer is in the form of a RAW file, although PowderX accepts a number of formats. This information is plotted in the form of a histogram, an example of which is shown in figure 5.1.

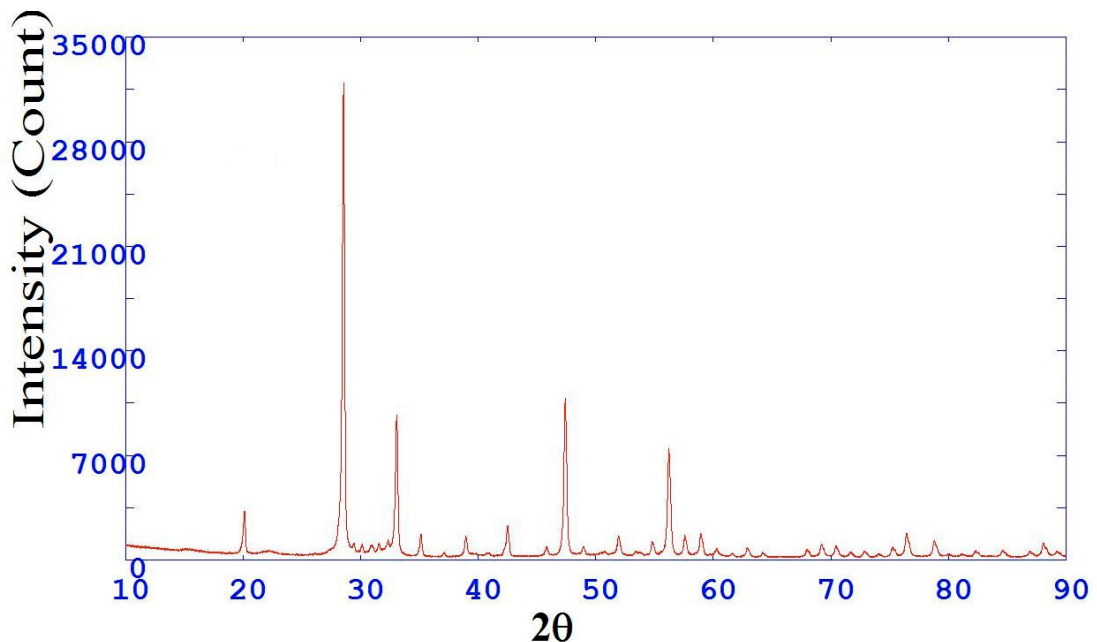


*Figure 5.1 Raw data (intensity versus  $2\theta$ ) displayed in PowderX.*

The three functions of PowderX used in this work were:

- (i) removing the part of the histogram attributable to  $K\alpha_2$  radiation.
- (ii) removing the background contribution i.e. bringing the Bragg peaks down to the  $2\theta$  axis.
- (iii) identification of the peak positions.

Figure 5.2 shows the above histogram after these processes have been applied.

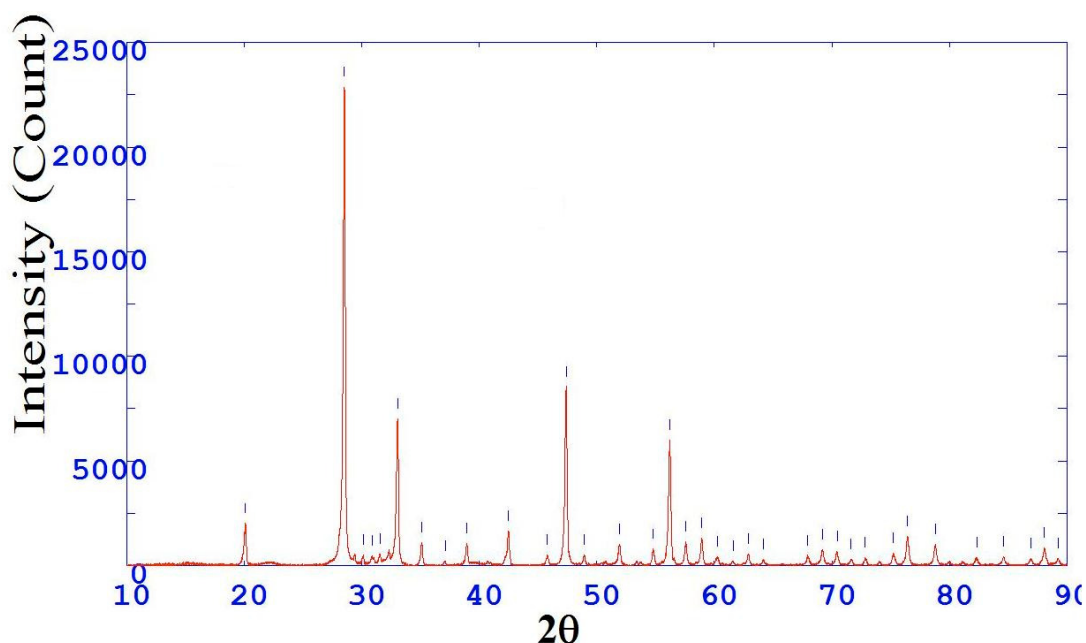


*Figure 5.2 Histogram after removal of  $K\alpha_2$  contribution, background and identification of peak positions.*

A list of the identified line positions can be saved as a text file, ready for use in an indexing program. The adjusted pattern can then be saved in a form for use in the full profile refinement program GSAS.

WINPLOTR (Roisnel and Rodriguez-Carvajal 2010) is another graphical program for analysis of XRPD patterns and comes as part of the Fullprof Suite, written by the same authors. In this work it has been used solely for calculation of peak height/area and for graphically stacking patterns from ramps and anneals.

### 5.1.2 Indexing – the Crysfire Indexing Suite and GRAPHPRO

The Crysfire Indexing Suite (Shirley 2002) has brought together 10 indexing programs, allowing the user to access them all through a single interface. The peak positions, established above via PowderX, are entered into Crysfire once. Each indexing program can then be applied to the data in turn and will generate a number of possible solutions. As each program generates solutions these are added to a summary file, which, after using all the indexing programs, can be quite extensive. Figure 5.3 shows the input screen of Crysfire where the user enters the peak positions. The screenshot is at the stage of entering the position of the 4<sup>th</sup> Bragg reflection.

```
C:\Windows\system32\cmd.exe
Max no. of obs lines: 1000
Max no. of calc lines: 20000
Main screen output will repeat to <Dset>.CF0 file by default
** No observed pattern loaded yet - to input one, run L0, IM or OB **
Crysfire 2004 v9.52.11 - Next command or ? for Help: ob
    OB = Input Observed Pattern (terminated with zero entry)
Intensities [I] or Icodes <1-9> [C] to be included? - <I/C/N, default=N>: n
CRYST accepts 2Theta degrees, Sinq theta, Q in QU., or d-spacing in A.
Please type I, S, Q or D to specify data type: t
Data type is 2Theta (degrees), using wavelength 1.540600 A
Scaling factor F is used to multiply input values to give 2Theta
Input new F (default: previous F = 1.000000): 1.000000 (no change)
1 2Theta = 20.115   Qobs = 513.984   ok
2 2Theta = 28.533   Qobs = 1023.472  ok
3 2Theta = 29.402   Qobs = 1085.369  ok
4 2Theta = 30.130
```

Figure 5.3 Crysfire peak position input screen.

As well as employing the widely used programs ITO, DICVOL and TREOR, Crysfire also contains the programs TAUP (Taupin 1973), KOHL (Kohlbeck and Hörl 1978), FJZN6 (Visser and Shirley 2000), LZON (Shirley *et al* 1978) and LOSHFZRF (Shirley and Louër 1978). An example of a summary file is shown in figure 5.4.

Running summary of all solutions logged so far for this dataset name,  
sorted in descending order of I20 then Merit (as defined by each program)

| I(20) | Merit | Volume  | V/V1 | BL | IndexProg  | Date            | Time  | Pedig | a       | b       | c      | alpha   | beta    | gamma   | Q(A)     |
|-------|-------|---------|------|----|------------|-----------------|-------|-------|---------|---------|--------|---------|---------|---------|----------|
| 20    | 46.4  | 740.62  | 1.00 | C  | IT012/log  | 1Feb09 00:51:01 |       | 121   | 8.8750  | 15.3629 | 5.4319 | 90.000  | 90.000  | 90.000  | 126.959  |
| 20    | 45.5  | 122.56  | .17  | F  | IT012/log  | 1Feb09 00:51:01 |       | 451   | 5.5902  | 6.4836  | 3.5596 | 102.112 | 100.931 | 79.739  | 338.971  |
| 20    | 27.0  | 270.41  | .37  | F  | IT012/log  | 1Feb09 00:51:01 |       | 252   | 5.4924  | 7.8532  | 6.4782 | 101.933 | 98.469  | 88.255  | 338.843  |
| 20    | 24.26 | 131.389 | .18  | F  | LZONv6.23b | 1Feb09 00:54:08 |       | 20001 | 5.4791  | 7.6726  | 3.1579 | 90.000  | 98.219  | 90.000  | 340.0557 |
| 20    | 23.51 | 159.302 | .22  | F  | TAUPv3.3a  | 1Feb09 00:50:22 | Ort_2 |       | 3.8332  | 5.4246  | 7.6613 | 90.000  | 90.000  | 90.000  | 680.5873 |
| 20    | 23.81 | 218.653 | .30  | F  | LZONv6.23b | 1Feb09 01:17:11 |       | 30691 | 4.4413  | 12.5758 | 3.9599 | 94.308  | 97.183  | 87.264  | 515.7905 |
| 20    | 22.8  | 305.18  | .41  | I  | IT012/log  | 1Feb09 01:13:02 |       | 253   | 4.8405  | 12.6586 | 5.1331 | 97.745  | 101.707 | 88.433  | 445.121  |
| 20    | 22.57 | 215.399 | .29  | F  | LZONv6.23b | 1Feb09 01:17:11 |       | 31120 | 5.4834  | 12.7354 | 3.1667 | 95.982  | 98.291  | 81.027  | 346.7514 |
| 20    | 22.16 | 422.377 | .57  | F  | LZONv6.23b | 1Feb09 01:17:11 |       | 31031 | 10.0563 | 13.0082 | 3.3548 | 94.198  | 92.741  | 104.686 | 106.1777 |
| 20    | 20.82 | 159.135 | .21  | F  | LZONv6.23b | 1Feb09 00:54:08 |       | 20002 | 5.4240  | 7.6675  | 3.8264 | 90.000  | 90.000  | 90.000  | 339.9084 |
| 20    | 20.5  | 270.31  | .36  | F  | IT012/log  | 1Feb09 00:51:01 |       | 251   | 5.4919  | 7.8530  | 6.4769 | 101.936 | 98.469  | 88.255  | 338.905  |
| 20    | 20.40 | 261.038 | .35  | F  | LZONv6.23b | 1Feb09 01:17:11 |       | 31147 | 5.4293  | 12.7281 | 3.8357 | 95.737  | 89.967  | 98.165  | 346.2968 |

Figure 5.4 Summary file of indexing results.

Figure 5.4 shows a set of results from Crysfire, listed in order of merit. As an example, the best fit to the experimental data is the top entry, with a figure of merit of 46.4. This set of unit cell parameters has enabled the indexing of all the first 20 lines in the pattern, shown by the value of  $I(20) = 20$ . The unit cell for this trial structure is orthorhombic ( $a = 8.875\text{\AA}$ ,  $b = 15.3629\text{\AA}$ ,  $c = 5.4319\text{\AA}$ ). Many trial structures may be generated from a diffraction pattern and it is quite possible that the actual solution is not allocated the top position in the summary file, if it is found at all. The user is able to change the tolerance in  $2\theta$  i.e. to adjust how far from the actual peak positions the calculated positions are allowed to stray. In some cases increasing this tolerance may bring the actual solution into the summary list if it wasn't already present, but this is at the expense of accepting poor data from the diffractometer. The indexing process is often regarded as the most difficult stage in the process of structure solution. This is because just a small error in measuring the peak positions can generate many unnecessary trial cells, even missing the actual cell altogether. The process of identifying potential cells from the summary list is often one of trial and error. The need for accurately measuring the Bragg reflections and assigning the peak positions is clear.

Although only used in this work when Crysfire failed, GRAPHPRO is a program written by myself for quickly indexing cubic cells.

### 5.1.3 Space group determination - CHEKCELL

CHEKCELL (Laugier and Bochu) is a program for both manually and automatically finding the best unit cell parameters and space group for the unit cell and has been designed to work in tandem with Crysfire. The peak positions and possible cells are taken from the relevant Crysfire files. An example is shown in figure 5.5.

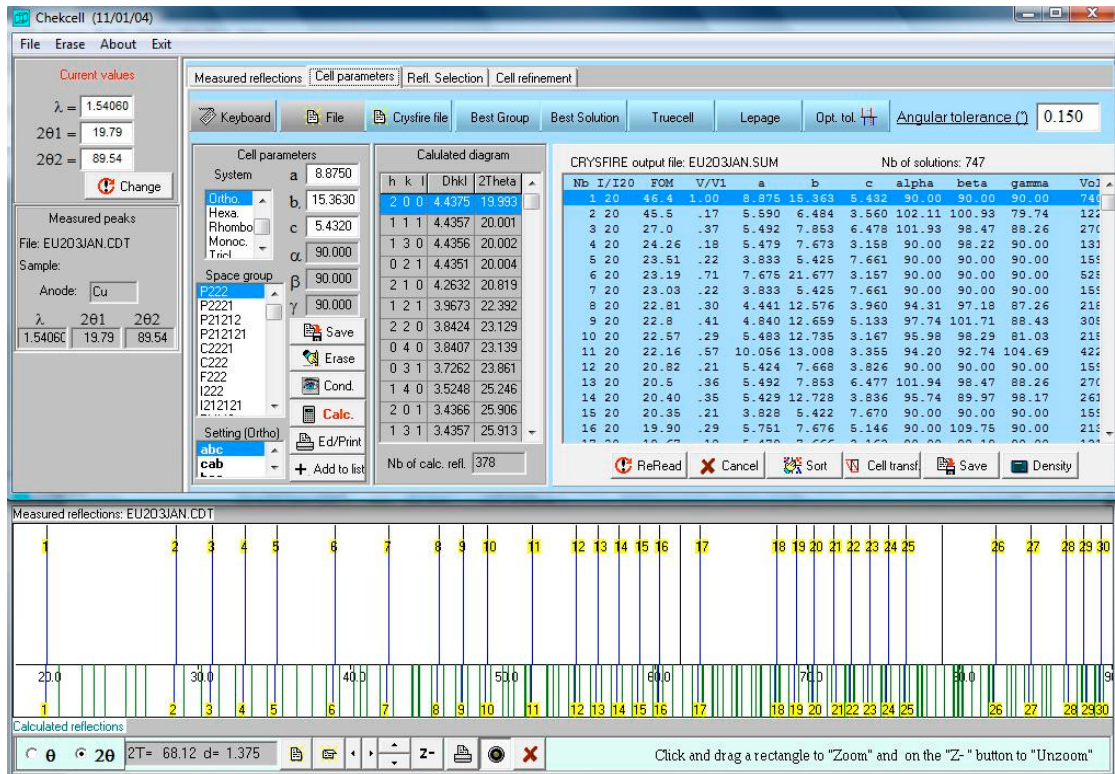


Figure 5.5 CHEKCELL main screen showing trial cells (top half) and comparison of measured and calculated peak positions (bottom half).

Each possible cell, together with the space groups available for it, is used to generate Bragg peak positions. From all the trial cells used, the best fit to the experimental data is taken as a possible solution for the cell (see figure 5.6). It is then possible to refine the trial unit cell parameters to get a better fit to the measured peak positions (see figure 5.7). This is the trial cell to be used in Rietveld refinement.

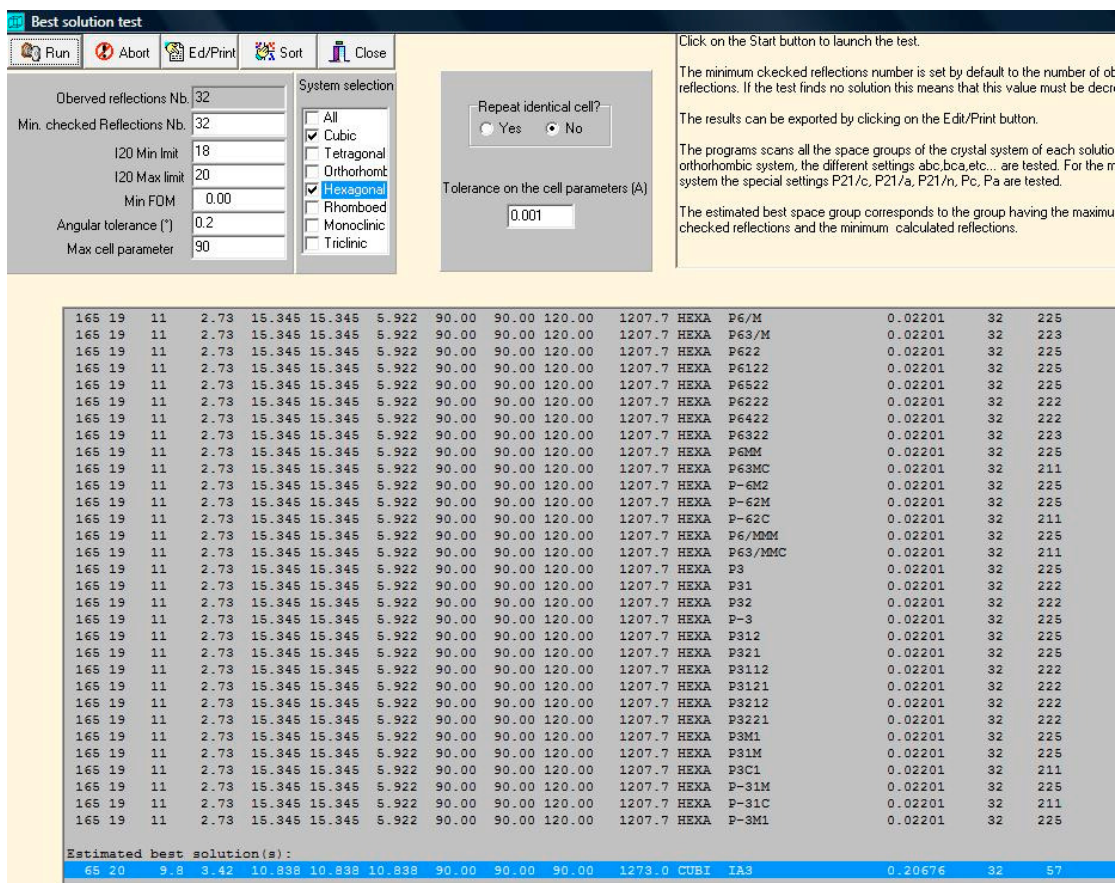


Figure 5.6 Best solution from CHEKCELL (highlighted at the foot of the image).

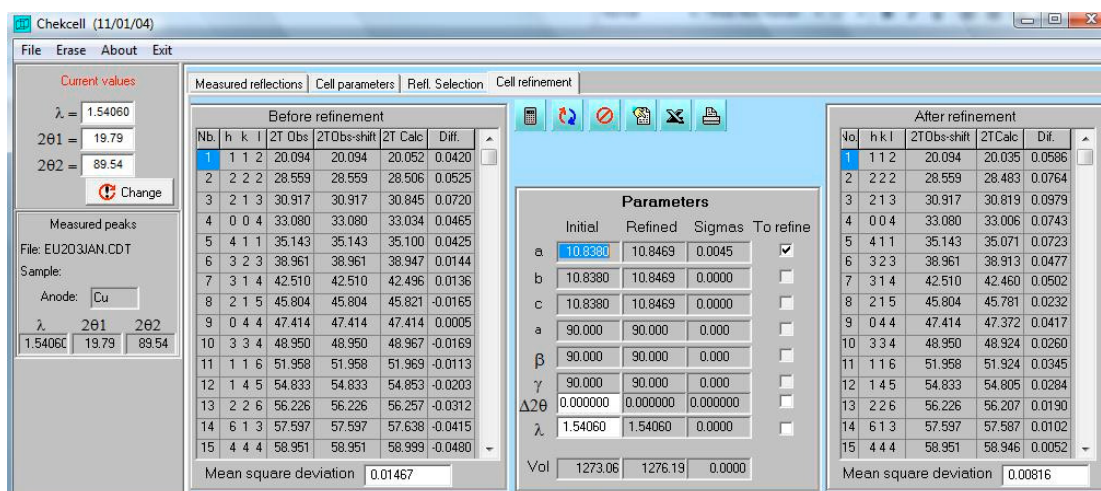
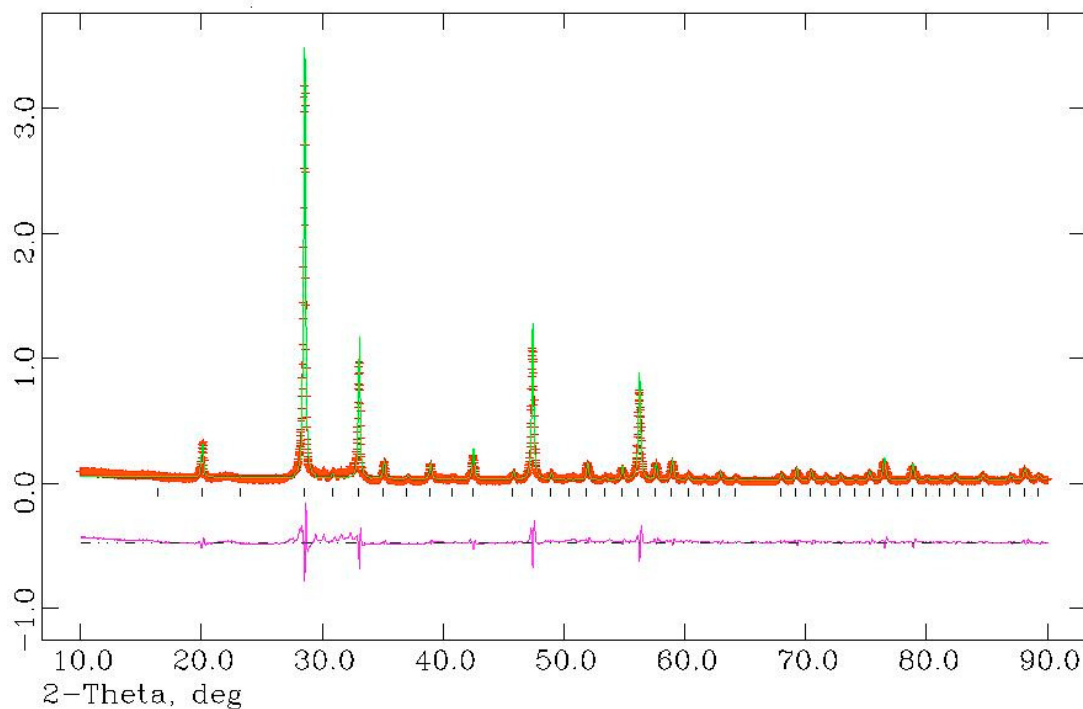


Figure 5.7 Unit cell refinement in CHEKCELL (mean square deviation for the refined unit cell parameters is lower than initial parameters).

#### 5.1.4 Full profile refinement – GSAS

GSAS (General Structure Analysis System) (Larson and Von Dreele 1994) is a program for performing Rietveld refinement on XRPD data. GSAS itself is a DOS environment application but a graphical user interface, EXPGUI, has recently been developed to assist in its use (Toby 2001). The essential factor with use of full profile refinement is that a close fit to the structure has already been found, which should prevent the program from becoming trapped in local minima. GSAS allows for refinement of the parameters discussed in chapter 2, namely the unit cell parameters, the atomic positions, peak asymmetry, peak profile, preferred orientation and temperature factors. At each stage of refinement a comparison between the experimental and calculated XRPD patterns is made by means of a difference line and a measure of fitness. Ideally only a few parameters should be refined at a time. GSAS is not an automated program and relies on some expertise on behalf of the user. This involves a visual inspection of the two patterns at each stage. For example, if all the peaks are displaced by the same amount there may be a zero error adjustment. If the 2 patterns are slightly out of scale the unit cell parameters may need refining. If the peak heights do not quite match then the atom positions can be adjusted. Asymmetry in the measured peaks can be modelled by adjusting the peak profile parameters. Figure 5.8 shows an example of a pattern where a close match has been achieved using GSAS.



*Figure 5.8 Histogram after refinement in GSAS.*

*Lines represent data as follows: experimental data is the series of horizontal ticks marking the wave envelope. Calculated pattern follows the same profile but as a solid line. Difference plot is shown by the lower line. Peak positions are shown by vertical tick marks. Intensity is in arbitrary units.*

The full crystal structure obtained from GSAS, consisting of the unit cell parameters, atom positions, occupancies and thermal parameters can then be put into a standard crystal structure file format such as CIF or SHELXL. This can then be used in crystal structure plotting software, examples of which are given in figures 7.15 to 7.17.

## **5.2 SOFTWARE FOR DSC-TG**

The Netzsch DSC is supplied with software for both recording and analysing data from the machine. The recording software allows input of sample information including identity and weight. It is also possible to use the in-built balance to weigh the sample. An instruction file can then be written which creates a heating programme for the machine.

The Netzsch software was used predominantly for identification of transition temperatures and mass changes due to oxidation and reduction. A typical example of the screen display is shown in figure 5.9.

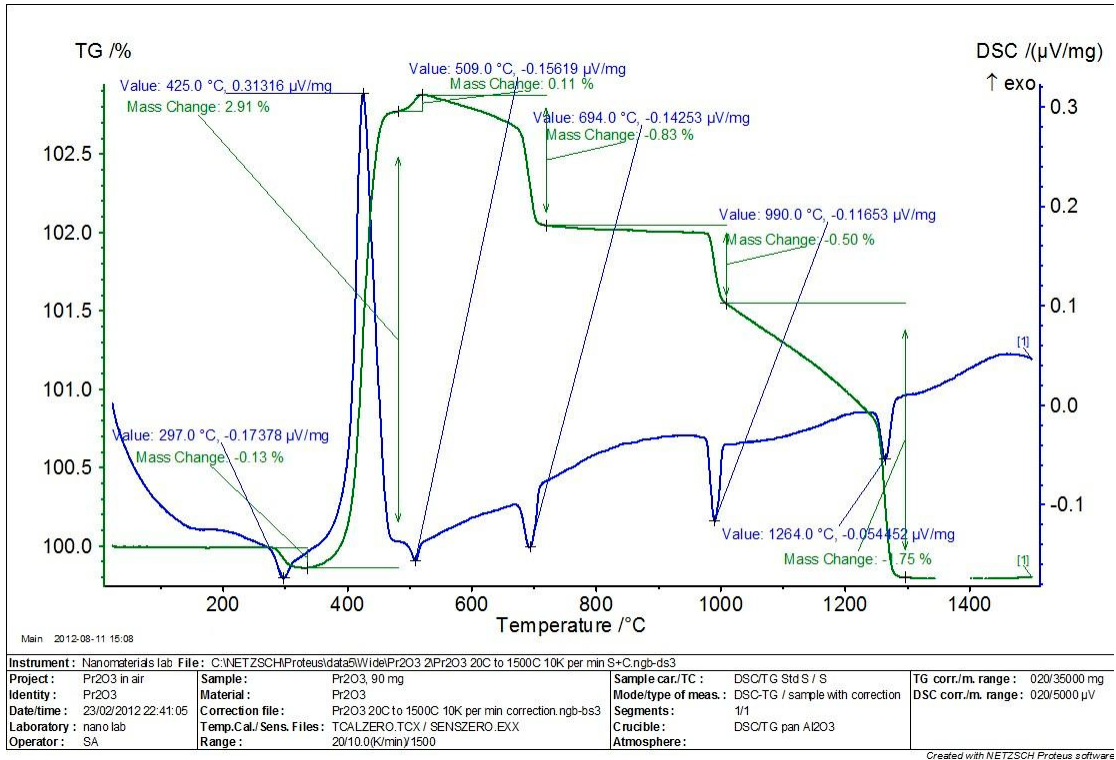


Figure 5.9 Combined DSC-TG plot. DSC plot shows sharp peaks; TG mass changes are highlighted..

From the image it is evident that the thermal events shown by the deflections in the DSC plot are all accompanied by changes in the weight of the sample. The sample represented is a metal oxide and the weight changes all show either oxidation or reduction.

## 6 SAMPLE PREPARATION AND EXPERIMENTAL CONDITIONS

This chapter contains all the experimental details for the work carried out in this thesis. The work consisted of three areas: ambient temperature XRPD on commercially-obtained samples and on the same samples following annealing; in-situ high-temperature XRPD; and DSC-TG. The work was carried out with the intention of demonstrating phase changes and determining kinetic data.

### 6.1 AMBIENT TEMPERATURE XRPD

Samples of polycrystalline material were obtained as follows:

| Material (sample number in parentheses) | Supplier      |
|---|---------------|
| (1) $\text{Eu}_2\text{O}_3$             | Alfa Aesar    |
| (2) $\text{Gd}_2\text{O}_3$             | Alfa Aesar    |
| (3) $\text{Yb}_2\text{O}_3$             | Alfa Aesar    |
| (4) $\text{Pr}_2\text{O}_3$             | Sigma-Aldrich |
| (5) $\text{Tb}_2\text{O}_3$             | Sigma-Aldrich |
| (6) $\text{Pr}_2\text{O}_3$             | Alfa Aesar    |
| (7) $\text{Yb}_2\text{O}_3$             | Alfa Aesar    |
| (8) $\text{Gd}_2\text{O}_3$             | Apollo        |
| (9) $\text{Nd}_2\text{O}_3$             | Alfa Aesar    |
| (10) $\text{Sm}_2\text{O}_3$            | Alfa Aesar    |
| (11) $\text{Eu}_2\text{O}_3$            | Alfa Aesar    |

*Table 6.1 Samples obtained for XRPD and DSC-TG.*

#### 6.1.1 Preliminary XRPD patterns on untreated samples

Each of the samples (1) to (5) and (9) to (11) was thoroughly ground with a pestle and mortar and XRPD data recorded using  $\text{Cu K}\alpha$  radiation according to the following table.

| Sample                              | Diffractometer | Range        | Step  | Time     | Standard |
|-------------------------------------|----------------|--------------|-------|----------|----------|
| (1) Eu <sub>2</sub> O <sub>3</sub>  | Siemens D500   | 10° - 90°    | 0.01° | 12 hours | Quartz   |
| (2) Gd <sub>2</sub> O <sub>3</sub>  | Siemens D500   | 10° - 90°    | 0.01° | 12 hours | Quartz   |
| (3) Yb <sub>2</sub> O <sub>3</sub>  | Siemens D500   | 10° - 90°    | 0.01° | 12 hours | Quartz   |
| (4) Pr <sub>2</sub> O <sub>3</sub>  | Bruker D8      | 10° - 92.43° | 0.01° | 12 hours | Corundum |
| (5) Tb <sub>2</sub> O <sub>3</sub>  | Bruker D8      | 10° - 92.43° | 0.01° | 12 hours | Corundum |
| (9) Nd <sub>2</sub> O <sub>3</sub>  | Bruker D8      | 10° - 92.43° | 0.01° | 1 hour   | Corundum |
| (10) Sm <sub>2</sub> O <sub>3</sub> | Bruker D8      | 10° - 92.43° | 0.01° | 1 hour   | Corundum |
| (11) Eu <sub>2</sub> O <sub>3</sub> | Bruker D8      | 10° - 92.43° | 0.01° | 1 hour   | Corundum |

*Table 6.2 XRPD schedule for samples.*

### 6.1.2 Sample annealing

Samples were annealed according to table 6.3.

| Sample                             | Furnace        | Temperature | Time    | Cooling     |
|------------------------------------|----------------|-------------|---------|-------------|
| (1) Eu <sub>2</sub> O <sub>3</sub> | Carbolite tube | 1334°C      | 1 hour  | Slow cooled |
| (2) Gd <sub>2</sub> O <sub>3</sub> | Carbolite tube | 1334°C      | 1 hour  | Slow cooled |
| (2) Gd <sub>2</sub> O <sub>3</sub> | Heraeus CL-G77 | 1500°C      | 1 hour  | Quenched    |
| (2) Gd <sub>2</sub> O <sub>3</sub> | Heraeus CL-G77 | 1500°C      | 7 hours | Quenched    |
| (3) Yb <sub>2</sub> O <sub>3</sub> | Heraeus CL-G77 | 1500°C      | 1 hour  | Quenched    |
| (3) Yb <sub>2</sub> O <sub>3</sub> | Heraeus CL-G77 | 1500°C      | 5 hours | Quenched    |
| (7) Yb <sub>2</sub> O <sub>3</sub> | Glass furnace  | 1800°C      | 5 hours | Quenched    |
| (8) Gd <sub>2</sub> O <sub>3</sub> | Netsch DSC     | 1500°C      | 7 hours | Quenched    |

*Table 6.3 Heating scheme for samples.*

### 6.1.3 Post-annealing XRPD

The annealed samples were reground and powder diffraction patterns taken according to the following table. Sample (8) was mounted on a 0.5mm glass capillary and exposed to 0.827130Å synchrotron radiation. For the remainder of the samples Cu K $\alpha$  radiation was used.

| Sample                             | Anneal            | Diffractometer   | Range         | Step   | Time | Standard |
|------------------------------------|-------------------|------------------|---------------|--------|------|----------|
| (1) Eu <sub>2</sub> O <sub>3</sub> | 1 hour at 1334°C  | Siemens D500     | 10° - 90°     | 0.01°  | 12h  | Quartz   |
| (2) Gd <sub>2</sub> O <sub>3</sub> | 1 hour at 1334°C  | Siemens D500     | 10° - 90°     | 0.01°  | 12h  | Quartz   |
| (2) Gd <sub>2</sub> O <sub>3</sub> | 1 hour at 1500°C  | Siemens D500     | 10° - 90°     | 0.01°  | 12h  | Quartz   |
| (2) Gd <sub>2</sub> O <sub>3</sub> | 7 hours at 1500°C | Siemens D500     | 10° - 90°     | 0.01°  | 22h  | Quartz   |
| (3) Yb <sub>2</sub> O <sub>3</sub> | 1 hour at 1500°C  | Siemens D500     | 10° - 90°     | 0.01°  | 12h  | Quartz   |
| (3) Yb <sub>2</sub> O <sub>3</sub> | 5 hours at 1500°C | Siemens D500     | 10° - 90°     | 0.01°  | 22h  | Quartz   |
| (7) Yb <sub>2</sub> O <sub>3</sub> | 5 hours at 1800°C | Bruker D8        | 10° - 92.43°  | 0.01°  | 12h  | Corundum |
| (8) Gd <sub>2</sub> O <sub>3</sub> | 7 hours at 1500°C | DLS beamline I11 | 0° - 149.999° | 0.001° | 1h   | Quartz   |

*Table 6.4 XRPD schedule for annealed samples.*

## 6.2 IN SITU HIGH-TEMPERATURE XRPD

### 6.2.1 Praseodymia ramp in air

Sample (4) Pr<sub>2</sub>O<sub>3</sub> was mounted in a PANalytical X'Pert diffractometer and XRPD data recorded at ambient temperature for  $2\theta$  between 18° and 60° in 0.03° steps. The whole scan took 15 minutes. The sample was then heated in air from 25°C to 800°C and back to 125°C, in 25°C steps. At each temperature an XRPD pattern was recorded from 18° to 60° of  $2\theta$ .

### 6.2.2 Praseodymia isothermal hold in air - phase change at 275°C

A sample of (4) Pr<sub>2</sub>O<sub>3</sub> was mounted in the PANalytical X'Pert diffractometer, held at 230°C in air and XRPD data recorded every 5 minutes from 18° to 60° of  $2\theta$  until the reactant material had converted. The process was repeated for new samples at 240°C, 250°C, 260°C, 270°C and 280°C.

### 6.2.3 Praseodymia quench in air

The 280°C sample from 6.2 was quenched to ambient temperature XRPD data recorded from 18° to 60° of  $2\theta$ .

## 6.3 DSC-TG

### 6.3.1 Praseodymia

#### 6.3.1.1 Wide run in nitrogen

4 Samples of (4) Pr<sub>2</sub>O<sub>3</sub> were heated in the Netzsch STA449 F3 DSC using a protective nitrogen gas of 20ml/min and a purge of nitrogen at 60ml/min. The DSC-TG measurements were made from 20°C to 1550°C at 10°C/min. The samples used in the third and fourth runs were subject to heating in an attempt to remove any bound gas prior to placing in the DSC, as follows:

| Sample                             | Run | Temperature | Time    |
|------------------------------------|-----|-------------|---------|
| (4) Pr <sub>2</sub> O <sub>3</sub> | 3   | 170°C       | 10 mins |
| (4) Pr <sub>2</sub> O <sub>3</sub> | 4   | 380°C       | 30 mins |

Table 6.5 Pre-DSC-TG heating schedule for sample (4).

#### 6.3.1.2 Wide run in air

2 samples of (6) Pr<sub>2</sub>O<sub>3</sub> were heated in the Netzsch STA449 F3 DSC in air. The DSC-TG measurements were made from 20°C to 1400°C at 10°C/min.

2 samples of the same material were heated in air from 20°C to 1400°C and back again to look for reversibility of reactions.

#### 6.3.1.3 Ramps in nitrogen

Seven temperature ramps were performed on (4) Pr<sub>2</sub>O<sub>3</sub> in nitrogen using a protective nitrogen gas of 20ml/min and a purge of nitrogen at 60ml/min. The DSC-TG measurements were made from 200°C to 600°C. The heating rates were 1, 2, 4, 7, 10, 15 and 20°C/min.

#### *6.3.1.4 Ramps in air*

Seven temperature ramps were performed on (6) Pr<sub>2</sub>O<sub>3</sub> in air. The DSC and TG measurements were made from 200°C to 500°C. The heating rates were 1, 2, 4, 7, 10, 15 and 20°C/min. A second set of ramps on (6) Pr<sub>2</sub>O<sub>3</sub> was performed at the above rates, from 20°C to 1500°C.

#### *6.3.1.5 Gas absorption*

Sample (6) Pr<sub>2</sub>O<sub>3</sub> was left exposed to the atmosphere for an extended time to determine what effect this had on the chemical structure. A DSC-TG measurement was carried out from 20°C to 1500°C at 10°C/min after 7, 78 and 85 days respectively.

### *6.3.2 Terbia*

#### *6.3.2.1 Wide run in nitrogen*

2 samples of (5) Tb<sub>2</sub>O<sub>3</sub> were heated in the Netzsch STA449 F3 DSC using a protective nitrogen gas of 20ml/min and a purge of nitrogen at 60ml/min. The DSC-TG measurements were made from 20°C to 1550°C at 10°C/min. 1550°C represents the temperature limit of the instrument. The phase diagram indicates a cubic to monoclinic phase transition at about 1600°C. The purpose of this experiment was to determine whether the transition could be induced below this temperature. However, nothing was seen in the DSC data to warrant further mention in the results section. This indicates that the transition is indeed beyond the range of the instrument.

## **7 RESULTS FROM X-RAY POWDER DIFFRACTION**

This chapter contains all the XRPD work carried out on  $\text{PrO}_x$ ,  $\text{Nd}_2\text{O}_3$ ,  $\text{Sm}_2\text{O}_3$ ,  $\text{Eu}_2\text{O}_3$ ,  $\text{Gd}_2\text{O}_3$  and  $\text{Yb}_2\text{O}_3$ . The work had six aims, namely:

- (i) to establish the ambient phase(s);
- (ii) to induce phase changes by heating;
- (iii) to determine the non-ambient phases either in situ or after quenching;
- (iv) to perform kinetic measurements using in situ data;
- (v) to match phase changes against the published phase diagrams;
- (vi) and to note any discrepancies between this work and the published phase diagrams.

### **7.1 AMBIENT TEMPERATURE XRPD**

#### *7.1.1 Diffraction patterns*

The XRPD patterns recorded at ambient temperature are shown in figures 7.1 to 7.13 below.

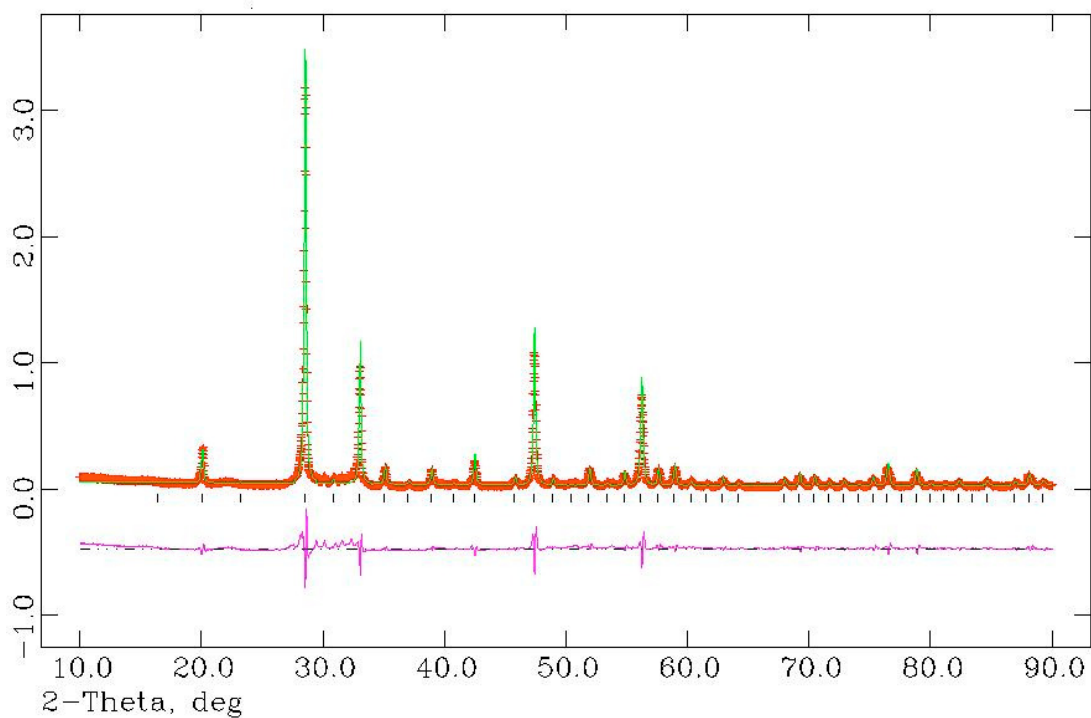


Figure 7.1 XRPD pattern for sample (1)  $\text{Eu}_2\text{O}_3$ . Intensity in arbitrary units.

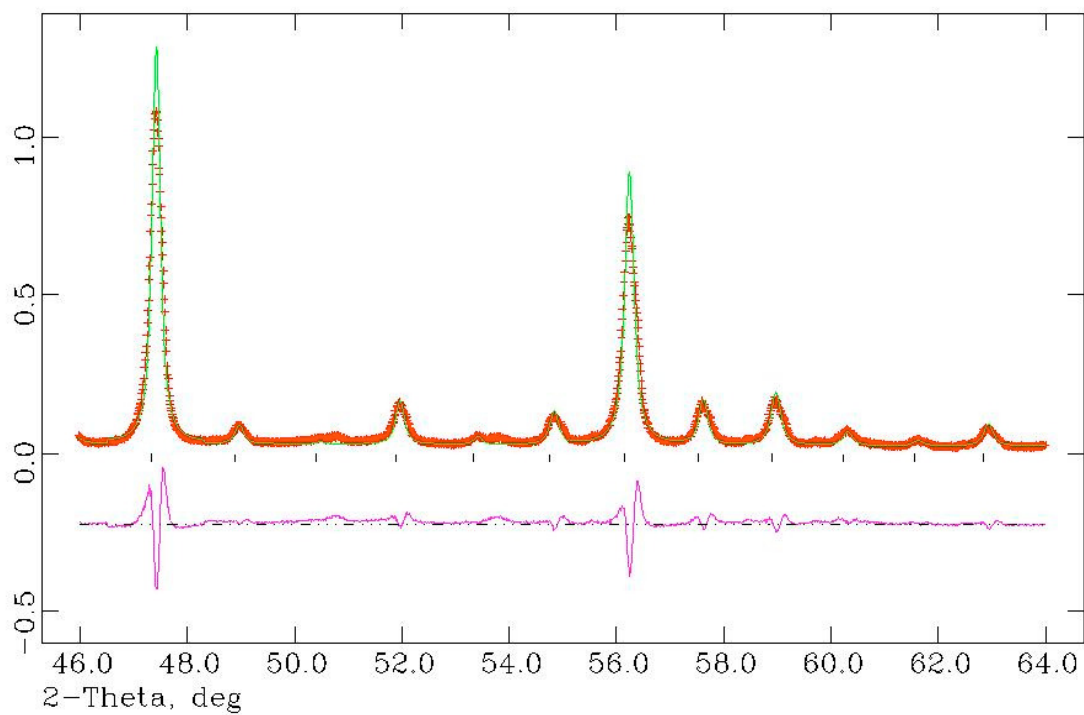


Figure 7.2 XRPD pattern for sample (1)  $\text{Eu}_2\text{O}_3$  showing the region between  $46^\circ$  and  $64^\circ$  in more detail.

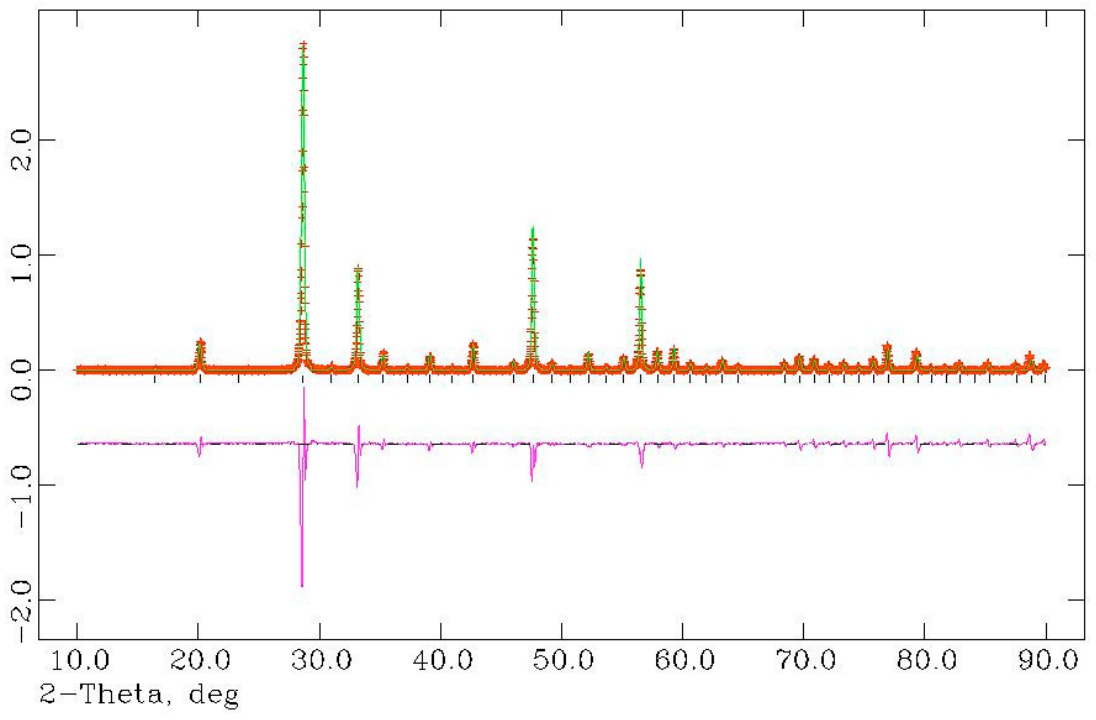


Figure 7.3 XRPD pattern for sample (2)  $Gd_2O_3$ .

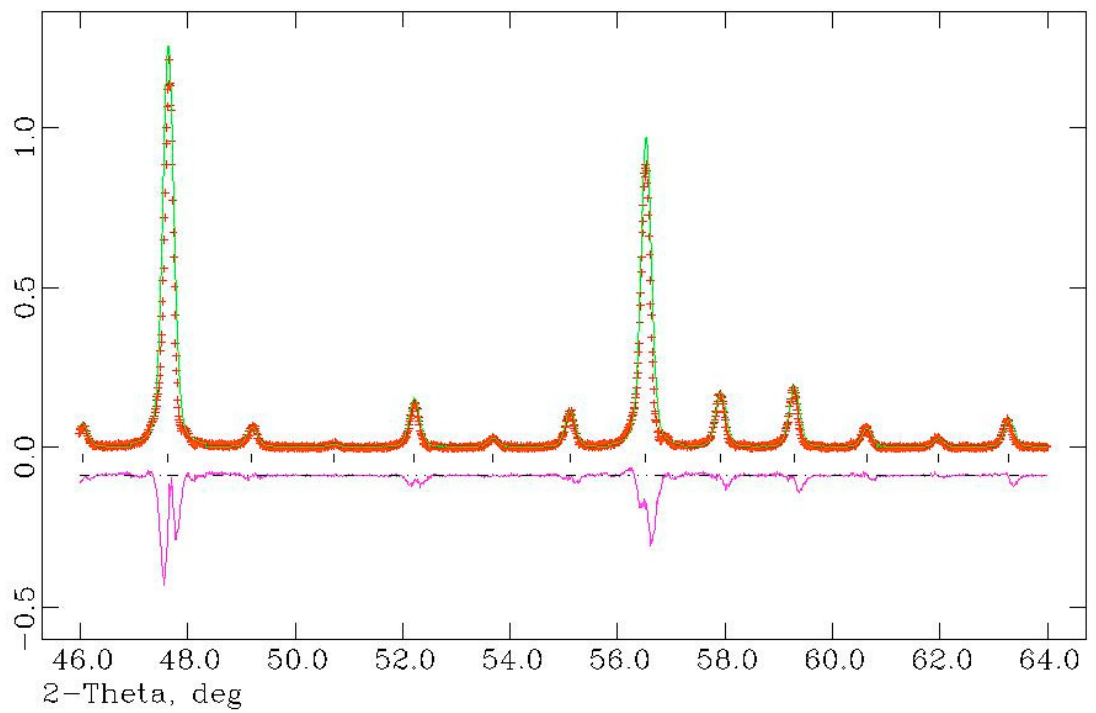


Figure 7.4 XRPD pattern for sample (2)  $Gd_2O_3$  showing the region between  $46^\circ$  and  $64^\circ$  in more detail.

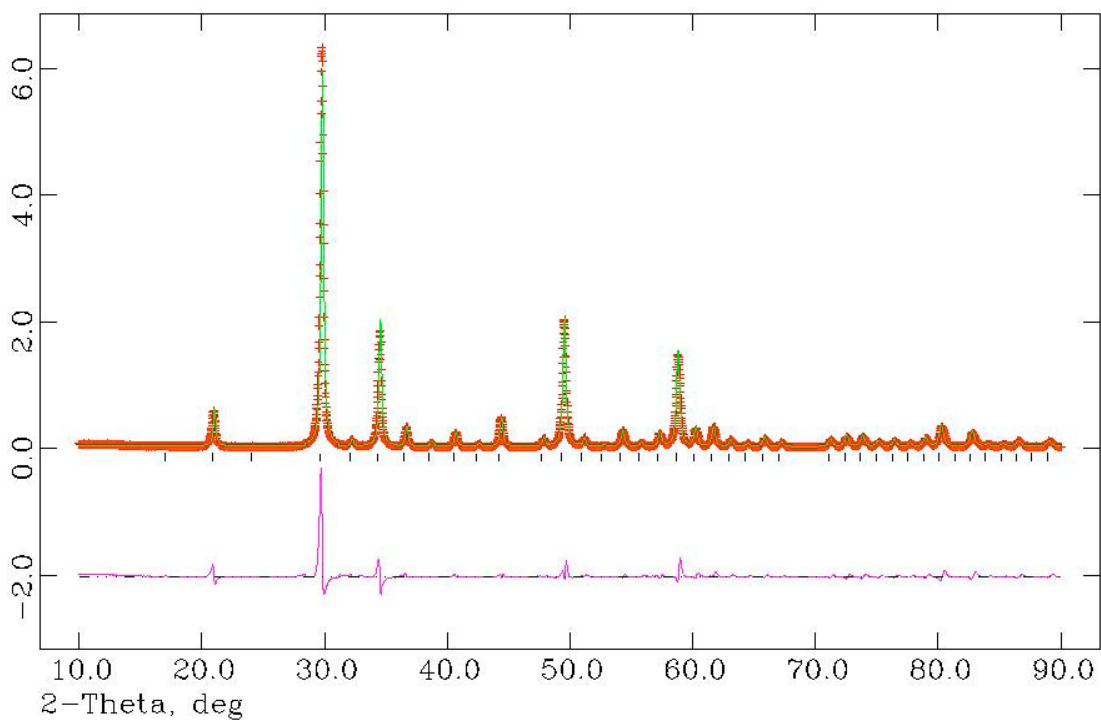


Figure 7.5 XRPD pattern for sample (3)  $\text{Yb}_2\text{O}_3$ .

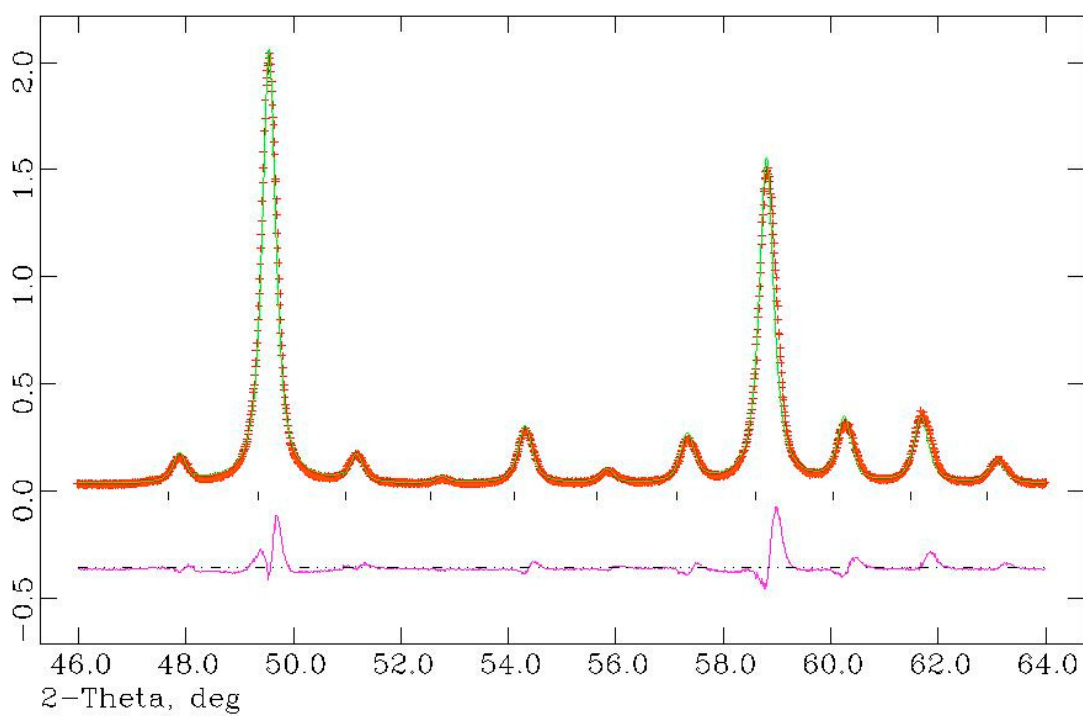


Figure 7.6 XRPD pattern for sample (3)  $\text{Yb}_2\text{O}_3$  showing the region between  $46^\circ$  and  $64^\circ$  in more detail.

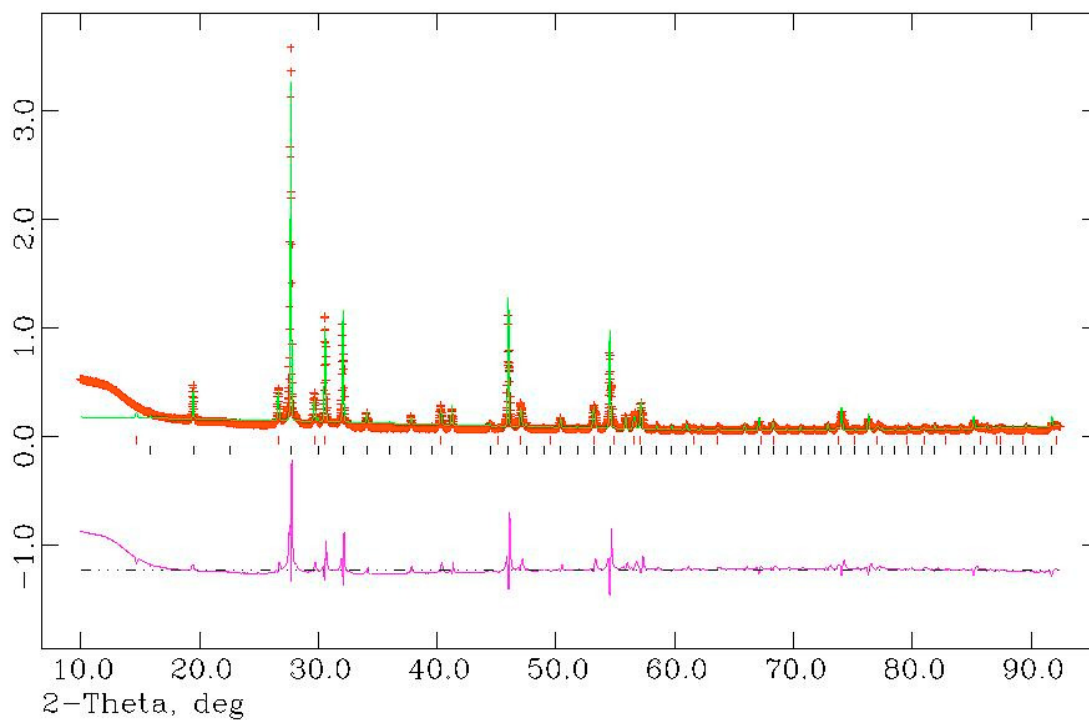


Figure 7.7 XRPD pattern for sample (4)  $\text{Pr}_2\text{O}_3$ . Upper tick marks show the hexagonal phase, lower tick marks cubic.

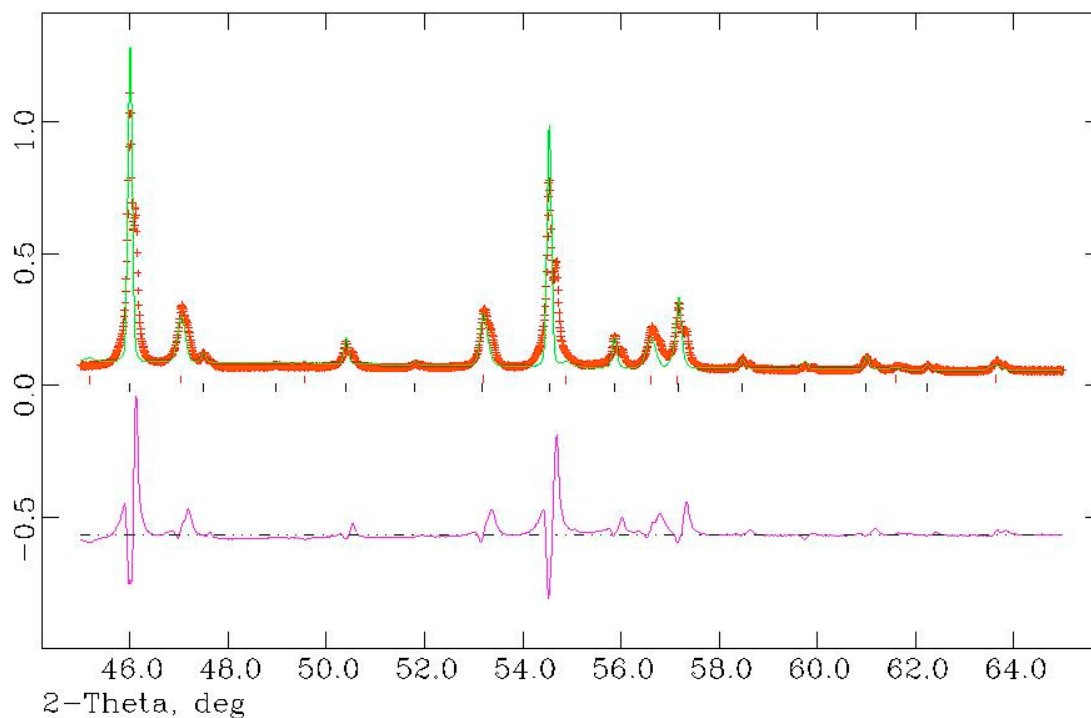


Figure 7.8 XRPD pattern for sample (4)  $\text{Pr}_2\text{O}_3$  showing the region between  $46^\circ$  and  $64^\circ$  in more detail.

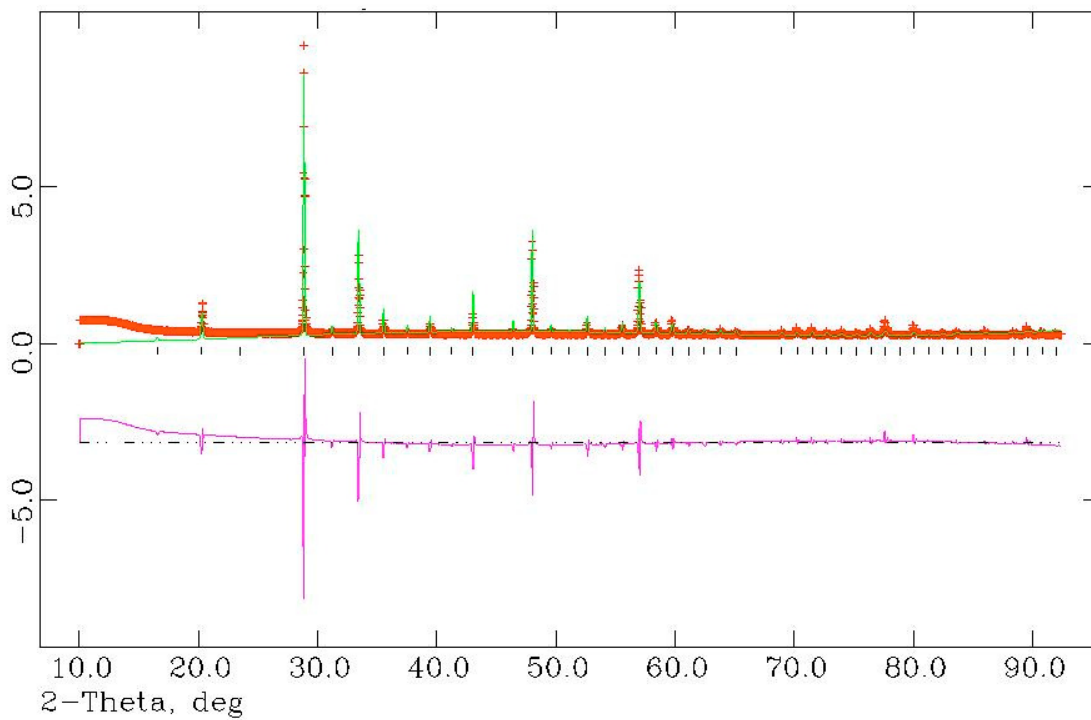


Figure 7.9 XRPD pattern for sample (5)  $Tb_2O_3$

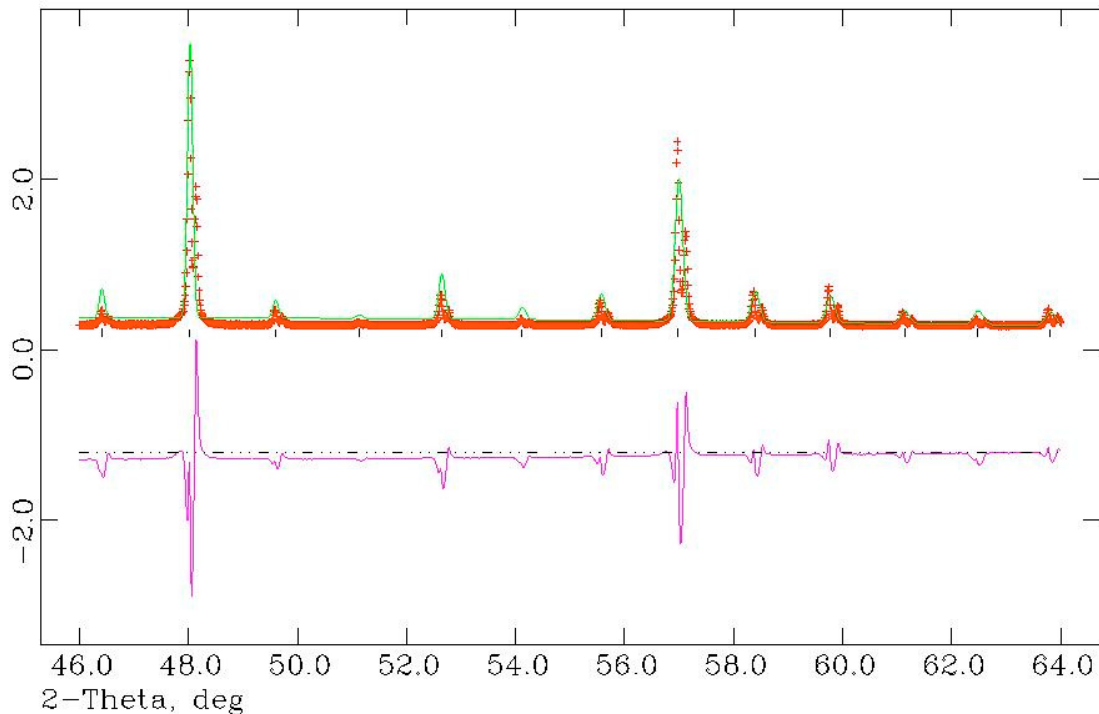


Figure 7.10 XRPD pattern for sample (5)  $Tb_2O_3$  showing the region between  $46^\circ$  and  $64^\circ$  in more detail. Tick marks show reflections from both  $Cu\ K\alpha_1$  and  $K\alpha_2$  radiation.

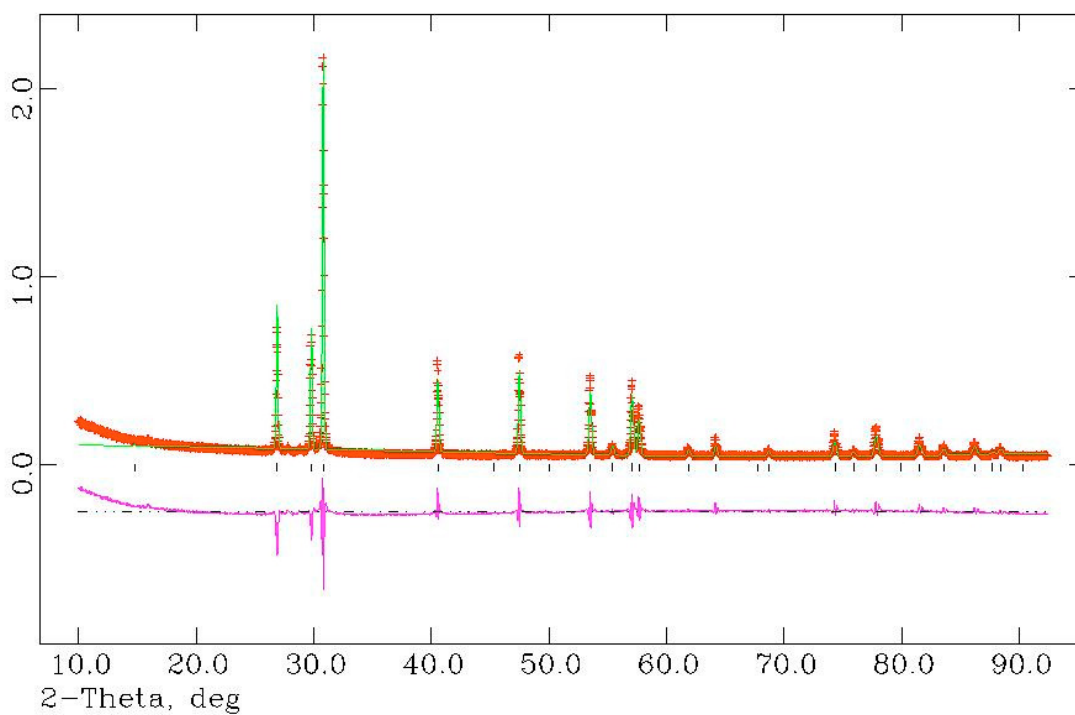


Figure 7.11 XRPD pattern for sample (9)  $\text{Nd}_2\text{O}_3$ .

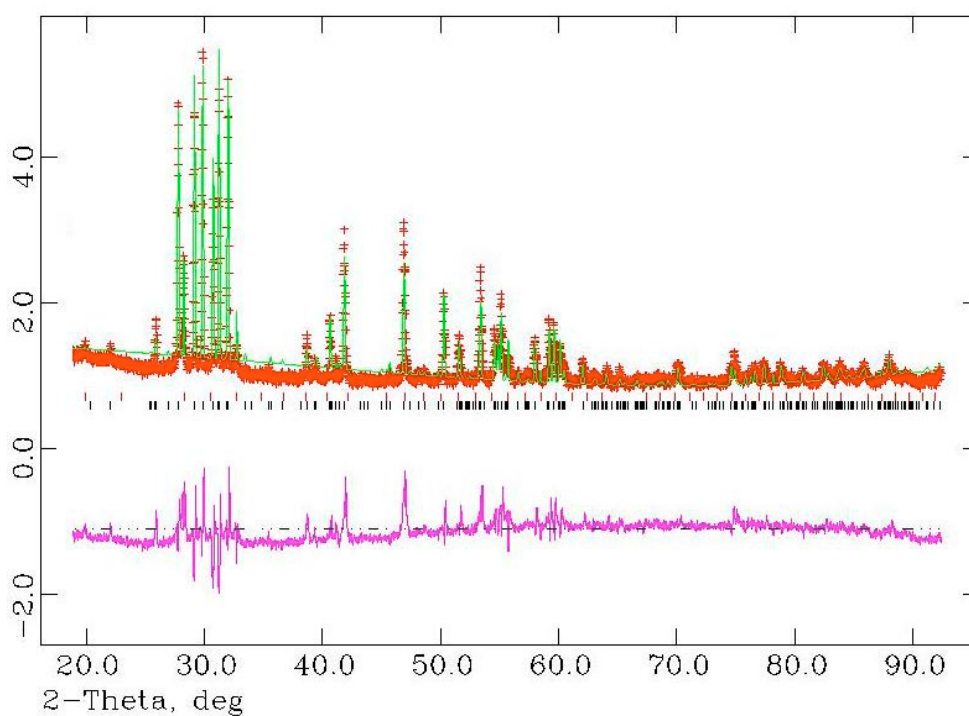


Figure 7.12 XRPD pattern for sample (10)  $\text{Sm}_2\text{O}_3$ . Upper tick marks show the cubic phase, lower tick marks monoclinic.

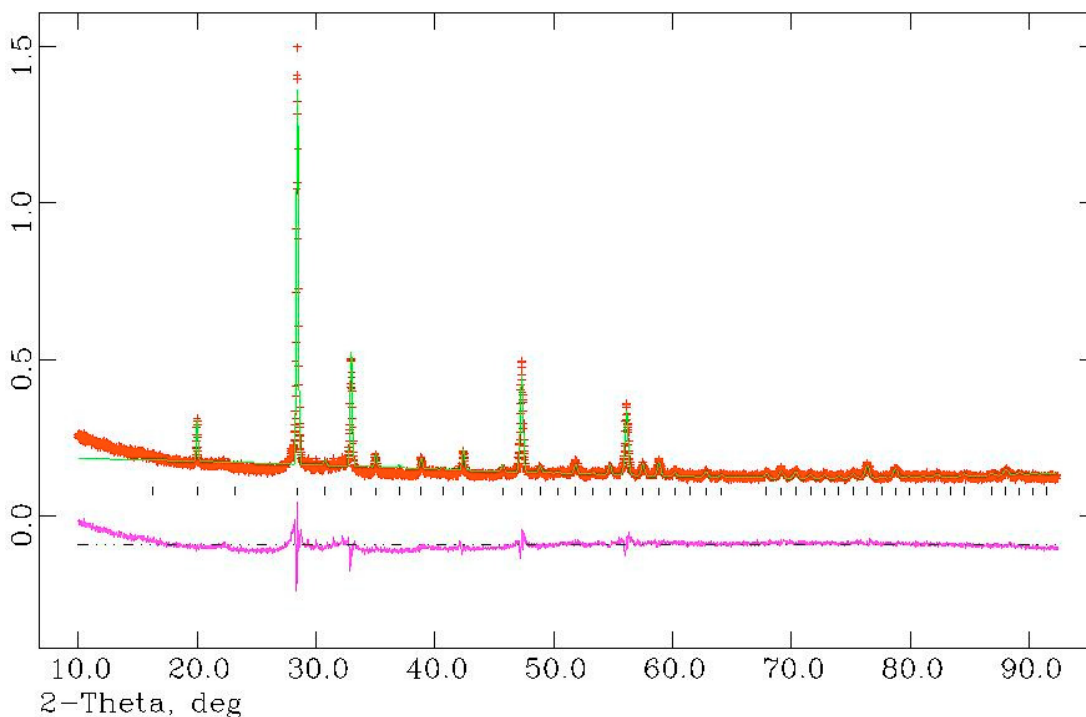


Figure 7.13 XRPD pattern for sample (11)  $\text{Eu}_2\text{O}_3$ .

### 7.1.2 Ambient temperature cell types

The unit cell parameters for sample (1) to (5) and (9) to (11) are given in table 7.1 below.

| Sample | Material                | Phase          | Cell parameters (Å)  | Space group |
|--------|-------------------------|----------------|--|-------------|
| (1)    | $\text{Eu}_2\text{O}_3$ | Cubic          | $a = 10.860(2)$  | $Ia-3$      |
| (2)    | $\text{Gd}_2\text{O}_3$ | Cubic          | $a = 10.786(2)$  | $Ia-3$      |
| (3)    | $\text{Pr}_2\text{O}_3$ | Cubic 56%      | $a = 11.152(2)$  | $Ia-3$      |
|        |                         | Hexagonal 44%  | $a = 3.860(2)$<br>$c = 6.017(2)$   | $P-3m1$     |
| (4)    | $\text{Yb}_2\text{O}_3$ | Cubic          | $a = 10.437(2)$  | $Ia-3$      |
| (5)    | $\text{Tb}_2\text{O}_3$ | Cubic          | $a = 10.711(2)$  | $Ia-3$      |
| (9)    | $\text{Nd}_2\text{O}_3$ | Hexagonal      | $a = 3.828(2)$<br>$c = 5.996(2)$   | $P-3m1$     |
| (10)   | $\text{Sm}_2\text{O}_3$ | Monoclinic 97% | $a = 14.168(2),$<br>$b = 3.624(2),$<br>$c = 8.848(2),$<br>$\beta = 100.05^\circ$ | $C2/m$      |
|        |                         | Cubic 3%       | $a = 10.928(2)$  | $Ia-3$      |
| (11)   | $\text{Eu}_2\text{O}_3$ | Cubic          | $a = 10.860(2)$  | $Ia-3$      |

Table 7.1 Refined unit cell parameters for samples (1) to (5) and (9) to (11).

To reflect the lanthanide contraction, the following image shows unit cell parameter against atomic number for the cubic cells in table 7.1.

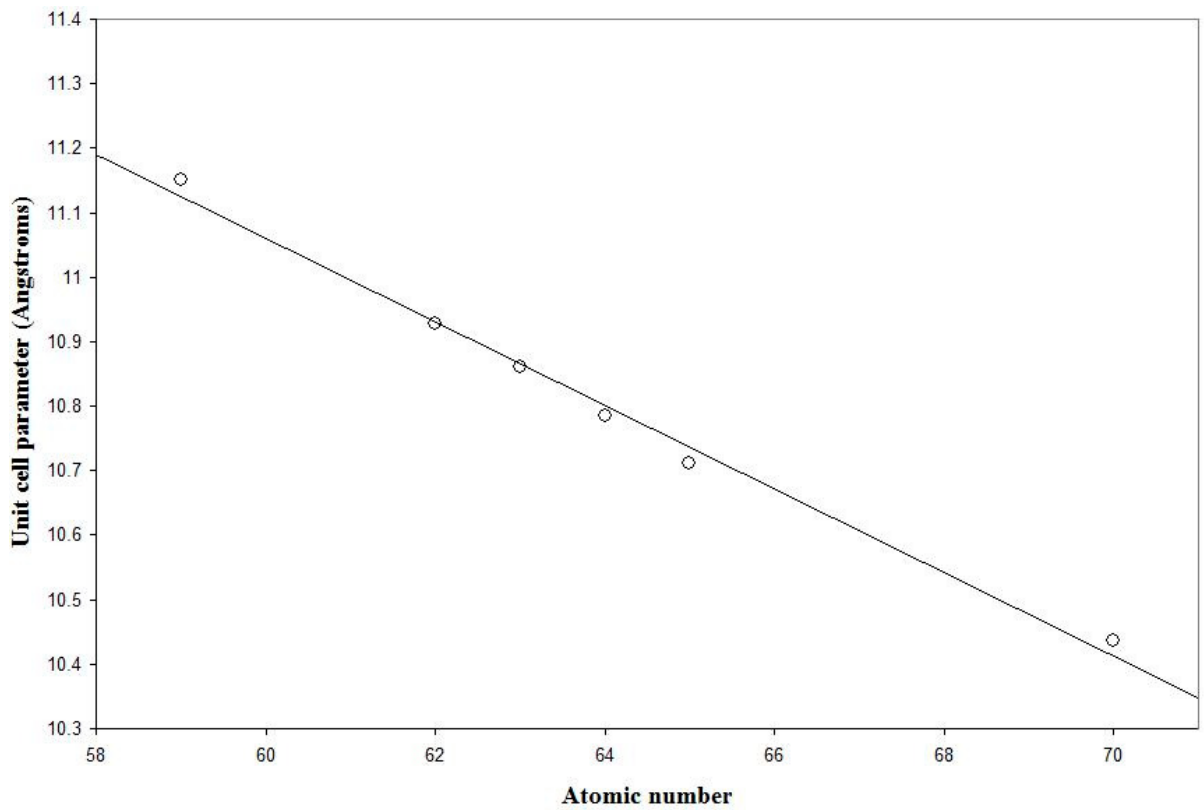


*Figure 7.14 Plot of unit cell parameter against atomic number for the C-type cell.*

*Error bars are within the data points.*

Analysis of the data in figure 7.14 showed that the unit cell parameter decreased on average by  $0.065\text{\AA}$  for each unit increase in atomic number.

### 7.1.3 Ambient temperature crystal structures

The cell contents after refinement for all phases are given below.

#### 7.1.3.1 The C-type phase

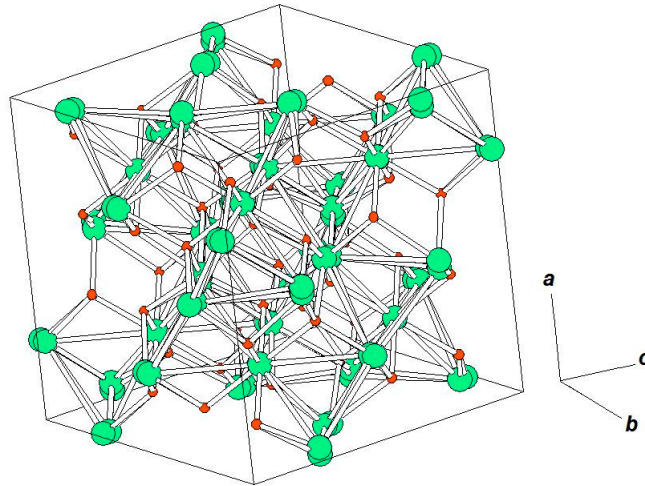


Figure 7.15 Crystal structure of the C-type cubic phase in space group  $Ia-3$ . Larger spheres represent the metallic atoms.

$\text{Pr}_2\text{O}_3$   $a = 11.152(2)\text{\AA}$ , sg  $Ia-3$ ,  $R_{\text{wp}} = 0.3271^*$

| Site | x        | y        | Z        | Occupancy |
|------|----------|----------|----------|-----------|
| Pr1  | 0.25     | 0.25     | 0.25     | 1         |
| Pr2  | 0.973872 | 0        | 0.25     | 1         |
| O1   | 0.364587 | 0.151367 | 0.364111 | 1         |

Table 7.2 Crystal structure of cubic  $\text{Pr}_2\text{O}_3$ . \*total value for the C and A mixed phase.

$\text{Eu}_2\text{O}_3$  sample (1)  $a = 10.860(2)\text{\AA}$ , sg  $Ia-3$ ,  $R_{\text{wp}} = 0.2151$

| Site | x       | y       | z       | Occupancy |
|------|---------|---------|---------|-----------|
| Eu1  | 0.25    | 0.25    | 0.25    | 1         |
| Eu2  | 0.96958 | 0       | 0.25    | 1         |
| O1   | 0.39050 | 0.15783 | 0.38611 | 1         |

Table 7.3 Crystal structure of cubic  $\text{Eu}_2\text{O}_3$ .

Eu<sub>2</sub>O<sub>3</sub> sample (11)  $a = 10.860(2)\text{\AA}$ , sg *Ia-3*,  $R_{\text{wp}} = 0.0741$

| Site | <i>x</i> | <i>y</i> | <i>z</i> | Occupancy |
|------|----------|----------|----------|-----------|
| Eu1  | 0.25     | 0.25     | 0.25     | 1         |
| Eu2  | 0.969358 | 0        | 0.25     | 1         |
| O1   | 0.396584 | 0.147428 | 0.399414 | 1         |

*Table 7.4 Crystal structure of cubic Eu<sub>2</sub>O<sub>3</sub>.*

Gd<sub>2</sub>O<sub>3</sub>  $a = 10.786(2)\text{\AA}$ , sg *Ia-3*,  $R_{\text{wp}} = 0.5869$

| Site | <i>x</i> | <i>Y</i> | <i>z</i> | Occupancy |
|------|----------|----------|----------|-----------|
| Gd1  | 0.25     | 0.25     | 0.25     | 1         |
| Gd2  | 0.969583 | 0        | 0.25     | 1         |
| O1   | 0.39107  | 0.15586  | 0.37911  | 1         |

*Table 7.5 Crystal structure of cubic Gd<sub>2</sub>O<sub>3</sub>.*

Tb<sub>2</sub>O<sub>3</sub>  $a = 10.711(2)\text{\AA}$ , sg *Ia-3*

| Site | <i>x</i> | <i>y</i> | <i>z</i> | Occupancy |
|------|----------|----------|----------|-----------|
| Tb1  | 0.25     | 0.25     | 0.25     | 1         |
| Tb2  | 0.958688 | 0        | 0.25     | 1         |
| O1   | 0.373145 | 0.156786 | 0.350571 | 1         |

*Table 7.6 Crystal structure of cubic Tb<sub>2</sub>O<sub>3</sub>.*

Yb<sub>2</sub>O<sub>3</sub>  $a = 10.437(2)\text{\AA}$ , sg *Ia-3(206)*,  $R_{\text{wp}} = 0.2164$

| Atom | <i>X</i> | <i>y</i> | <i>z</i> | Occupancy |
|------|----------|----------|----------|-----------|
| Yb1  | 0.25     | 0.25     | 0.25     | 1         |
| Yb2  | 0.96744  | 0        | 0.25     | 1         |
| O1   | 0.39349  | 0.15304  | 0.38678  | 1         |

*Table 7.7 Crystal structure of cubic Yb<sub>2</sub>O<sub>3</sub>.*

### 7.1.3.2 The B-type phase

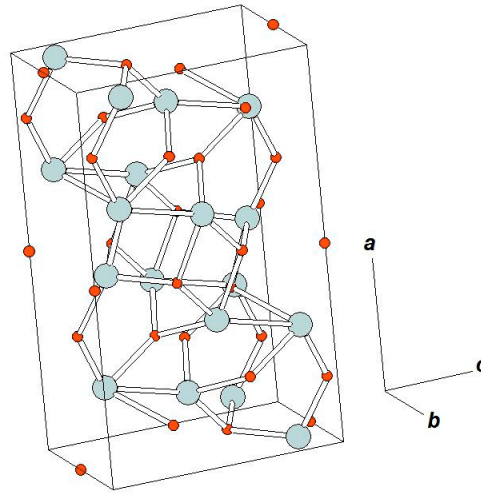


Figure 7.16 Crystal structure of the B-type monoclinic phase in space group  $C2/m$ . Larger spheres represent the metallic atoms.

$\text{Sm}_2\text{O}_3$   $a = 14.168(2)\text{\AA}$ ,  $b = 3.624(2)\text{\AA}$ ,  $c = 8.848(2)\text{\AA}$ ,  $\beta = 100.05^\circ$ , sg  $C2/m$ ,  $R_{\text{wp}} = 0.1700$

| Site | $x$      | $y$ | $z$      | Occupancy |
|------|----------|-----|----------|-----------|
| Sm1  | 0.132074 | 0.5 | 0.500535 | 1         |
| Sm2  | 0.193545 | 0.5 | 0.162728 | 1         |
| Sm3  | 0.472639 | 0.5 | 0.201875 | 1         |
| O1   | 0.101440 | 0   | 0.409000 | 1         |
| O2   | 0.423910 | 0.5 | 0.047833 | 1         |
| O3   | 0.399147 | 0.5 | 0.377914 | 1         |
| O4   | 0.537647 | 0   | 0.445264 | 1         |
| O5   | 0        | 0.5 | 0        | 1         |

Table 7.8 Crystal structure of monoclinic  $\text{Sm}_2\text{O}_3$ .

### 7.1.3.3 The A-type phase

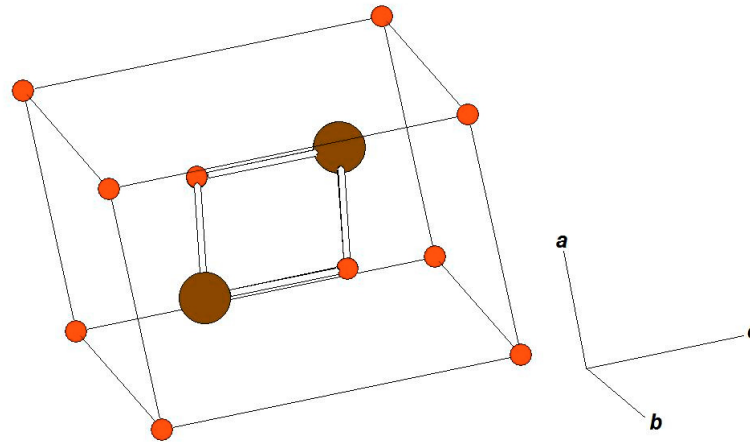


Figure 7.17 Crystal structure of the A-type hexagonal phase in space group  $P-3m1$ .

Larger spheres represent the metallic atoms.

$\text{Pr}_2\text{O}_3$   $a = 3.860(2)\text{\AA}$ ,  $c = 6.017(2)\text{\AA}$ , sg  $P-3m1$ ,  $R_{\text{wp}} = 0.3271^*$

| Site | x        | y        | z        | Occupancy |
|------|----------|----------|----------|-----------|
| Pr1  | 0.674413 | 0.325587 | 0.269493 | 1         |
| Pr2  | 0.719677 | 0.280324 | 0.610808 | 1         |
| O1   | 0        | 0        | 0        | 1         |

Table 7.9 Crystal structure of hexagonal  $\text{Pr}_2\text{O}_3$ . \*total value for the C and A mixed phase.

$\text{Nd}_2\text{O}_3$   $a = 3.828(2)\text{\AA}$ ,  $c = 5.996(2)\text{\AA}$ , sg  $P-3m1$ ,  $R_{\text{wp}} = 0.2143$

| Site | x        | y        | z        | Occupancy |
|------|----------|----------|----------|-----------|
| Nd1  | 0.341433 | 0.658566 | 0.238656 | 1         |
| Nd2  | 0.428594 | 0.714297 | 0.642839 | 1         |
| O1   | 0        | 0        | 0        | 1         |

Table 7.10 Crystal structure of hexagonal  $\text{Nd}_2\text{O}_3$ .

### 7.1.4 Discussion on ambient temperature results

To obtain the above results, the diffraction patterns obtained were run through the CRYSFIRE indexing suite, the indexing program GRAPHPRO and Chekcell to find the best match and space group. Full profile Rietveld refinement was performed using GSAS. The  $\text{Gd}_2\text{O}_3$  pattern was successfully indexed using CRYSFIRE. However, the patterns for  $\text{Eu}_2\text{O}_3$ ,  $\text{Pr}_2\text{O}_3$ ,  $\text{Yb}_2\text{O}_3$ ,  $\text{Tb}_2\text{O}_3$ ,  $\text{Nd}_2\text{O}_3$  and  $\text{Sm}_2\text{O}_3$  could not be indexed using

CRYSFIRE. GRAPHPRO was used to determine the unit cell parameters for sample (1)  $\text{Eu}_2\text{O}_3$ ,  $\text{Yb}_2\text{O}_3$ ,  $\text{Tb}_2\text{O}_3$  and sample (11)  $\text{Eu}_2\text{O}_3$ , the initial values being  $a = 10.828\text{\AA}$ ,  $10.405\text{\AA}$ ,  $10.699\text{\AA}$  and  $10.8232\text{\AA}$  respectively. Relaxing the  $2\theta$  tolerance in CRYSFIRE from the default of 0.04 degrees to 0.1 degrees meant that CRYSFIRE was able to locate solutions for  $\text{Eu}_2\text{O}_3$  ( $10.8379\text{\AA}$ ),  $\text{Yb}_2\text{O}_3$  ( $10.4068\text{\AA}$ ) and  $\text{Nd}_2\text{O}_3$  ( $a = 3.828\text{\AA}$ ,  $c = 5.994\text{\AA}$ ). Relaxing the tolerance further to 0.15 degrees meant the indexing of  $\text{Tb}_2\text{O}_3$  was successful ( $10.712\text{\AA}$ ). The space group in each case was found to be  $Ia-3$  via Chekcell. GRAPHPRO was unable to index the  $\text{Pr}_2\text{O}_3$  pattern.

As might be expected, the patterns for the cubic cells appear essentially the same for all samples, with just slight shifts on the  $2\theta$  axis reflecting the changes in unit cell parameter. With increasing atomic number of the rare earth metal, the unit cell parameter decreases according to the lanthanide contraction (shown in figure 7.14) and  $2\theta$  positions increase according to the Bragg equation. However, for  $\text{Eu}_2\text{O}_3$  there were a number of low-intensity lines around  $2\theta = 30^\circ$  which could not be explained by the cubic indexing. Since the phase diagram implied that no high-temperature phase existed at ambient temperature, these were at first thought to be due to an impurity. However, it will be shown later that this was due to the unexpected presence of the high-temperature modification.

The pattern for sample (3)  $\text{Pr}_2\text{O}_3$  was different to those of the other samples because it contained many more peaks. Analysis of the data showed that the sample consisted of both cubic and hexagonal phases, which is consistent with the phase diagram in chapter 1. Its cubic cell was estimated at  $11.2\text{\AA}$  by extrapolation from the other known cubic cells in the series. Taking the initial atom positions to be the same as for europia, GSAS was used to refine the cubic cell to a parameter of  $11.152\text{\AA}$ . Once the cubic lines in the pattern were identified, CRYSFIRE was run on the remaining lines to index the other cell contributing to the pattern. GSAS was again used to refine this cell to  $a = 3.860\text{\AA}$  and  $c = 6.017\text{\AA}$ . Analysis of the pattern from the refined phase fractions in GSAS showed there to be approximately 56% of the cubic phase and 44% of the hexagonal phase present.

From figure 1.5  $\text{Nd}_2\text{O}_3$  was provisionally expected to be cubic with a cell side around  $11.06\text{\AA}$  (found by interpolation), or perhaps mixed phase. However, the histogram showed there to be 100% hexagonal (high-temperature) phase present.

Again from figure 1.5,  $\text{Sm}_2\text{O}_3$  was expected to show cubic phase ( $10.93\text{\AA}$  by interpolation) with perhaps a small degree of monoclinic. However, the histogram showed there to be 97% monoclinic phase present. The supplier was contacted and stated that the crystal structure should be cubic. However, on further enquiry it was found that the sesquioxide had been generated via a multi-stage process, by dissolving the bastnaesite ore in acid, precipitating the carbonate and calcining to the oxide. As the material had been exposed to elevated temperature in its preparation, the monoclinic phase was already present in the commercial sample.

## **7.2 XRPD AFTER ANNEALING**

### *7.2.1 Diffraction patterns*

The XRPD patterns recorded after annealing are shown in figures 7.18 to 7.27 below. Rietveld refinements of the data were carried out where significant conversion to the high temperature phase had occurred (figures 7.18, 7.21, 7.22, 7.26, 7.27).

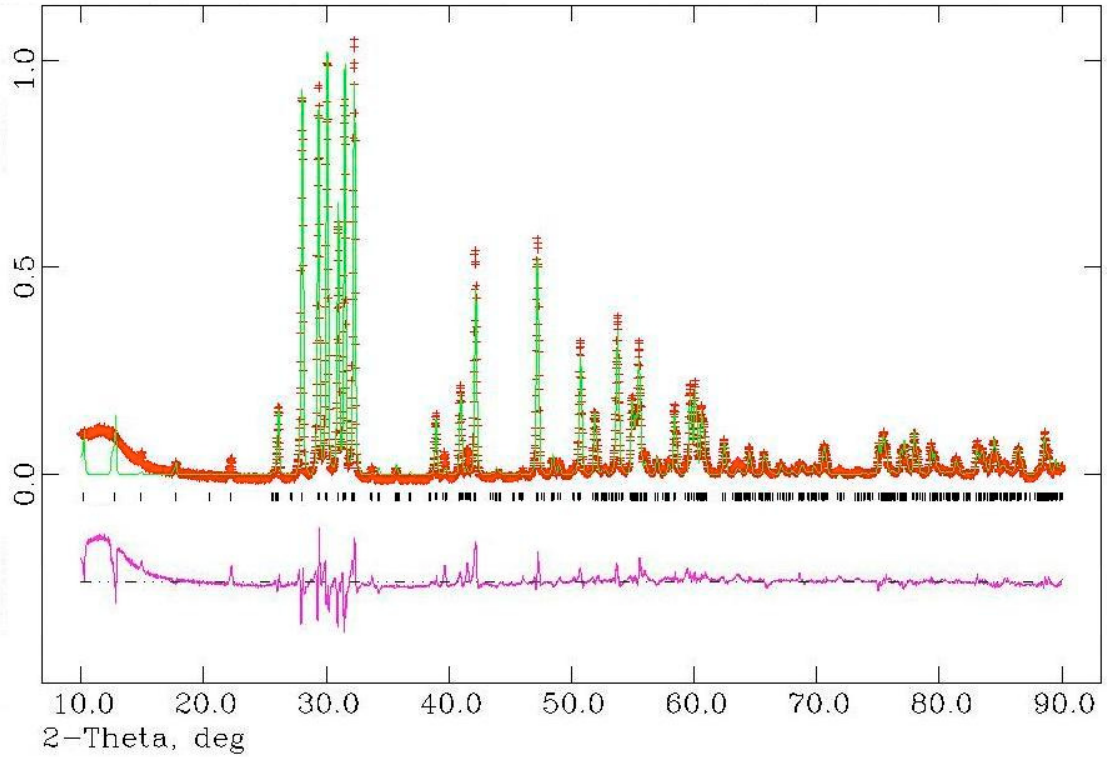


Figure 7.18 XRPD pattern for sample (1)  $\text{Eu}_2\text{O}_3$  following 1 hour anneal at  $1334^\circ\text{C}$  and slow cooling.

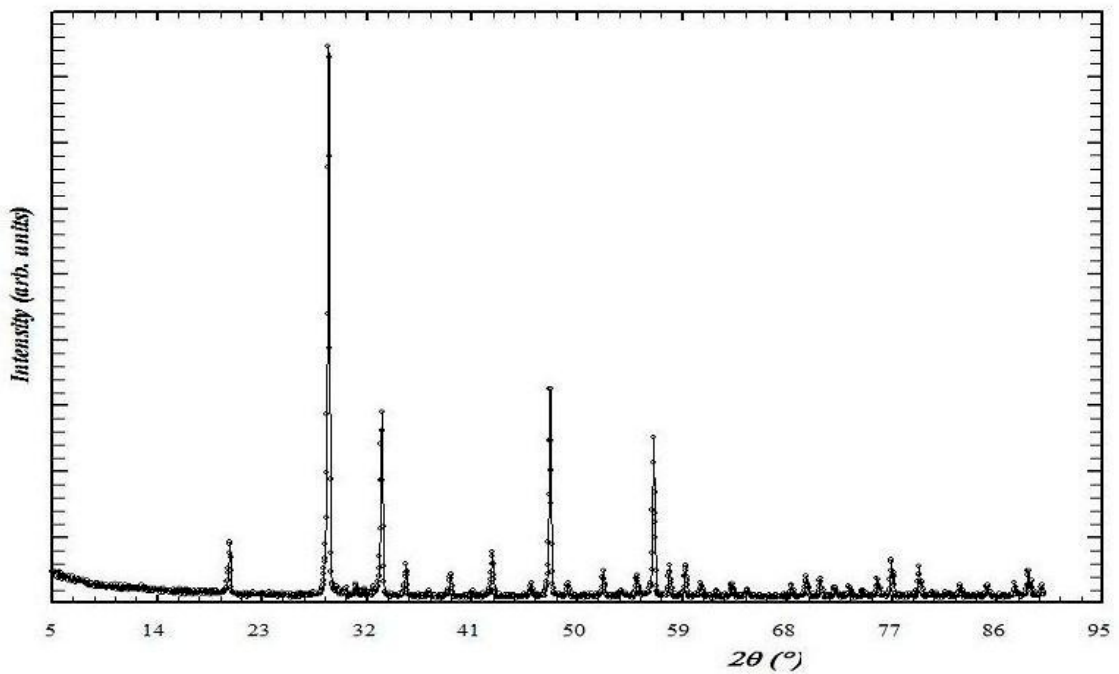


Figure 7.19 XRPD pattern for sample (2)  $\text{Gd}_2\text{O}_3$  following 1 hour anneal at  $1334^\circ\text{C}$  and slow cooling.

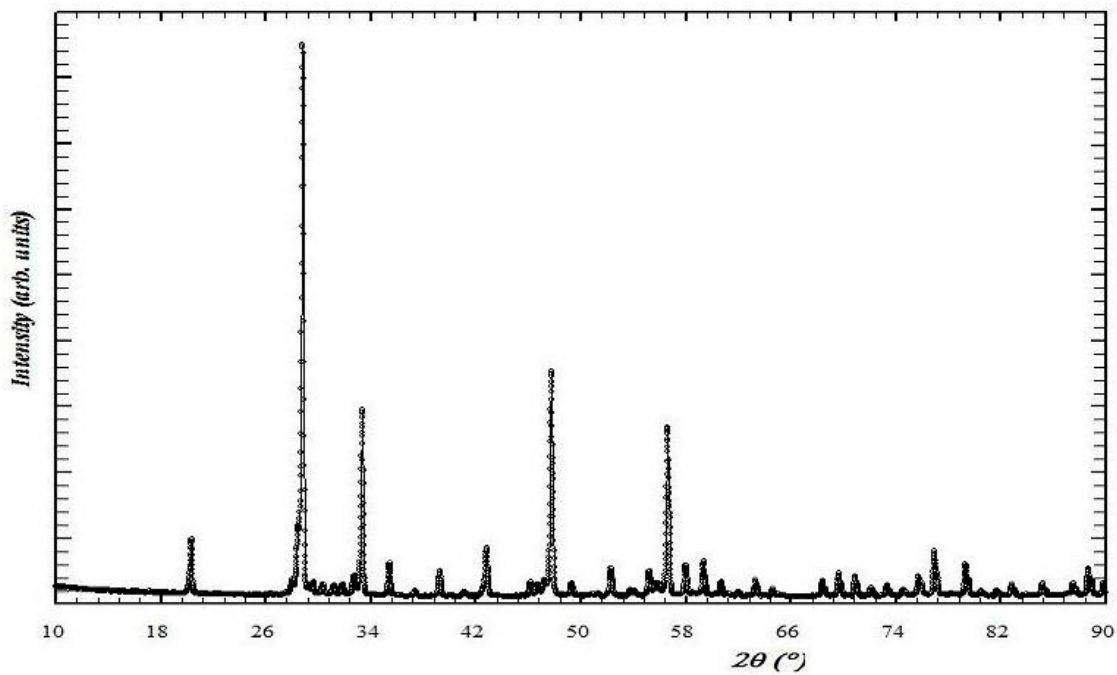


Figure 7.20 XRPD pattern for sample (2)  $Gd_2O_3$  following 1 hour anneal at  $1500^\circ C$  and quenching.

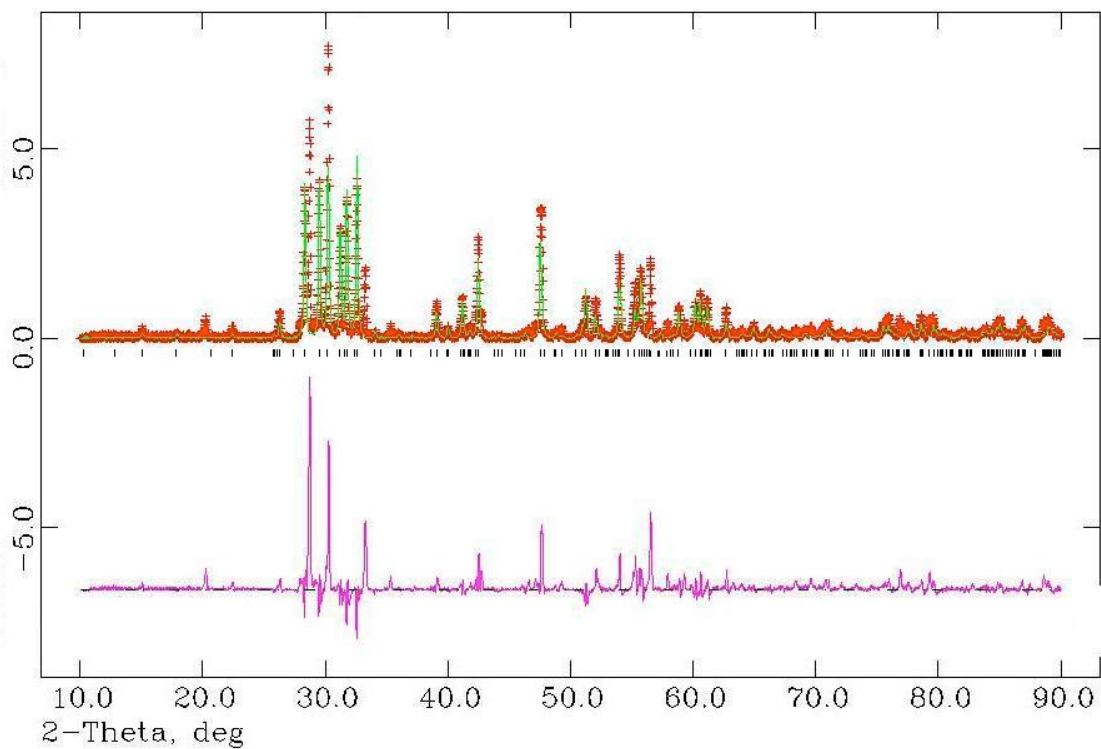


Figure 7.21 XRPD pattern for sample (2)  $Gd_2O_3$  following 7 hour anneal at  $1500^\circ C$  and quenching.

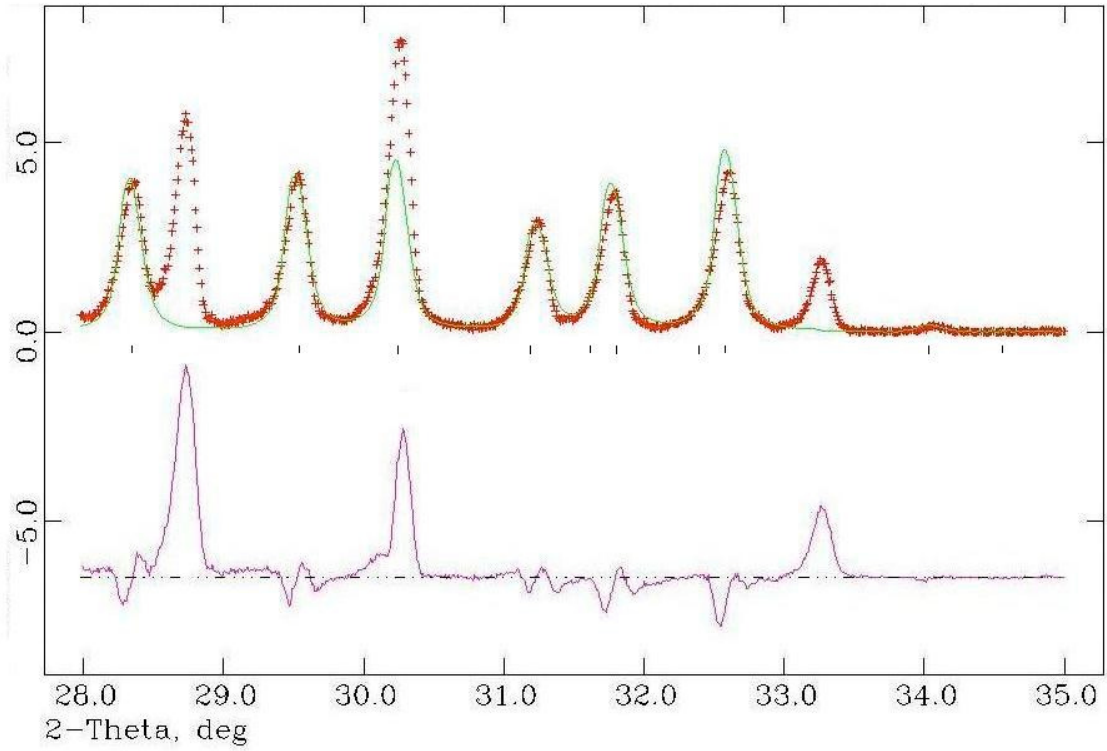


Figure 7.22 XRPD pattern for sample (2)  $Gd_2O_3$  following 7 hour anneal at  $1500^\circ C$  and quenching showing the region between  $28^\circ$  and  $35^\circ$  in more detail.

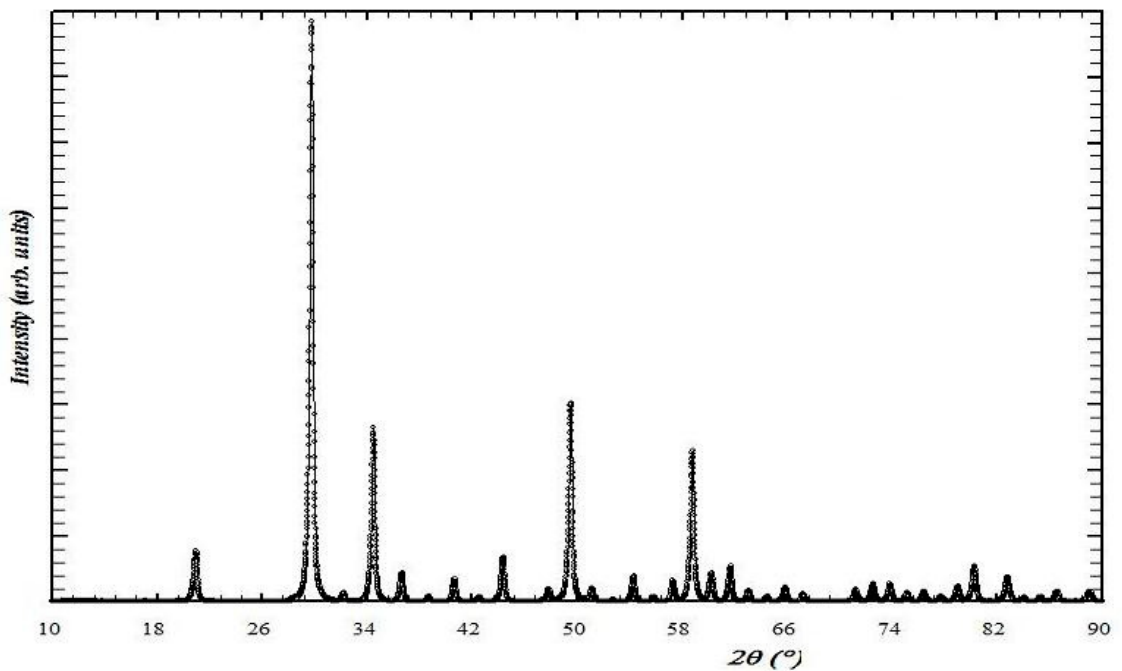


Figure 7.23 XRPD pattern for sample (3)  $Yb_2O_3$  following 1 hour anneal at  $1500^\circ C$  and quenching.

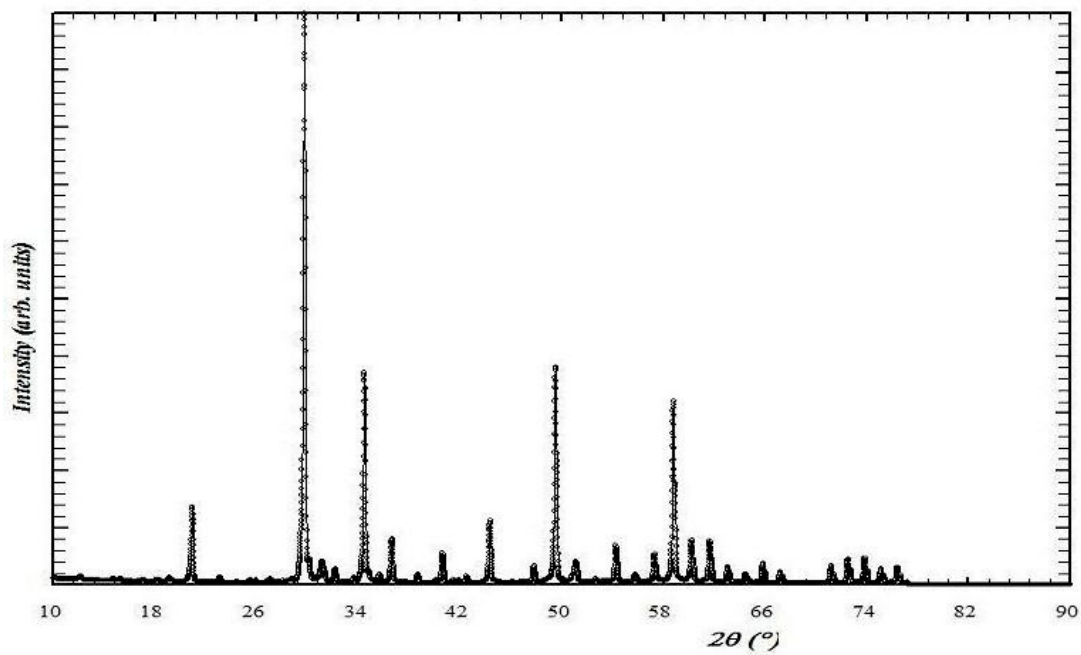


Figure 7.24 XRPD pattern for sample (3)  $\text{Yb}_2\text{O}_3$  following 5 hour anneal at  $1500^\circ\text{C}$  and quenching.

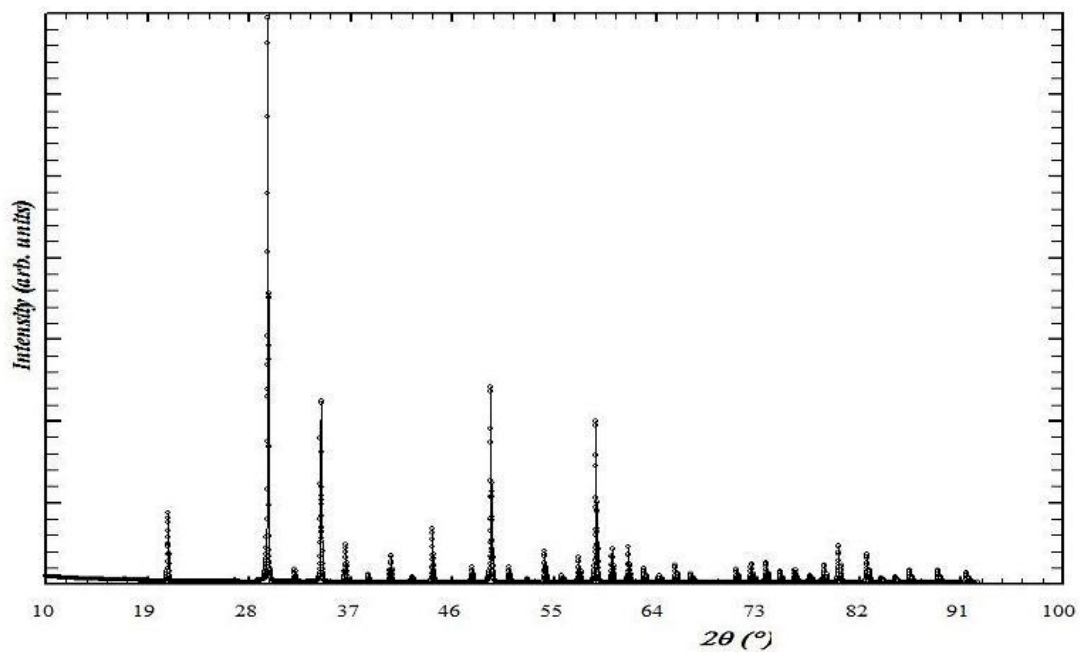


Figure 7.25 XRPD pattern for sample (7)  $\text{Yb}_2\text{O}_3$  following 5 hour anneal at  $1800^\circ\text{C}$  and quenching.

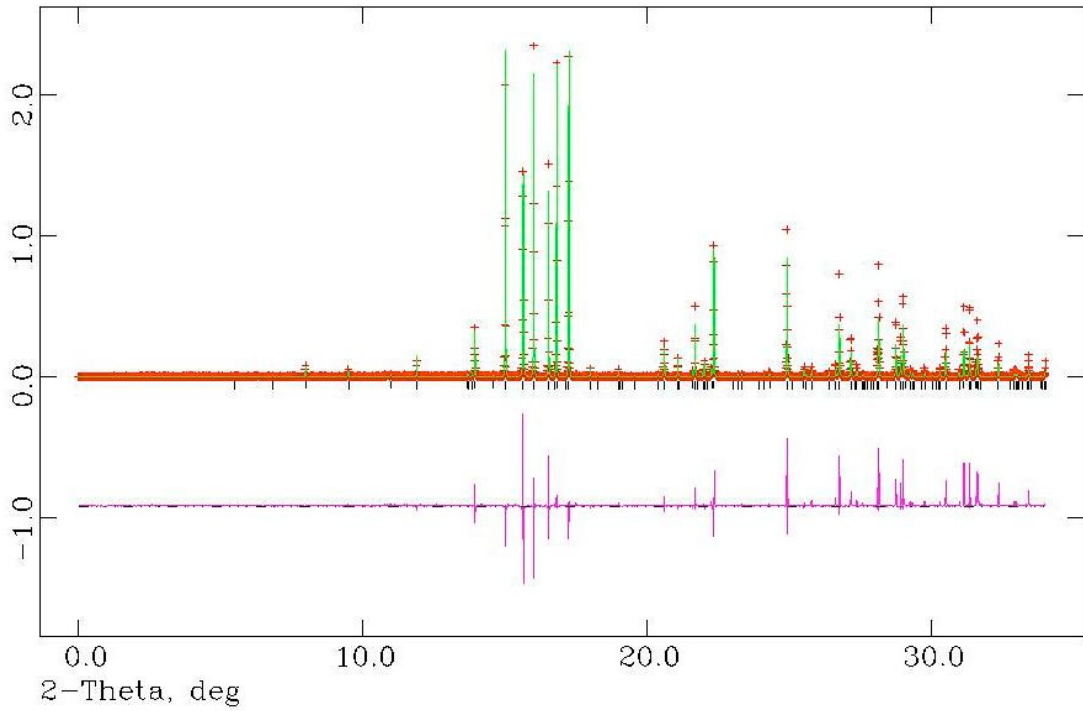


Figure 7.26 XRPD pattern for sample (8)  $Gd_2O_3$  following 7 hour anneal at  $1500^\circ\text{C}$  and quenching.

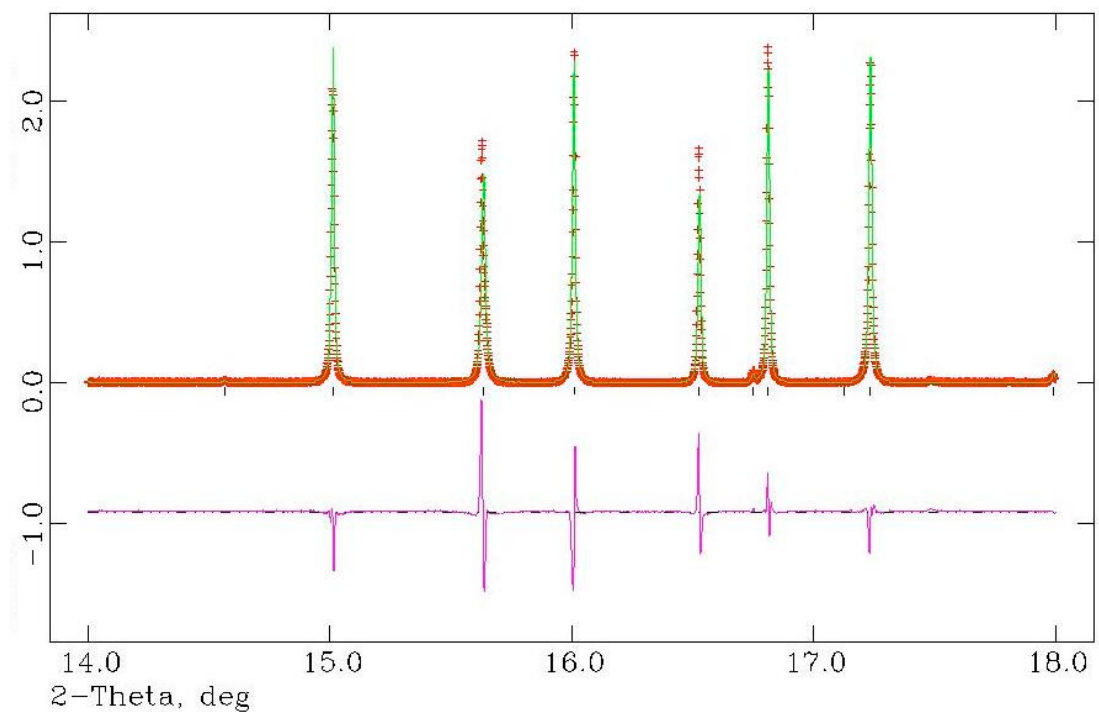


Figure 7.27 XRPD pattern for sample (8)  $Gd_2O_3$  following 7 hour anneal at  $1500^\circ\text{C}$  and quenching showing the region between  $14^\circ$  and  $18^\circ$  in more detail.

### 7.2.2 Cell types following annealing

The unit cell parameters for samples (1), (2), (3), (7) and (8) following annealing are given in table 7.11 below.

| Sample                             | Anneal            | Phase                        | Cell parameters (Å)  | Space group                |
|------------------------------------|-------------------|------------------------------|--|----------------------------|
| (1) Eu <sub>2</sub> O <sub>3</sub> | 1 hour at 1334°C  | Monoclinic 95%<br>(Cubic 5%) | $a = 14.110(2)$<br>$b = 3.602(2)$<br>$c = 8.808(2)$<br>$\beta = 100.06^\circ$                    | <i>C2/m</i>                |
| (2) Gd <sub>2</sub> O <sub>3</sub> | 1 hour at 1334°C  | Cubic 99%<br>(Monoclinic 1%) | $a = 10.860(2)$  | <i>Ia-3</i>                |
| (2) Gd <sub>2</sub> O <sub>3</sub> | 1 hour at 1500°C  | Cubic 99%<br>(Monoclinic 1%) | $a = 10.860(2)$  | <i>Ia-3</i>                |
| (2) Gd <sub>2</sub> O <sub>3</sub> | 7 hours at 1500°C | Monoclinic 97%<br>(Cubic 3%) | $a = 14.073(2)$<br>$b = 3.572(2)$<br>$c = 8.755(2)$<br>$\beta = 100.03^\circ$                    | <i>C2/m</i>                |
| (3) Yb <sub>2</sub> O <sub>3</sub> | 1 hour at 1500°C  | Cubic 99%<br>(Monoclinic 1%) | $a = 10.406(2)$  | <i>Ia-3</i>                |
| (3) Yb <sub>2</sub> O <sub>3</sub> | 5 hours at 1500°C | Cubic 99%<br>Monoclinic 1%   | $a = 10.406(2)$<br>$a = 13.740(2)$<br>$b = 3.400(2)$<br>$c = 8.593(2)$<br>$\beta = 100.12^\circ$ | <i>Ia-3</i><br><i>C2/m</i> |
| (7) Yb <sub>2</sub> O <sub>3</sub> | 5 hours at 1800°C | Cubic 100%                   | $a = 10.435(2)$  | <i>Ia-3</i>                |
| (8) Gd <sub>2</sub> O <sub>3</sub> | 7 hours at 1500°C | Monoclinic 100%              | $a = 14.0980(8)$<br>$b = 3.5750(8)$<br>$c = 8.7670(8)$<br>$\beta = 100.08^\circ$                 | <i>C2/m</i>                |

Table 7.11 Unit cell parameters for samples (1), (2), (3), (7) and (8) after annealing..

To reflect the lanthanide contraction, the following image shows unit cell parameters against atomic number for the monoclinic cells in tables 7.1 and 7.11.

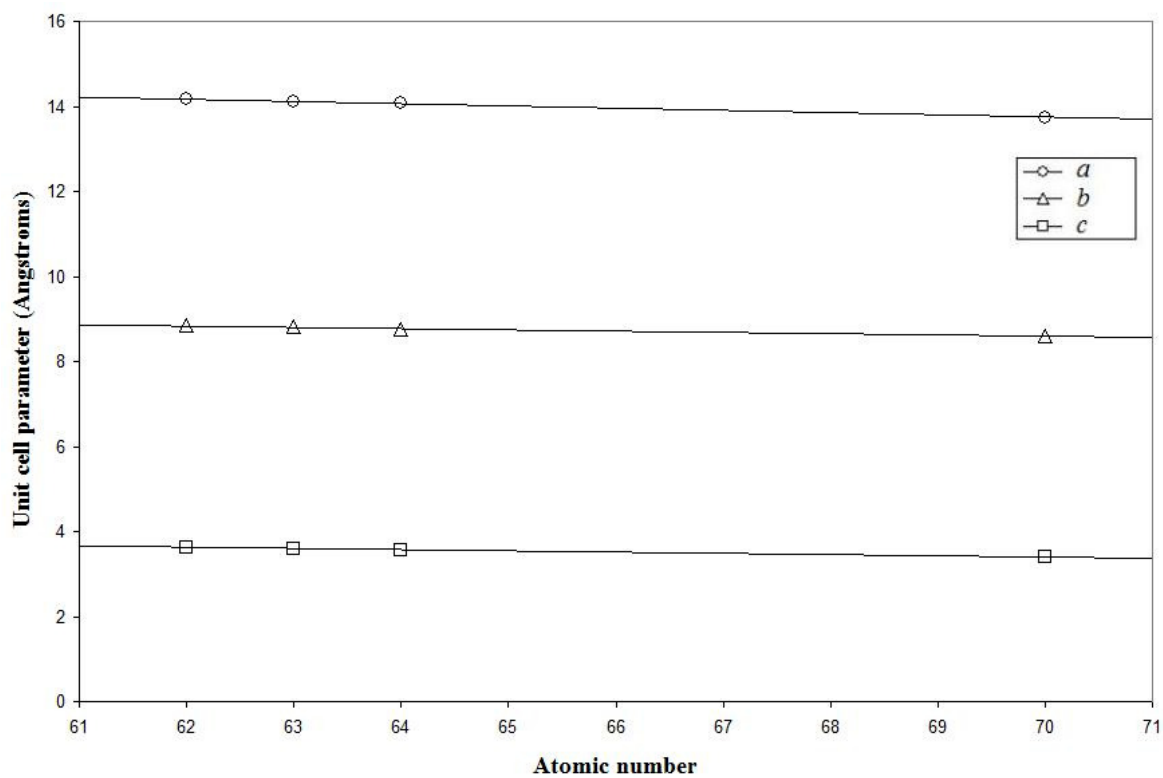


Figure 7.28 Plot of unit cell parameter against atomic number for the B-type cell.

Error bars are within the data points.

### 7.2.3 High-temperature crystal structures

The cell contents for all phases after refinement are given below. For completeness, the structures for gadolinia taken from both laboratory and synchrotron data are included.

### 7.2.3.1 The B-type phase

$\text{Eu}_2\text{O}_3$   $a = 14.110(2)\text{\AA}$ ,  $b = 3.602(2)\text{\AA}$ ,  $c = 8.808(2)\text{\AA}$ ,  $\beta = 100.06^\circ$ , sg  $C2/m$

| Site | x       | y   | z       | Occupancy |
|------|---------|-----|---------|-----------|
| Eu1  | 0.13325 | 0.5 | 0.49001 | 1         |
| Eu2  | 0.19061 | 0.5 | 0.14136 | 1         |
| Eu3  | 0.46897 | 0.5 | 0.19012 | 1         |
| O1   | 0.11556 | 0   | 0.28831 | 1         |
| O2   | 0.36952 | 0.5 | 0.00401 | 1         |
| O3   | 0.38693 | 0.5 | 0.40872 | 1         |
| O4   | 0.48730 | 0   | 0.36007 | 1         |
| O5   | 0       | 0.5 | 0       | 1         |

Table 7.12 Crystal structure of monoclinic  $\text{Eu}_2\text{O}_3$ .

$\text{Gd}_2\text{O}_3$   $a = 14.073(2)\text{\AA}$ ,  $b = 3.572(2)\text{\AA}$ ,  $c = 8.755(2)\text{\AA}$ ,  $\beta = 100.03^\circ$ , sg  $C2/m$ ,  $R_{\text{wp}} = 0.5147$

| Site | x       | y   | Z       | Occupancy |
|------|---------|-----|---------|-----------|
| Gd1  | 0.13229 | 0.5 | 0.48514 | 1         |
| Gd2  | 0.19332 | 0.5 | 0.13665 | 1         |
| Gd3  | 0.47041 | 0.5 | 0.18702 | 1         |
| O1   | 0.12246 | 0   | 0.32855 | 1         |
| O2   | 0.34297 | 0.5 | 0.00172 | 1         |
| O3   | 0.30732 | 0.5 | 0.36905 | 1         |
| O4   | 0.48348 | 0   | 0.33026 | 1         |
| O5   | 0       | 0.5 | 0       | 1         |

Table 7.13 Crystal structure of monoclinic  $\text{Gd}_2\text{O}_3$  from lab data.

$\text{Gd}_2\text{O}_3$   $a = 14.0980(2)\text{\AA}$ ,  $b = 3.5750(2)\text{\AA}$ ,  $c = 8.7670(2)\text{\AA}$ ,  $\beta = 100.08^\circ$ , sg  $C2/m$ ,  $R_{\text{wp}} = 0.4709$

| Site | x       | y   | z       | Occupancy |
|------|---------|-----|---------|-----------|
| Gd1  | 0.13485 | 0.5 | 0.48879 | 1         |
| Gd2  | 0.18928 | 0.5 | 0.13617 | 1         |
| Gd3  | 0.46561 | 0.5 | 0.18799 | 1         |
| O1   | 0.12638 | 0   | 0.28385 | 1         |
| O2   | 0.33025 | 0.5 | 0.04017 | 1         |
| O3   | 0.29291 | 0.5 | 0.37098 | 1         |
| O4   | 0.47671 | 0   | 0.35531 | 1         |
| O5   | 0       | 0.5 | 0       | 1         |

Table 7.14 Crystal structure of monoclinic  $\text{Gd}_2\text{O}_3$  from synchrotron data.

### 7.2.3.2 Praseodymia $\beta$ phase ( $Pr_6O_{11}$ )

$$a = 5.4790(2)\text{\AA}, \text{ sg } Fm-3m$$

| Site | <i>x</i> | <i>y</i> | <i>z</i> | Occupancy |
|------|----------|----------|----------|-----------|
| Pr1  | 0        | 0        | 0        | 1         |
| O1   | 0.25     | 0.25     | 0.25     | 0.915     |

Table 7.15 Crystal structure of  $Pr_6O_{11}$ .

### 7.2.3.3 Praseodymia $\iota$ phase ( $Pr_7O_{12}$ )

$$a = 10.3460(2)\text{\AA}, c = 9.6430(2)\text{\AA}, \text{ space group } R-3, R_{wp} = 0.2957$$

| Atom | <i>x</i> | <i>y</i> | <i>z</i> | Occupancy |
|------|----------|----------|----------|-----------|
| Pr1  | 0        | 0        | 0        | 1         |
| Pr2  | 0.121139 | 0.411048 | 0.006016 | 1         |
| O1   | 0.166206 | 0.280304 | 0.447745 | 1         |
| O2   | 0.249534 | 0.104719 | 0.083884 | 1         |

Table 7.16 Crystal structure of  $Pr_7O_{12}$ .

## 7.2.4 Discussion on annealed sample results

### 7.2.4.1 Europia

Indexing of the (1)  $Eu_2O_3$  pattern taken post-heating using CRYSFIRE/Chekcell gave a monoclinic cell with  $a = 14.110\text{\AA}$ ,  $b = 3.602\text{\AA}$ ,  $c = 8.808\text{\AA}$ ,  $\beta = 100.06^\circ$  and space group  $C2/m$ . The cubic pattern was found to have almost completely disappeared. Interestingly, the inexplicable lines present in the diffraction pattern from the cubic phase had intensified, indicating that the feature initially thought to be caused by impurity was due to the presence of a small proportion of monoclinic phase in the commercially-obtained material. Further analysis of the ambient temperature pattern in figure 7.1 using GSAS showed there to be approximately 95% of the monoclinic phase and 5% of the cubic phase present.

### 7.2.4.2 Gadolinia

The pattern for (2)  $Gd_2O_3$  obtained after 1 hour in the Carbolite furnace at  $1334^\circ\text{C}$  appeared virtually identical to that prior to annealing. However, there was a small but noticeable change in the appearance of a number of extremely low-intensity reflections around the  $2\theta = 30^\circ$  mark, as shown in figure 7.29 below.

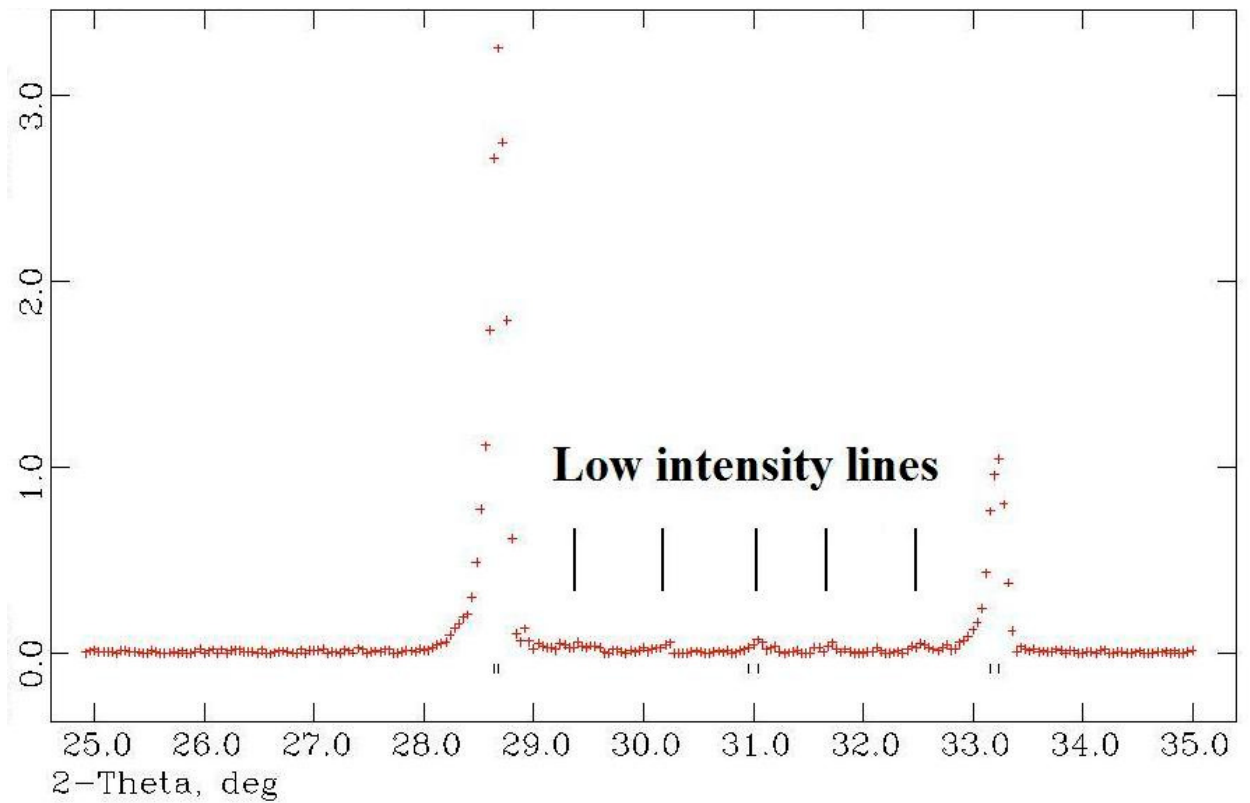


*Figure 7.29 Diffraction pattern of  $Gd_2O_3$  following 1 hour anneal at  $1334^\circ C$  showing low-intensity reflections due to the monoclinic phase.*

The pattern for  $Gd_2O_3$  obtained after 1 hour in the Heraeus furnace at  $1500^\circ C$  again appeared virtually identical to that prior to heating. As with the Carbolite furnace experiment, the same low-intensity reflections appeared around  $2\theta = 30^\circ$ . In addition, there were also two low intensity reflections around  $2\theta = 46.6^\circ$  and  $47.2^\circ$ . These are indicated in figure 7.30 below.

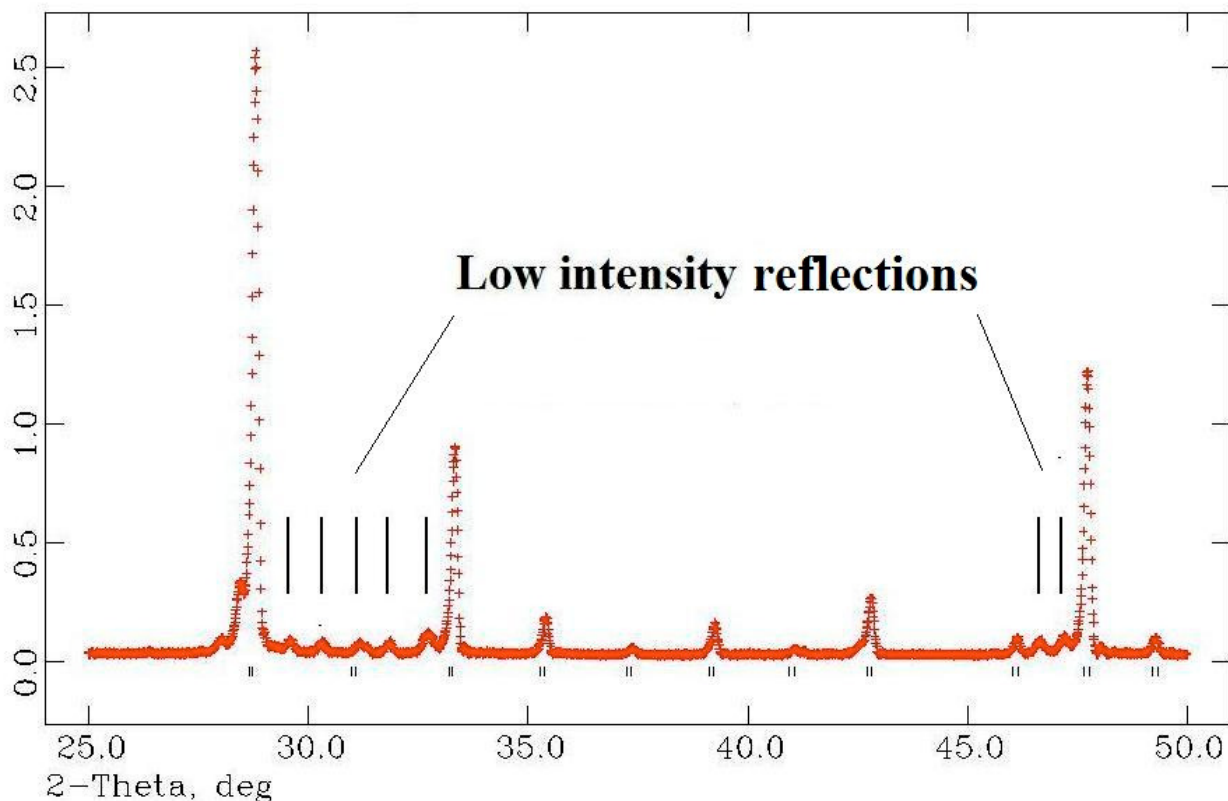


*Figure 7.30 Diffraction pattern of  $Gd_2O_3$  following 1 hour anneal at  $1500^\circ C$  showing low-intensity reflections due to the monoclinic phase.*

Because of the similarity with the europia cubic pattern it was assumed that these low intensity lines in the  $Gd_2O_3$  XRPD patterns were due to the presence of some monoclinic phase. These 5 lines were run through CRYSFIRE to see if anything significant was found. None of the indexing programs found a solution that seemed reasonable and approximating to that of monoclinic  $Eu_2O_3$ . The 5 lines were then put into Chekcell and a set of calculated reflections generated from the monoclinic  $Eu_2O_3$  unit cell parameters. These parameters were refined until the experimental and calculated lines converged. Thus a set of approximate unit cell parameters for monoclinic  $Gd_2O_3$  were found, namely  $a = 14.05\text{\AA}$ ,  $b = 3.52\text{\AA}$ ,  $c = 8.58\text{\AA}$ ,  $\beta = 100.19^\circ$ .

The pattern for  $Gd_2O_3$  obtained after 7 hours' annealing at  $1500^\circ C$  in the Heraeus furnace showed an almost complete conversion to the monoclinic phase. Figure 7.31 shows the original cubic pattern and the monoclinic pattern. The 4 lowest angle cubic lines still retained are marked. These lines were at  $2\theta = 20.28^\circ$ ,  $28.73^\circ$ ,  $33.23^\circ$  and

35.38°. Other reflections due to the cubic cell were also present at higher angles ( $2\theta = 56.55^\circ, 57.89^\circ, 59.26^\circ, 63.24^\circ, 68.36^\circ, 69.56^\circ, 76.91^\circ$  and  $88.59^\circ$ ).

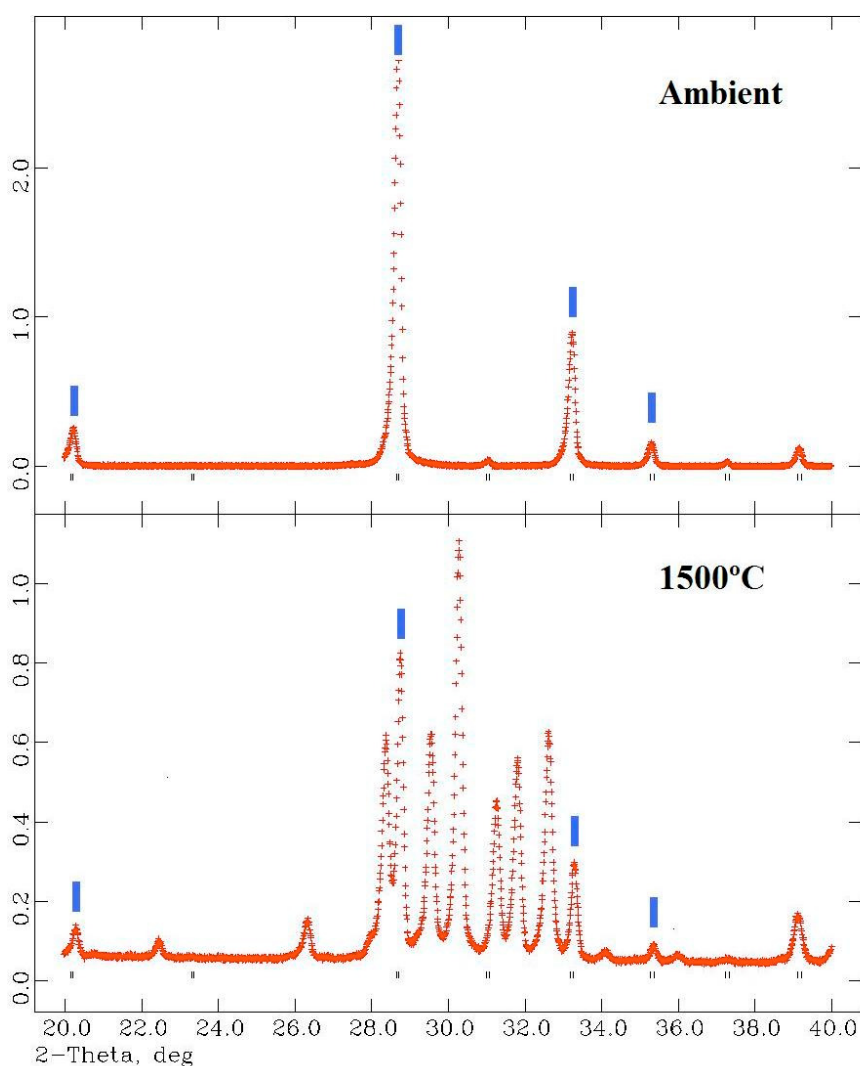


*Figure 7.31 Cubic (upper image) and monoclinic (following 7 hour anneal at 1500°C) patterns for  $Gd_2O_3$ . The 4 marks indicate the cubic lines which were retained after annealing.*

Indexing of the 7-hour annealed gadolinia pattern using CRYSFIRE/Chekcell was attempted, discarding the 4 cubic lines and allowing for a zero shift in the pattern of 0.2 degrees following the running of a quartz standard in the diffractometer. However, no results analogous to that of monoclinic europia were obtained. It was therefore decided to use the approximate unit cell parameters obtained above. These parameters proved too far from the solution for GSAS to converge. It was then decided to estimate the unit cell parameters of monoclinic  $Gd_2O_3$  by looking at the known cell parameters for its

neighbours samaria, europia and terbia and interpolating to find those for gadolinia. Figure 7.32 shows this process for estimating the value of the  $a$  parameter, although in practice this process was repeated for the other unit cell parameters. A similar method has been applied for the determination of the lutetia cell (Sun *et al* 2007) although in this reference the cell of B-type  $\text{Sm}_2\text{O}_3$  was used as the starting point.

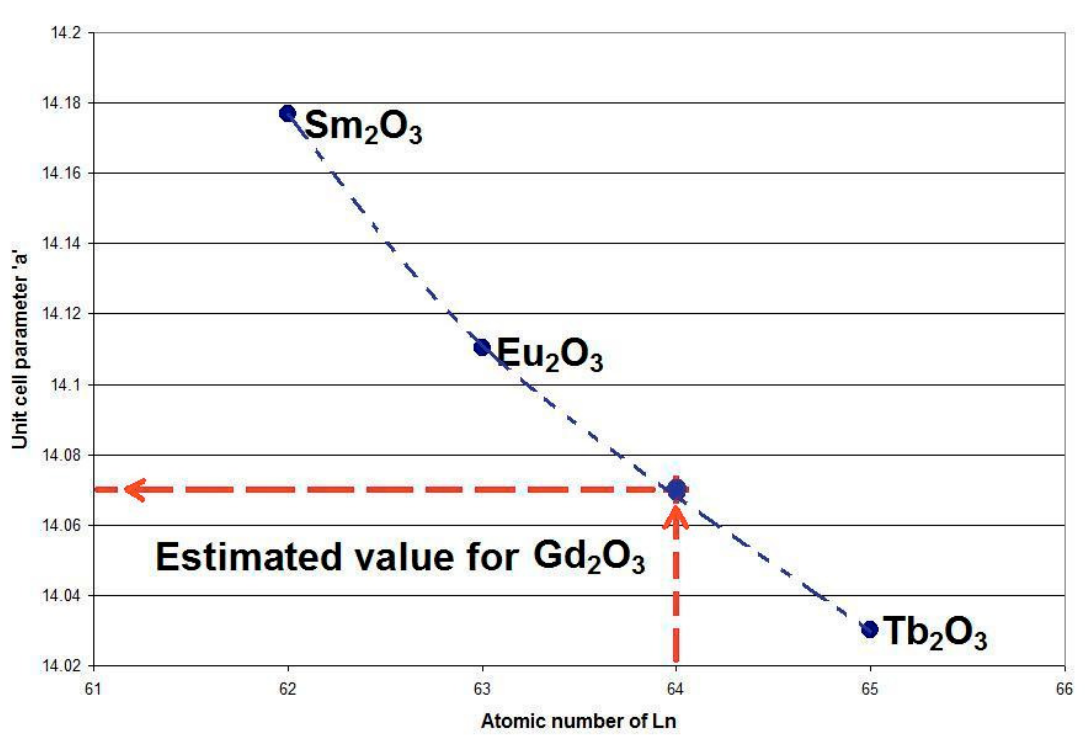


Figure 7.32 Estimation of unit cell parameter ' $a$ ' for monoclinic  $\text{Gd}_2\text{O}_3$  by a method of interpolation.

The provisional unit cell parameters for monoclinic  $\text{Gd}_2\text{O}_3$  were estimated at  $a = 14.07\text{Å}$ ,  $b = 3.57\text{Å}$ ,  $c = 8.77\text{Å}$ ,  $\beta = 100.07^\circ$ . It should be noted that although  $a$  and  $b$  are close to those estimated from the 1 hour heating data, the value of  $c$  is significantly higher.

Least squares refinement still left a discrepancy in intensity for the  $2\theta = 30.06^\circ$  peak ( $40\bar{2}$  plane). The remainder of the peaks were well fitted. It was thought that the discrepancy might be explained by preferred orientation of the microcrystalline sample. To this end, the sample was reground and the pattern collected again. However, the pattern showed no change. This discrepancy was seen neither with the europia

monoclinic pattern nor the second gadolinia sample exposed to synchrotron radiation. There is no ambient phase peak in the same  $2\theta$  region that might cause superposition. The problem peak was therefore put down to preferred orientation that was not sufficiently ground out.

Analysis of the pattern from the refined phase fractions in GSAS showed there to be approximately 97% of the monoclinic phase and 3% of the cubic phase present.

Because of the significantly greater energy input required to force the conversion in gadolinia compared to europia, it was decided to repeat an XRPD pattern at a later date in order to determine if there had been any change in the phase fractions. The sample was analysed 5 months after annealing and found to contain the same proportion of B-type oxide.

Unlike sample (2), sample (8)  $Gd_2O_3$  showed a complete conversion following the same time at what was believed to be the same temperature. Sample (2) was annealed in a cylindrical crucible with the open end exposed to the air. Sample (8) was annealed in the enclosed space of the DSC. It is likely that the temperature for sample (8) was slightly higher and not subject to the cooling effect of direct exposure to the atmosphere. The diffraction pattern (figure 7.26) shows distinct and narrow Bragg reflections characteristic of those generated using synchrotron radiation. Although the data was captured up to  $149.99^\circ$  of  $2\theta$  it was not possible to load the entire diffraction pattern into the relevant software due to the file size. Instead the characteristic region below  $40^\circ$  was chosen. To ensure there was nothing other than monoclinic phase present the entire diffractogram was loaded into a spreadsheet and compared against a calculated pattern. The patterns were found to correspond exactly, meaning that the sample had completely converted to the monoclinic phase. This is contrary to sample (2), where 100% conversion to the monoclinic phase did not occur.

#### *7.2.4.3 Ytterbia*

Heating the  $Yb_2O_3$  sample for 1 hour in the Heraeus furnace produced virtually no change in the diffraction pattern. As with  $Gd_2O_3$  there was a small change with the

appearance of low intensity lines around  $2\theta = 30^\circ$ , although this time they were considerably weaker than for gadolinia. This is to be expected, since increasing atomic number of the rare earth is accompanied by a sharp increase in the energy needed to make the phase transition.

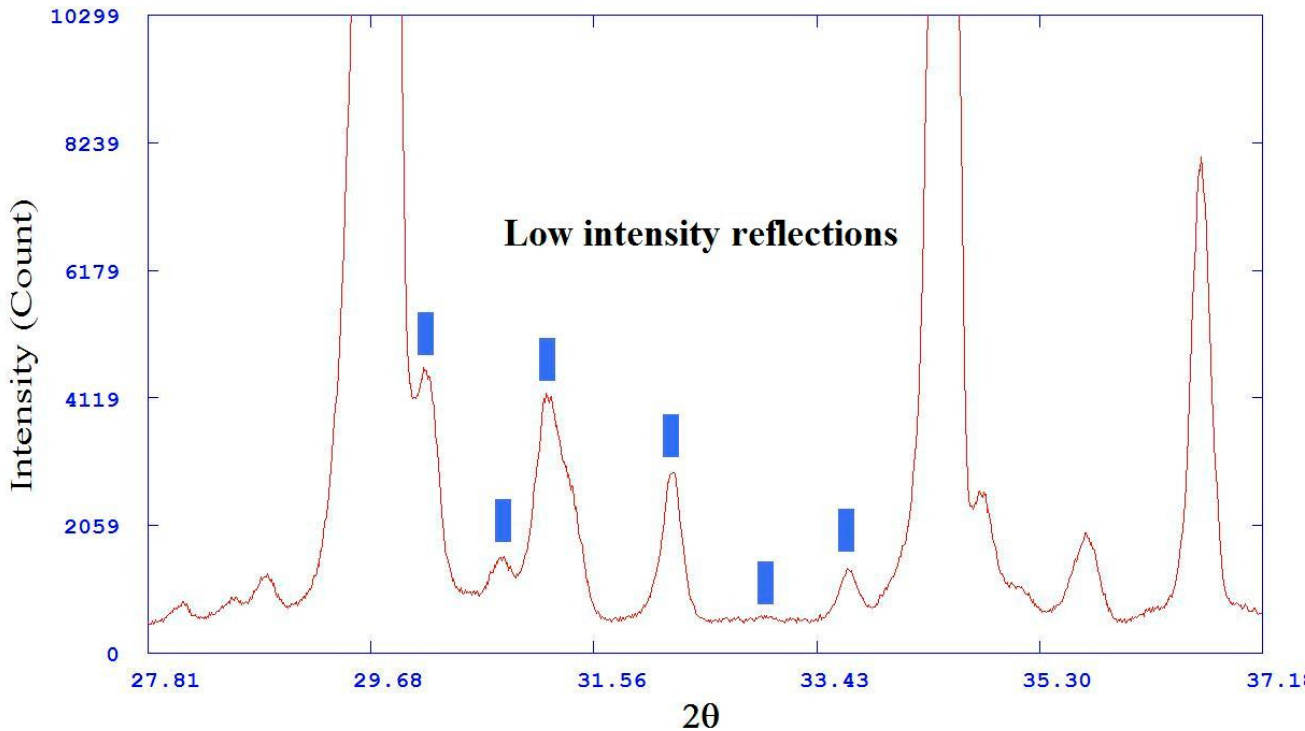


*Figure 7.33 XRPD pattern of  $\text{Yb}_2\text{O}_3$  post-heating to  $1500^\circ\text{C}$  showing low-intensity reflections due to the monoclinic phase.*

Because of the similarity with the  $\text{Gd}_2\text{O}_3$  pattern in figure 7.20 (and the cubic europia pattern in figure 7.1) it was again assumed that the low intensity lines in the  $\text{Yb}_2\text{O}_3$  pattern around  $2\theta = 30^\circ$  were due to the presence of a monoclinic phase. These 6 lines were run through CRYSFIRE to determine if anything significant could be found. None of the software found a solution that seemed reasonable or approximated to that of monoclinic  $\text{Eu}_2\text{O}_3$ . The 6 lines were then put into Chekcell and a set of calculated lines generated from unit cell parameters extrapolated from monoclinic europia. The starting points were taken as  $a = 13.75\text{\AA}$ ,  $b = 3.45\text{\AA}$ ,  $c = 8.5\text{\AA}$  and  $\beta = 100.2^\circ$ . These parameters were refined until the experimental and calculated lines converged. Thus a set of approximate unit cell parameters for monoclinic  $\text{Yb}_2\text{O}_3$  were found, namely  $a = 13.740(2)\text{\AA}$ ,  $b = 3.400(2)\text{\AA}$ ,  $c = 8.593(2)\text{\AA}$  and  $\beta = 100.12^\circ$ . The existence of this phase

is contrary to the phase diagram and also to recently published work (Guo, Harvey *et al* 2007), (Meyer *et al* 1995).

The pattern for  $\text{Yb}_2\text{O}_3$  obtained post-heating for 7 hours in the Heraeus furnace again showed little conversion to the monoclinic phase. The same 6 monoclinic lines were visible around  $2\theta = 30^\circ$  but there was no increase in intensity relative to the other lines. Because of this no further work was carried out on the diffraction pattern.

Using the estimated unit cell parameters for ytterbia and assuming the atom positions to be the same as for gadolinia, analysis of the pattern from the refined phase fractions in GSAS showed there to be approximately 99% of the cubic phase and 1% of the monoclinic phase present.

The pattern for  $\text{Yb}_2\text{O}_3$  obtained post-heating for 5 hours at  $1800^\circ\text{C}$  showed no conversion to the monoclinic phase. There was a 2-week delay between the annealing and the diffraction pattern being collected. It would be reasonable to assume that the material had converted at least as much as sample (3) in the furnace and possibly more because of the increased temperature. However, the monoclinic phase of ytterbia is obviously very unstable under ambient conditions. To show the change, the immediate recording of XRPD data under ambient conditions or, ideally, in situ XRPD, would be needed.

### **7.3 IN SITU HIGH TEMPERATURE XRPD**

#### *7.3.1 Praseodymia ramp in air*

The purpose of this section was to identify the temperatures of the phase transitions within the range of the diffractometer with the intention of then carrying out the kinetic study detailed in 7.3.2. Sample (4) was heated in  $25^\circ$  steps from  $25^\circ\text{C}$  to  $800^\circ\text{C}$  and cooled back in  $25^\circ\text{C}$  steps to  $125^\circ\text{C}$ . At each temperature a diffraction pattern was recorded. The 33 XRPD patterns obtained from  $25^\circ\text{C}$  to  $800^\circ\text{C}$  are shown stacked together in the 3 images below.

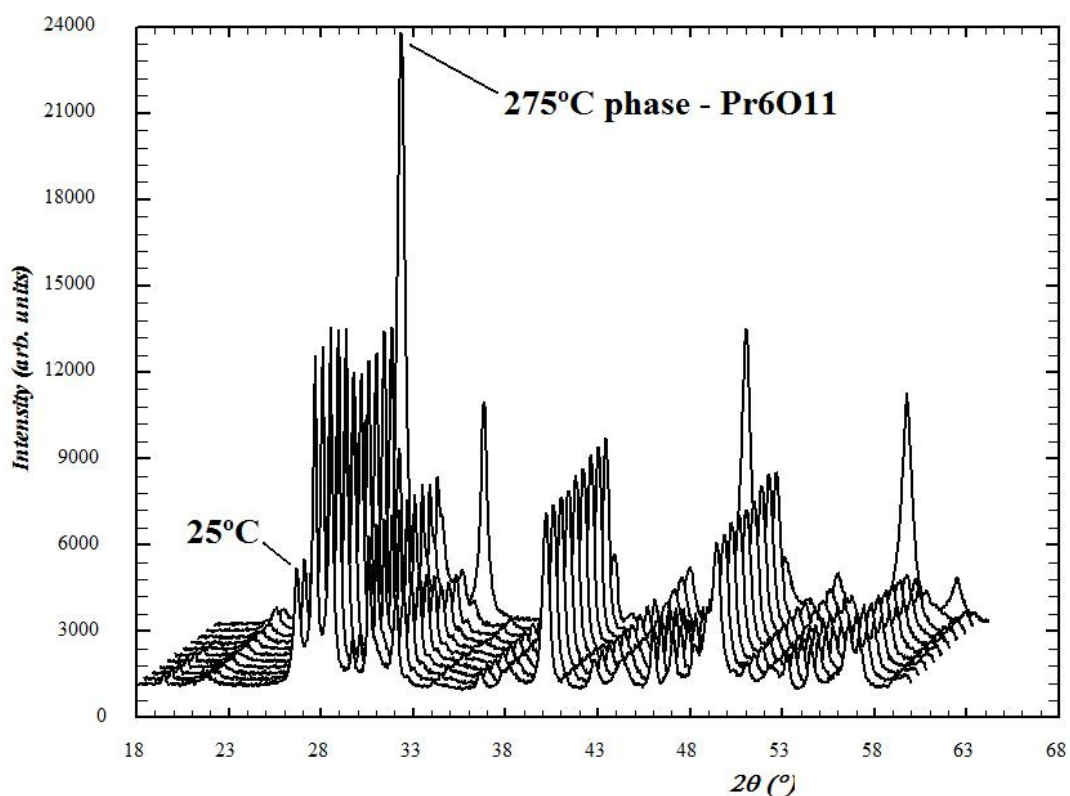


Figure 7.34 Praseodymia ramp 25°C to 275°C showing the appearance of the ceria-type  $\beta$  phase ( $\text{Pr}_6\text{O}_{11}$ ) at 275°C.

Figure 7.34 shows the sudden appearance of the  $\beta$  phase at 275°C. Here the pattern corresponding to the mixed A and C-type phases transforms to the 5-peak pattern of the  $\text{CeO}_2$  structure. This structure is represented in the phase diagram in figure 1.9 by a narrow vertical section to the bottom right. The 5 peaks were run through CRYSFIRE. However, the program was unable to index the XRPD pattern because of the small number of lines. GRAPHPRO returned the unit cell parameter as 5.476 Å. Full profile refinement using GSAS was carried out using the atom positions in the ICDD database reference 42-1121. The refined unit cell parameter was 5.4790(2)Å.

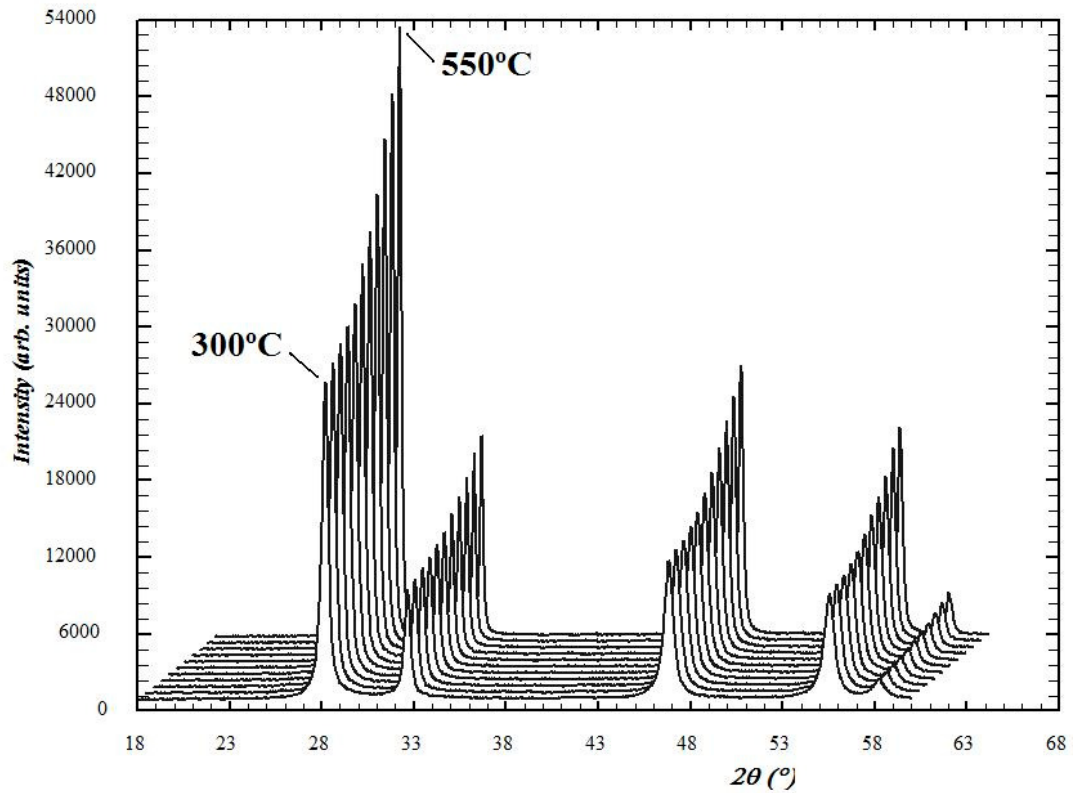


Figure 7.35 Praseodymia ramp 300°C to 550°C showing the ceria cell throughout.

Figure 7.35 shows no change throughout the temperature ramp other than an intensifying of the reflections. Although the phase diagram shows there are 3 phases in this range (the  $\delta$ ,  $\epsilon$  and  $\zeta$  phases), there was no indication of any structural change from the XRPD patterns. This is to be expected as the changes are solely due to the different oxygen compositions whilst still retaining the ceria-type cubic cell. The contribution to peak intensities from oxygen is small compared to that of praseodymium.

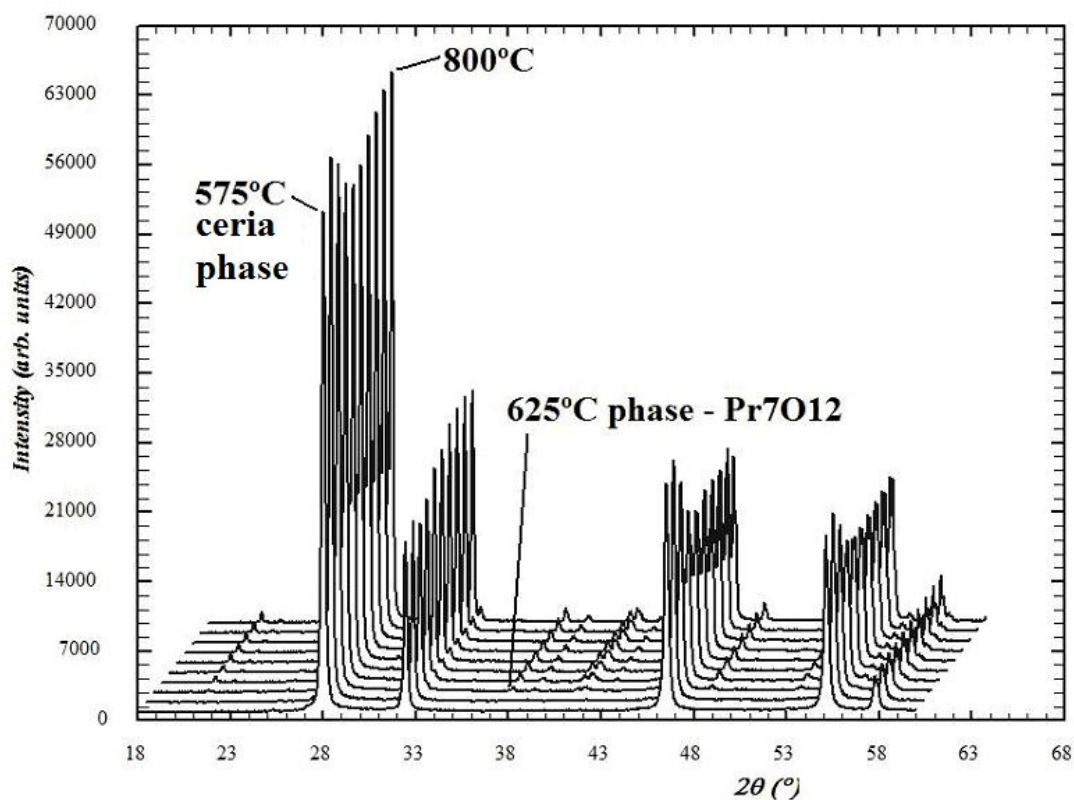


Figure 7.36 Praseosymia ramp 575°C to 800°C showing the appearance of the  $t$  phase ( $Pr_7O_{12}$ ) at 625°C.

It is not until 625°C that a new cell type is discernible in the diffractograms, where the  $t$  phase slowly emerges over a series of patterns in figure 7.36. Its presence is indicated by the weak reflection present between the 5 stronger reflections already present. CRYSFIRE was unable to index the XRPD pattern of this new structure. Full profile refinement using GSAS was carried out using the atom positions in the ICDD database reference 7-0449. The refined unit cell parameters were  $a = 10.3460(2)\text{\AA}$  and  $c = 9.6430(2)\text{\AA}$ , space group  $R-3$ .

The diffraction patterns for both the  $\beta$  and  $t$  phases are shown in figures 7.37 and 7.38.

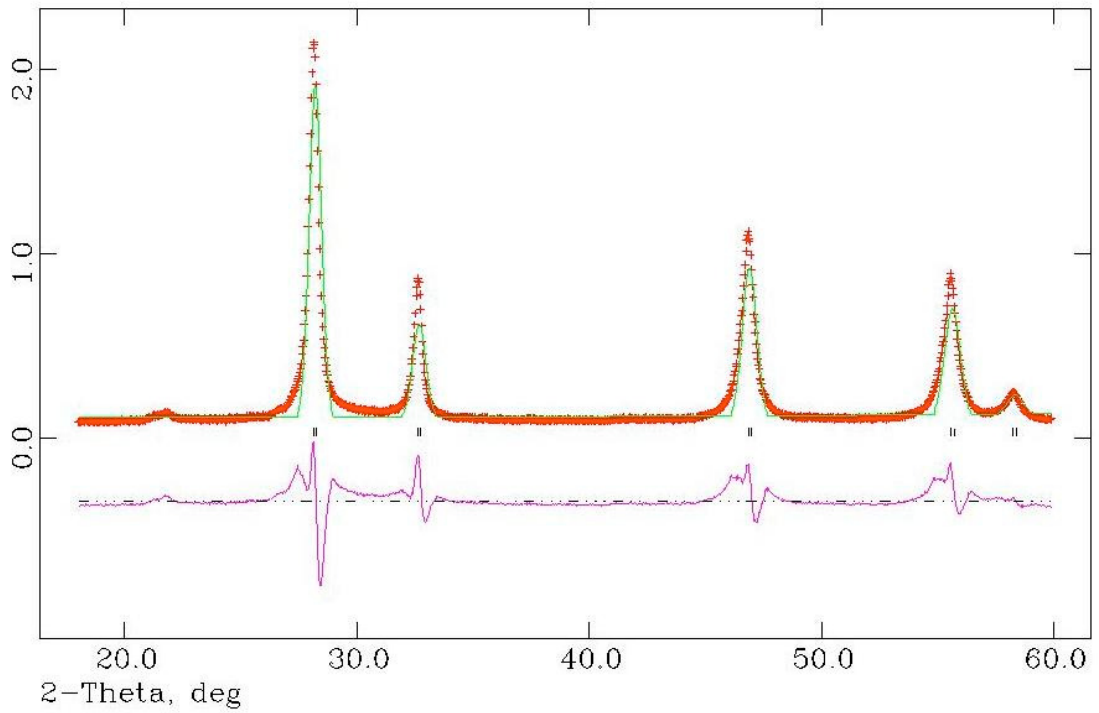


Figure 7.37 Final stage of refinement of the  $\beta$  phase ( $\text{Pr}_6\text{O}_{11}$ ) of praseodymia.

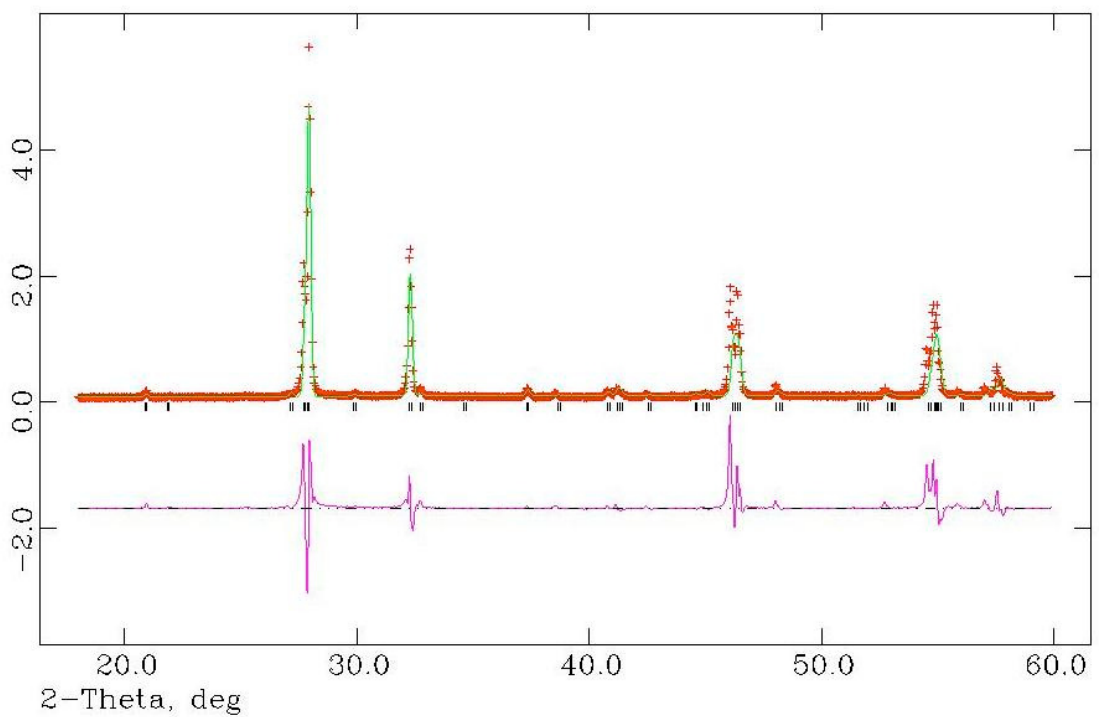


Figure 7.38 Final stage of refinement of the  $t$  phase ( $\text{Pr}_7\text{O}_{12}$ ) of praseodymia.

The 28 XRPD patterns obtained on cooling back from 800°C to 125°C are shown stacked together in the 2 images below.

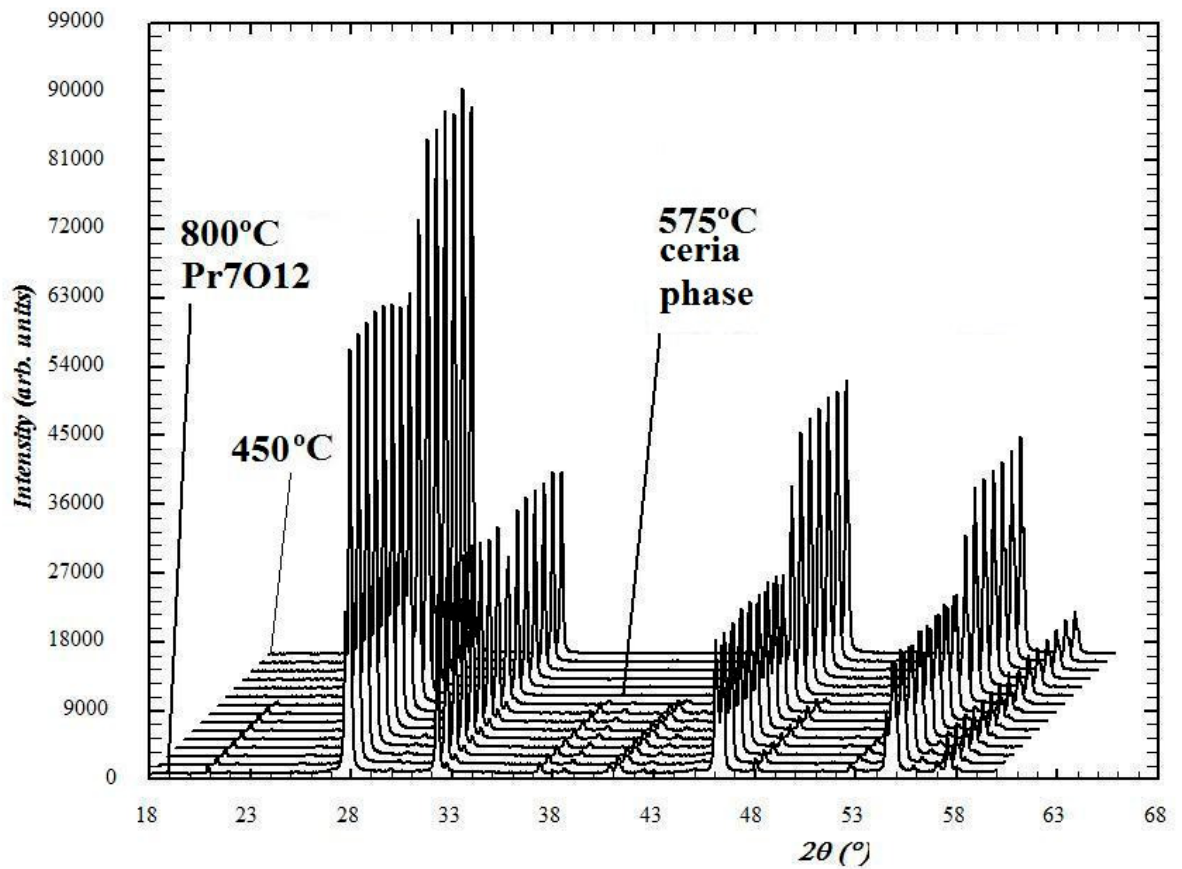


Figure 7.39 Praseodymia ramp 800°C to 450°C showing the loss of the  $t$  phase of  $Pr_7O_{12}$  at 575°C.

Figure 7.39 shows that on cooling the sample back from 800°C, the  $t$  phase which had appeared at 625°C when the temperature was ascending disappeared at 575°C. This marks the point where the conversion back to the ceria cell occurred. More detailed examples of hysteresis in the Pr-O system will be shown in chapter 8.

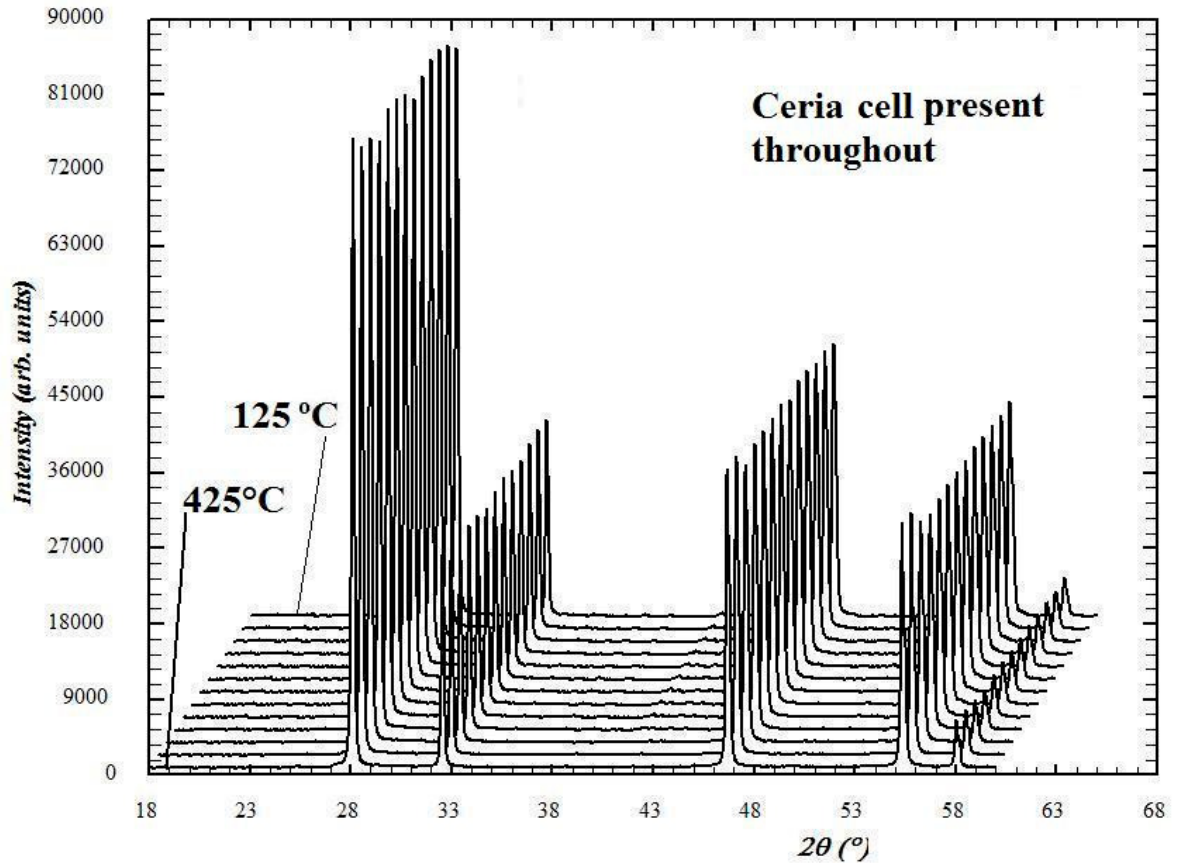


Figure 7.40 Praseodymia ramp 425°C to 125°C showing the ceria cell throughout.

Figure 7.40 shows that further cooling showed no change in the XRPD pattern i.e. the ambient temperature phase did not appear below 300°C. This echoes findings with europia and gadolinia; some high-temperature phases are metastable.

### 7.3.2 Praseodymia isothermal holds in air - conversion from $Pr_2O_3$ to $Pr_6O_{11}$ at 275 °C

Now that the transition temperature for formation of the  $\beta$  phase had been established at approximately 275°C it was possible to perform a series of isothermal holds close to this temperature to observe how fast the reaction proceeded with temperature.

#### 7.3.2.1 Peak heights and intensities

Figure 7.41 shows an example of the ambient temperature phase transforming into the  $\beta$ -phase over a period of 45 minutes.

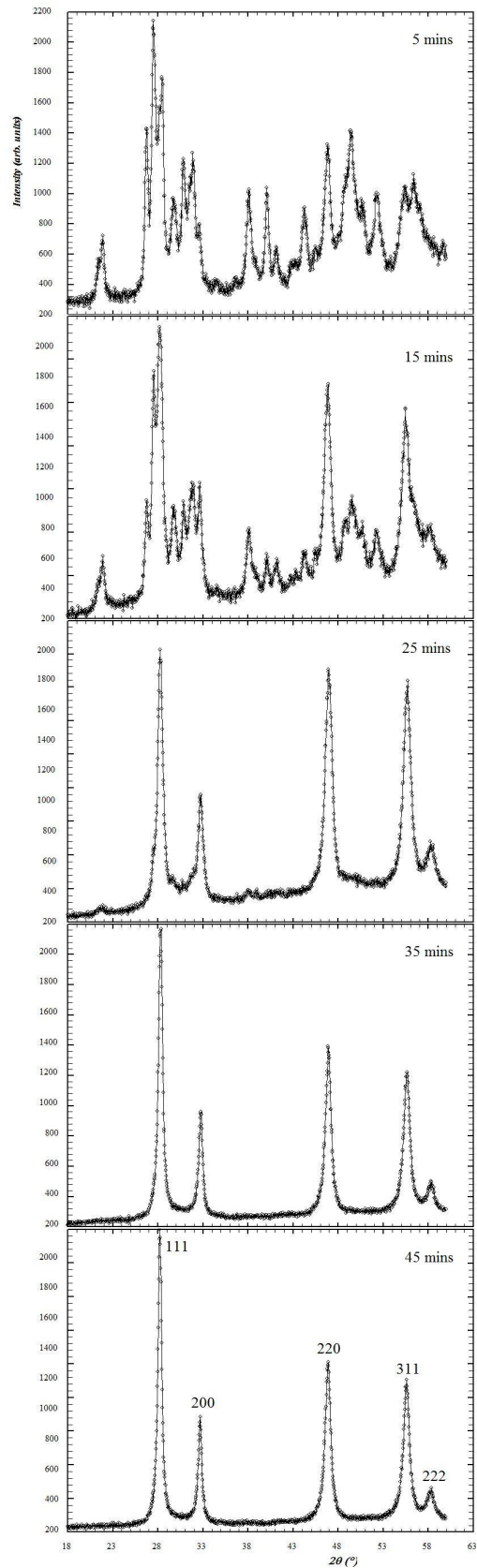


Figure 7.41 The five Bragg peaks of the  $\beta$  phase emerging from the ambient mixed phase during the 250 °C isothermal hold.

The diffraction patterns in figure 7.41 clearly show the 5 peaks of the high-temperature phase emerging from the pattern of the ambient mixed phase. Two characteristic peaks were chosen for analysis. These were at  $47.2^\circ$  (corresponding to the 220 plane in the  $\beta$  phase) and  $41.4^\circ$  (the 012 plane in the ambient cubic phase). The integrated intensities of these peaks were recorded across each isothermal hold and the fractional changes in the peaks plotted against time. The following chart illustrates the degree of conversion to the  $\beta$  phase as measured by the increase in intensity of the  $47.2^\circ$  peak.

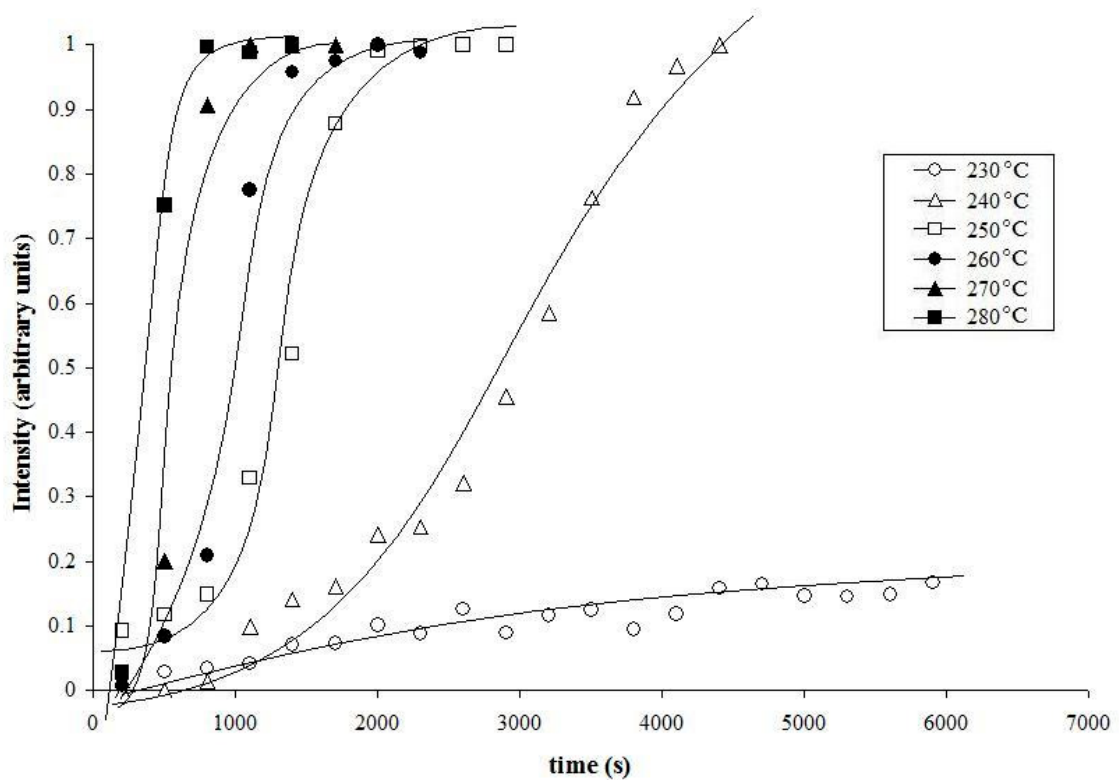


Figure 7.42 Conversion against time for  $Pr_2O_3$  to  $Pr_6O_{11}$  phase change using the increase in intensity of the  $47.2^\circ$  ( $\beta$  phase 220 plane) peak.

### 7.3.2.2 Shrinking Sphere model

The fractional conversions for the  $230^\circ\text{C}$  holds were discarded as there were found to be anomalies in the data due to operational error. Use of the Shrinking Sphere model on the remaining holds at  $240^\circ\text{C}$ ,  $250^\circ\text{C}$ ,  $260^\circ\text{C}$ ,  $270^\circ\text{C}$  and  $280^\circ\text{C}$  gave the set of kinetic isotherms in figure 7.43.

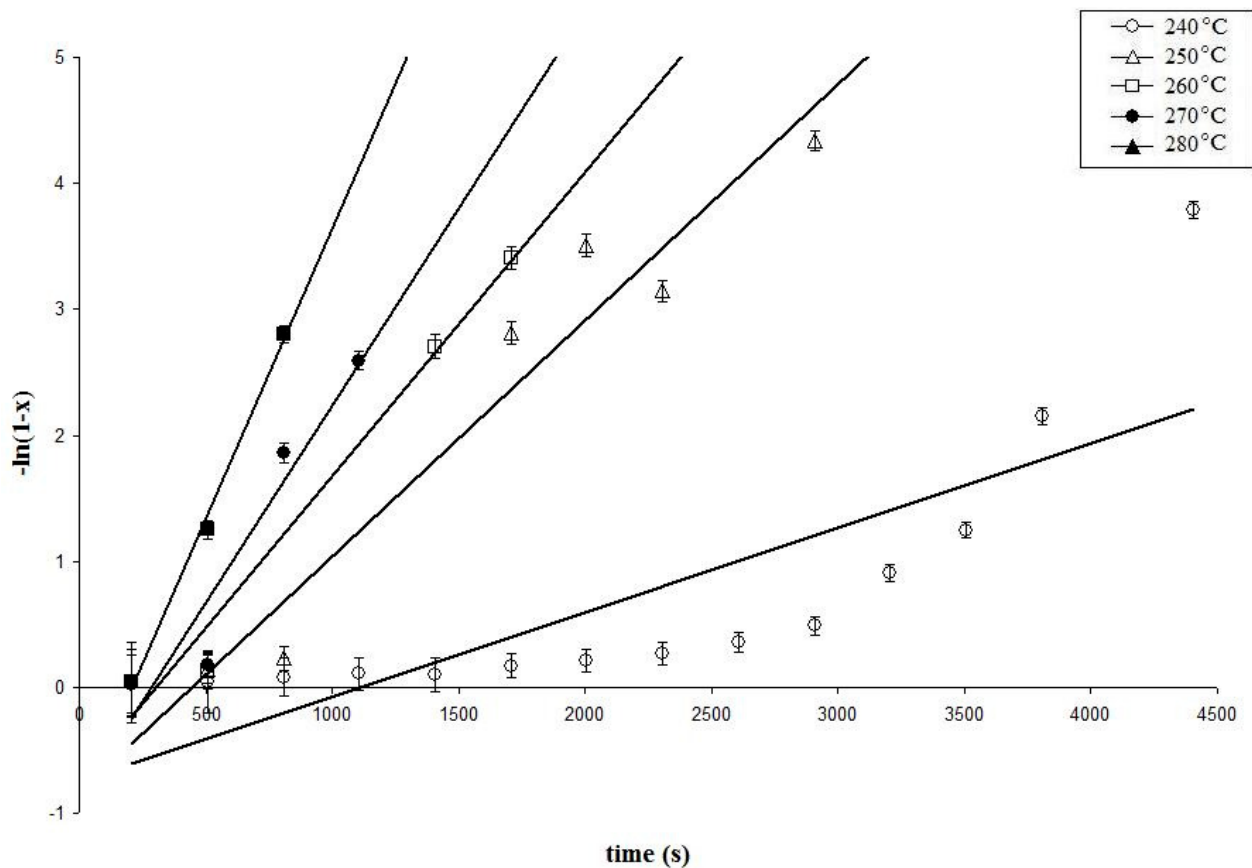


Figure 7.43 Shrinking Sphere kinetic isotherms for the 47.2° ( $\beta$  phase 220 plane) peak.

Use of the data in the above chart gave the following set of values for the rate constant,  $k$ .

| Temp (°C) | $k$ (s <sup>-1</sup> ) |
|-----------|------------------------|
| 240       | $7 \times 10^{-4}$     |
| 250       | $3.2 \times 10^{-3}$   |
| 260       | $2.8 \times 10^{-3}$   |
| 270       | $7.9 \times 10^{-3}$   |
| 280       | $9.7 \times 10^{-3}$   |

Table 7.17 Values of the rate constant,  $k$ , for the 47.2° ( $\beta$  phase 220 plane) peak.

A plot of  $\ln k$  against reciprocal temperature is shown below.

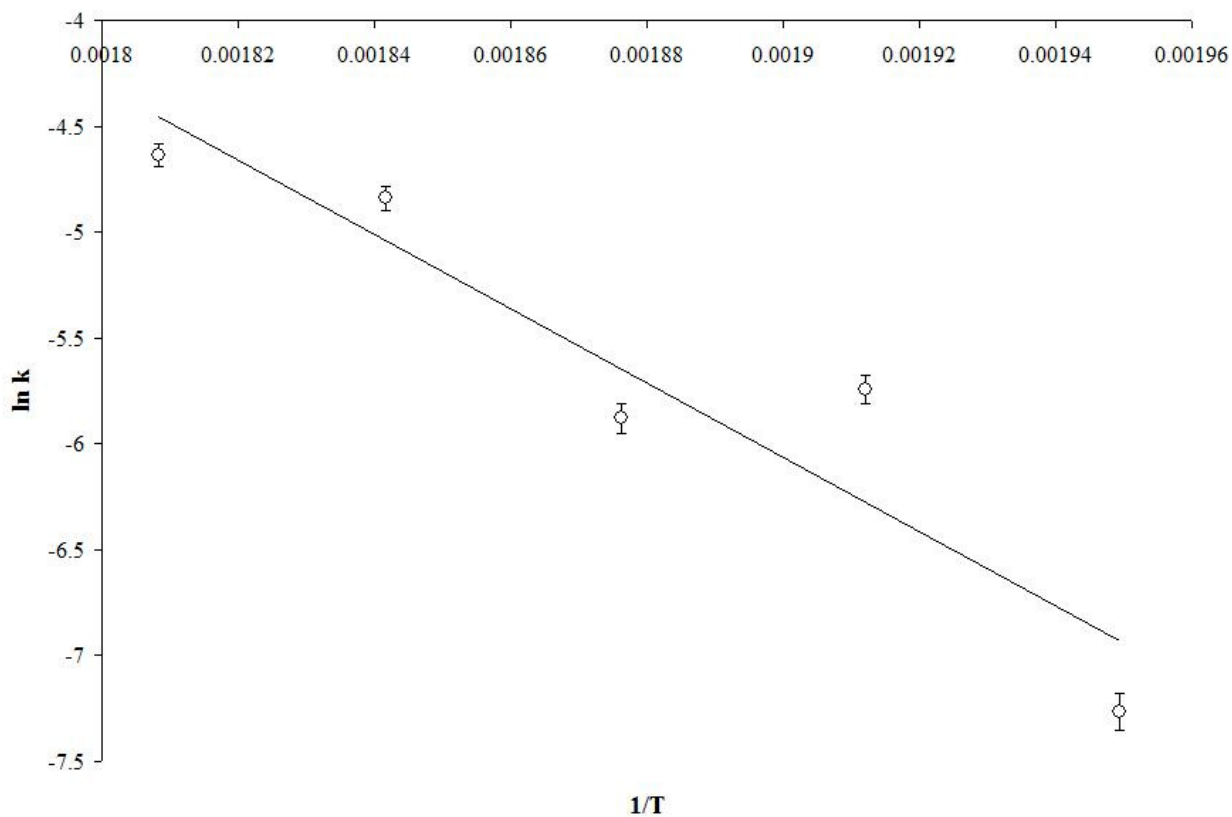


Figure 7.44 Plot of  $\ln k$  against  $1/T$  for the  $47.2^\circ$  ( $\beta$  phase 220 plane) peak.

Further analysis of the above data generated value of  $-146(2) \text{ kJ.mol}^{-1}$  for the activation energy.

### 7.3.2.3 JMAK model

Starting with the same fractional conversion data as in 7.3.2.2, use of the JMAK model gave the following double log plot.

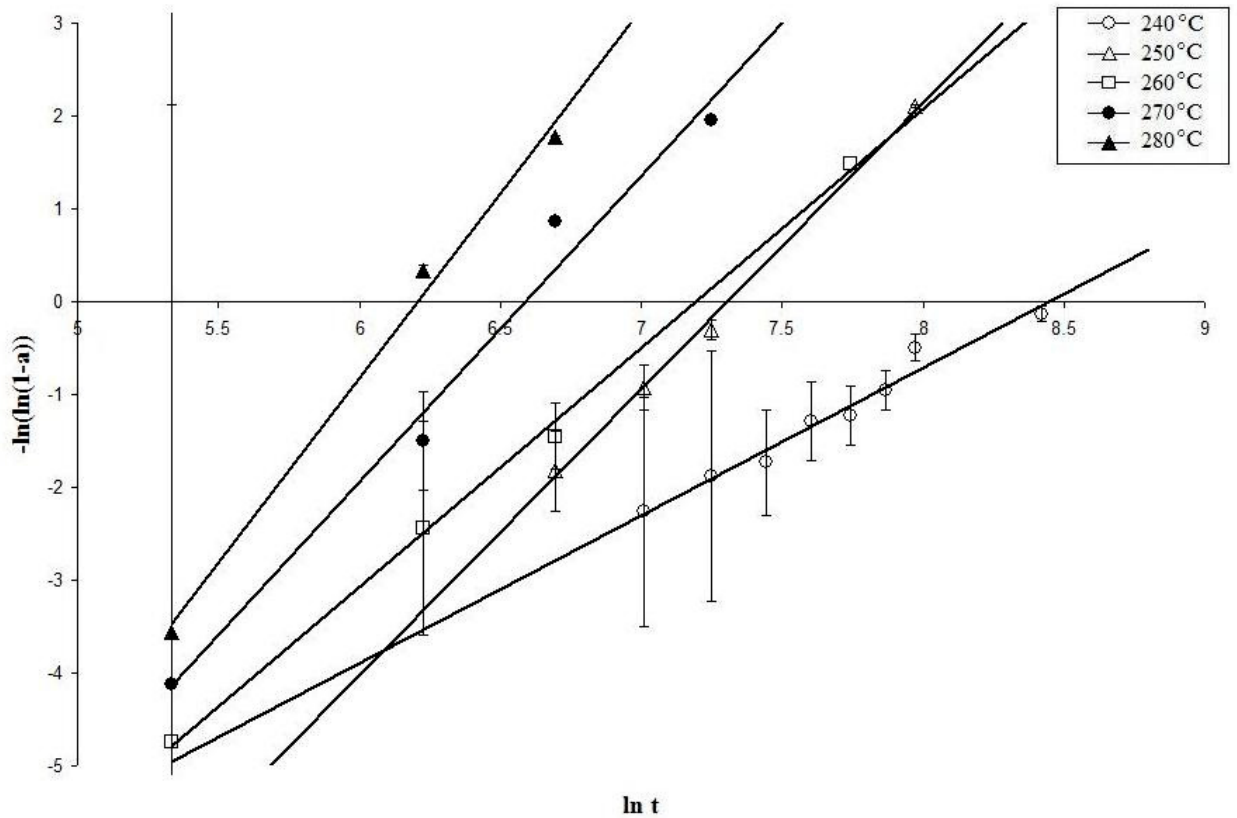


Figure 7.45 JMAK kinetic isotherms for the 47.2° ( $\beta$  phase 220 plane) peak.

Use of the data in the above chart gave the following set of values for the rate constant,  $k$  and Avrami exponent,  $n$ .

| Temp (°C) | $K$ ( $s^{-1}$ )        | $n$                   |
|-----------|-------------------------|-----------------------|
| 230       | Not able to determine   | Not able to determine |
| 240       | $2.972 \times 10^{-7}$  | 1.80(59)              |
| 250       | $1.68 \times 10^{-10}$  | 3.08(25)              |
| 260       | $9.182 \times 10^{-9}$  | 2.57(7)               |
| 270       | $3.777 \times 10^{-10}$ | 3.29(6)               |
| 280       | $1.308 \times 10^{-9}$  | 3.24(11)              |

Table 7.18 Values of the rate constant and Avrami exponent for the 47.2° ( $\beta$  phase 220 plane) peak.

JMAK data obtained from accurately recorded data should yield a series of plots in figure 7.45 with similar gradient, corresponding to the Avrami exponent. In turn, the plot in figure 7.46 should be a downward sloping line. Because of the lack of data (only 5 data points) and the erratic spread of Avrami exponents in table 7.18 it was decided to

take a practical approach and only use the data giving similar gradients in figure 7.45. The relevant temperature holds were 250°C, 270°C and 280°C. A plot of  $\ln k$  against reciprocal temperature is shown below.

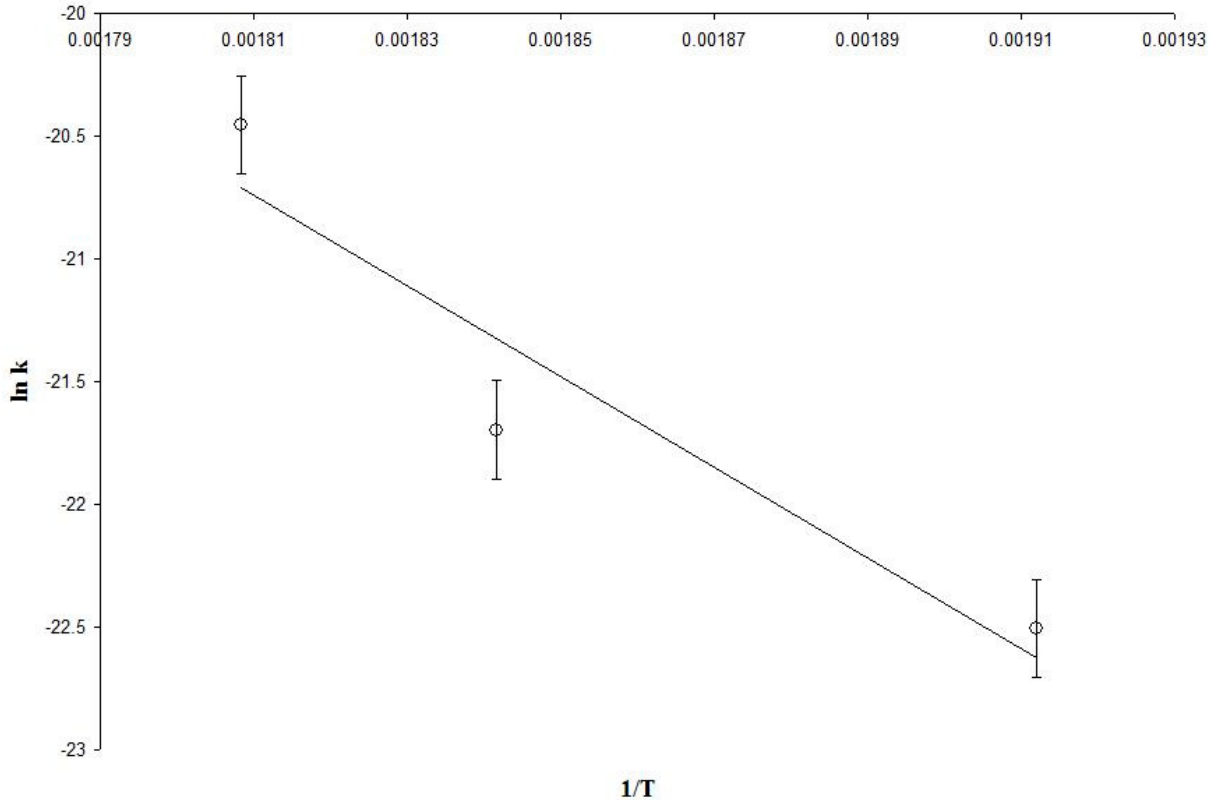


Figure 7.46 Plot of  $\ln k$  against  $1/T$  for the  $47.2^\circ$  ( $\beta$  phase 220 plane) peak.

Further analysis of the above data generated a value of  $-154(2)$   $\text{kJ}\cdot\text{mol}^{-1}$  for the activation energy.

Figure 7.42 clearly shows that the isothermal hold at  $230^\circ\text{C}$  was not long enough for significant conversion to take place. As a result of this, the data was of no use in determining the Avrami exponent. The  $240^\circ\text{C}$  data does not level out, meaning that 100% conversion did not occur. Again, this meant that the value for the Avrami exponent could not be deemed accurate. The remaining 4 values for the Avrami exponent do show some agreement, although had other holds been possible, perhaps at intermediate temperatures eg  $245^\circ\text{C}$ ,  $255^\circ\text{C}$  etc, the value for the activation energy might have been improved. The JMAK model is useful in providing the dimensionality information via the Avrami exponent, but to obtain it we must effectively take the log

of both sides of the Shrinking Sphere equation. The Shrinking Sphere model plots  $-\ln(1 - x)$  against  $t$  whereas the JMAK model plots  $\ln(-\ln(1 - x))$  against  $\ln t$ . In taking this secondary log, significant error is introduced into the working and therefore into the values for the Avrami exponent and activation energy. To counter this, it would be useful to record XRPD patterns more often. This would improve the kinetic isotherms and hopefully the values for the above quantities.

A summarised set of results, including that for the 41.4° peak, is given in the table below. The values for the activation energy obtained by both models for the 47.2° peak are close. Encouragingly, they correspond to the value of  $-149(10)$  kJ.mol<sup>-1</sup> for the 40.1° peak, where it had been assumed that the kinetics attributable to a collapsing peak in the XRPD pattern would be the same as that for a growing peak.

| Peak  | Phase             | Method           | EA (kJ.mol <sup>-1</sup> ) | $n$         |
|-------|-------------------|------------------|----------------------------|-------------|
| 41.4° | Ambient hexagonal | Shrinking sphere | -149(10)                   | N/A         |
| 47.2° | High temp cubic   | Shrinking sphere | -146(2)                    | N/A         |
| 47.2° | High temp cubic   | JMAK             | -154(2)                    | 3.05(7) avg |

Table 7.19 Values for activation energy for the  $\phi \rightarrow \beta$  transition in Pr-O.

Referring to table 4.1, the value of  $n$  being between 3 and 4 indicates that the product phase propagates three-dimensionally from existing nucleation sites in the reactant material.

### 7.3.3 Praseodymia quench in air

The  $\iota$  phase, which appeared at 625°C when the temperature was ascending, was retained up to the maximum temperature reached of 800°C. On quenching, the ceria phase was retained at ambient temperature as the  $\beta$  form.

### 7.3.4 Change in unit cell parameter with temperature

The temperature ramp in 7.3.1 showed 2 distinct changes to the XRPD pattern. At about 275°C there was a significant change, corresponding to the mixed A and C-type

phase converting to  $\text{Pr}_6\text{O}_{11}$ . At  $625^\circ\text{C}$  there was a more subtle change in the pattern with  $\text{Pr}_6\text{O}_{11}$  converting to  $\text{Pr}_7\text{O}_{12}$ . With increasing temperature there is an associated thermal expansion of the crystal lattice, indicated by a small shift in the positions of the Bragg reflections. This phenomenon is often used as a means of measuring temperature in situ when XRPD data is being collected at high temperature. In such a case, a known material such as platinum is introduced to the sample and the shift in its Bragg peaks used to determine temperature. The following table shows the values for the unit cell parameters between  $275^\circ\text{C}$  and  $800^\circ\text{C}$ , obtained by observing the change in the position of the 111 reflection.

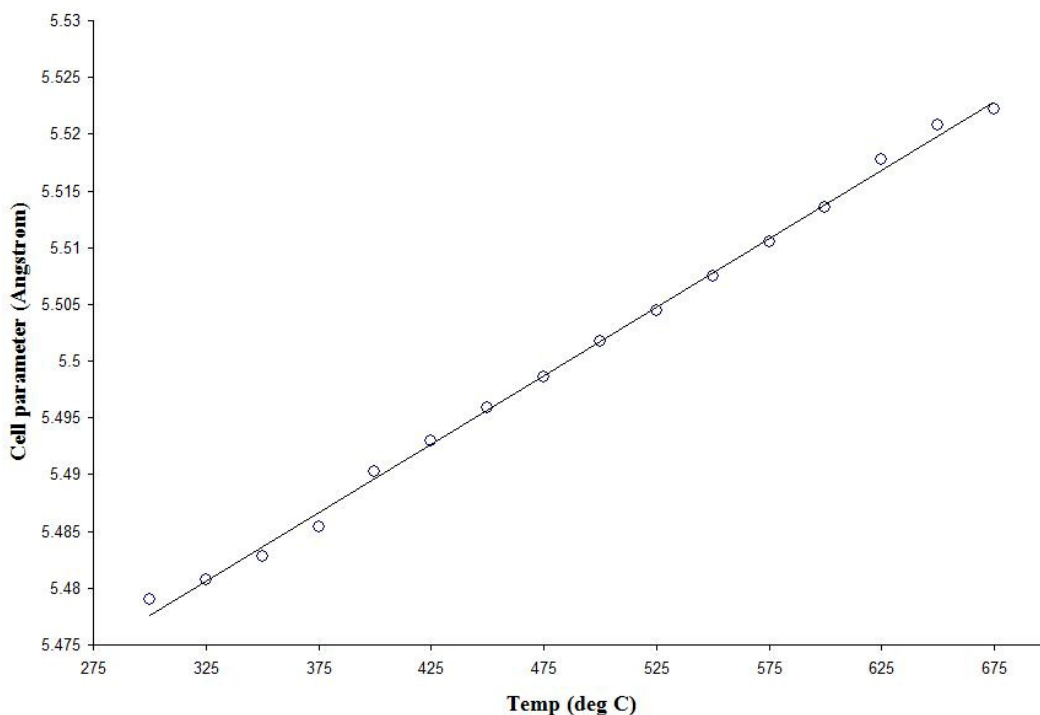


*Figure 7.47 Variation in unit cell parameter with temperature for  $\text{Pr}_6\text{O}_{11}$ . Error bars are within the data points.*

Figure 7.47 shows a linear correlation between unit cell parameter and temperature.

## 7.4 COMPARISON WITH OTHER WORK

The study of the lanthanoid oxides is a long and well-established tradition and there is a vast amount of data in the available literature. The crystal structures of the sesquioxides are well known and they are in general agreement with the phase diagram in figure 1.5.

However, there are notable exceptions. The phase diagram does not indicate that high temperature modifications exist at ambient temperature. This work has shown that  $\text{Sm}_2\text{O}_3$ ,  $\text{Eu}_2\text{O}_3$  and  $\text{Gd}_2\text{O}_3$  can all persist under ambient conditions. Additionally, high-temperature modifications exist which are not indicated in the diagram as existing at all, notably  $\text{Er}_2\text{O}_3$  and  $\text{Yb}_2\text{O}_3$ , and may be quenched to ambient temperature.

Historically, there has been limited kinetic work done on the Pr-O system, the bulk of the data on the lanthanides lying with the oxides of neodymium to gadolinium. The main sources of XRPD data are Stecura and Ainscough, whose data is presented in table 7.20.

| Oxide                   | Ambient phase | Reaction                    | EA ( $\text{kJ}\cdot\text{mol}^{-1}$ ) |
|-------------------------|---------------|-----------------------------|--|
| $\text{Nd}_2\text{O}_3$ | Cubic         | C-type $\rightarrow$ A-type | 502 <sup>1</sup>                       |
| $\text{Sm}_2\text{O}_3$ | Cubic         | C-type $\rightarrow$ B-type | 628 <sup>1</sup>                       |
| $\text{Eu}_2\text{O}_3$ | Cubic         | C-type $\rightarrow$ B-type | 691 <sup>1</sup>                       |
| $\text{Eu}_2\text{O}_3$ | Cubic         | C-type $\rightarrow$ B-type | 493 <sup>2</sup>                       |
| $\text{Gd}_2\text{O}_3$ | Cubic         | C-type $\rightarrow$ B-type | 787 <sup>1</sup>                       |

*Table 7.20 Activation energies for the lanthanide oxides.*

<sup>1</sup> (Stecura 1966). <sup>2</sup> (Ainscough et al 1975)

The value for the activation energy of the  $\phi \rightarrow \beta$  transformation in praseodymia is considerably lower. There is correlation between the 2 values obtained using the increase in height of the  $47.2^\circ$  Bragg reflection in the product phase ( $-146(2) \text{ kJ}\cdot\text{mol}^{-1}$  obtained via a shrinking sphere model and  $-154(2) \text{ kJ}\cdot\text{mol}^{-1}$  obtained via the JMAK model). The value obtained by looking at the fall in the  $41.4^\circ$  Bragg reflection in the reactant phase ( $-149(10) \text{ kJ}\cdot\text{mol}^{-1}$ ) corresponds to the former two values, indicating the the assumption in its derivation was correct i.e. it is possible to use changes in either reactant or product peaks to obtain the same result. In addition to their closeness, the three values are relatively small when compared with the much higher values for the heavier oxides. The kinetic data obtained via XRPD will be discussed further in chapter 8 alongside the results obtained from DSC-TG both historically and in this work.

## 8 RESULTS FROM DIFFERENTIAL SCANNING CALORIMETRY

This chapter contains all the DSC work carried out on  $\text{PrO}_x$ . The work had five aims, namely:

- (i) to identify phase changes in the system;
- (ii) to perform kinetic measurements where possible;
- (iii) to match phase changes against the published phase diagram;
- (iv) to note any discrepancies between this work and the phase diagram;
- (v) and to determine the extent of degradation of the material in air.

### 8.1 FULL RANGE DSC-TG IN NITROGEN

The results obtained from sample (4) using the full temperature range (up to 1550°C) of the instrument are given in the following 4 images.

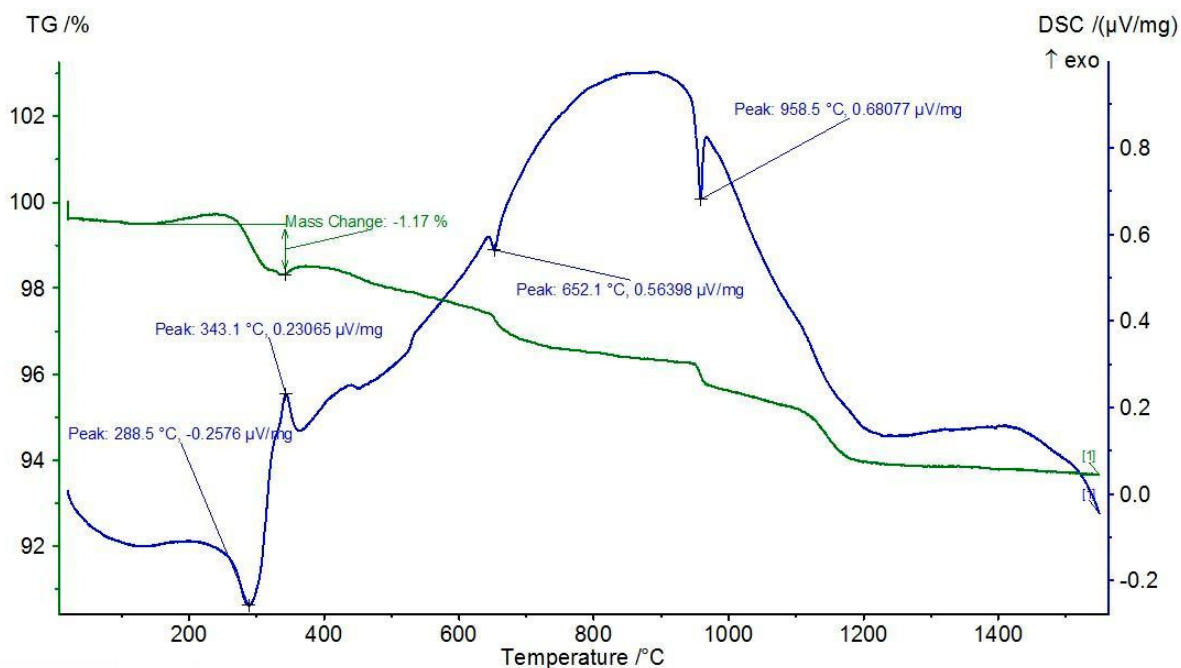


Figure 8.1 DSC-TG recorded on sample (4)  $\text{Pr}_2\text{O}_3$  from 20 °C to 1550 °C at 10K/min under nitrogen.

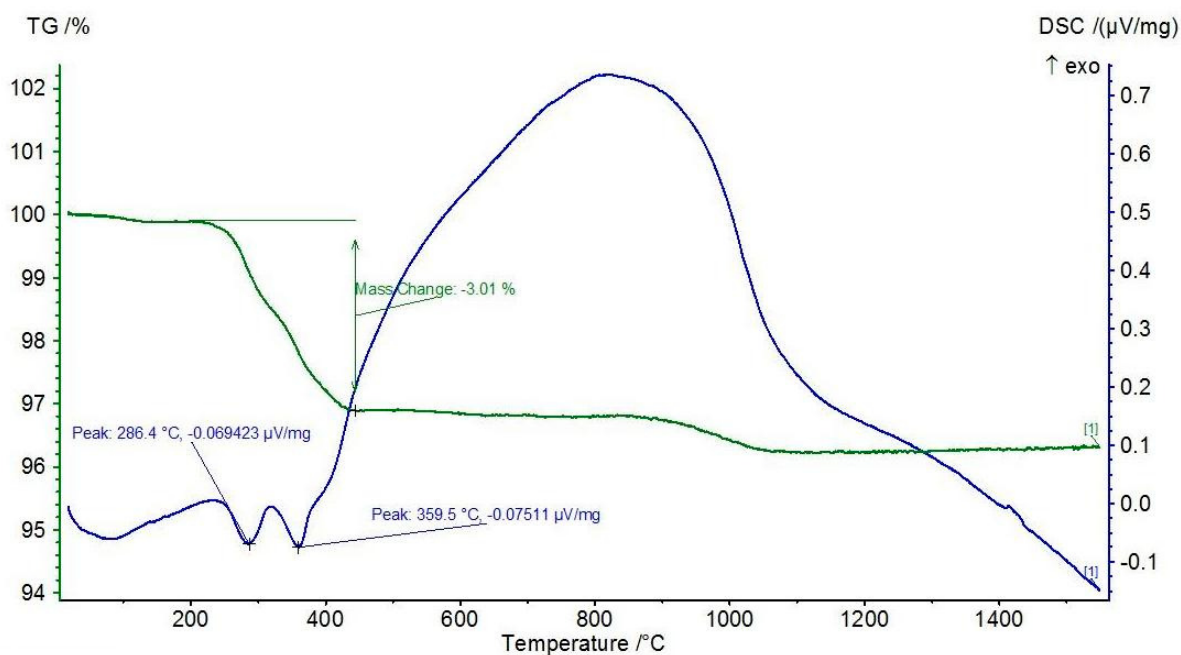


Figure 8.2 DSC-TG recorded on sample (4)  $\text{Pr}_2\text{O}_3$  from 20 °C to 1550 °C at 10K/min under nitrogen. 2<sup>nd</sup> attempt, showing greater mass loss compared to figure 8.1.

The phase diagram for praseodymium sesquioxide (figure 1.5) shows only 2 structures: the cubic C form and the hexagonal A form. The transition temperature from one form to the other is not well defined in the diagram but appears to be around 500°C. Therefore a deflection was expected to be seen in the DSC around this temperature. However, this was not observed. Looking at the above images, there were two deflections between 280°C and 360°C and a large and broad peak after this temperature. Figure 8.1 shows deflections at 288.5°C, 343.1°C, 652.1°C and 958.5°C; the deflection at 288.5°C is accompanied by a small mass loss of 1.17%. Figure 8.2 still shows 2 deflections between 280°C and 360°C, but the other peaks present in figure 8.1 are absent, the remainder of the DSC line having become a large hump. The mass loss has now increased to 3.01%. The broad peak in all of figures 8.1 to 8.4 was not explainable in terms of the deflections expected from the phase diagram and a machine fault was suspected. What was interesting to note was that the sample removed from the DSC was no longer pale green but red-black, indicating that oxidation may have occurred. The phase diagram for the praseodymium-oxygen system (figure 1.9) was consulted. The diagram indicates that the hexagonal  $\theta$  phase (sesquioxide) exists above 800°C, although in chapter 7 it has been established by XRPD that it can exist at

ambient temperature. It was at first surprising to find that the sesquioxide was not retained on heating; it was assumed that the cubic  $\phi$  phase present in the sample would be converted to hexagonal, leaving only the  $\theta$  form. That this did not occur gave an indication of the complex nature of the Pr-O system and the readiness of praseodymium to undergo oxidation, even using a nitrogen atmosphere. That the oxidation occurs at a low temperature and was not prevented by the protective and purge gases indicated that the reaction had low activation energy. This was confirmed by the kinetic work in Chapters 7 and 8.

The conversion to the  $\beta$  phase was identified as a possible explanation for the deflections between 280°C and 360°C. The Pr-O phase diagram indicates a temperature of about 275°C for this change, which is in agreement with the DSC results. However, oxidation of  $\text{Pr}_2\text{O}_3$  to  $\text{Pr}_6\text{O}_{11}$  would result in a mass increase of 3.2%, not a mass loss. It was believed that any mass increase was being masked by a larger loss, resulting in a net loss on the TG.  $\text{Pr}_2\text{O}_3$  is known for absorbing carbon dioxide and water from the air (Anderson and Gallagher 1963). The possibility of mass loss due to the release of bound water or carbon dioxide was considered. The initial sample (4) came sealed in a glass ampoule and between the initial XRPD pattern and one taken 2 months later there was some change, albeit both cubic and hexagonal phases were still readily discernible. The 3.2% increase in mass due to oxidation would be swamped by the loss of, say, a fraction of water or carbon dioxide. Additionally, the TG in figures 8.1 and 8.2 do not show agreement in mass loss; this may be due to the sample degrading over time.

To investigate the mass loss, a further 2 runs were carried out on sample (4). This time the sample was pre-heated prior to using the DSC with the intention of driving off any absorbed gas but without inducing any oxidation or phase change.

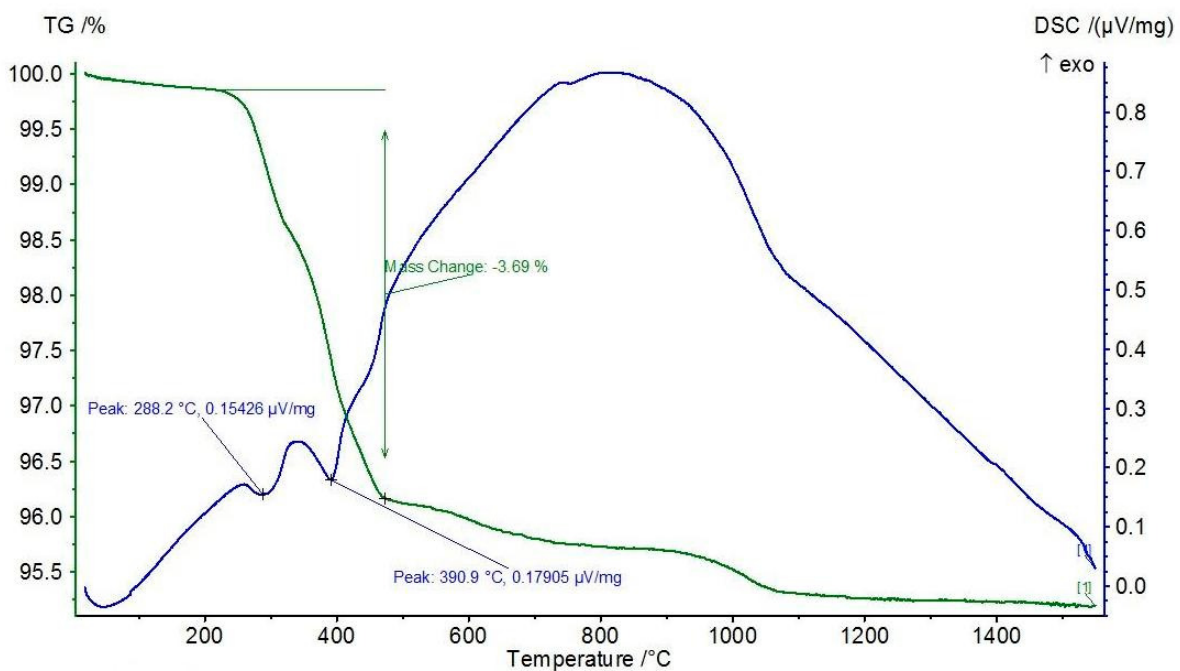


Figure 8.3 DSC-TG recorded on sample (4)  $Pr_2O_3$  from 20 °C to 1550 °C at 10K/min under nitrogen following heating at 170 °C for 10 minutes.

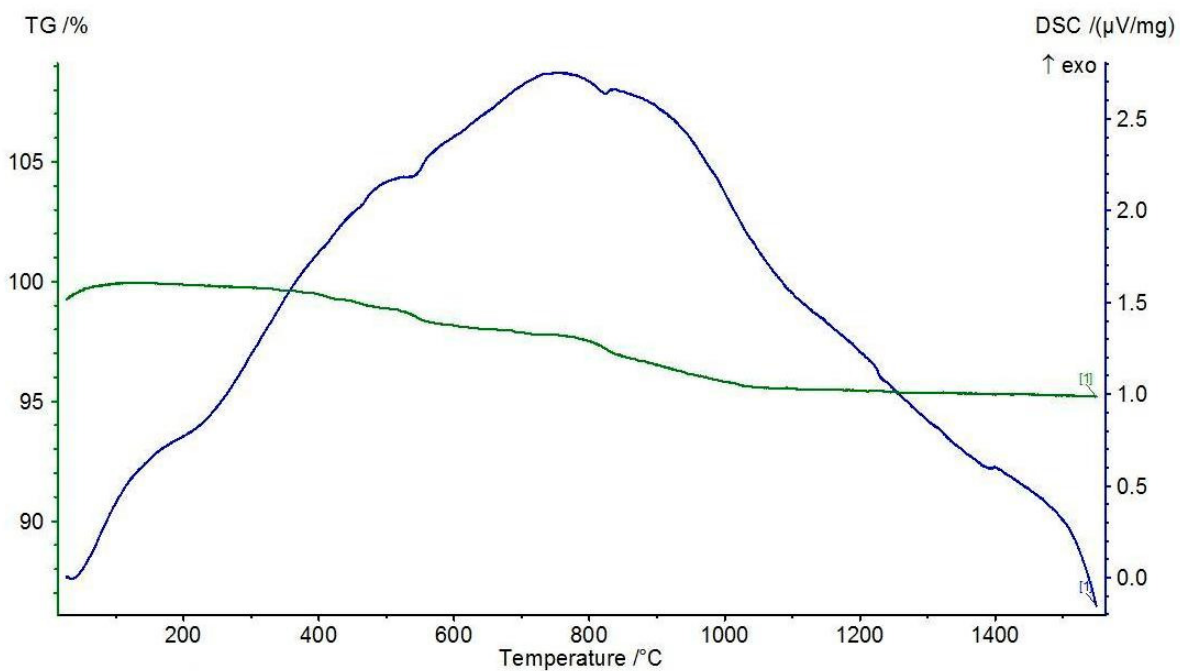


Figure 8.4 DSC 4 recorded on sample (4)  $Pr_2O_3$  from 20 °C to 1550 °C at 10K/min under nitrogen following heating at 380 °C for 30 minutes.

Figure 8.3 shows 2 deflections between 280°C and 400°C. As with figure 8.2 the other deflections are absent, the remainder of the DSC plot having become a large hump. The mass loss has now increased a small amount to 3.69%. Figure 8.4 shows that the deflections between 280°C and 400°C have disappeared, although 2 peaks have appeared at 516°C and 822°C which may correspond to those in figure 8.1, although they have appeared at much lower temperatures. The mass loss has now dropped to below 0.5%.

The results following pre-heating indicate two properties of  $\theta$  phase  $\text{Pr}_2\text{O}_3$ . Firstly, heating the sample to 170°C is not hot enough to drive off any bound gas. It may be that heating for an extended period at this temperature would cause a slow release of gas, but such facilities were not available. Secondly, the oxidation and the gas loss occur at the same point. It may be the case that the structural change from the hexagonal  $\theta$  phase to the cubic ceria structure forces the release of gas from the lattice.

Following these unexpected results and to determine whether or not there were instrumental problems, the sample was run on a Mettler Toledo DSC. The resultant DSC-TG is shown in figure 8.5.

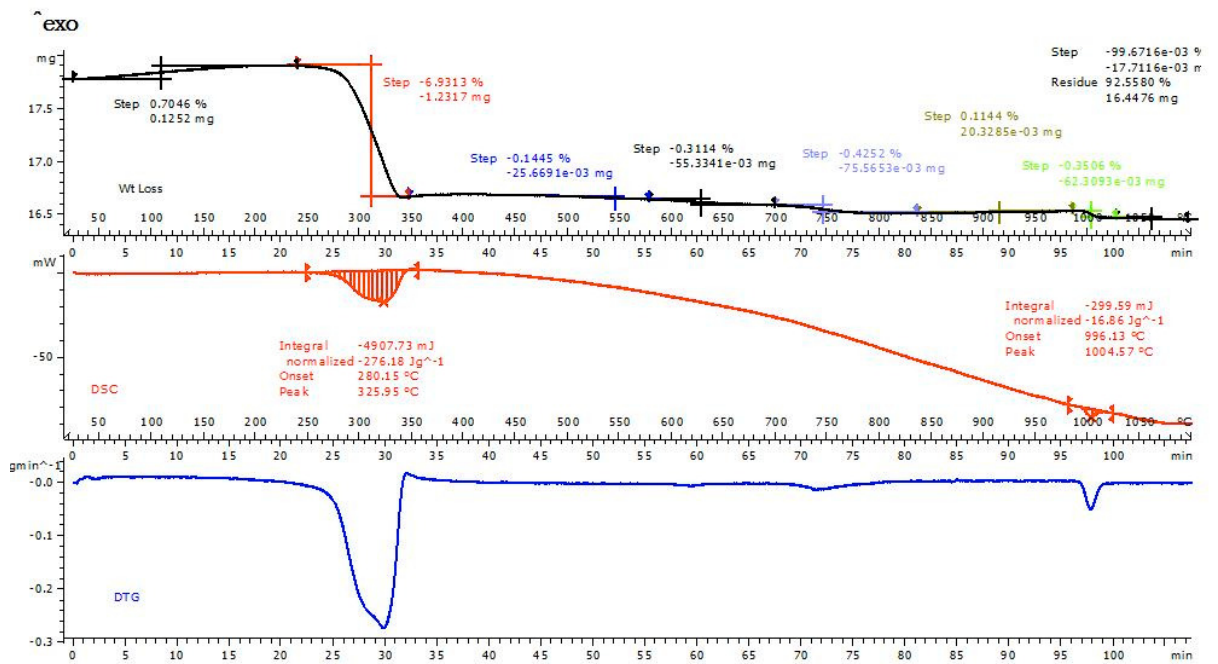


Figure 8.5 Mettler DSC-TG recorded on sample (4)  $\text{Pr}_2\text{O}_3$  from 20 °C to 1100 °C under nitrogen.

The Mettler data shows the same deflection around 300°C. Additionally it identifies a deflection around 400°C (as figure 8.1) and 900°C (as figures 8.1 and 8.4). There is clearly a difference in the quality of the baseline between the machines. Of interest is the mass loss around 275°C, which has increased to 7.15% ie almost double that in figure 8.4. This indicates that the material is still absorbing gas from the atmosphere, the Mettler Toledo being used a month after the results from the Netzsch machine.

## 8.2 FULL RANGE DSC-TG IN AIR

Because of the possibility of sample (4) degrading further a new sample (6)  $\text{Pr}_2\text{O}_3$  was obtained. The following image shows the initial DSC-TG recorded on this material.

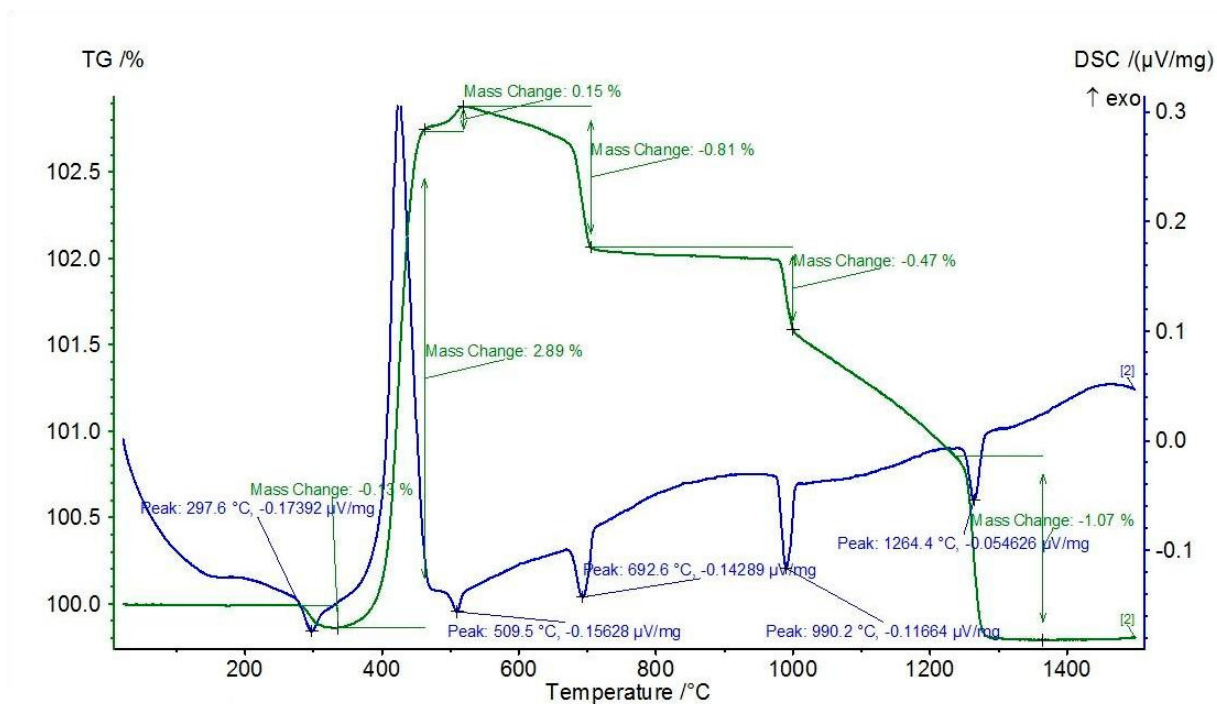


Fig 8.6 DSC-TG recorded on sample (6) from 20 °C to 1500 °C at 10K/min under air.

The DSC-TG for sample (6) was very different to those obtained from sample (4). Where, for sample (4), there had been a series of peaks around 300°C, there was now a small endotherm followed by a large exotherm. It was initially taken that this small endotherm might correspond to gas loss. Each deflection across the DSC was discernible as a discrete peak and many of these peaks could be related to known transitions on the Pr-O phase diagram. What is notable is that the broad hump had disappeared. The different look of the image for sample (6) is due to two factors. Firstly, sample (4) contained a mixture of cubic and hexagonal phases whereas sample (6) contained only the hexagonal phase. Secondly, sample (4) has absorbed significant gas before any DSC-TG work was performed on it. The degradation in the sample can be seen by comparing figures 7.7 and 7.34.

It is known from the Pr-O phase diagram that the ambient Pr<sub>2</sub>O<sub>3</sub> phase oxidises at 275°C. From the sesquioxide phase diagram it is unclear at exactly what temperature the cubic phase will convert although it appears to be in the region of 500°C. Furthermore, the sesquioxide diagram does not show oxidation, although it should be assumed that heating cubic Pr<sub>2</sub>O<sub>3</sub> is likely to result in oxidation too, presumably to Pr<sub>6</sub>O<sub>11</sub>. It may be that in addition to the sharp DSC peaks when the starting point is

pure hexagonal  $\text{Pr}_2\text{O}_3$  there is some additional contribution from the cubic phase that masks the detail obtained from the pure hexagonal phase. Conversion of the cubic phase may be sluggish, occurring over much of the run, resulting in a wide hump, as shown in figures 8.1 to 8.4.

The TG for sample (6) shows a small mass loss of 0.13% around 275°C. This is likely to be gas loss from the sample; there has already been a small absorption from the air in the time the bottle had been opened. Following this mass loss there is a large gain of 2.89%, presumably due to oxidation. The expected mass gain for  $\text{Pr}_2\text{O}_3 \rightarrow \text{Pr}_6\text{O}_{11}$  would be 3.2%.

### 8.3 RAMPS IN NITROGEN

The DSC data recorded during the 7 ramps performed on sample (4) are shown in figure 8.7 below.

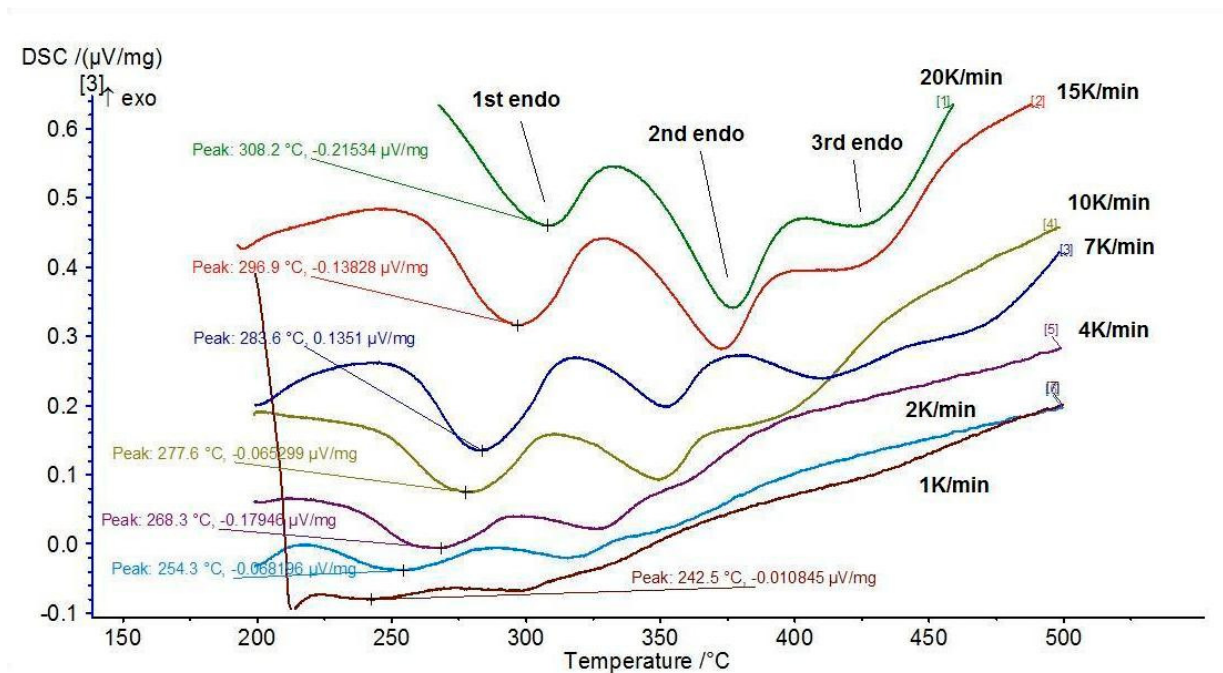


Figure 8.7 DSC recorded on sample (4)  $\text{Pr}_2\text{O}_3$  from 200 °C to 500 °C under nitrogen. Heating rates are indicated beside the lines.

The reaction appears to follow a three-stage process. This is understandable as there are likely to be deflections for the loss of gas, and also for both ambient phases converting

to the high-temperature phase. The table below lists the temperature ramps and the corresponding transition temperatures as identified by the maximum deflection for the first endotherm. The calculations are taken from the method given in Chapter 4.

| Heating rate, $\phi$<br>(K/min) | Temp of max<br>deflection, $T_m$ (°C) | $T_m$ (K) | $T_m^{-1}$ | $\ln(\phi/T_m^2)$ |
|---------------------------------|---------------------------------------|-----------|------------|-------------------|
| 1                               | 242.5                                 | 515.7     | 0.001939   | -12.491           |
| 2                               | 254.3                                 | 527.5     | 0.001896   | -11.843           |
| 4                               | 268.3                                 | 541.5     | 0.001847   | -11.202           |
| 7                               | 277.6                                 | 550.8     | 0.001816   | -10.677           |
| 10                              | 283.6                                 | 556.8     | 0.001796   | -10.342           |
| 15                              | 296.9                                 | 570.1     | 0.001754   | -9.984            |
| 20                              | 308.2                                 | 581.4     | 0.001720   | -9.735            |

Table 8.1 Kissinger analysis for 1<sup>st</sup> endotherm - sample (4) Pr<sub>2</sub>O<sub>3</sub>.

Figures 8.8 and 8.9 below show the plot of temperature against heating rate and the linear plot from which the activation energy can be calculated.

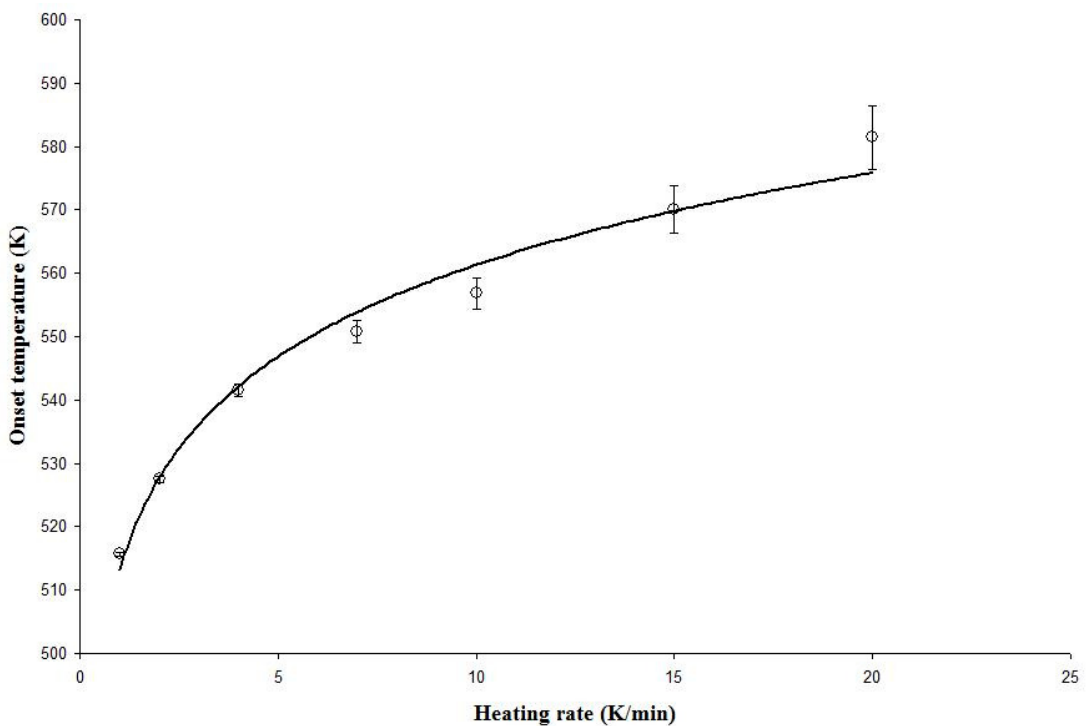


Figure 8.8 Temperature of maximum deflection,  $T_m$ , versus heating rate,  $\phi$ , for sample (4) Pr<sub>2</sub>O<sub>3</sub> 1<sup>st</sup> endotherm.

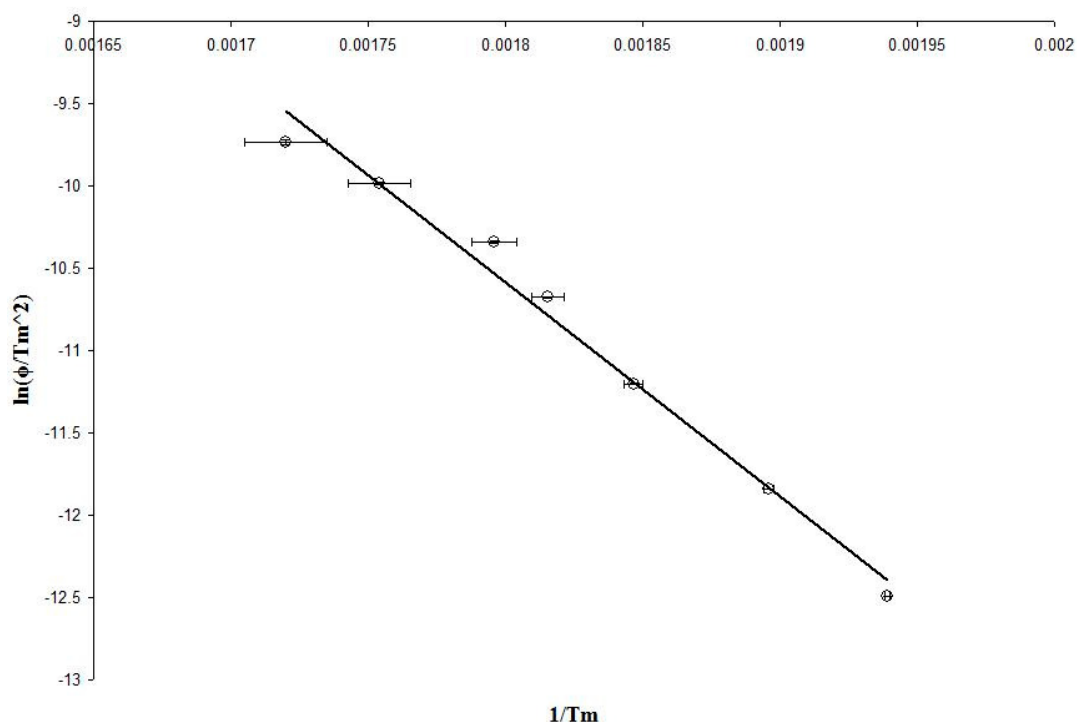


Figure 8.9 Plot of  $\ln(\phi/T_m^2)$  against  $1/T_m$  for sample (4)  $Pr_2O_3$  1<sup>st</sup> endotherm.

In chapter 4 it was shown that the gradient of the straight line is equal to  $-E_A/R$ . Therefore the activation energy was calculated to be 108(9)  $\text{kJ}\cdot\text{mol}^{-1}$ .

Because the conversion is a multi-stage process (there are 3 endotherms) it was decided to analyse the other two peaks in the same way. Kissinger Analysis is dependent upon the shift in peaks with heating rate rather than their absolute positions, so this seemed a reasonable step to take.

| $\phi$ (K/min) | $T_m$ (°C) | $T_m$ (K) | $T_m^{-1}$  | $\ln(\phi T_m^2)$ |
|----------------|------------|-----------|-------------|-------------------|
| 1              | 296.7      | 569.9     | 0.001755(4) | -12.691(6)        |
| 2              | 315.5      | 588.7     | 0.001699    | -12.063(6)        |
| 4              | 326.6      | 599.8     | 0.001667    | -11.407(6)        |
| 7              | 349.8      | 623       | 0.001605    | -10.923(6)        |
| 10             | 351.8      | 625       | 0.001600    | -10.573(6)        |
| 15             | 372.5      | 645.7     | 0.001549    | -10.233(6)        |
| 20             | 377.0      | 650.2     | 0.001538    | -9.959(6)         |

Table 8.2 Kissinger analysis for 2<sup>nd</sup> endotherm - sample (4)  $Pr_2O_3$ .

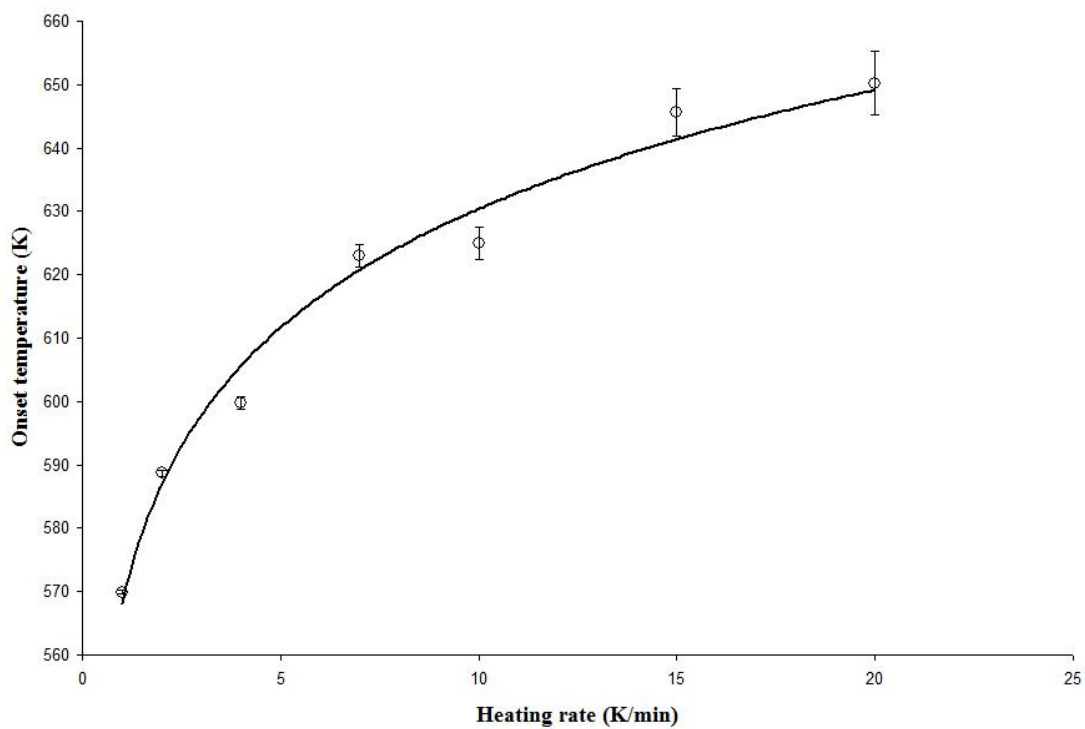


Figure 8.10 Temperature of maximum deflection,  $T_m$ , versus heating rate,  $\phi$ , for sample (4)  $Pr_2O_3$  2<sup>nd</sup> endotherm.

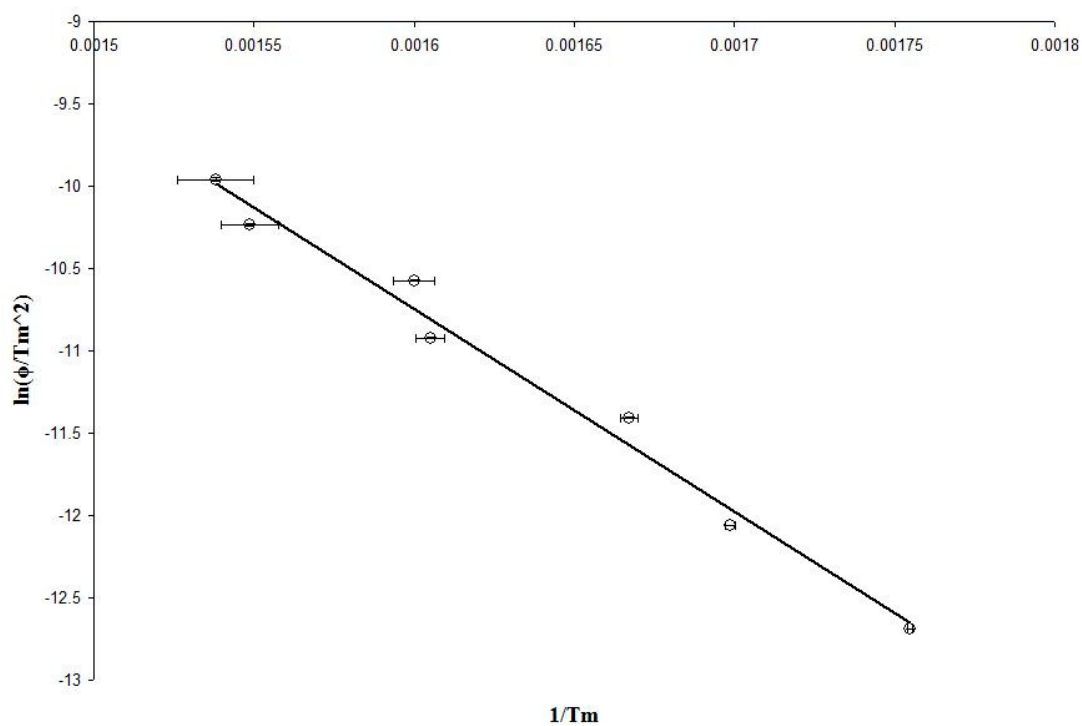


Figure 8.11 Plot of  $\ln(\phi/T_m^2)$  against  $1/T_m$  for sample (4)  $Pr_2O_3$  2<sup>nd</sup> endotherm.

| $\phi$ (K/min) | $T_m$ ( $^{\circ}$ C) | $T_m$ (K) | $T_m^{-1}$ | $\ln(\phi/T_m^2)$ |
|----------------|-----------------------|-----------|------------|-------------------|
| 1              | Not discernible       |           |            |                   |
| 2              | 349.0                 | 622.2     | 0.001607   | -12.173(6)        |
| 4              | 361.0 (unclear)       | 634.2     | 0.001577   | -11.518(6)        |
| 7              | 395.6 (unclear)       | 668.8     | 0.001495   | -11.065(6)        |
| 10             | 410.3                 | 683.5     | 0.001463   | -10.752(6)        |
| 15             | 416.7 (unclear)       | 689.9     | 0.001449   | -10.365(6)        |
| 20             | 422.9                 | 696.1     | 0.001437   | -10.095(6)        |

Table 8.3 Kissinger analysis for 3<sup>rd</sup> endotherm - sample (4) Pr<sub>2</sub>O<sub>3</sub>.

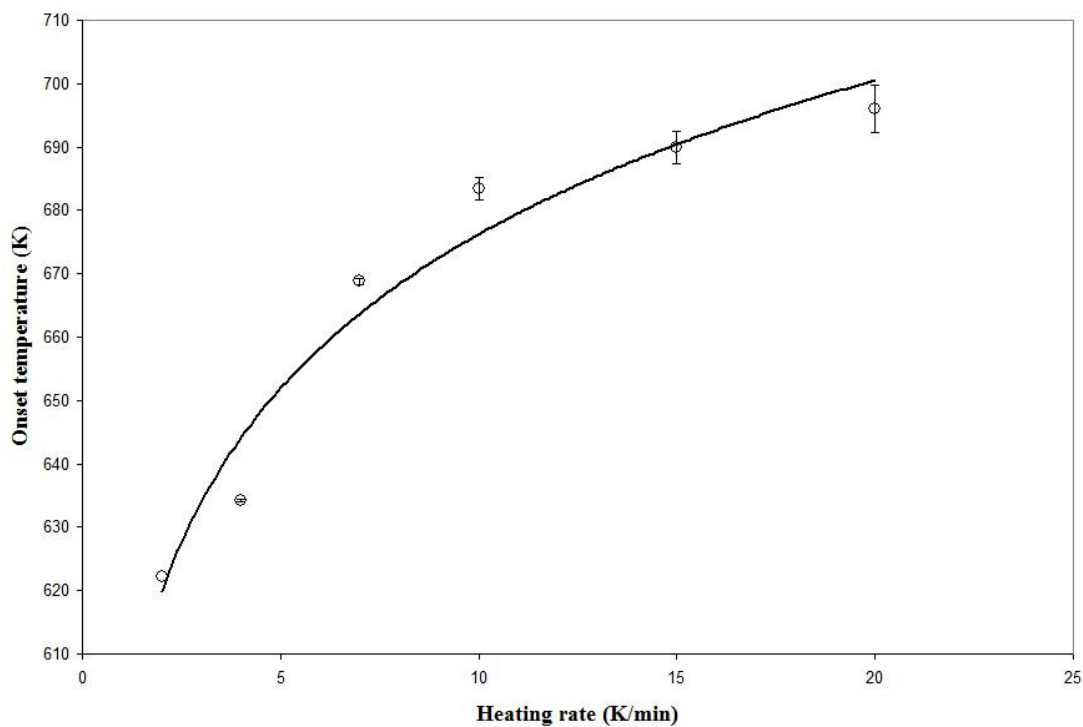


Figure 8.12 Temperature of maximum deflection,  $T_m$ , versus heating rate,  $\phi$ , for sample (4) Pr<sub>2</sub>O<sub>3</sub> 3<sup>rd</sup> endotherm.

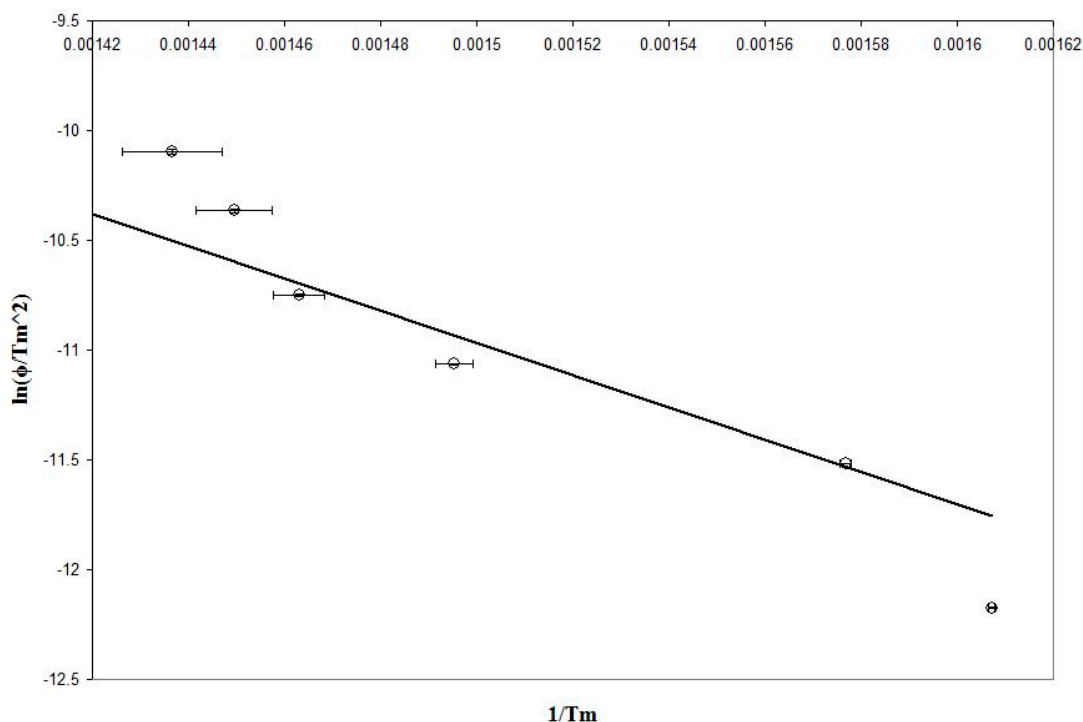


Figure 8.13 Plot of  $\ln(\phi/T_m^2)$  against  $1/T_m$  for sample (4)  $\text{Pr}_2\text{O}_3$  3<sup>rd</sup> endotherm.

The activation energy for endotherm 2 was calculated to be 103(6)  $\text{kJ}\cdot\text{mol}^{-1}$ . For endotherm 3 the figure is 61(3)  $\text{kJ}\cdot\text{mol}^{-1}$  if all data points are used. However, there was some difficulty measuring the troughs for the 4, 7 and 15K/minute runs. The Netzsch software was unable to pick them up and so they had to be determined manually. Omitting these 3 points the figure is 56(3)  $\text{kJ}\cdot\text{mol}^{-1}$ , which is still close to the former reading.

## 8.4 RAMPS IN AIR

### 8.4.1 Ramp performed between 20 °C and 600 °C

The DSC recorded during the 7 ramps performed between 20°C and 600°C on sample (6) are shown in figure 8.14 below.

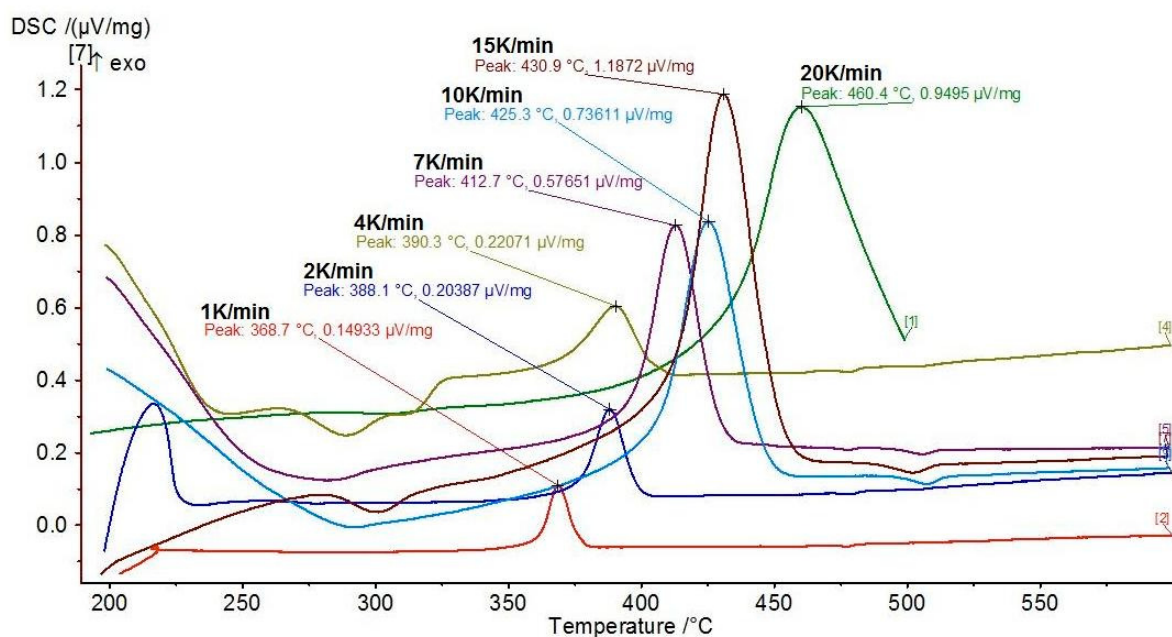


Figure 8.14 DSC ramps on sample (6)  $Pr_2O_3$  from 200 °C to 600 °C in air.

As with figure 8.6, the DSC data collected from sample (6) shows a single deflection around 400°C rather than the three shown by sample (4). The sample (6) deflections do not follow as smooth a shift with heating rate as for sample (4); the 15K/min and 10K/min peaks are close, as are those for 4K/min and 2K/min. The table below lists the temperature ramps and the corresponding temperatures of the maximum deflection for this exotherm.

| $\phi$ (K/min) | $T_m$ (°C) | $T_m$ (K) | $T_m^{-1}$ | $\ln(\phi/T_m^2)$ |
|----------------|------------|-----------|------------|-------------------|
| 1              | 368.7      | 641.9     | 0.001558   | -12.929           |
| 2              | 388.1      | 661.3     | 0.001512   | -12.295           |
| 4              | 390.3      | 663.5     | 0.001507   | -11.609           |
| 7              | 412.7      | 685.9     | 0.001458   | -11.116           |
| 10             | 425.3      | 698.5     | 0.001432   | -10.795           |
| 15             | 430.9      | 704.1     | 0.001420   | -10.406           |
| 20             | 460.4      | 733.6     | 0.001363   | -10.200           |

Table 8.4 Kissinger analysis for 1<sup>st</sup> exotherm - sample (6)  $Pr_2O_3$ . Data recorded from 200 °C to 600 °C.

Figures 8.15 and 8.16 below show the plot of temperature against heating rate and the linear plot from which the activation energy can be calculated.

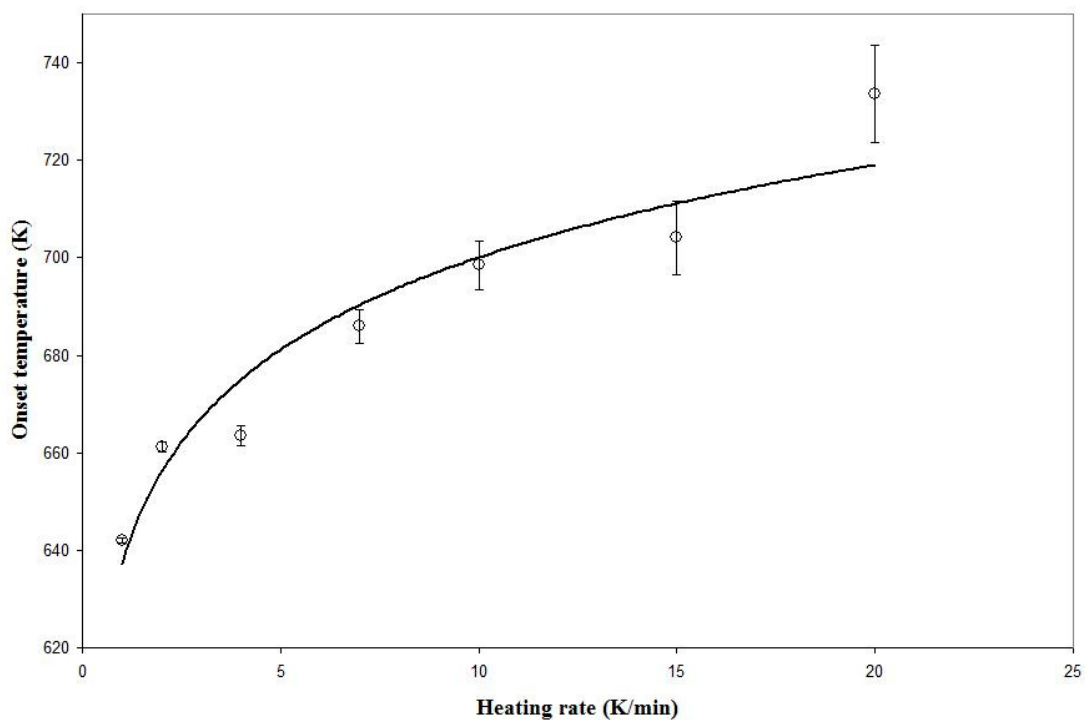


Figure 8.15 Temperature of maximum deflection,  $T_m$ , versus heating rate,  $\phi$ , for sample (6)  $\text{Pr}_2\text{O}_3$  1<sup>st</sup> exotherm.

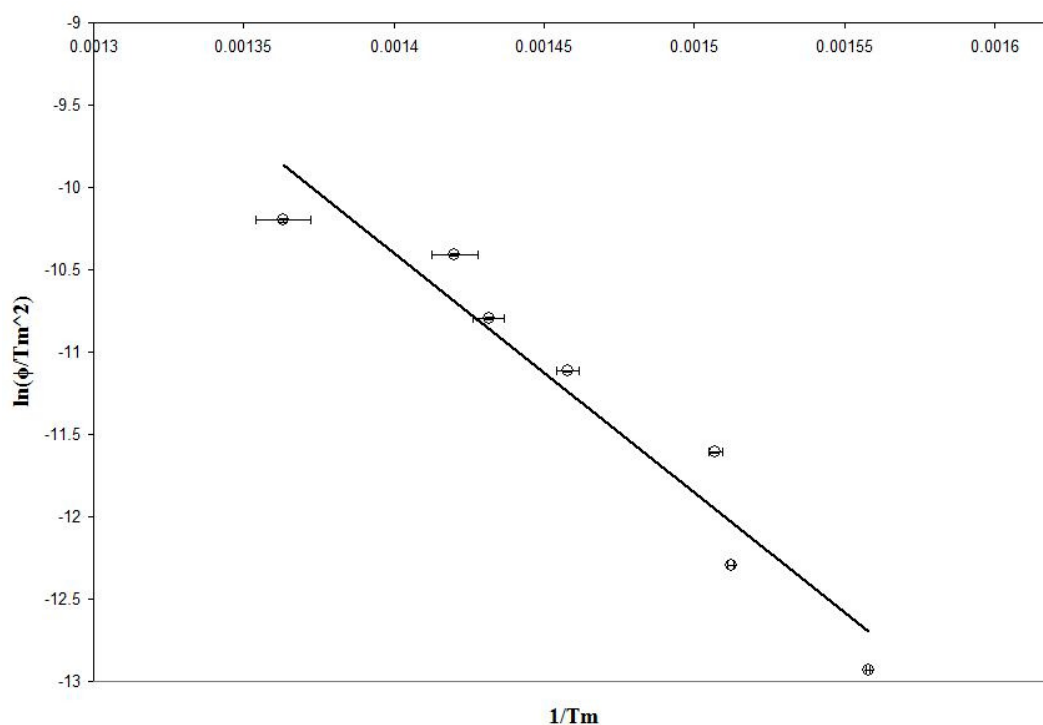


Figure 8.16 Plot of  $\ln(\phi/T_m^2)$  against  $1/T_m$ , for sample (6)  $\text{Pr}_2\text{O}_3$  1<sup>st</sup> exotherm.

The activation energy for the exotherm in sample (6) was calculated to be  $-122(6)$   $\text{kJ}\cdot\text{mol}^{-1}$ . It was notable that the DSC data for the 4K/min ramp showed other features,

similar to figure 8.7 and presumably due to gas absorption. This was confirmed by the associated TG plot, which was very different to those for the other ramps. Furthermore, the temperature of maximum deflection for the 4K/min ramp lies unusually close to that for the 2K/min ramp (see table 8.4), again presumably because of sample contamination. Omitting the 4K/min data point the activation energy becomes  $-128(6)$   $\text{kJ}\cdot\text{mol}^{-1}$ .

It is notable that figures 8.7 and 8.17 both show a smooth shift of peak position with heating rate. However, there still appears to be a problem with figure 8.14 in that the 20K/min data point does not follow this trend. The exact reason for this is not known and due to instrument availability it was not possible to repeat the recording. Although it would have been useful to repeat the 20K/min ramp, if both 20K/min and 4K/min data points are omitted the value for the activation energy is  $-152(8)$   $\text{kJ}\cdot\text{mol}^{-1}$ .

#### 8.4.2 Ramp performed between 20 °C and 1500 °C

The DSC recorded for the 7 ramps performed between 20°C and 1500°C on sample (6) are shown in figure 8.17 below. The labelled peak is the 1<sup>st</sup> exotherm.

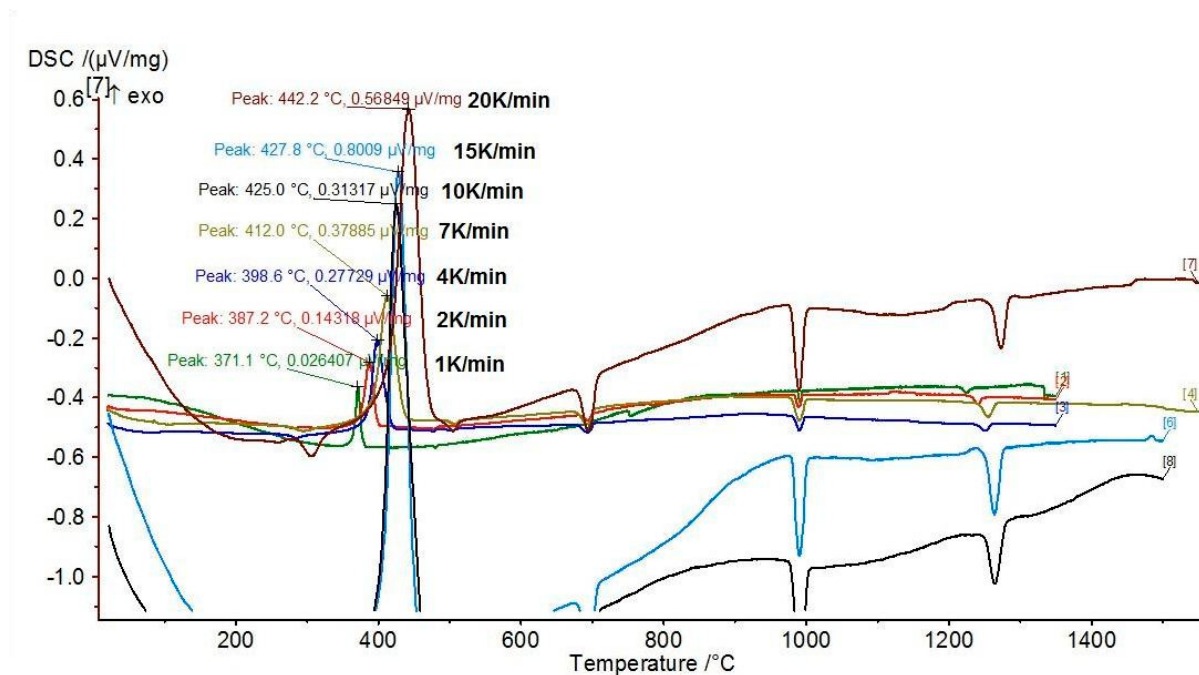


Figure 8.17 DSC ramps on sample (6)  $\text{Pr}_2\text{O}_3$  from 20 °C to 1500 °C in air.

The change in peak temperature with heating rate is more uniform than for the 20°C to 600°C run, although the 15K/min and 10K/min peaks are still close. The table below lists the temperature ramps and the corresponding temperatures of the maximum deflection for the same exotherm studied in the 20°C to 500°C runs above.

| $\phi$ (K/min) | $T_m$ (°C) | $T_m$ (K) | $T_m^{-1}$ | $\ln(\phi/T_m^2)$ |
|----------------|------------|-----------|------------|-------------------|
| 1              | 371.1      | 644.3     | 0.001552   | -12.936           |
| 2              | 387.2      | 660.4     | 0.001514   | -12.292           |
| 4              | 398.6      | 671.8     | 0.001489   | -11.634           |
| 7              | 412        | 685.2     | 0.001460   | -11.113           |
| 10             | 425        | 698.2     | 0.001432   | -10.794           |
| 15             | 427.8      | 701.0     | 0.001427   | -10.397           |
| 20             | 442.2      | 715.4     | 0.001398   | -10.150           |

Table 8.5 Kissinger analysis for 1<sup>st</sup> exotherm - sample (6) Pr<sub>2</sub>O<sub>3</sub>. Data recorded from 20°C to 1500°C.

Figures 8.18 and 8.19 below show the plot of temperature against heating rate and the linear plot from which the activation energy can be calculated.

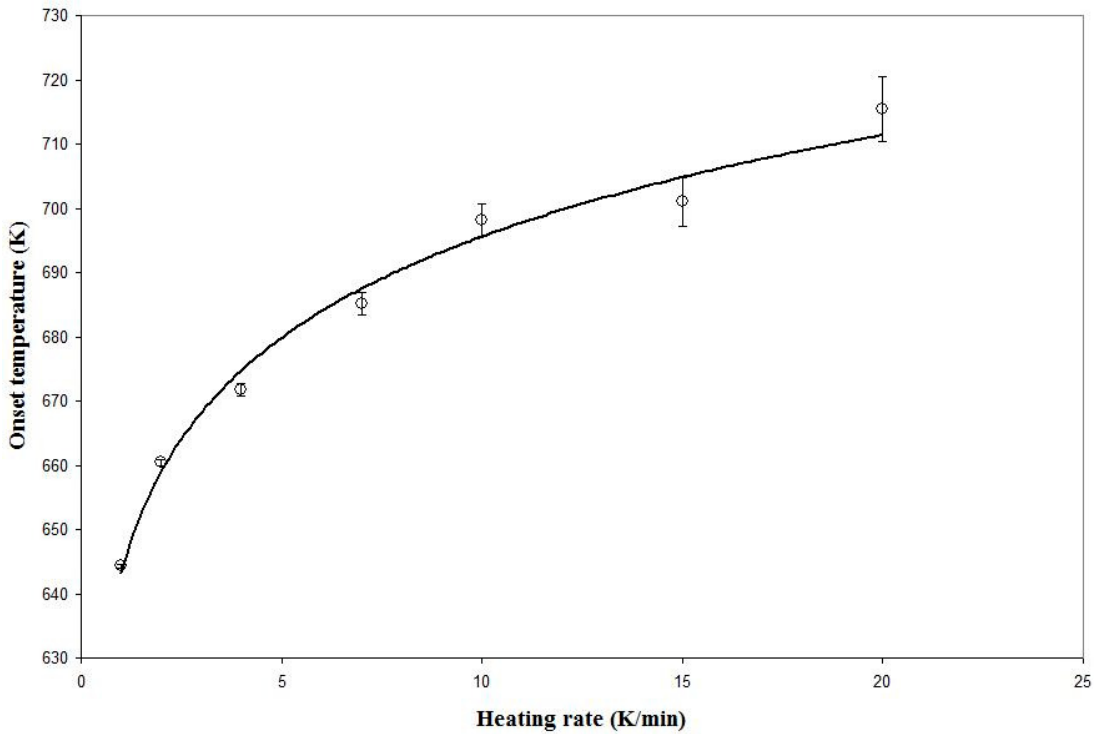


Figure 8.18 Temperature of maximum deflection,  $T_m$ , versus heating rate,  $\phi$ , for sample (6) Pr<sub>2</sub>O<sub>3</sub> 1<sup>st</sup> exotherm.

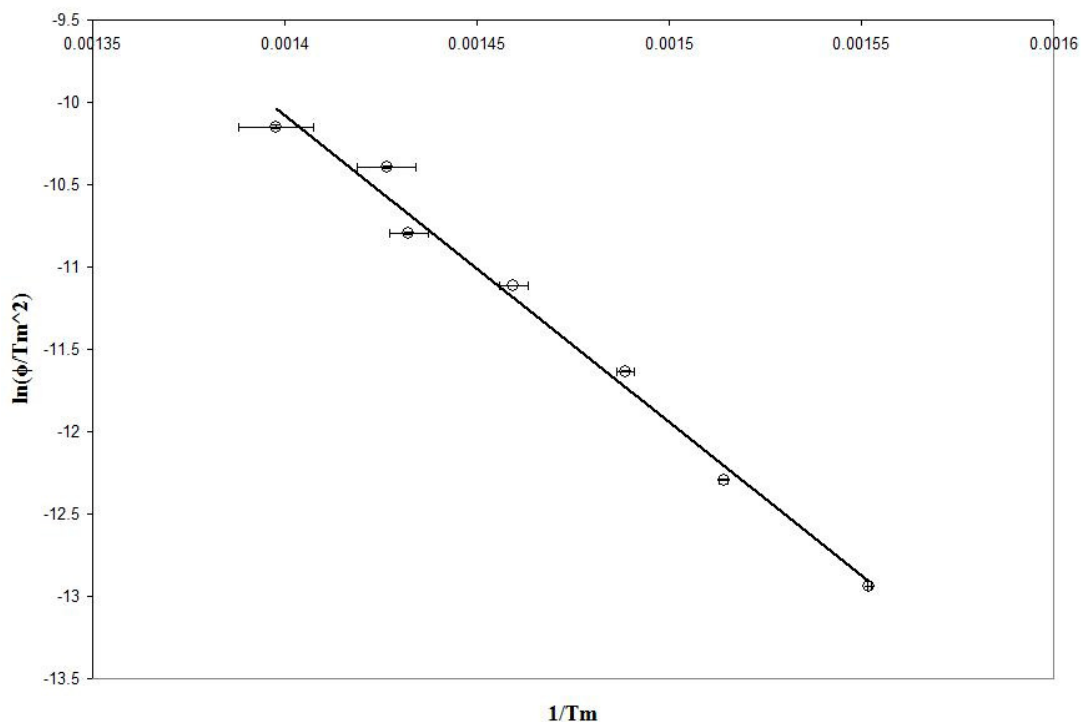


Figure 8.19 Plot of  $\ln(\phi/T_m^2)$  against  $1/T_m$  for sample (6)  $\text{Pr}_2\text{O}_3$  1<sup>st</sup> exotherm.

Analysis of the above results gave an activation energy for the exotherm in sample (6) of  $-155(10) \text{ kJ}\cdot\text{mol}^{-1}$ .

The data in figure 8.17 was also used to examine the four deflections above  $400^\circ\text{C}$ . The only transition which produced meaningful data was the one occurring around  $1250^\circ\text{C}$ , where the  $\sigma$  phase converts to the highest temperature phase of  $\theta \text{Pr}_2\text{O}_3$ . The data for this endotherm is given in table 8.6 below.

| $\phi$ (K/min) | $T_m$ ( $^\circ\text{C}$ ) | $T_m$ (K) | $T_m^{-1}$ | $\ln(\phi/T_m^2)$ |
|----------------|----------------------------|-----------|------------|-------------------|
| 1              | 1224.3                     | 1497.5    | 0.0006680  | -14.622           |
| 2              | 1240.2                     | 1513.4    | 0.0006609  | -13.951           |
| 4              | 1250.3                     | 1523.5    | 0.0006566  | -13.271           |
| 7              | 1254.9                     | 1528.1    | 0.0006545  | -12.716           |
| 10             | 1264.4                     | 1537.6    | 0.0006506  | -12.373           |
| 15             | 1263.9                     | 1537.1    | 0.0006510  | -11.966           |
| 20             | 1273.1                     | 1546.3    | 0.0006468  | -11.691           |

Table 8.6 Kissinger analysis for endotherm at  $1250^\circ\text{C}$  - sample (6)  $\text{Pr}_2\text{O}_3$ . Data recorded from  $20^\circ\text{C}$  to  $1500^\circ\text{C}$ .

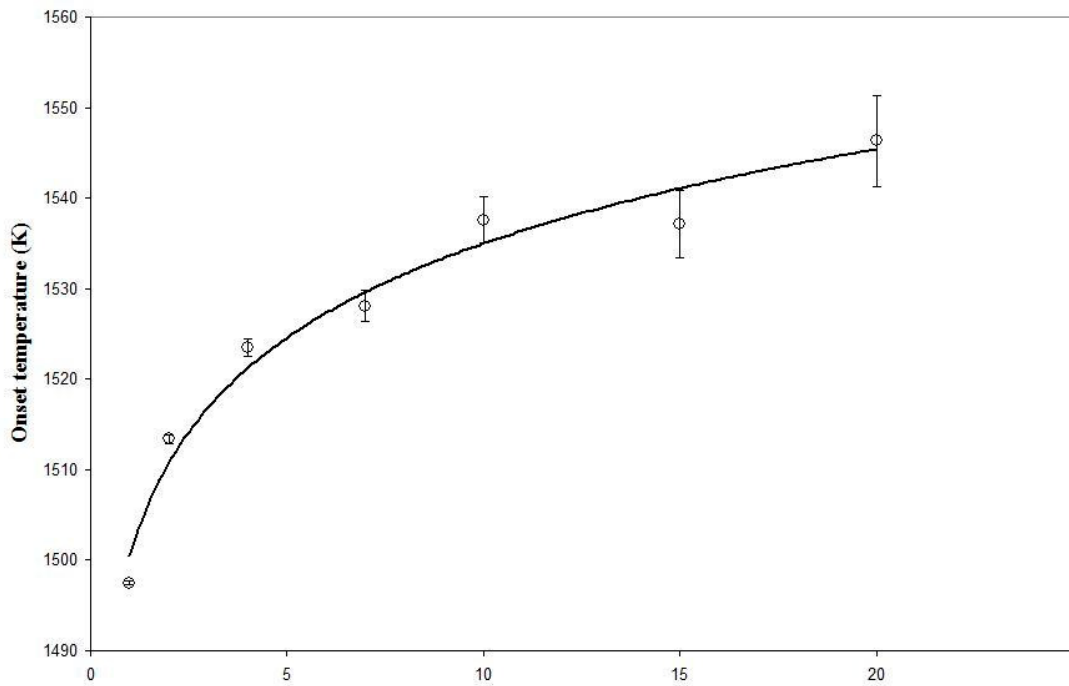


Figure 8.20 Temperature of maximum deflection,  $T_m$ , versus heating rate,  $\phi$ , for sample (6) 1250 °C endotherm.

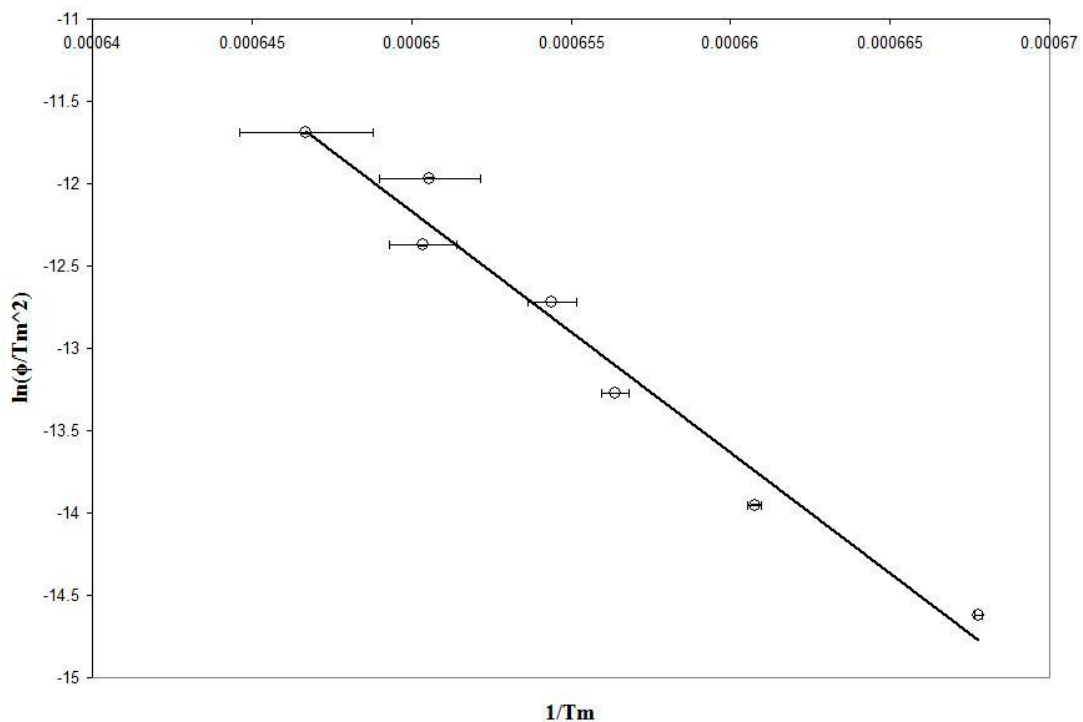


Figure 8.21 Plot of  $\ln(\phi/T_m^2)$  against  $1/T_m$ , for sample (6) 1250 °C endotherm.

Analysis of the above results gave an activation energy of 1224(122) kJ.mol<sup>-1</sup> for the endotherm at 1250°C.

### 8.4.3 Summary of activation energies

| Sample                             | Ramp           | Peak                      | EA <sub>1</sub> (kJ.mol <sup>-1</sup> ) | EA <sub>2</sub> * | EA <sub>3</sub> * |
|------------------------------------|----------------|---------------------------|---|-------------------|-------------------|
| (4) Pr <sub>2</sub> O <sub>3</sub> | 200°C to 500°C | 1 <sup>st</sup> endotherm | 108(9)                                  |                   |                   |
| (4) Pr <sub>2</sub> O <sub>3</sub> | 200°C to 500°C | 2 <sup>nd</sup> endotherm | 103(6)                                  |                   |                   |
| (4) Pr <sub>2</sub> O <sub>3</sub> | 200°C to 500°C | 3 <sup>rd</sup> endotherm | 61(3)                                   |                   |                   |
| (6) Pr <sub>2</sub> O <sub>3</sub> | 20°C to 500°C  | 1 <sup>st</sup> exotherm  | -122(6)                                 | -128(6)           | -152(8)           |
| (6) Pr <sub>2</sub> O <sub>3</sub> | 20°C to 1500°C | 1 <sup>st</sup> exotherm  | -155(10)                                |                   |                   |
| (6) Pr <sub>2</sub> O <sub>3</sub> | 20°C to 1500°C | 1250°C endotherm          | 1224(122)                               |                   |                   |

Table 8.7 Activation energies for phase changes in samples (4) and (6). \* indicates omitted data point(s).

## 8.5 TWO-DIRECTIONAL DSC-TG: 20°C TO 1400°C AND BACK

To determine whether any of the transitions in the Pr-O system were reversible, sample (6) was heated to 1400°C and cooled back again. The recorded DSC is shown in figure 8.22.

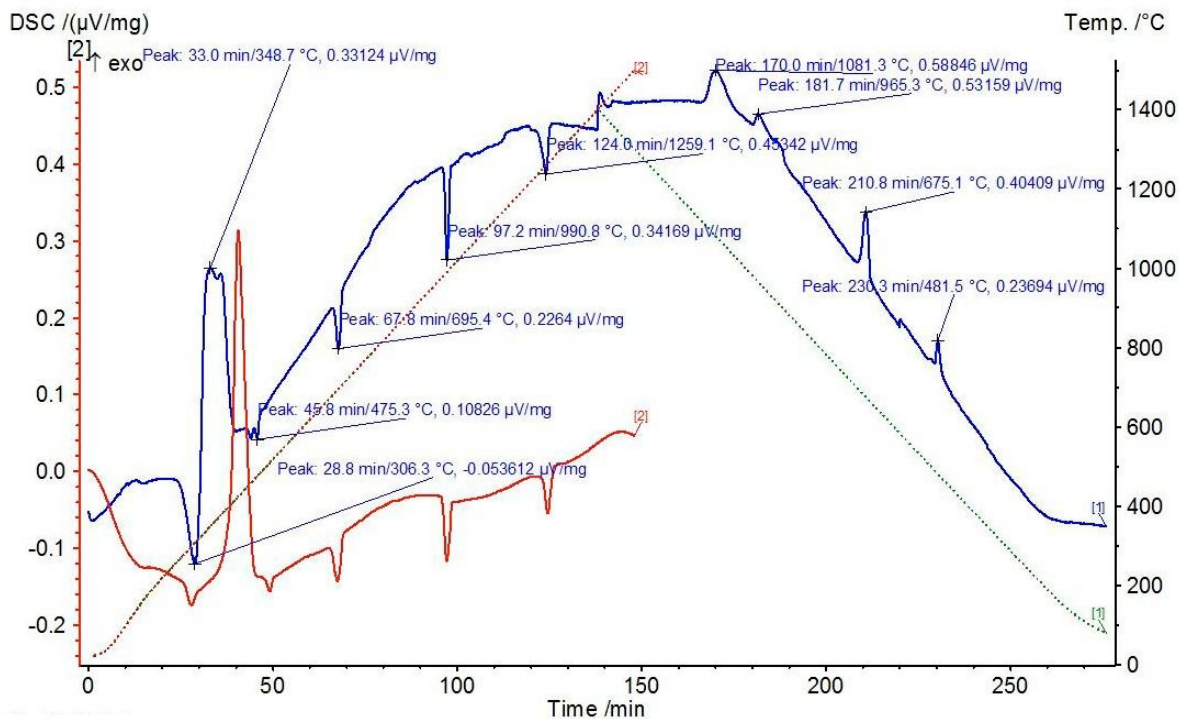


Figure 8.22 DSC recorded on sample (6)  $Pr_2O_3$  from 20 °C to 1400 °C and back at 10K/min in air. The data collected from 20 °C to 1500 °C (from figure 8.6) is shown on the left for comparison.

There is a clear vertical correlation in figure 8.22 between the two lines, as should be expected since they are of the same sample, albeit at different ages. As this was one of the later experiments on sample (6) there has been considerable gas absorption, shown by the TG curve in figure 8.23, below.

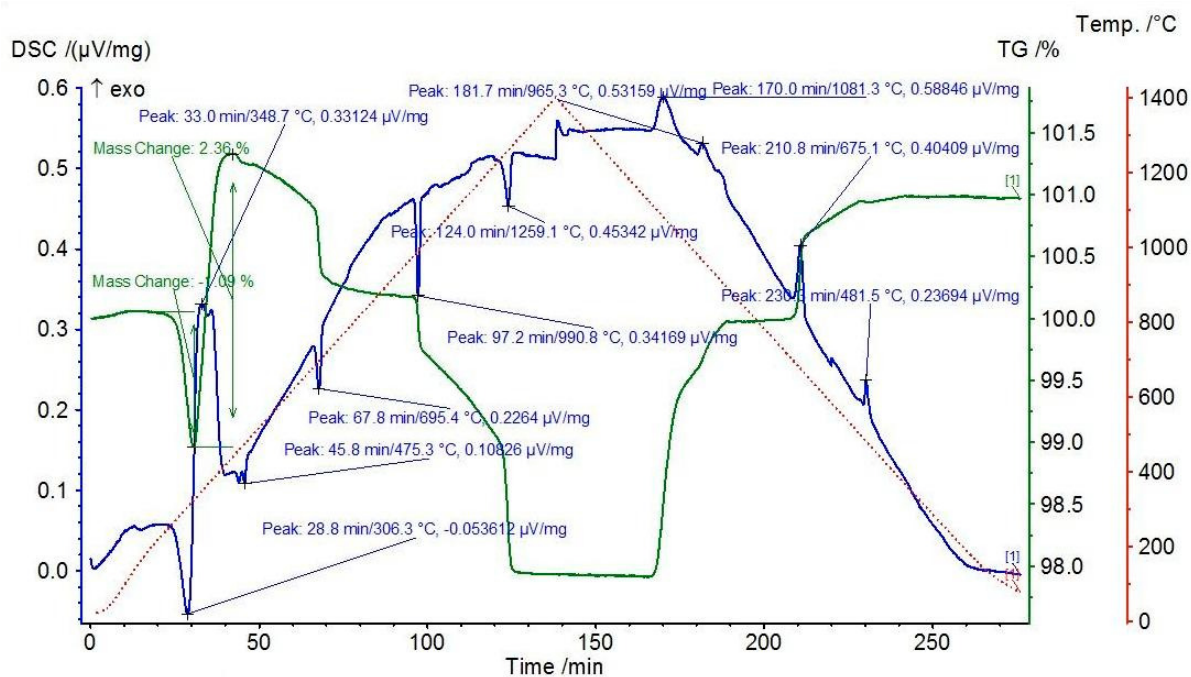


Figure 8.23 DSC-TG recorded on sample (6)  $Pr_2O_3$  from 20  $^{\circ}C$  to 1400  $^{\circ}C$  and back at 10K/min in air.

Figure 8.6 showed a mass loss on sample (6) of 0.13% and a mass gain due to oxidation of 2.89%. Figure 8.23 shows the sample 2 months later. There is now a greater mass loss (1.09%). There is also a change to the profile of the corresponding exotherm for the oxidation. Other than the weight loss at approximately 300 $^{\circ}C$ , the TG appears fairly symmetrical about the centre of the figure. This point represents 1400 $^{\circ}C$  where the instrument began to cool the sample. Figure 8.24 shows a wrapped image.

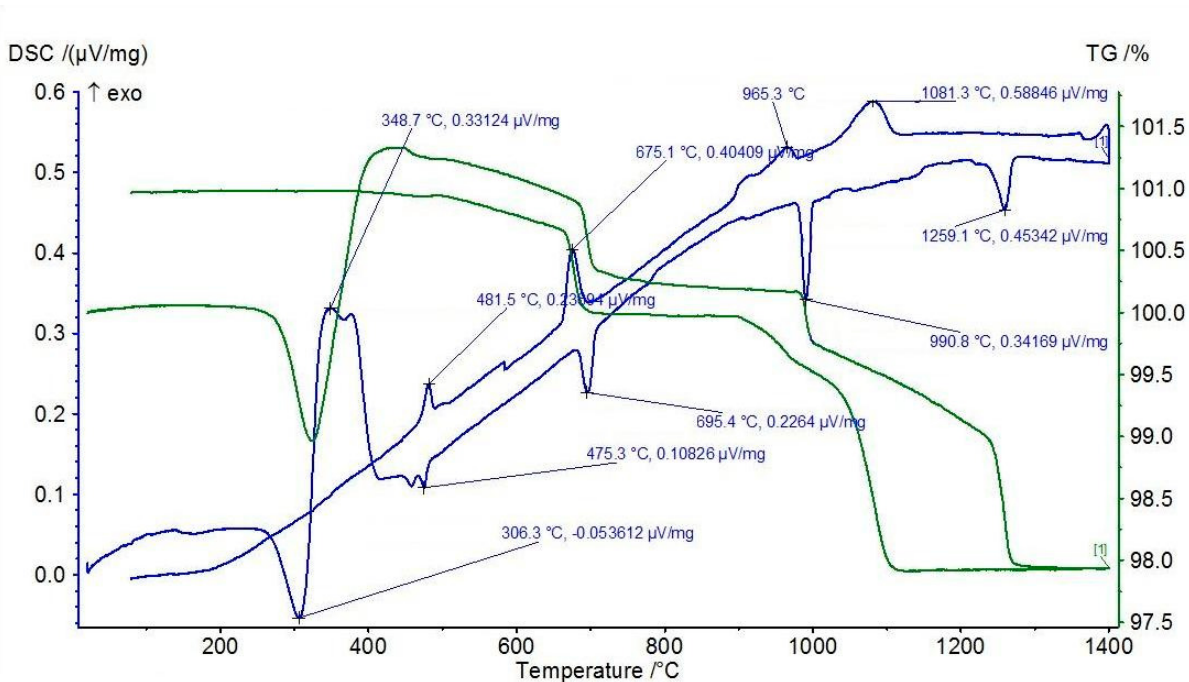


Figure 8.24 DSC-TG recorded on sample (6)  $Pr_2O_3$  from 20 °C to 1400 °C and back at 10K/min in air. Image wrapped to compare associated transitions.

Figure 8.25 shows the values for the mass changes.

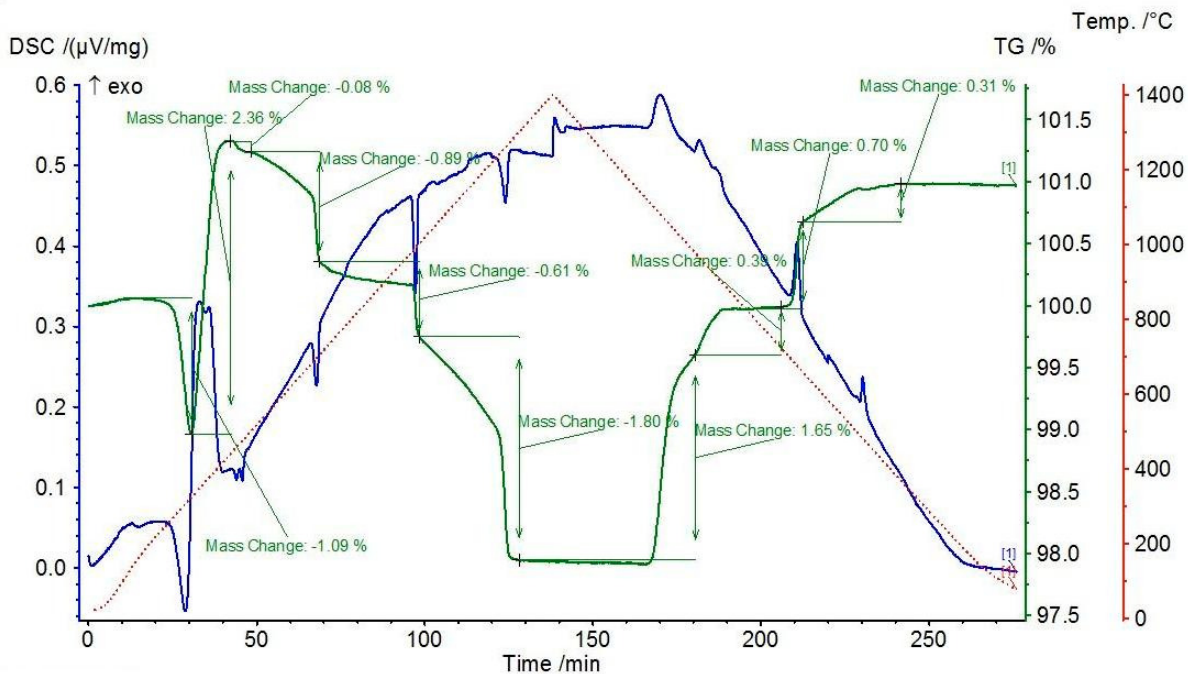


Figure 8.25 DSC-TG recorded on sample (6)  $Pr_2O_3$  from 20 °C to 1400 °C and back at 10K/min in air. Mass changes are shown.

The transition temperatures and mass changes occurring during the heating and cooling ramp show hysteresis. This has been tabulated below.

| Feature         | DSC temp (°C) | TG temp (°C) | Mass change (%) | Ramp    |
|-----------------|---------------|--------------|-----------------|---------|
| 1               | 306.3         | 264.8        | -1.09           | Heating |
| 2               | 348.7         | 322.3        | +2.36           | Heating |
| 3 <sup>1</sup>  | 475.3         | 452.7        | -0.09           | Heating |
| 4 <sup>2</sup>  | 695.4         | 688.0        | -0.88           | Heating |
| 5 <sup>3</sup>  | 990.8         | 981.5        | -0.61           | Heating |
| 6 <sup>4</sup>  | 1259.1        | 1238.1       | -1.80           | Heating |
| 7 <sup>4</sup>  | 1081.3        | 1114.4       | +1.65           | Cooling |
| 8 <sup>3</sup>  | 965.3         | 970.8        | +0.39           | Cooling |
| 9 <sup>2</sup>  | 675.1         | 697.0        | +0.70           | Cooling |
| 10 <sup>1</sup> | 481.5         | 493.4        | +0.31           | Cooling |

Table 8.8 Transition temperatures for sample (6) Pr<sub>2</sub>O<sub>3</sub> taken from 10K/min DSC-TG data. Paired transitions are indicated by superscripts.

Figure 8.25 and table 88 indicate that the final state of the material is the  $\beta$  phase, Pr<sub>6</sub>O<sub>11</sub>. For each DSC deflection and mass change when the temperature is rising, other than the initial gas loss and the first oxidation to Pr<sub>6</sub>O<sub>11</sub>, there is a corresponding reversal when the temperature is falling. The  $\beta$  phase is therefore stable under ambient conditions, also demonstrated by the pan containing a red-black powder rather than the green of the sesquioxide.

## 8.6 GAS ABSORPTION

Praseodymium sesquioxide is known for absorbing both water and carbon dioxide readily from the air. As discussed earlier in this chapter, if gas was being lost at the point of phase change, this relatively large mass loss would hide the small gain due to oxidation. The image below shows the DSC-TG on sample (6) taken after 85 days from opening the sample. A portion of sample (6) was spread in a thin layer and left directly exposed to the air. The weight loss results for this experiment on sample (6) are given below in table 8.9.

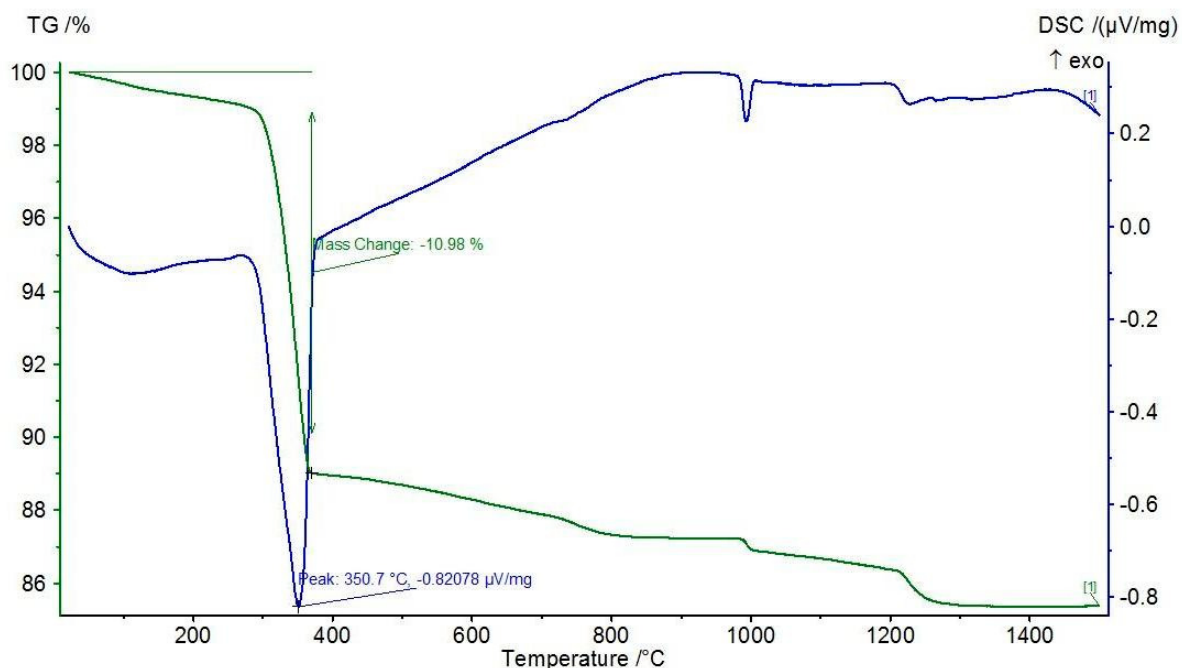


Fig 8.26. Gas loss from sample (6)  $\text{Pr}_2\text{O}_3$  after 85 days' exposure to air.

It is interesting to note the change in the DSC-TG from that shown in figure 8.6. The large exotherm at around 400°C in figure 8.6 has gone, replaced by a large endotherm. This endotherm appears to be the same as the 1<sup>st</sup> endotherm in the DSC-TG for sample (4). As it was known that sample (6) was a pure hexagonal phase, it can be proposed that this point corresponds to release of bound gas from the material, there being no endo/exotherms associated with a structural change from the ambient cubic phase. The same endotherm exists in DSC-TG runs for earlier runs of sample (6), when there was much less gas contamination; figure 8.6 shows a small endotherm at 297.6°C, before the large exotherm at 425°C which represents the phase change. Other than this, the remaining deflections in both the DSC and TG appear to match up, indicating that the material present above 425°C is the same.

| Time (days)                     | Weight loss (%) | Temperature of endotherm (°C) |
|---------------------------------|-----------------|-------------------------------|
| 7 (1 <sup>st</sup> measurement) | -10.50          | 370.0                         |
| 7 (2 <sup>nd</sup> measurement) | -10.33          | 372.0                         |
| 78                              | -11.30          | 347.1                         |
| 85                              | -11.14          | 350.7                         |

Table 8.9 Weight loss on sample (6)  $\text{Pr}_2\text{O}_3$  on exposing to air.

Assuming that it is water that is being absorbed, the following calculations can be made:

Original material ( $\text{Pr}_2\text{O}_3$ ) + water  $\rightarrow$  hydrates to the hydroxide  $\text{Pr}(\text{OH})_3$

RMM of  $\text{Pr}_2\text{O}_3$  (equivalent to  $\text{PrO}_{1.5}$ ) is 329.8 (164.9 per Pr atom)

RMM of  $\text{Pr}(\text{OH})_3$  is 191.924

RMM of  $\text{Pr}_6\text{O}_{11}$  (equivalent to  $\text{PrO}_{1.833}$ ) (the  $\beta$  phase of praseodymium oxide) is 1021.4 (170.23 per Pr atom)

Assuming the reaction proceeds as follows:



\* equivalent mass relative to one atom of Pr

This loss of water followed by oxidation should therefore result in a net mass change of  $-10.9\%$ . This is very close to the figure of  $-11.14\%$  measured after 85 days of exposing powdered sample (6) to the atmosphere, which indicates that it is indeed hydrating to the hydroxide. It should be noted that prior to the DSC-TG work the sample bottle had been in use for 4 months, albeit closed for much of the time, and so some degradation would also have occurred during this period. Table 8.8 only shows further degradation when it was decided to completely expose the sample to the air. Sample (6) arrived as sintered chips rather than powder; it is believed that this afforded it some protection from the air, due to the reduced surface area exposed to the atmosphere. As a comparison, sample (4) had already degraded within the bottle prior to the DSC being used.

## 8.7 RELATING THE DSC-TG TO THE PHASE DIAGRAM

As already discussed, the Pr-O phase diagram is complex and this is reflected in the DSC-TG for sample (6). Figure 8.6 shows that after the gas loss endotherm, there are 5 deflections in the DSC. Figure 8.27 below shows all the peaks and mass changes with labels.

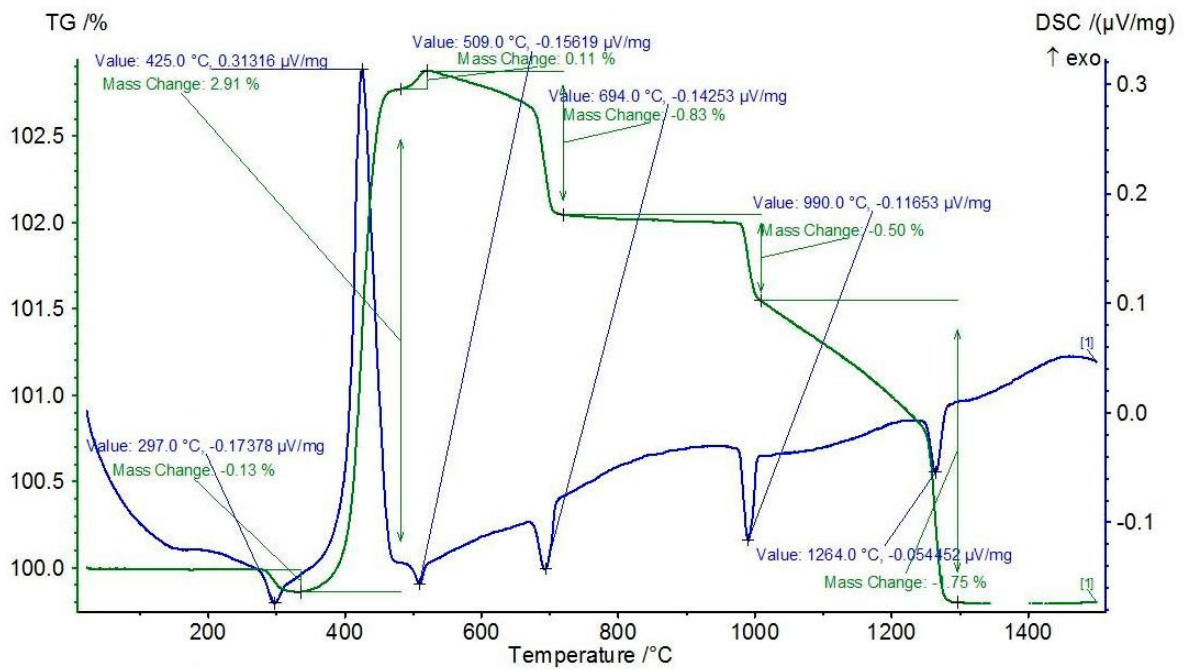


Fig 8.27 DSC-TG recorded on sample (6)  $\text{Pr}_2\text{O}_3$  from 20 °C to 1500 °C at 10K/min in air. Mass changes are indicated.

Because of the additional weight due to water absorption, the TG values need to be adjusted such that the mass is 100% after the first weight loss. Figure 8.25 below is a plot of temperature versus  $x$  in  $\text{PrO}_x$  following this adjustment for the 10K/minute ramp. The inset shows the known phases. The points labelled 1 to 7 identify the phases of interest.

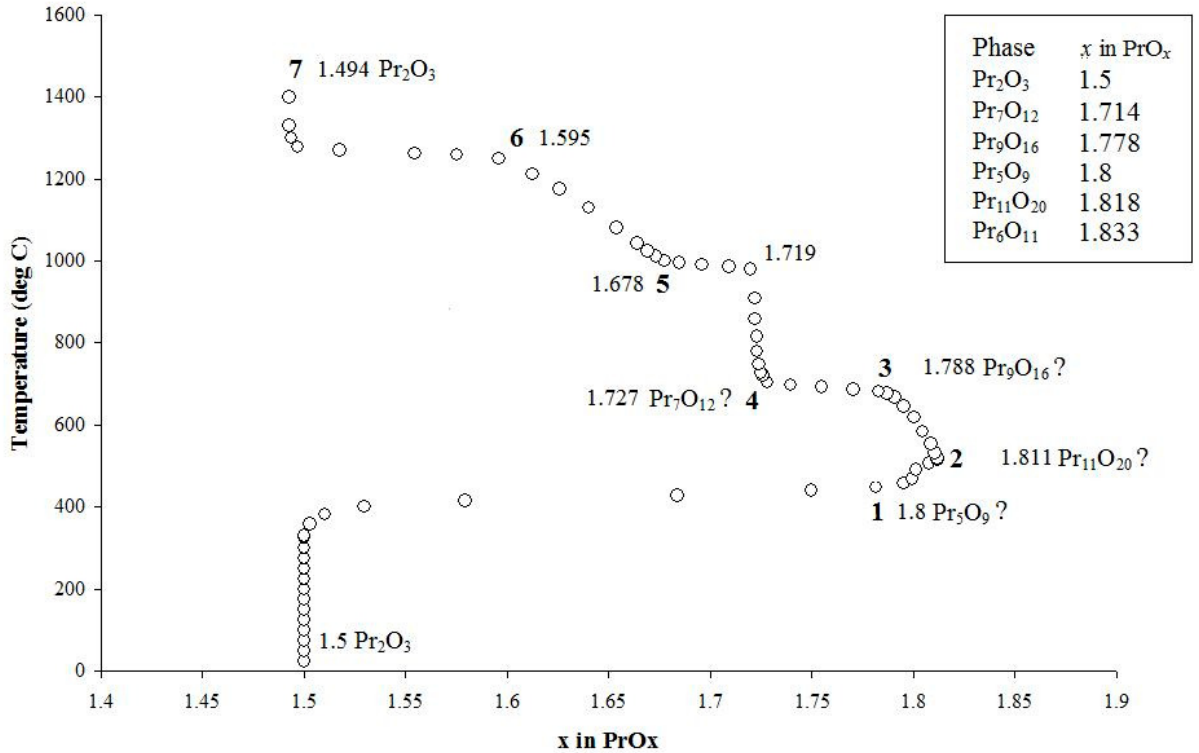


Figure 8.28 Temperature versus oxygen in the Pr-O system for DSC recorded on sample (6) Pr<sub>2</sub>O<sub>3</sub> at 10K/min in air.

Figure 8.28 shows that the ambient form of hexagonal Pr<sub>2</sub>O<sub>3</sub> is stable up to about 350°C where there is a sudden and significant mass gain to point 1 (PrO<sub>1.800</sub>), followed by a small and gradual mass gain to point 2 (PrO<sub>1.811</sub>) and a small and gradual mass loss to point 3 (PrO<sub>1.788</sub>). These three points clearly correspond to the area of the phase diagram where the  $\beta$ ,  $\delta$ ,  $\epsilon$  and  $\zeta$  phases lie. However, to ascertain exactly which phase corresponds to which point in figure 8.28 is difficult, particularly because the stoichiometries of these phases are very close. The phase with highest oxygen content is expected to be Pr<sub>6</sub>O<sub>11</sub> (PrO<sub>1.833</sub>). However, the highest value of  $x$  from the 10K/min run was 1.811, implying this phase was actually Pr<sub>11</sub>O<sub>20</sub>. The gradual mass loss from  $x = 1.811$  to 1.788 does not indicate any of the discrete phases (the closest would be the  $\zeta$  phase) but instead the non-stoichiometric  $\alpha$  phase, the boundary for which, in figure 1.9, follows a similar slope. From  $x = 1.788$  there is a sudden drop to 1.727 at about 700°C. This appears to mark the appearance of the  $\iota$  phase of Pr<sub>7</sub>O<sub>12</sub>. As in the phase diagram the stoichiometry is steady up to about 1000°C, where there is a sudden drop to  $x = 1.678$ . This phase gradually loses oxygen for the next 250 degrees and represents

a wide range of oxygen content, down to  $x = 1.595$ . Finally, at about 1250°C there is a sudden mass loss to the  $\theta$  phase of  $\text{Pr}_2\text{O}_3$ . Figure 8.29 shows the combined TG data from all runs on sample (6) and table 8.10 gives the values of  $x$  in  $\text{PrO}_x$ .

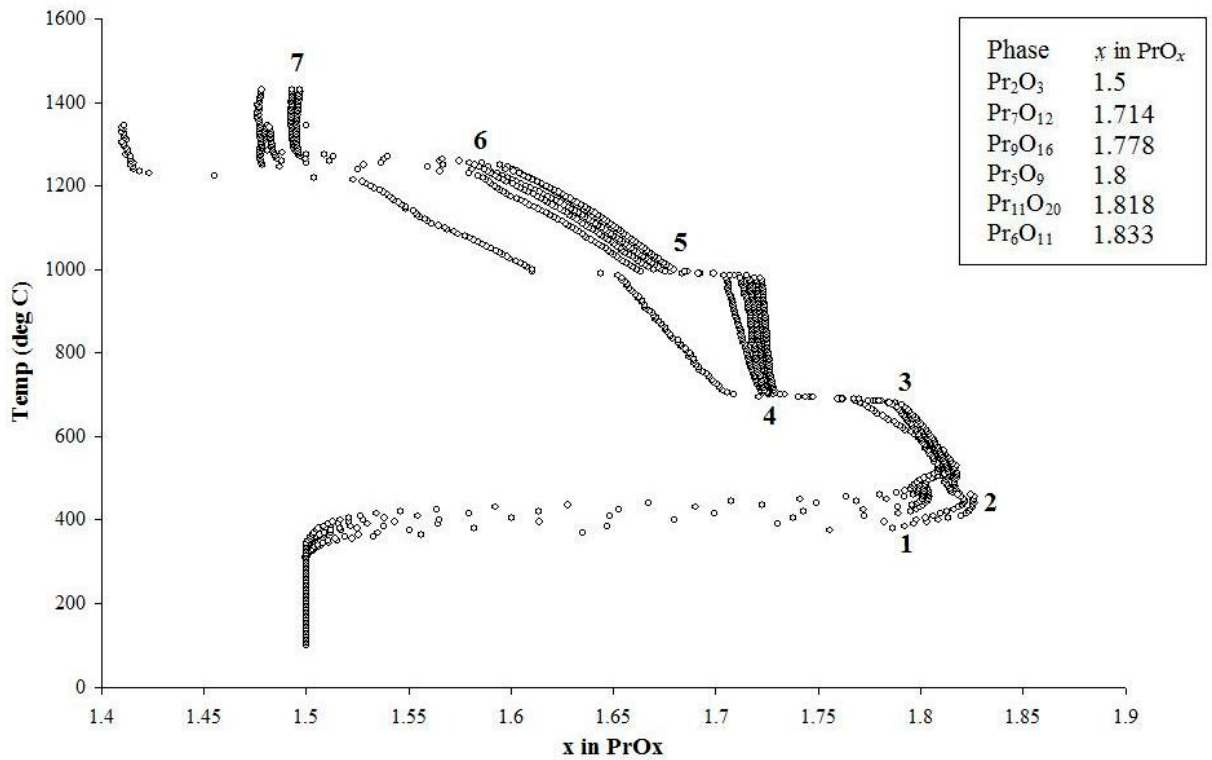


Figure 8.29 Temperature versus oxygen content for all DSC recorded on sample (6)  $\text{Pr}_2\text{O}_3$  from 20°C to 1500°C in air. Labels correspond to superscript numbers in table 8.10.

| Ramp    | 375°C <sup>1</sup> | 530°C <sup>2</sup>         | 680°C <sup>3</sup> | 705°C <sup>4</sup> | 1000-1250°C <sup>5-6</sup> | 1275°C <sup>7</sup> |
|---------|--------------------|----------------------------|--------------------|--------------------|----------------------------|---------------------|
| 1K/min  | 1.786              | 1.827, 1.817, 1.818        | 1.768              | 1.709              | 1.611 to 1.523             | 1.411               |
| 2K/min  | 1.798              | 1.822, 1.816, 1.812, 1.814 | 1.781              | 1.726              | 1.664 to 1.580             | 1.481               |
| 4K/min  | 1.789              | 1.804, 1.802, 1.812        | 1.785              | 1.728              | 1.678 to 1.590             | 1.482               |
| 7K/min  | 1.789              | 1.801, 1.802, 1.813        | 1.788              | 1.732              | 1.680 to 1.598             | 1.497               |
| 10K/min | 1.792              | 1.800, 1.801, 1.811        | 1.788              | 1.728              | 1.678 to 1.595             | 1.493               |
| 20K/min | 1.788              | 1.795, 1.800, 1.809        | 1.785              | 1.725              | 1.670 to 1.580             | 1.478               |

Table 8.10 Values of  $x$  in  $\text{PrO}_x$  for DSC-TG recorded on sample (6). Superscripts beside temperatures correspond to points in figures 8.28 and 8.29.

All but one of the runs in figure 8.26 show precision; however, the run at 1K/min has deviated somewhat, shown particularly by the final value of  $x$  being 1.411. The 1K/min and 2K/min runs both show an initial maximum in the TG, followed by a small

decrease, a small increase, then a fall; the other runs build to the maximum. The exact route through the phases in this temperature region therefore appears different depending upon the heating rate. The largest of these maxima is shown by the 1K/min run at an oxygen content of 1.827. As the 2 highest values for  $x$  on the phase diagram are 1.818 and 1.833, it is reasonable to assume that this maximum point corresponds to the  $\beta$  phase of  $\text{Pr}_6\text{O}_{11}$ . It is notable that amongst the remaining ramps the maximum oxygen content was only 1.811, implying the presence of the  $\delta$  phase  $\text{Pr}_{11}\text{O}_{20}$ , the  $\beta$  phase  $\text{Pr}_6\text{O}_{11}$  not being attained.. With the deviation in the 1K/min final value, it might be expected that all the 1K/min values were unreliable. However, the 1K/min and 2K/min ramps shows a proximity in their values for the oxygen contents across the majority of the temperature range. The 2K/min ramp maximum of 1.822 correlates with the maximum for the 1K/min ramp, indicating that the  $\beta$  phase is indeed present.

The first mass change gives a value of  $x$  of approximately 1.790, which appears to be the  $\varepsilon$  phase. The order of the phases as they appear for the 1K/min and 2K/min ramps is therefore believed to be as in table 8.11. For the remaining ramps the only difference appears to be that the  $\delta$  phase appears immediately before the  $\beta$  phase.

| Phase         | Temperature (°C) | $x$ in $\text{PrO}_x$ (from TG) | Formula                       |
|---------------|------------------|---------------------------------|-------------------------------|
| $\varepsilon$ | 400-420          | 1.798-1.813                     | $\text{Pr}_5\text{O}_9$       |
| $\beta$       | 420-445          | 1.813-1.822                     | $\text{Pr}_6\text{O}_{11}$    |
| $\delta$      | 470-490          | 1.815-1.812                     | $\text{Pr}_{11}\text{O}_{20}$ |
| $\alpha$      | 520-680          | 1.814-1.785                     | Non-stoichiometric            |
| $\iota$       | 705-985          | 1.723-1.704                     | $\text{Pr}_7\text{O}_{12}$    |
| $\sigma$      | 995 to 1225      | 1.664-1.584                     | Non-stoichiometric            |
| $\theta$      | 1250-            | 1.479-1.481                     | $\text{Pr}_2\text{O}_3$       |

Table 8.11 Order of appearance of phases in the Pr-O system with temperature for the 2K/min ramp.

This information is also shown in figure 8.30, below.

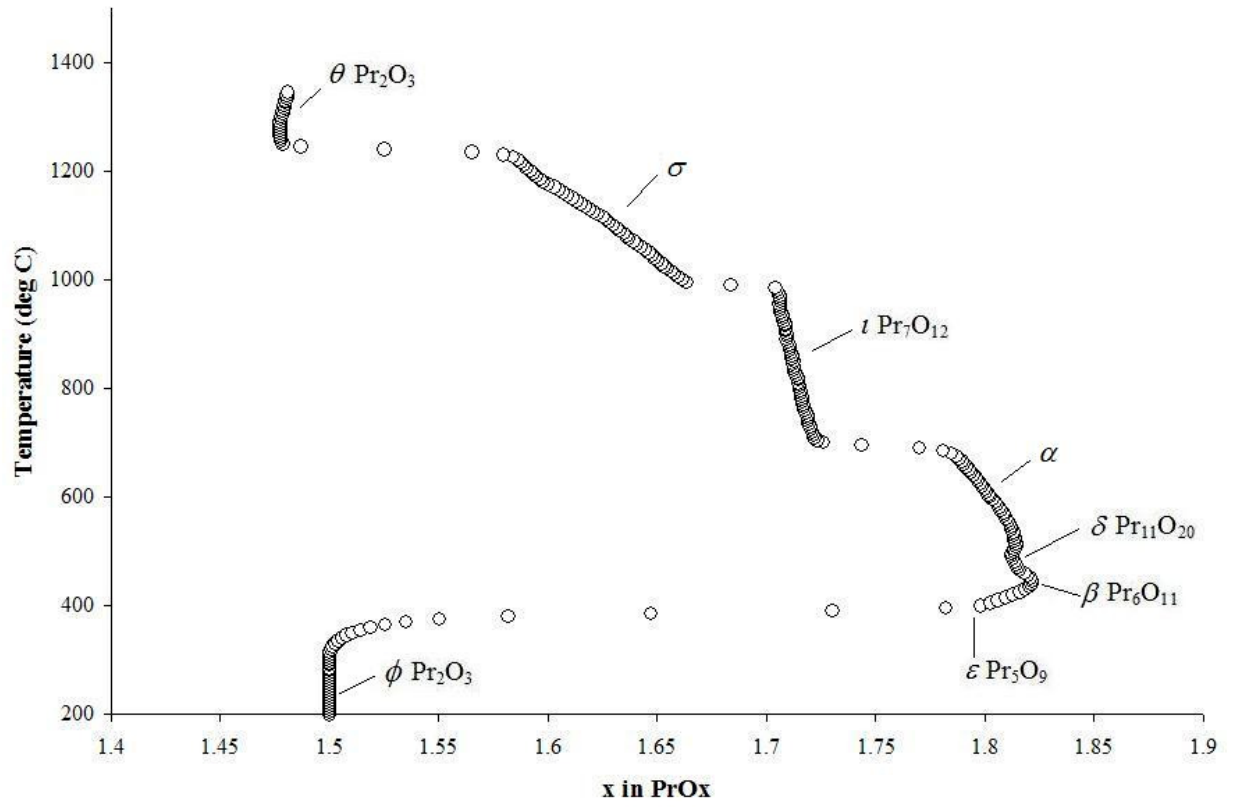


Figure 8.30 DSC recorded on sample (6)  $\text{Pr}_2\text{O}_3$  at 2K/min in air with phases marked.

Figure 8.31 shows the paths through the phases, according to temperature.

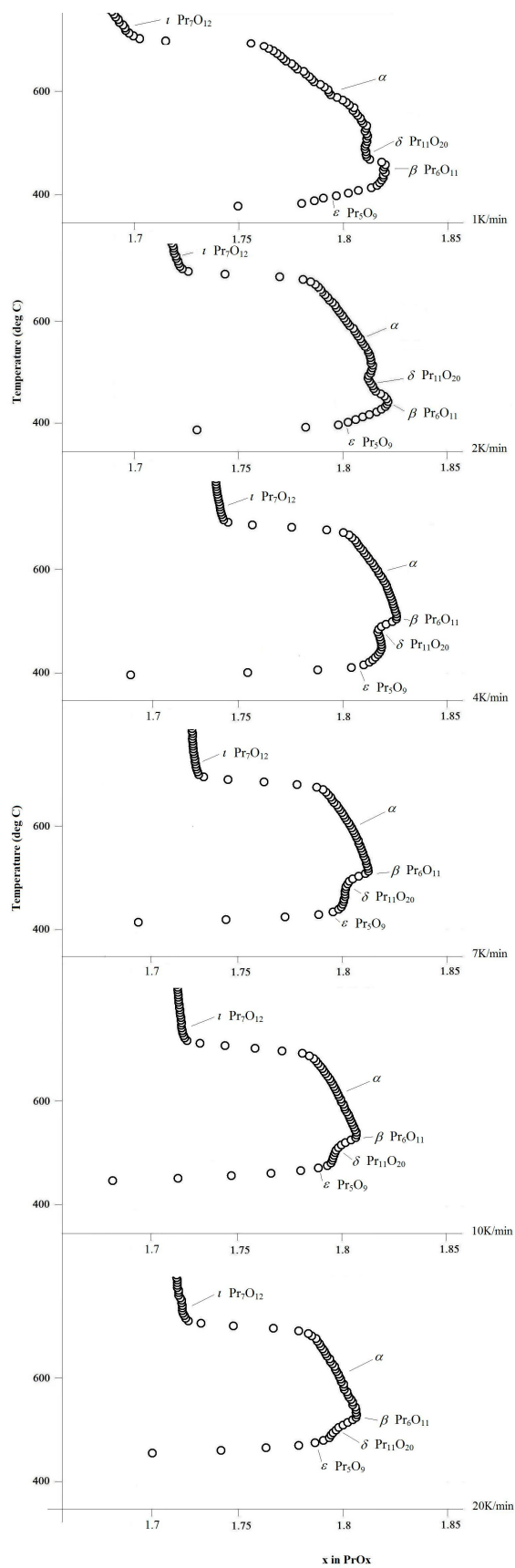


Figure 8.31 Phases attained during ramps on sample (6) Pr<sub>2</sub>O<sub>3</sub>.

Much of the temperature-composition diagram can be explained by the existence of discrete monophasic regions in the phase diagram, shown by little or no change in  $x$  with temperature. The only section of figure 8.29 that remains to be explained is the region between 1000°C and 1250°C. The region appears to correspond to the low oxygen boundary of the  $\sigma$  phase in the Pr-O phase diagram of figure 1.9. However, Hyde *et al* do not show oxygen composition above 1100°C. Also, the phase diagram does not show oxygen content above this temperature. A search through the PDF-2 database produced a reference for PrO<sub>1.57</sub> which is a cubic cell with the ceria structure, the oxygen sites being occupied only to 0.78. The material is described in the report as 'green brownish red'. This value of  $x$  is in the middle of the sloping line for this phase in figure 8.29 so it appears that the phase detected by DSC-TG is cubic. To support this, Hyde *et al* do state that their  $\sigma$  phase is cubic. It would be reasonable to assume that this line in figure 8.29 represents a continuity of stoichiometries and a slow release of oxygen from the cell. This is supported in the literature (Hyde *et al* 1965), (Adachi and Imanaka 1998). This data represents an addition to the existing phase diagram.

The change in the XRPD around 600°C (figure 7.36) can now be explained by the appearance of the  $\iota$  phase, Pr<sub>7</sub>O<sub>12</sub>. The initial change from the hexagonal ambient phase to the cubic  $\beta$  phase is clear to see as it involves a change of cell type. However, many of the other Pr-O phase changes merely correspond to loss or gain of oxygen on the 8c Wyckoff sites of the ceria cell. These light atom changes are very difficult to detect using a laboratory diffractometer. It is only when the cell type again changes from the  $\alpha$  phase (cubic) to the  $\iota$  phase of Pr<sub>7</sub>O<sub>12</sub> (rhombohedral) that a change in the XRPD pattern is noticed. The phase change is shown as occurring at 625°C on heating and disappearing at 575°C on cooling. This point corresponds to the vertical section in the middle of the Pr-O phase diagram in figure 1.9 and also to region 4 in figure 8.29. Figure 8.32 shows the hysteresis loop for this transition.

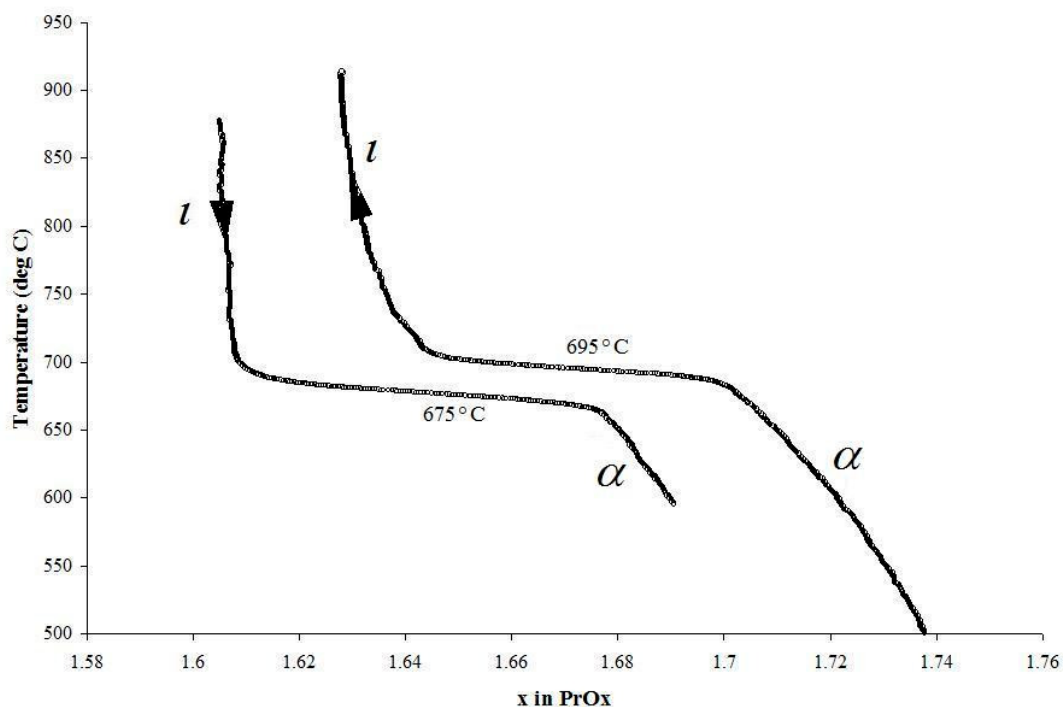


Figure 8.32 Hysteresis loop for the  $\alpha$  phase to  $l$  phase ( $Pr_7O_{12}$ ) transition.

In a temperature-composition diagram, a vertical line typically indicates a monophasic region i.e. the presence of a discrete compound that is structurally highly-ordered, where heating and cooling paths are often coincident. A horizontal line, where there is a sudden change of composition with little change of temperature, typically indicates a diphasic region where heating and cooling paths are not expected to coincide. This is illustrated in figure 8.32. Sloping temperature-composition lines which are coincident on heating and cooling also indicate a monophasic region, but with a disordered and non-stoichiometric phase. Where heating and cooling paths are not coincident, a multiphasic and non-stoichiometric region is inferred. The latter example is the case with the  $\sigma$  phase shown in the TG data, and illustrated in figure 8.33, below.

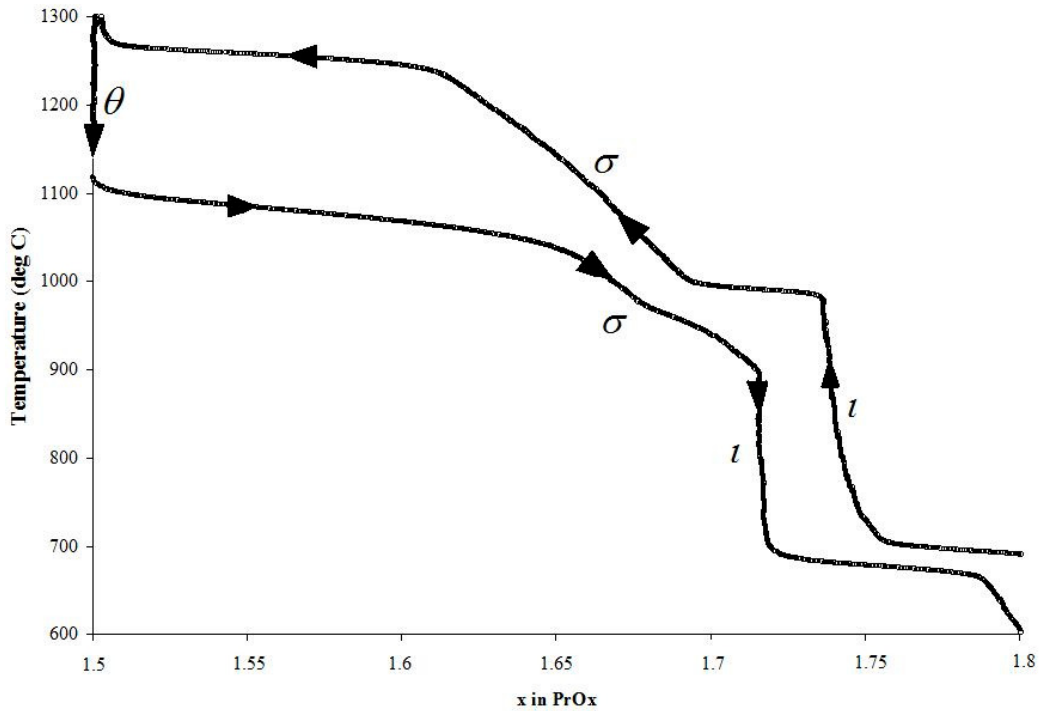


Figure 8.33 Temperature-composition plot for the  $\iota$ - $\sigma$ - $\theta$  region.

Other than the fact that there is some horizontal displacement between the heating and cooling plots, figure 8.33 shows that the path through the  $\sigma$  phase is not the same in both directions; on cooling, the sample oxidises rapidly below 1100°C to an oxygen composition of  $x = 1.65$ , rather than  $x = 1.6$  which marked the low-oxygen end of the  $\sigma$  phase on heating.

## 8.8 COMPARISON WITH OTHER WORK

The  $\delta$  ( $x = 1.816$ ) phase is the most recently established (Hyde *et al* 1965) and these results have demonstrated its fleeting existence. In figure 8.31 it appears as a brief kink in the TG data either just before or just after the appearance of the  $\beta$  phase. This point in the data is most pronounced in the 2K/min and 4K/min runs. The kink which appears to mark the  $\epsilon$  phase is less pronounced, and does not appear in the 1K/min and 2K/min runs. Hyde and co-workers only found the  $\delta$  phase at low pressure, during the 45mm Hg run. They also note the ease with which oxygen is exchanged between solid  $\text{PrO}_x$  and the gas phase. This is confirmed by the close grouping of the  $\epsilon$ ,  $\beta$  and  $\delta$  phases in

figure 8.29 and the corresponding lack of change in the XRPD in this temperature region (figure 7.35).

Hyde *et al* performed 4 heating experiments on praseodymium oxide at different pressures. They found that the order of appearance of phases changed with pressure. For example, in the run at 10mm Hg, the phases were  $\epsilon$  (<497°C);  $\zeta$  appearing at 497°C;  $\iota$  appearing at 588°C;  $\sigma$  appearing at 906°C and showing the range  $1.65 \geq x \geq 1.60$ ; and  $\theta$  appearing at 1068°C. However, the run at 45mm Hg, which began with the  $\beta$  phase, showed the  $\delta$  phase occurring briefly between the  $\beta$  and  $\epsilon$  phases. For the run at 650mm Hg, the closest to that in this work (atmospheric pressure), the  $\beta$  phase existed below 300°C; rather than  $\delta$  and  $\epsilon$ , the  $\alpha$  phase appeared at 470°C;  $\iota$  appeared at 795°C;  $\sigma$  existed between 1065°C and 1150°C; and  $\iota$  reappeared on cooling at 1069°C. In this thesis the only significant change between the different ramps was the order of appearance of the  $\beta$  and  $\delta$  phases. The general pathway of Hyde *et al* ( $\beta$  -  $\alpha$  -  $\iota$  -  $\sigma$ ) is in partial accord with the results in this work ( $\epsilon$  -  $\beta$  -  $\delta$  -  $\alpha$  -  $\iota$  -  $\sigma$ ). However, my work also appeared to show the existence of the  $\epsilon$  and  $\delta$  phases at ambient pressure, contrary to the results of Hyde *et al*.

Hyde *et al* note the coincidence of heating and cooling curves for the higher oxygen content phases ( $\beta$ ,  $\delta$ ,  $\epsilon$  and  $\xi$ ), but not for the higher temperature transitions. In this thesis, this pattern was noted. At 10mm Hg they noted the lack of the  $\sigma$  phase on cooling, the  $\theta$  phase converting directly into the  $\iota$  phase. In general, their heating and cooling curves at high temperature were not coincident. They attribute this to the presence of a mixed  $\theta$  and  $\sigma$  phase at the point of commencement of cooling, with the  $\sigma$  phase immediately starting to oxidise on cooling but the  $\theta$  phase not oxidising until a break temperature of about 1050°C. Their isobaric runs are shown in figure 8.34.

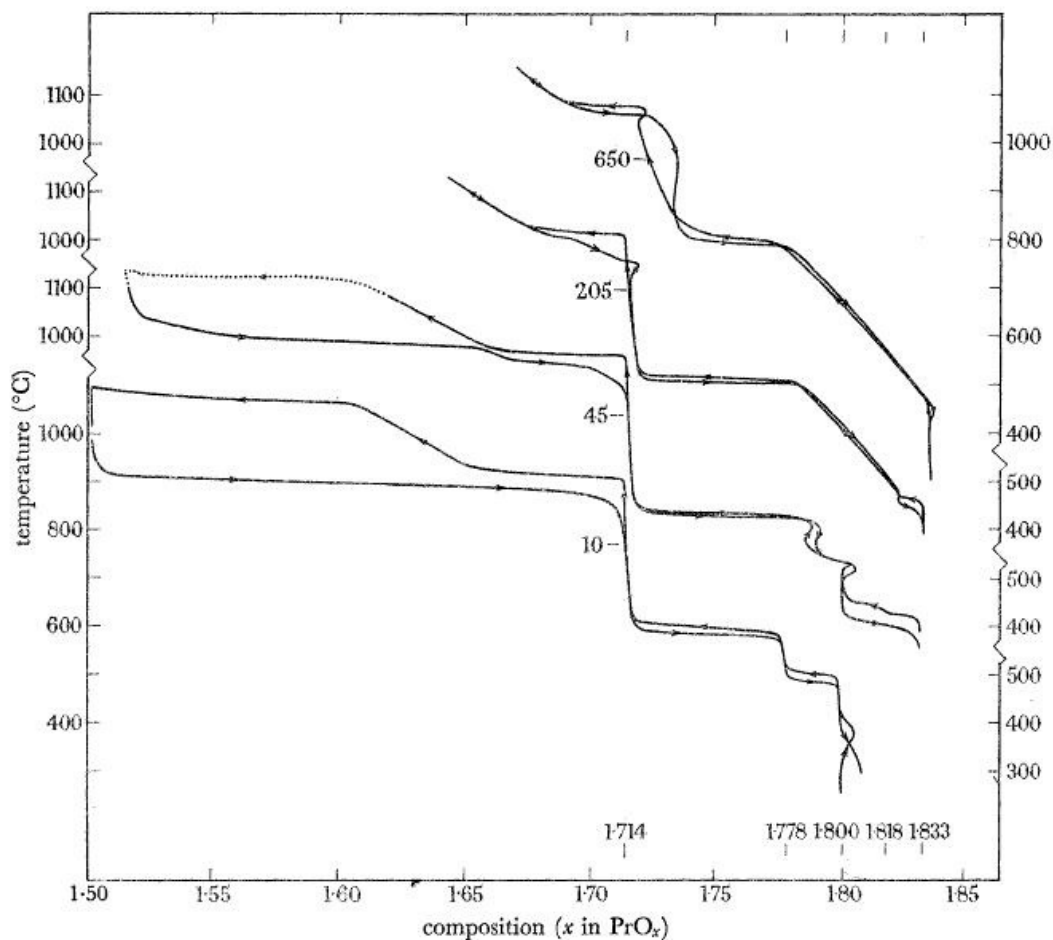


Figure 8.34 Isobaric runs on  $\text{Pr}_2\text{O}_3$ . Figures against curves indicate pressure in mm Hg (Hyde *et al* 1965).

This behaviour has been observed by others (Sonström 2010). A similar divergence of curves was noted in my work. Figure 8.33 clearly shows a different pathway for  $\theta$  -  $\sigma$  -  $\iota$  on heating than on cooling, confirming the hysteresis. Additionally, the run of Hyde *et al* carried out at 650mm Hg shows different ascending and descending curves for the  $\iota$  -  $\sigma$  boundary. In their paper this is the only pressure at which this occurs, all other runs showing coincident curves. The work in this thesis was done at a similar pressure and shows a similar divergence.

Finally, Hyde *et al* note the appearance of  $\varepsilon$  and  $\zeta$  only at low pressure; they appear in the 10mm and 45mm Hg runs as vertical sections. However, in the 205mm and 650mm Hg runs the prominent feature in this region is a sloping line indicating the  $\alpha$  phase. The appearance of  $\alpha$  (and the consequential absence of  $\zeta$ ) was a prominent feature of

the work in this thesis. However, contrary to the work of Hyde *et al*, the  $\varepsilon$  phase does appear to be present in the images of figure 8.31.

Although there have been many studies on the Pr-O system, there have been very few kinetic studies, as already mentioned in chapter 7. One study (Inaba *et al* 1980) looked at the conversion between the  $\xi$  and  $\iota$  phases over the temperature range 535-570°C and obtained a value of 189.7kJ.mol<sup>-1</sup> for the activation energy. A second study (Hyde *et al* 1965) studied oxidation of the  $\beta$  phase to the dioxide in the range 265-307°C, obtaining a value of 112.6kJ/g-atom of O for the activation energy. Figure 8.32, which shows the  $\iota$  -  $\alpha$  transition, is consistent with the historical work on this phase transition (Inaba *et al* 1981). This reference demonstrated a reproducible hysteresis loop with varying oxygen pressure and an activation energy of 60.9kcal.mol<sup>-1</sup> (255.0kJ.mol<sup>-1</sup>) on reduction and 75.0kcal.mol<sup>-1</sup> (314.0kJ.mol<sup>-1</sup>) on oxidation. Although it was not possible to determine the activation energy from the DSC-TG data in this thesis, this value appears consistent with the other values for phase changes in this system. The authors noted an inflexion in the hysteresis loop at PrO<sub>1.75</sub>, although this was not observed in my work.

The activation energy values obtained in my work were -154(7) kJ.mol<sup>-1</sup> (avg) for the  $\phi$  to  $\beta$  phase transition, occurring between 368°C and 460°C and 1224(122) kJ.mol<sup>-1</sup> for the  $\sigma$  to  $\theta$  phase transition, occurring between 1224°C and 1273°C. These are tabulated below together with the historic values.

| <b>Transition</b>                | <b>Temperature range (°C)</b> | <b>EA (kJ.mol<sup>-1</sup>)</b>                         |
|----------------------------------|-------------------------------|---|
| $\phi \rightarrow \beta$         | 368 to 460                    | -154(7) avg   |
| $\beta \rightarrow \text{PrO}_2$ | 265 to 307                    | 112.6kJ/g-atom of O <sup>1</sup><br>Equivalent to 306.3 |
| $\xi \rightarrow \iota$          | 535 to 570                    | 189.7 (oxidation) <sup>2</sup>                          |
| $\alpha \leftrightarrow \iota$   | 655 to 715                    | 255.0 (reduction)<br>314.0 (oxidation) <sup>3</sup>     |
| $\sigma \rightarrow \theta$      | 1224 to 1273                  | 1224(122)   |

Table 8.12 Kinetic data for the Pr-O system.

<sup>1</sup> (Hyde *et al* 1965)<sup>2</sup> (Inaba *et al* 1980)<sup>3</sup> (Inaba *et al* 1981)

Although the available data is limited, there is a correlation between temperature of phase change and activation energy. Encouragingly, the value of  $-154(7)$   $\text{kJ}\cdot\text{mol}^{-1}$  obtained for the  $\phi \rightarrow \beta$  transition agrees with that obtained in Chapter 7 via XRPD data.

## **9 CONCLUSIONS AND SUGGESTIONS FOR FUTURE WORK**

### **9.1 SUMMARY**

This work has demonstrated the following:

- (i) the high-temperature phases of some lanthanoid oxides can be quenched to ambient temperature, contrary to the phase diagram;
- (ii) structural modifications exist which are not indicated by the phase diagram;
- (iii) high-temperature phases may already exist in commercially available samples, contrary to the supplier's information;
- (iv) kinetic data in the Pr-O system obtained via different sources show correlation, and activation energies are generally much lower than for the sesquioxides;
- (v) phase pathway can depend upon heating rate;
- (vi) indexing of XRPD data is not straightforward and it is not even guaranteed that high-symmetry cells will always index;
- (vii) it is possible to index a cell from limited XRPD data when the Bragg reflections contribute only a small fraction to the overall diffraction wave envelope;

The above summary is detailed in the following sections.

### **9.2 LANTHANIDE OXIDE CRYSTAL STRUCTURES**

The phase diagram for the sesquioxides shown in figure 1.5 indicated that no monoclinic phases were present at ambient temperature. However, it was immediately found that the commercially-obtained sample of europia already contained a small quantity of the B-type phase. More surprisingly, samaria contained 97% B-type phase, even though the supplier stated the cell type to be cubic. The metastability of B-type europia was demonstrated by heating to 1334°C, holding for 1 hour and cooling slowly. The short anneal time and lack of quenching were expected to be detrimental to the creation and retention of the B-type phase. However, it was shown that monoclinic europia is relatively easy to generate and stable enough for the bulk material to

maintain 100% B phase on standing. Figure 1.5 indicates a higher temperature is required to perform the same treatment on gadolinia. In practice it took significantly more energy than was expected in order to force the change. Considering the sample of gadolinia was heated over 160°C higher than the sample of europia and also cooled rapidly it seemed reasonable to predict that a significant proportion of monoclinic structure should have been retained. However, this was not the case. An anneal for 7 hours at 1500°C was required to completely transform the structure. Again, this change was maintained in the bulk material, and long enough for it to be posted to Diamond Light Source. A 5-hour run at the same temperature led to the creation of 97% B phase; clearly the reaction in gadolinia requires considerably more energy than for europia. Both the laboratory and synchrotron data allowed the previously unpublished structure of monoclinic gadolinia to be determined.

To demonstrate whether B-type gadolinia was as stable as B-type europia, an XRPD pattern on the sample used in figure 7.21 was taken 5 months later. The phase fractions were found to have stayed the same, showing that B-type gadolinia, too, may persist at ambient temperature.

Because of lack of facilities it was not possible to determine the structure for B-type Yb<sub>2</sub>O<sub>3</sub>. However, the cell type was shown to be monoclinic, again demonstrating the existence of a phase contrary to figure 1.5. The energy required to force the change in ytterbia is so high that either melting and quenching, or in situ XRPD, would be required to demonstrate the structure. Whatever conversion was achieved in the furnace at 1500°C, after quenching only 1% B phase was detected. The presence of B-type Yb<sub>2</sub>O<sub>3</sub> after heating to a relatively low temperature is contrary to recent work (Guo, Harvey *et al* 2007), (Meyer *et al* 1995). The former reference states that flame synthesis at high temperature (up to 2800°C) and ambient temperature, followed by rapid cooling, is necessary to create the monoclinic phases of Er<sub>2</sub>O<sub>3</sub>, Tm<sub>2</sub>O<sub>3</sub> and Yb<sub>2</sub>O<sub>3</sub>, and that lower temperature (2680°C) only led to the cubic phases. Meyer *et al* state that a temperature of 2000°C is not sufficient for the B-type structure to be attained. My work has shown that heating in a laboratory bench-top furnace to 1500°C will create a small amount of B-type Yb<sub>2</sub>O<sub>3</sub> in the bulk material. Reflecting my results, Sun and co-workers (Sun *et al* 2007) were able to identify the cell type from a residue of

monoclinic lutetia existing within an otherwise cubic sample, but state there are high uncertainties in the recorded lattice parameters.

Although monoclinic ytterbia was present as a residue, the calculated lattice parameters compare favourably with those obtained historically. The cell reported in this work was  $a = 13.740(2)\text{\AA}$ ,  $b = 3.400(2)\text{\AA}$ ,  $c = 8.593(2)\text{\AA}$  and  $\beta = 100.12^\circ$ . Previously reported cells are  $a = 13.73(1)\text{\AA}$ ,  $b = 3.425(3)\text{\AA}$ ,  $c = 8.452(8)\text{\AA}$  and  $\beta = 100.17(5)^\circ$  (Hoekstra 1966) and  $a = 13.72\text{\AA}$ ,  $b = 3.428\text{\AA}$ ,  $c = 8.437\text{\AA}$  and  $\beta = 100.18^\circ$  (Coutures *et al* 1972).

It is noteworthy that the metastability of the B-type phases for the intermediate weight oxides and their existence at ambient temperature indicates that the phase diagram according to Foëx and Traverse is somewhat misleading. Such irreversibility of phase conversion was also seen in the Pr-O system with the  $\phi$  to  $\beta$  phase change, occurring at only  $275^\circ\text{C}$  on heating. The actual pathway through the Pr-O phases appears to depend on heating rate, but the final phase is the  $\theta$  phase. However, on cooling back, the  $\beta$  phase is the last to form i.e. the  $\phi$  phase does not reappear. The activation energy of around  $-150\text{ kJ}\cdot\text{mol}^{-1}$  for the  $\phi \rightarrow \beta$  transition was found to be much less than that of the well-researched europium sesquioxide  $\text{C} \rightarrow \text{B}$  transition, at  $650\text{ kJ}\cdot\text{mol}^{-1}$ .

### 9.3 INDEXING

Although the cubic gadolinia pattern indexed successfully using CRYSFIRE, those of europia and ytterbia did not. However, on relaxing the tolerance in the allowed  $2\theta$  difference between matching experimental and calculated lines, CRYSFIRE found the correct solutions. It is noted that reliance should always be placed on an accurately recorded pattern rather than a reduction in the strictness of the indexing parameters; it is all too easy to find a solution which appears to match the experimental data, when in fact it is not the correct solution. As an aside, to test the efficacy of the indexing programs, a set of theoretical Bragg reflections for a cubic cell were created and entered into CRYSFIRE; none of the indexing programs was able to find the correct solution.

It is notable that CRYSFIRE failed to index the B-type gadolinia pattern. Had it not been for the fact that the cell parameters for europia were known, this would have been a serious obstacle to the determination of the crystal structure. It serves as an illustration that the indexing stage is often the most problematic in the sequence and is also the most difficult and most time-consuming part of the process.

The lack of significant changes in the gadolinia and ytterbia patterns on heating was initially considered to be a stumbling block in the investigation of their monoclinic phases. However, it was decided to investigate just the lines which had appeared on heating. Surprisingly, by making assumptions about cell parameters and minimising the differences between the actual and calculated lines it was possible to estimate the cell parameters of the respective materials. It was, of course, not possible to carry out full profile refinement using GSAS because only a fragment of the monoclinic pattern was being observed and even then, the intensities were very low. But this exercise in 'forensic diffractometry' serves to show that it is possible to use limited information together with certain assumptions to determine crystal habit.

#### **9.4 COMPARISON OF KINETIC DATA FROM XRPD AND DSC**

Although some problems were experienced in obtaining kinetic data, most notably due to the mixed phase and gas contamination of sample (4)  $\text{Pr}_2\text{O}_3$ , there are definite correlations in the data. Analysis of isothermal holds using XRPD data gave activation energy values of  $-149(10) \text{ kJ.mol}^{-1}$ ,  $-146(2) \text{ kJ.mol}^{-1}$  and  $-154(2) \text{ kJ.mol}^{-1}$  using 2 different methods for the  $\phi$  to  $\beta$  phase transition. These values were supported by those obtained through DSC, which indicates the data to be accurate and obtained using sound methods. The kinetic data is summarised in table 9.1.

| Sample                             | Low temp phase | Reaction                    | Feature                   | Method | EA (kJ.mol <sup>-1</sup> )                                   |
|------------------------------------|----------------|-----------------------------|---------------------------|--------|--|
| (4) Pr <sub>2</sub> O <sub>3</sub> | Cubic+hex      | $\phi \rightarrow \beta$    | 47.2° peak                | XRPD   | -146(2) (ShSp <sup>1</sup> )<br>-154(2) (JMAK <sup>2</sup> ) |
| (4) Pr <sub>2</sub> O <sub>3</sub> | Cubic+hex      | $\phi \rightarrow \beta$    | 41.4° peak                | XRPD   | -149(10) (ShSp <sup>1</sup> )                                |
| (4) Pr <sub>2</sub> O <sub>3</sub> | Cubic+hex      | $\phi \rightarrow \beta^3$  | 1 <sup>st</sup> endo      | DSC    | 108(9)   |
| (4) Pr <sub>2</sub> O <sub>3</sub> | Cubic+hex      | $\phi \rightarrow \beta^3$  | 2 <sup>nd</sup> endo      | DSC    | 103(6)   |
| (4) Pr <sub>2</sub> O <sub>3</sub> | Cubic+hex      | $\phi \rightarrow \beta^3$  | 3 <sup>rd</sup> endo      | DSC    | 61(3)  |
| (6) Pr <sub>2</sub> O <sub>3</sub> | Hex            | $\phi \rightarrow \beta$    | 1 <sup>st</sup> exo 450°C | DSC    | 152(8)   |
| (6) Pr <sub>2</sub> O <sub>3</sub> | Hex            | $\phi \rightarrow \beta$    | 1 <sup>st</sup> exo 450°C | DSC    | 155(10)  |
| (6) Pr <sub>2</sub> O <sub>3</sub> | Cubic          | $\sigma \rightarrow \theta$ | 1250°C endotherm          | DSC    | 1224(122)  |

<sup>1</sup> obtained via a Shrinking Sphere model      <sup>2</sup> obtained via JMAK model

<sup>3</sup> Believed to proceed as Pr(OH)<sub>3</sub> → Pr<sub>2</sub>O<sub>3</sub> → Pr<sub>6</sub>O<sub>11</sub>

Table 9.1 Comparison of activation energy data from XRPD and DSC.

Had facilities continued to be available, it would have been useful to compare the activation energy value of approximately -150 kJ.mol<sup>-1</sup> for praseodymia with those for neodymia, samaria and europia via DSC and to then relate these to the values obtained historically by Stecura and Ainscough. Table 9.2 shows the values obtained above with these historical values.

| Oxide                              | Ambient phase | Reaction   | Method | EA (kJ.mol <sup>-1</sup> )    |
|------------------------------------|---------------|--|--------|-------------------------------|
| (4) Pr <sub>2</sub> O <sub>3</sub> | Cubic+hex     | Pr <sub>2</sub> O <sub>3</sub> → Pr <sub>6</sub> O <sub>11</sub> | XRPD   | -146(2) (ShSp <sup>3</sup> )  |
| (4) Pr <sub>2</sub> O <sub>3</sub> | Cubic+hex     | Pr <sub>2</sub> O <sub>3</sub> → Pr <sub>6</sub> O <sub>11</sub> | XRPD   | -154(2) (JMAK <sup>4</sup> )  |
| (4) Pr <sub>2</sub> O <sub>3</sub> | Cubic+hex     | Pr <sub>2</sub> O <sub>3</sub> → Pr <sub>6</sub> O <sub>11</sub> | XRPD   | -149(10) (ShSp <sup>3</sup> ) |
| (6) Pr <sub>2</sub> O <sub>3</sub> | Hex           | Pr <sub>2</sub> O <sub>3</sub> → Pr <sub>6</sub> O <sub>11</sub> | DSC    | -152(8)                       |
| (6) Pr <sub>2</sub> O <sub>3</sub> | Hex           | Pr <sub>2</sub> O <sub>3</sub> → Pr <sub>6</sub> O <sub>11</sub> | DSC    | -155(10)                      |
| Nd <sub>2</sub> O <sub>3</sub>     | Cubic         | C type → A type  | XRPD   | 502 <sup>1</sup>              |
| Sm <sub>2</sub> O <sub>3</sub>     | Cubic         | C type → B type  | XRPD   | 628 <sup>1</sup>              |
| Eu <sub>2</sub> O <sub>3</sub>     | Cubic         | C type → B type  | XRPD   | 691 <sup>1</sup>              |
| Eu <sub>2</sub> O <sub>3</sub>     | Cubic         | C type → B type  | XRPD   | 493 <sup>2</sup>              |
| Gd <sub>2</sub> O <sub>3</sub>     | Cubic         | C type → B type  | XRPD   | 787 <sup>1</sup>              |

Table 9.2 Activation energies for the lanthanide oxides.

<sup>1</sup> (Stecura 1966)    <sup>2</sup> (Ainscough *et al* 1975)

<sup>3</sup> obtained via a Shrinking Sphere model.    <sup>4</sup> obtained via JMAK model

Had the diffractometer hot stage been able to reach a higher temperature than 800°C, two further changes in the XRPD patterns would be expected. These would be the  $\iota$  phase changing to the  $\sigma$  phase around 1000°C and finally the  $\sigma$  phase changing to the A-type ( $\theta$  phase) sesquioxide at 1200°C. The access to a diffractometer capable of reaching 1500°C would enable a more detailed study of the Pr-O phase diagram; it is

the high-temperature and low-oxygen region of the diagram that is lacking in information.

## 9.5 COMPARISON OF DSC-TG DATA WITH HISTORIC DATA

The 2 transitions for which kinetic data were obtained in my work ( $\phi \rightarrow \beta$  and  $\sigma \rightarrow \theta$ ) do not appear to have been investigated previously. The data presented in chapter 8 is repeated below, including the historic data for the  $\beta \rightarrow \text{PrO}_2$ , the  $\xi \rightarrow \iota$  and the  $\alpha \leftrightarrow \iota$  transitions.

| Transition                       | Temperature range (°C) | EA (kJ.mol <sup>-1</sup> )                                       |
|----------------------------------|------------------------|--|
| $\phi \rightarrow \beta$         | 368 to 460             | -151(16) avg   |
| $\beta \rightarrow \text{PrO}_2$ | 265 to 307             | 112.6kJ/g-atom of O <sup>1</sup><br>Equivalent to 306.3          |
| $\xi \rightarrow \iota$          | 535 to 570             | 189.7 (oxidation) <sup>2</sup>                                   |
| $\alpha \leftrightarrow \iota$   | 655 to 715             | 255.0 (reduction) <sup>3</sup><br>314.0 (oxidation) <sup>3</sup> |
| $\sigma \rightarrow \theta$      | 1224 to 1273           | 1219.9   |

<sup>1</sup> (Hyde *et al* 1965)<sup>2</sup> (Inaba *et al* 1980)<sup>3</sup> (Inaba *et al* 1981)

Table 9.3 Kinetic data for the Pr-O system.

Whilst there is little kinetic data against which to review the results from this thesis, the transitions in the high oxygen composition of the phase diagram are all considerably less than those involving the C  $\rightarrow$  B phase transitions in the sesquioxides. It is known that the activation energies for the C  $\rightarrow$  B transformation in the intermediate weight oxides are in the range 500 to 800kJ.mol<sup>-1</sup> (Stecura 1966). It should be expected that activation energies in the high oxygen region of the Pr-O system would be significantly less, because of the ease with which oxygen exchanges between the solid and the gas phase and indeed this is the case with the above data.

There were two notable results from the DSC-TG work on Pr-O. Firstly, the exact pathway through the phases appears to depend upon heating rate. Figure 8.31 shows that for the slower heating rates (2K/min and 1K/min) the pathway for ascending temperature is  $\phi \rightarrow \epsilon \rightarrow \beta \rightarrow \delta \rightarrow \alpha \rightarrow \iota \rightarrow \theta$ . However, for the faster ramps (20K/min down to 4K/min), the pathway is  $\phi \rightarrow \epsilon \rightarrow \delta \rightarrow \beta \rightarrow \alpha \rightarrow \iota \rightarrow \theta$  i.e. the appearance of  $\beta$  and  $\delta$  are reversed. The former path is the expected one when considering the temperature range through which the species occur in the phase diagram (figure 1.9).

However, it appears that for this to be observed, a slow and prolonged input of heat is required. Secondly, Eyring and his co-workers were only able to demonstrate the existence of the  $\epsilon$  phase up to 45mm Hg pressure, and yet it appears to be present in the 4, 7, 10 and 20K/min ramps of figure 8.31, recorded at atmospheric pressure. The appearance of the  $\epsilon$  phase in the DSC-TG data was always slight, being no more than an inflexion in the curve, although its prominence increased with temperature ramp. However, it does seem reasonable that its existence at ambient temperature is possible, since the other two phases in this close triplet ( $\beta$  and  $\delta$ ) are merely the same structure but with different oxygen content.

## 9.6 REDRAWING THE PHASE DIAGRAMS

Table 9.4 lists the temperatures of phase transformations in  $\text{Ln}_2\text{O}_3$  recorded historically and also in this work.

| Oxide                   | Phase change      | Temperature (°C) | Author                        |
|-------------------------|-------------------|------------------|-------------------------------|
| $\text{La}_2\text{O}_3$ | C $\rightarrow$ A | 450              | Stecura <sup>1</sup>          |
| $\text{Nd}_2\text{O}_3$ | C $\rightarrow$ A | 850-1050         | Stecura <sup>1</sup>          |
| $\text{Sm}_2\text{O}_3$ | C $\rightarrow$ B | 950-1100         | Stecura <sup>1</sup>          |
| $\text{Eu}_2\text{O}_3$ | C $\rightarrow$ B | 1072-1347        | Beljaev <sup>2</sup>          |
|                         |                   | 1334             | My work                       |
|                         |                   | 1297             | Sun <i>et al</i> <sup>3</sup> |
|                         |                   | 1050-1300        | Stecura <sup>1</sup>          |
|                         |                   | 1175-1200        | Ainscough                     |
|                         |                   | 1127             | <i>et al</i> <sup>4</sup>     |
| $\text{Gd}_2\text{O}_3$ | C $\rightarrow$ B | 1334-1500        | My work                       |
|                         |                   | 1397             | Sun <i>et al</i> <sup>3</sup> |
|                         |                   | 1260-1400        | Stecura <sup>1</sup>          |
| $\text{Yb}_2\text{O}_3$ | C $\rightarrow$ B | 1500+            | My work                       |

<sup>1</sup> (Stecura 1966) <sup>2</sup> (Beljaev 1974) <sup>3</sup> (Sun *et al* 2003) <sup>4</sup> (Ainscough *et al* 1975) <sup>5</sup> (Antic *et al* 1997)

Table 9.4 Temperatures of phase transformations in  $\text{Ln}_2\text{O}_3$ .

To reflect the data in table 9.3, the phase diagram in figure 1.5 has been redrawn below.

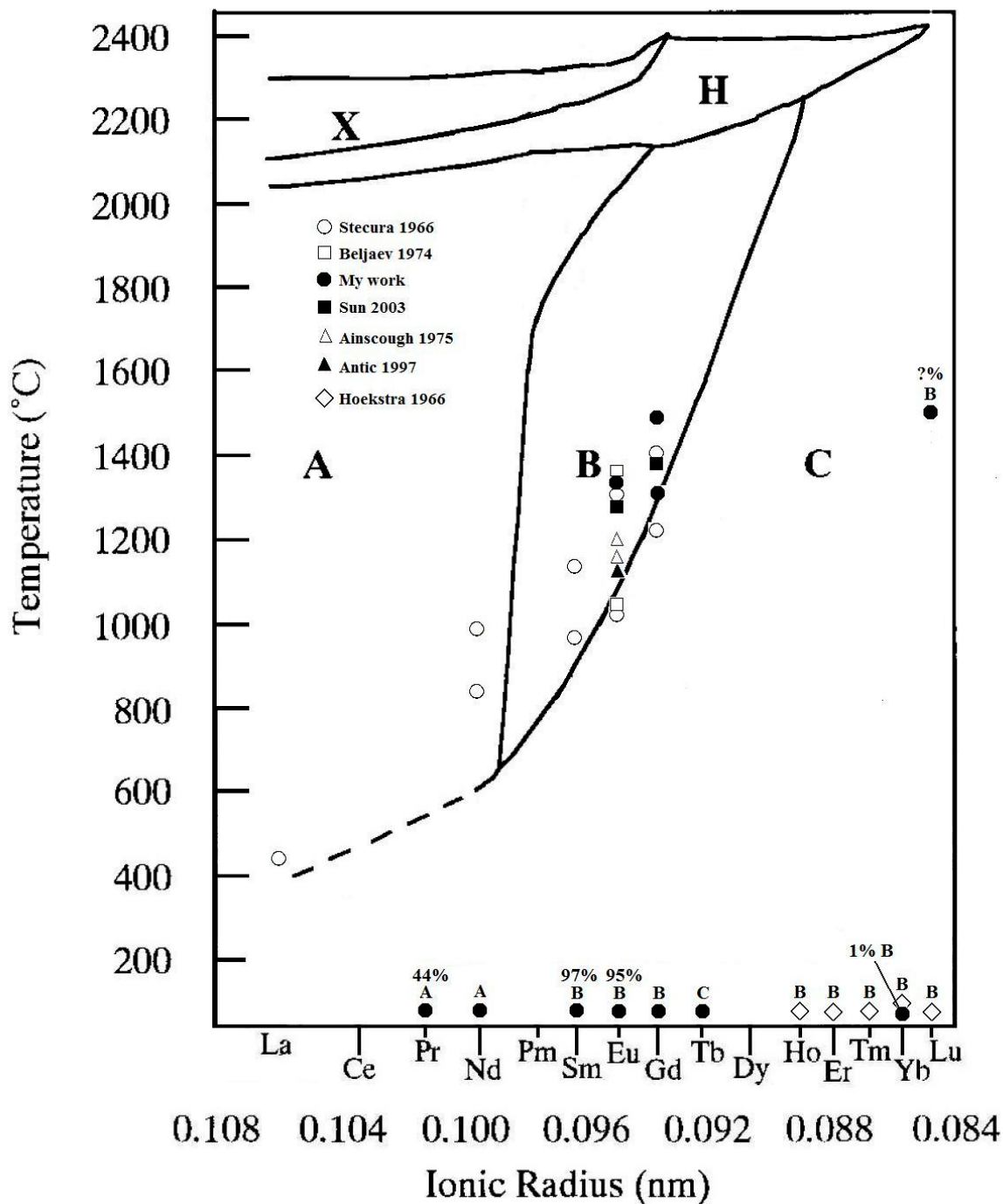


Figure 9.1 Amended phase diagram for the lanthanide sesquioxides.

Where conversion temperatures are stated, much of the work following that of Foëx and Traverse is consistent with figure 1.5 i.e. the data follows the C → B boundary. However, there are discrepancies. It has been demonstrated that it is possible to flame synthesise and quench monoclinic  $\text{Er}_2\text{O}_3$  from 2800°C (Guo, Harvey *et al* 2007). Monoclinic erbia has also been created between 9.9 and 16.3GPa at 1000°C and

quenched (Guo, Zhao *et al* 2007). Yet in figure 1.5  $\text{Er}_2\text{O}_3$  is clearly shown as having no B-type phase. My work has shown that a small percentage of  $\text{Yb}_2\text{O}_3$  was present after heating for 5 hours at  $1500^\circ\text{C}$  and quenching. The percentage conversion at this temperature is not known, but it is clear that phases exist contrary to the phase diagram. What is needed is an estimate for where the  $\text{C} \rightarrow \text{B}$  boundary continues after  $\text{Gd}_2\text{O}_3$ . Looking at Stecura's data, the temperature range across which the transformation occurs to any degree decreases with increasing atomic number of the lanthanide. For example, the range for  $\text{Nd}_2\text{O}_3$  is 200 degrees and for  $\text{Gd}_2\text{O}_3$  it is 122 degrees. Assuming a linear relationship and extrapolating to  $\text{Yb}_2\text{O}_3$  gives a value of approximately zero for the range. Clearly this is not reasonable, as we would expect some kinetic element to any data collected. However, it may be that the range is indeed very narrow. With only one data point collected in my work it is not possible to draw the new boundary, but it must encompass the point at  $1500^\circ\text{C}$  recorded in section 7.2 with  $\text{Yb}_2\text{O}_3$ . It may be that it also encompasses the oxide  $\text{Lu}_2\text{O}_3$ .

Also of note is the stability of many of the B-type oxides. My work has shown that monoclinic  $\text{Eu}_2\text{O}_3$  and  $\text{Gd}_2\text{O}_3$  are stable at ambient temperature i.e. the reaction is not reversible. The commercial sample of  $\text{Eu}_2\text{O}_3$  already contained a trace of B-type phase and the sample of  $\text{Sm}_2\text{O}_3$  contained 97% B-type phase, contrary to the supplier's information. The existence of heavier oxides at ambient temperature after heating to  $2800^\circ\text{C}$  and quenching has been demonstrated (Guo, Harvey *et al* 2007).

The work in chapter 8 did allow a study of the existence of the  $\sigma$  phase of Pr-O above the temperature reached by Hyde et al and figure 9.2 shows this pathway.

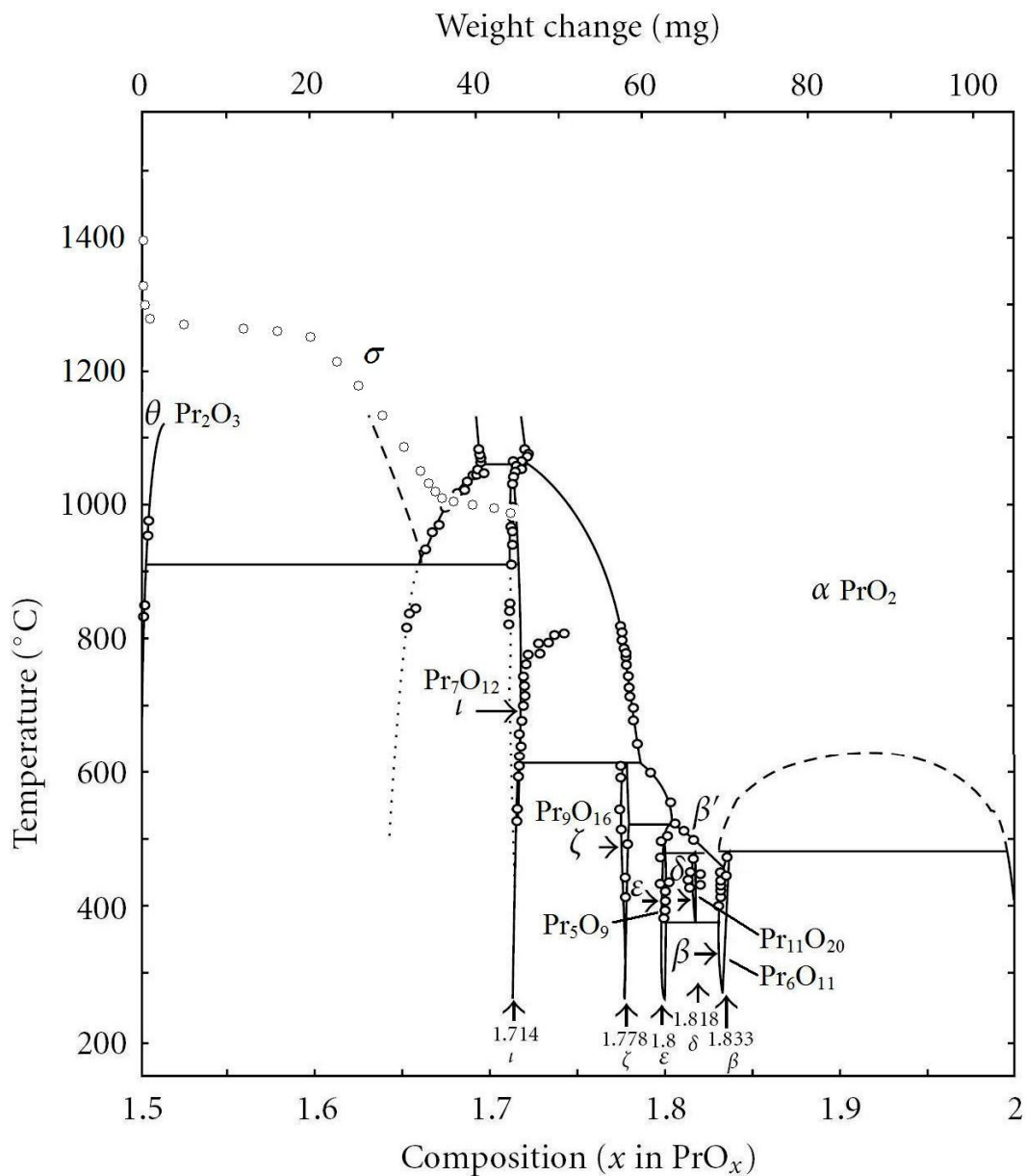


Figure 9.2. Amended phase diagram for the praseodymium-oxygen system showing the  $\sigma$  phase.

## 9.7 SUGGESTED FUTURE WORK

The most pressing work must be the obtaining of DSC data for  $\text{Nd}_2\text{O}_3$ ,  $\text{Sm}_2\text{O}_3$  and  $\text{Eu}_2\text{O}_3$  to enable a kinetic study. The results could then be compared to those of Ainscough and Stecura and to the boundary line for the cubic-monoclinic interface in figure 1.5.

The monoclinic forms of the heavier lanthanide sesquioxides (Sm-Yb) are now all known to exist. Heating ytterbia for longer in a furnace and quenching is a possibility but considering the phase diagram in figure 1.5 the XRPD pattern might need to be recorded in situ. If this were possible then a kinetic study could be made. It would also enable the redrawing of the C  $\rightarrow$  B boundary. However, such facilities are rare and the intense conditions detrimental to the sample environment. An alternative would be to melt and fuse the material in an oxy-acetylene flame, grind up the cooled solid and run the pattern again, on the assumption that it would remain stable back to ambient temperature. Monoclinic Sm<sub>2</sub>O<sub>3</sub> has been obtained by this method (Douglas and Staritsky 1956), although of course the stability of samaria at ambient temperature would be far greater than that of B-type ytterbia. However, there is a possibility that the B phase of ytterbia might be locked in on fusing and even if 100% conversion is not retained, there may be enough product phase present to enable the atom positions to be determined. That monoclinic Er<sub>2</sub>O<sub>3</sub> was quenched to ambient conditions (Guo *et al* 2007) gives reason to believe that it may be possible with Yb<sub>2</sub>O<sub>3</sub>.

Regarding the existence of the  $\epsilon$  phase, the conflicting work of Eyring *et al* with figure 8.31 warrants further investigation. It appears that a fast heating rate is needed to more clearly show the transition from the  $\phi$  phase. The work in 6.3.1.4 could be repeated, and augmented with ramps at, say, 30K/min and 40K/min, which is the limit of the machine. Also, XRPD patterns could be recorded at a much faster heating rate to identify any change in the Bragg reflections attributable to the  $\epsilon$  phase. A characteristic region of  $2\theta$  would need to be identified in order to greatly reduce the counting time and allow the temperature to be changed more rapidly. Alternatively, the machine could be pre-heated to the required temperature and the sample mounted directly into a hot environment.

There exists the possibility of studying other series of compounds in which the recorded powder diffraction patterns and/or structures are not available. Compounds of the lanthanides are of particular interest because of the steady contraction in cell size that is seen across any particular series. This is a reflection of the lanthanide contraction of ionic radius across the series of tripositive lanthanide ions. This feature of lanthanoid

compounds means it is often possible to predict the structure of an unprepared species based on the structures of its neighbours in that particular series.

There are some absences in the anhydrous lanthanoid trichlorides. The members of the series  $\text{LnCl}_3$  are hexagonal from lanthanum to gadolinium. From terbium onwards there are hexagonal, tetragonal and orthorhombic structures present. However, from analysis of the Daresbury database, no crystal structures appear to have been recorded for the trichlorides of samarium, holmium, erbium, ytterbium and lutetium. In the PDF-2 database there are cell parameters for all except  $\text{HoCl}_3$ .

A review of the efficacy of the indexing programs within the CRYSFIRE suite would be of interest. It had been demonstrated in my preliminary work that the programs can often fail even for XRPD patterns of high symmetry (even cubic) systems.

## REFERENCES

- Adachi, G. and Imanaka, N. *Chem. Rev.* 1998, 98, 1479-1514
- Ainscough, J.B., Moore, D.A. and Osborn, S.C. *J. Nucl. Mat.* 1975, 55, 229-232
- Aldebert, P. and Traverse, J.P. *Mater. Res. Bull.* 1979, 14, 303
- Aléonard, S. and Pouzet, C. *J. Appl. Crystallogr.* 1968, 1, 113
- Anderson, J.S. and Gallagher, K.J. *J. Chem. Soc.* 1963, 52-61
- Antic, B., Mitric, M. and Rodic, D. *J. Phys.: Condens. Matter*, 1997, 9 363-374
- ASTM: ASTM E473 - 11a Standard Terminology Relating to Thermal Analysis and Rheology. Website at <http://www.astm.org/Standards/E473.htm>
- Avrami, M. *J. Chem Phys* 1939, 7, 1103, *ibid* 1940, 8, 212, *ibid* 1941, 9, 177
- Beljaev, R.A. *Svoistva Okislov Evropiya (Moskva: Atomizdat)* 1974
- Bernal, S., Blanco, G., Gatica, J.M., Omil, J.A.P., Pintado, J.M. and Vidal, H. *Chemical Reactivity of Binary Rare Earth Oxides*, in *Binary Rare Earth Oxides*, pg 9-56, Kluwer (2004). eBook ISBN 1-4020-2568-8
- Bjurström, T. *Z. Physik*, 1931, 69, 346
- Boultif, A. and Louër, D. *J. Appl. Cryst.* 2004, 37, 724-731
- Brauer, G. *Structural and solid state chemistry of pure rare earth oxides and hydroxides* in *Progress in the science and technology of the rare earths*, Vol. 3, Oxford: Pergamon Press (1968)
- Bunn, C.W. *Chemical Crystallography*, pg 144, Oxford: Clarendon Press (1961).
- Černý, V. A thermodynamic approach to the travelling salesman problem: An efficient simulation. *J. Optim. Theory Appl.* 1985, 45, 41-51
- CCP14 Collaborative Computational Project website <http://www.ccp14.ac.uk>
- Coutures, J.P., Coutures, J., Renard, R. and Benezech, G. *R. Acad. Sci.* 1972, 275, 1203
- Cromer, D.T., *J. Phys. Chem* 1957, 61, 753
- David, W.I.F., Shankland, .K., van de Streek, J., Pidcock, E., Motherwell, W.D.S. and Cole. J.C. *J. Appl. Cryst.* 2006, 39, 910-915
- D'Eye, R.W.M and Wait, E. *X-Ray Powder Photography in Inorganic Chemistry*, pg 80-83, Butterworths Scientific Publications (1960)
- DeWolff, P.M. *Acta Cryst.* 1957, 10, 590
- Dong, C. PowderX, hosted on the CCP14 website <http://www.ccp14.ac.uk/solution/indexing/>

Douglass, R.M. and Staritsky, E. *Anal. Chem.* 1956, 28, 552

Durisch, W. and Bitnar, B. *Solar Energy Materials and Solar Cells* 2010, 94, 960-965

Eyring, L. *Handbook on the Physics and Chemistry of Rare Earths*, Vol 3 pg 337, North-Holland, Amsterdam (1979)

Favre-Nicolin, V. and Černý, R. *J. Appl. Cryst.* 2002, 35, 734-743

Feldner, K. and Hoppe, R. *Z. Anorg. Allg. Chem.* 1980, 471, 131

Foëx, M. and Traverse, J.P. *Rev. Int. Hautes. Temp. Réfract.* 1966, 3, 429

Haire, R.G. and Eyring, L. *Comparisons of the binary oxides in Handbook on the physics and chemistry of the rare earths: Lanthanides/actinides chemistry*, Vol. 18, pg 413-503, Amsterdam: Elsevier Science (1994)

Goldschmidt, V.M., Ulrich, F. and Barth, T. *Skrifter Norske Videnskaps-Akad. Oslo: Mater. Naturv.* 1925, K1, 5

Grier, D. and McCarthy, G., North Dakota State University, Fargo, North Dakota, USA, ICDD Grant-in-aid, (1991)

Guentert, A. and Mozzi, B. *Acta Cryst.* 1958, 11, 746

Guo, B., Harvey, A.S., Neil, J., Kennedy, I.M., Navrotsky, A. and Risbud, S.H. *J. Am. Ceram. Soc.* 2007, 90, 3683-3686

Guo, Q., Zhao, Y., Jiang, C., Mao, W., Wang, Z., Zhang, J. and Wang, Y. *Inorg. Chem.* 2007, 46, 6164-6169

Harris, K.D.M., Johnston, R.L. and Kariuki, B.M. *Acta. Cryst.* 1998, A54, 632-645

Harris, K.D.M., Tremayne, M., Lightfoot, P. and Bruce, P.G. *J. Am. Chem. Soc.* 1994, 116, 8, 3543-3547

Hesse, R. *Acta. Cryst.* 1948, 1, 200-207

Hoekstra, H.R. *Inorg. Chem.* 1966, 5, 754-757

Hoekstra, H.R. and Gingerich, K.A. *Science* 1964, 146, 1163

Hull, A.W. and Davey, W.P. *Phys. Rev.* 1921, 17, 549

Hyde, B.G., Bevan, D.J.M. and Eyring, L. *Phil. Trans. R. Soc. Lond. A*, 1966 vol. 250 no. 1106, 583-614

Hyde, B.G., Garver, E.E., Kuntz, U.E. and Eyring, L. *J. Phys. Chem.* 1965, 69, 1667-1675

ICDD Powder Diffraction File PDF-2 database sets 1-45, Pennsylvania Joint Committee on Powder Diffraction Standards, International Centre for Diffraction Data, 1995 (CD ROM)

ICSD Daresbury Laboratory ICSD crystal structure database originally hosted at <http://cds/dl/ac/uk>

Inaba, H., Lin, S.H. and Eyring, L. *J. Solid State Chem.* 1981, 37, 58-66

Inaba, H., Pack, S.P., Lin, S.H. and Eyring, L. *J. Solid State Chem.* 1980, 33, 295-304

Ito, T. *Nature*, 1949, 4174, 755

Jander, W. *Z. Anorg. Allg. Chem.* 1927, 166, 31-52

Kashaev, A.A., Ushchapovskii, L.V. and Il'in, A.G. *Kristallografiya*, 1975, 20, 192-193

Kato, H., Asakura, K. and Kudo, A. *J. Am. Chem. Soc.* 2003, 125 issue 10, 3082-3089

Kirkpatrick, S., Gellett, C.D. and Vecchi, M.P. *Science*, 1983, 220 621-630

Kissinger, H. *J. Res. (NBS)*, 1955, 4, 217-221

Kohlbeck, F. and Hörl, E. M. *J. Appl. Cryst.* 1978, 11, 60-61

Krishna, M. G., Rajendran, M., Pyke, D. R., and Bhattacharya, A. K. *Solar Energy Materials and Solar Cells*, 1999, 59, 337-348

Larson, A.C. and Von Dreele, R.B. *General Structure Analysis System (GSAS)*, Los Alamos National Laboratory Report LAUR 86-748 (1994)

Laugier, J. and Bochu, B. *A modified version of CELREF for analysing the solutions given by the CRYSFIRE suite.* Hosted on the CCP14 website <http://www.ccp14.ac.uk/solution/indexing/>

Le Bail, A. *Materials Science Forum* 2001, 378-381, 65-70

LeBail, A., *McMaille: Monte Carlo and grid search powder pattern indexing program*, 2006. Hosted on the CCP14 website <http://www.ccp14.ac.uk/solution/indexing/>

Le Bail, A, Cranswick, L SDPD Round Robin 2002 Results hosted at <http://www.cristal.org/SDPDRR>

Lipson, H. *Acta. Cryst.* 1949, 2, 43-45

Marsh, J. *J. Chem. Soc.* 1946, 15-17

Metropolis, N., Rosenbluth, A.W., Rosenbluth, M.N., Teller, A.H. and Teller, E. *J. Chem. Phys.* 1953, 21, 1087-1092

Meyer, C., Sanchez, J.P. and Thomasson, J. *Phys. Rev. B.* 1995, 51, 187-193

Norrby, L.J. *J. Chem. Educ.* 1991, 68(2), 110

NETZSCH: user manual document *NGB • STA449 F3 • 2000 • 0308 • MMM*. Website at <https://www.netzsch.com>

Prandtl, A. *Z. Anorg. Chem.* 1925, 149, 235; *ibid* 1938, 238, 225

Pyykkö, P. and Descleaux, J.P. *Acc. Chem. Res.* 1979, 12(8), 276-281

Rietveld, H.M. *J. Appl. Cryst.* 1969, 2, 65-71

Rodriguez-Carvajal, J. *Physica B.* 1993, 192, 55

Roisnel, T. and Rodriguez-Carvajal, J. 2010 Hosted on the CCP14 website  
<http://www.ccp14.ac.uk/solution/indexing/>

Saiki, A., Ishizawa, N., Mizutani, N. and Kato, M. *Acta Cryst. B* 1984, 40, 76-82

Shannon, R.D. *Acta. Cryst.* 1976, A32, 751-761

Shirley, R. *The Crysfire 2002 System for Automatic Powder Indexing: User's Manual.*  
 The Lattice Press, 41 Guildford Park Avenue, Guildford, Surrey GU2 7NL, England  
 (2002)

Shirley, R. and Louër, D. *Acta Cryst.* 1978, A34, S382

Siddiqui, I. and Hoppe R. *Z. Anorg. Allg. Chem.* 1970, 374, 225

Sonström, P., Birkenstock, J., Borchert, Y., Schilinsky, L., Behrend, P., Gries, K.,  
 Müller, K., Rosenauer, A. and Bäumer, M. *ChemCatChem*, 2010, 2, 694-670

Warshaw, I. and Roy, R. *J. Phys. Chem.* 1961, 65 2048-2051

Stecura, S., National Bureau of Mines (USA) report 6166, 1966

Sun, L., Liao, C. and Yan, C. *J. Solid State Chem.* 2003, 171, 304-307

Sun, X.L., Tok. A.I.Y., Huebner, R. and Boey, F.Y.C. *J. European. Ceram. Soc.* 2007,  
 27, 125-130

Tamman, G. *Z. Anorg. Allg. Chem.* 1925, 149, 21-34

Tamman, G., *States of Aggregation*, Translation by R.F. Mehl, New York (1925)

Taupin, D. *J. Appl. Cryst.* 1973, 6, 380-385

Toby, B. H. EXPGUI: a graphical user interface for GSAS, *J. Appl. Cryst.* 2001, 34,  
 210-213

Urland, W., Feldner, K. and Hoppe, R. *Z. Anorg. Allg. Chem.* 1980, 465, 7

Visser, J.W. *J. Appl. Cryst.* 1969, 2, 89

Visser, J. and Shirley, R. *A modified version of Visser's ITO zone-indexing program,  
 using the Ishida & Watanabe PM criterion for zone evaluation*, 2000 (not yet  
 published)

Werner, P.E., Eriksson, L. and Westdahl, M. *J. Appl. Cryst.* 1985, 18, 367

Wontcheu, J. and Schleid, T. *Z. Anorg. Allg. Chem.* 2008, 634, 2091-2091

Wu, B., Zinkevich, M., Aldinger, F., Dingzhong, W. and Lu, C. *Journal of Solid State  
 Chemistry* 2007, 180, 3280-3287

Zachariasen, W.H. Skrifter Norske Videnskaps-Akad., Oslo: Matematisk-Naturvidenskapelig Klasse, 1928, 1-165

Zinkevich, M. *Progress in Materials Science*, 2007, 52, 597-647

Zintl, A. and Morawietz, B. *Z. Anorg. Chem.* 1940, 245, 26